

UNIVERSITY OF SOUTHAMPTON

FACULTY OF ENGINEERING AND THE ENVIRONMENT

Institute of Sound and Vibration Research

FEM Techniques for High Stress Prediction in Accelerated Fatigue Simulation

by

Marco Veltri

Thesis for the degree of Doctor of Philosophy

June 2017

UNIVERSITY OF SOUTHAMPTON

ABSTRACT

FACULTY OF ENGINEERING AND THE ENVIRONMENT

Institute of Sound and Vibration Research

Thesis for the degree of Doctor of Philosophy

FEM TECHNIQUES FOR HIGH STRESS PREDICTION IN ACCELERATED FATIGUE SIMULATION

Marco Veltri

This research is motivated by the need to accelerate fatigue analyses of complex mechanical systems, characterized by large numerical models, long time integration intervals and dynamic response. Numerical modelling is an essential tool for fatigue life determination of such systems. Despite the increased affordability of ever more capable hardware and software resources, however, the computational requirements combined with competitive time-to-market constraints remain a continued challenge for the structural durability engineer. In such an environment, the early detection of fatigue critical areas can lead to an informed reduction of the problem size, and a subsequent decrease in solution time and costs.

The investigation focuses on the applicability and merits of accelerated simulation procedures aimed at the fast identification of a subset of critical regions, also known as hotspots. The work presents the theory and a numerical validation study to support a novel method for the identification of fatigue hotspots, to be determined prior to entering the time domain problem. An original statistical assessment of risks and benefits in fatigue simulation acceleration provides the means for damage prediction quantification and comparison.

The proposed acceleration method is particularly suitable during the initial design stages of heavy-duty durability computations of complex mechanical structures typical of the transport and general machinery industry. The technique is applied to real life industrial cases in a comparative assessment with established practices, outlining applications, benefits and boundaries.

Table of Contents

Table of Contents	i
List of Tables.....	vii
List of Figures	ix
DECLARATION OF AUTHORSHIP	xix
Acknowledgements	xxi
Definitions and Abbreviations.....	xxiii
Chapter 1: Introduction	1
1.1 Background to fatigue simulation of mechanical systems	1
1.1.1 Early days of finite element modelling, fatigue and multibody dynamics simulation	2
1.1.2 Modern integrated CAE durability.....	3
1.1.3 Computational challenges in integrated durability	5
1.2 Motivation.....	8
1.3 Aims and objectives	9
1.4 Structure & Organisation	11
Chapter 2: Methods for fatigue simulation of mechanical systems	13
2.1 Part A: Time based dynamic simulation of mechanical system	13
2.1.1 Pseudostatic assumptions, unit loads and inertia relief.....	14
2.1.2 Dynamic solution with modal reduction techniques	17
2.1.3 Component-mode synthesis.....	21
2.1.4 Alternative component modes	26
2.1.5 Flexible bodies via component-mode synthesis in multibody systems ..	28
2.2 Part B: Numerical methods and modelling in fatigue analysis.....	29
2.2.1 Background and definitions for fatigue analysis	30
2.2.2 Local strain and energy modelling in fatigue.....	32
2.2.3 Fatigue and finite element simulation.....	33
2.2.4 Time history loads.....	33
2.2.5 Stress-strain combination parameters	34

2.2.6	Rainflow Cycle counting	35
2.2.7	Material fatigue models	38
2.2.8	Fatigue stress concentrations, notching and welds.....	42
2.2.9	Sources of variability and uncertainty in fatigue	44
2.2.10	Background to FE based accelerated fatigue simulation	48
2.2.11	Acceleration via model filtering.	52
2.3	Summary.....	56
Chapter 3:	Model filtering in accelerated fatigue simulation	59
3.1	Review of common assumptions in elimination based on peak-valley gating.	59
3.2	Treatment of errors in accelerated fatigue simulation	60
3.2.1	The All-Terrain Vehicle baseline test case.....	61
3.2.2	Approximations, errors and metrics in peak-valley filtering.....	62
3.2.3	Effects of damage value error, Error-Type I.....	63
3.2.4	Effects of damage ranking error, Error-Type II and III.....	67
3.2.5	False positives, Error-Type IV	69
3.2.6	Metrics for reliability and efficiency, Error-Type III and IV	70
3.3	<i>A priori</i> filtering alternative to online accelerated fatigue simulation.....	70
3.4	Summary.....	72
Chapter 4:	A priori hotspot filtering for simply supported beams and plates in bending.....	75
4.1	Aims and scope of the analytical investigation	75
4.2	Hotspot patterns in beams in bending under harmonic loading	76
4.2.1	Static and dynamic response to a concentrated harmonic force	78
4.2.2	Static and dynamic response under simple combined excitations.....	82
4.2.3	Stress concentrations from geometrical features	85
4.3	Harmonic response of simply supported plates in bending	85
4.3.1	Hotspot patterns under harmonic loading	87
4.4	Predictability of hotspots in beams and plates in bending	91
4.5	Hotspots prediction for a beam in bending with concentrated harmonic force ..	91
4.5.1	A priori hotspots candidates	92

4.5.2	Hotspot prediction metrics via diagnostic test.....	93
4.6	Summary and conclusions	96
Chapter 5:	Development of a priori hotspot prediction algorithms in FE based fatigue simulation	99
5.1	A priori accelerated fatigue simulation in FE framework	99
5.2	Hotspot prediction applied to FE processes	100
5.2.1	Hotspot prediction algorithm workflow	100
5.2.2	Element modal strain energy density.....	102
5.3	Implementation of a priori algorithm in MATLAB® with commercial FE codes ..	103
5.4	Application to thin plate in bending	104
5.4.1	Baseline fatigue analysis	106
5.4.2	A priori hotspot prediction	106
5.4.3	Multibody system of a dynamically responsive plate	107
5.4.4	Results for selected loading and boundary conditions	108
5.5	Application to thin L-plates in pseudostatic superposition of two corner forces.....	115
5.6	Observations for Test Cases 1-4	123
5.7	Chapter summary and conclusions.....	124
Chapter 6:	Fatigue simulation acceleration test cases	127
6.1	All-Terrain Vehicle fatigue analysis.....	127
6.1.1	Baseline simulations	127
6.2	Single event accelerated fatigue methods	128
6.2.1	Peak-valley and <i>first pass</i> fatigue analysis.....	128
6.2.2	Accelerated fatigue methods comparison	131
6.3	Duty cycle accelerated fatigue methods comparison	134
6.4	Summary and conclusions	138
Chapter 7:	Conclusions	141
7.1	Summary	141
7.2	Key findings.....	142

7.2.1	Simulation acceleration errors and metrics	142
7.2.2	Analytical models of beams and plates in bending.....	143
7.2.3	FE simulation of thin plates.....	144
7.2.4	FE simulation of thin L-plates	145
7.2.5	All-Terrain Vehicle single and duty-cycle simulation	145
7.3	Key Contributions to new knowledge	146
7.4	Areas for research continuation.....	147
7.4.1	A priori prediction with Bayesian update	148
7.4.2	Accelerated fatigue simulation with hybrid online-offline filtering.....	148
7.4.3	Accelerated fatigue simulation based on load sampling	148
7.4.4	Other industrial applications for collective damage index	149
7.5	Closing remarks	149
Appendices.....		151
Appendix A	Analytical and FE solutions of simply supported plates and beams in bending.....	153
A.1	Bernoulli-Euler beam formulation and modal energy density definition	154
A.1.1	Beam in bending analytical and FE modal validation	156
A.2	Kirchhoff formulation for plate in bending and modal energy density definition	157
A.2.1	Modal strain energy density.....	160
A.3	Analytical and FE validation of simply supported plates in bending	162
A.3.1	FE and analytical modes.....	164
A.3.2	Statically applied concentrated force	165
A.3.3	Harmonic response to single applied force.....	167
A.4	Solution sensitivities and performances	167
A.4.1	Sensitivity to modal basis truncation and load patch size	168
A.4.2	Static correction convergence study for plate in bending	171
Appendix B	Craig-Bampton method application to an All-Terrain Vehicle model	175
B.1	Background.....	175

B.2	Model description.....	175
B.3	Durability events schedule.....	178
Appendix C	Engineering software tools and versions	181
C.1	FE pre and post processing	181
C.2	FE based fatigue solvers.....	182
C.3	Multibody systems dynamics.....	182
C.4	Programming environment.....	183
Appendix D	Modal Strain Energy in FE simulation	185
D.1	Modal Strain Energy.....	185
D.2	Element Modal Strain Energy	186
List of References		189

List of Tables

Table 1. Qualitative comparison of selected methods in accelerated fatigue simulation.....	73
Table 2. Parameters description for uniform beam in bending	76
Table 3. Uniform beam parameters for baseline model	78
Table 4. Parameters for uniform plate in bending	86
Table 5. Parameters for baseline plate model.....	88
Table 6. Analogy between fatigue hotspot prediction and disease diagnosis testing ..	94
Table 7. Fixed boundary and Craig-Bampton (CB) modes of rectangular plate	105
Table 8. Summary of main fatigue analysis settings for baseline analysis	106
Table 9. Case 1 contingency tables at different prevalence values and for different a priori hotspot prediction model fractions	109
Table 10. Case 2 contingency tables at different fatigue damage prevalence values and with increasing model fractions in a priori hotspot prediction	112
Table 11. Contingency tables comparing a priori hotspot prediction, HPA, and two-pass accelerated fatigue simulation in L-plates	119
Table 12. Extended CDI statistics for case 4, perforated L-plate, comparing baseline results with a priori prediction (HPA) and two-pass method (2-Pass)	123
Table 13. All-Terrain Vehicle baseline fatigue analysis settings	128
Table 14. Solution time acceleration for single <i>Aggressive Hillwork</i> event with peak-valley gating respectively at 10% and 90% of maximum range.....	129
Table 15. Hotspot prediction assessment via contingency tables with varying assumed prevalence for Aggressive Hillwork event [24].....	134

Table 16. Fatigue durability schedule for duty cycle simulation [109].....	135
Table 17. Contingency tables for duty cycle analysis comparing limits only, two-pass and hotspot prediction algorithm (HPA)	136
Table 18. All-Terrain Vehicle collective damage index, CDI, statistics for duty cycle analysis.....	138
Table 19. Parameters description for uniform beam in bending	153
Table 20. Uniform beam parameters for baseline model	156
Table 21. Uniform beam in bending, analytical and FE natural frequencies	156
Table 22. Uniform plate parametric geometry and physical properties	158
Table 23. Parameters for baseline plate model	163
Table 24. Baseline simply supported plate, Analytical and FE natural frequencies [57].....	164
Table 25. Summary of All-Terrain Vehicle multibody model	176
Table 26. All-Terrain Vehicle frame, FE model and CMS description.....	177
Table 27. First fixed boundary and Craig-Bampton (CB) modes	178
Table 28. Full fatigue durability schedule for the All-Terrain Vehicle simulation [109]179	

List of Figures

Figure 1-1. Durability design cycle based on FE (quasi-static and modal transient) or MBD, with options for flex bodies integration via component-mode synthesis CMS (2.1.3) [24].....	4
Figure 1-2. Evolution of FE model size and scope over time, sources [6],[16], [19], [22], [25]–[34] and LAPCAD Engineering.	5
Figure 2-1. Effect of higher modes truncation to frequency domain response for an output quantity in MDOF systems [56],[57].....	19
Figure 2-2. FE example of a residual vector for a simply supported plate under a concentrated point loading located near an edge (10 fixed normal modes retained) [57].	21
Figure 2-3. Durability workflow integrating FE and multibody simulation with flexible bodies.....	29
Figure 2-4. Steel Weld Stress-Life curves, best and worst classes according to BS7608 Code of Practice for fatigue Design and Assessment of Steel structures [63]; plot generated in MSC Fatigue™ [68].	31
Figure 2-5. Resolution of normal stress to a critical plane; image from MSC Fatigue™ Theory Guide [68].	35
Figure 2-6. Regular cyclic signal (a) used for experimental test [2]; (b) excerpt of variable amplitude signal (uncalibrated) for a real life automotive suspension component [82].....	36
Figure 2-7. Rainflow cycle counting according to reservoir method [63].	37
Figure 2-8. Rainflow cycle counting histogram for a representative automotive suspension signal in Figure 2-6(b) [82]; the range, mean and counted cycles refer to 2800 seconds of signal duration; rainflow algorithm and graphics from DesignLife™ [83].	37

Figure 2-9. Bilinear S-N relationship in bi-logarithmic axes [63], [64]..... 39

Figure 2-10. (a) Strain-life curve (continuous line) in bi-logarithmic axes [2]; (b) Neuber's correction rule to convert linear elastic strains into elastic-plastic strains while preserving the deformation energy [2]. Images from MSC Software Corporation [84]. 40

Figure 2-11. Fatigue workflow based on rainflow counting and S-N material description, from [56]..... 42

Figure 2-12. S-N curve showing different scatter bands in different regimes, from [92]..... 45

Figure 2-13. Stress-Life Weld class F curve [63] centred between a 2 standard deviation scatter bands; graphics in MSC Fatigue™ [68]. 46

Figure 2-14. Contingency table in diagnostic testing with four possible classes. 48

Figure 2-15. A continuous signal (a) is equivalent in term of fatigue damage to a signal represented by its turning points, dashed line (b), [56]. 51

Figure 2-16. (a) Demonstration of multiple peak-valley application on 3 simultaneous channels. (b) A 70% gating on signal maximum range yields a 95% reduction in time history points. Peak-valley filtering and graphics in MSC Fatigue™ [68]. 52

Figure 2-17. The CAE fatigue time based flow diagram with the inclusion of offline and online filtering..... 54

Figure 3-1. All-Terrain Vehicle before instrumentation [109]..... 62

Figure 3-2. Example of combined loading where stress peaks occur at a time that is not a peak or valley in the isolated time histories [68]. 63

Figure 3-3. Effect of peak-valley with different filtering (% of peak) for the All-Terrain Vehicle *event-1*, with 112 simultaneous load channels, each with 157,000 points; peak-valley algorithm and graphics from MSC Fatigue™ [68]. 64

Figure 3-4. Fatigue life for the 500 most damaged elements in All-Terrain Vehicle event-5. The baseline reference result is compared to results at 10% and 90% gating levels [24].	65
Figure 3-5. Fatigue damage for most damaged elements in All-Terrain Vehicle, event-5. The highlighted area represents the collective damage at 0.5% model fraction.	66
Figure 3-6. Convergence study of collective damage index, CDI, at 0.1% and 10% model fraction and for different levels of peak-valley filtering (PVX).	67
Figure 3-7. Element damage rank in peak-valley filtering with 90% gating (PVX 90%) vs. baseline damage rank [24].	68
Figure 3-8. Critical element rank error % after peak-valley filtering with 90% gating (PVX 90%) [24].	69
Figure 4-1. Simply supported beam in bending with harmonic force F at $x=fa$.	76
Figure 4-2. Normalized frequency response of strain energy density, force located at 1/10 of the length ($fa=25.0$ mm, structural damping $\eta=0.1$).	78
Figure 4-3. Beam stress frequency response for harmonic force of 0.01 N amplitude positioned at 1/10 of beam length, structural damping $\eta=0.18$; the markers indicate the location of maximum stress amplitude [24].	79
Figure 4-4. Top view of diagram in Figure 4-3, the circled markers identify the locations of maximum stress [24].	79
Figure 4-5. Combined maximum stress pattern for forces symmetrically positioned at 1/10 (circle markers) and 9/10 of beam length (diamond markers).	80
Figure 4-6. Location of peak response in the frequency range [0 – 100], the force is located at 1/10 of beam, with varying structural damping coefficient.	81
Figure 4-7. Maximum stress patterns for 20 individual forces applied at regular intervals along the beam axis. The shaded areas show a larger shift per frequency increment.	82

Figure 4-8. Bending stress from the combination of equal intensity 0.01 N forces, in phase. Force(I) is located respectively at 1/11 (a), 3/11 (b) and 5/11 (c) of the beam length, while Force(II) is kept at beam half-length.....	83
Figure 4-9. Bending stress from the combination of 0.01 N forces in opposite phase. Force(I) is located respectively at 1/11 (a), 3/11 (b) and 5/11 (c) of the beam length, while Force(II) is kept at beam half length.	84
Figure 4-10. Response from a combination of mode 1 and mode 2 in terms of stress (a) and strain energy density (b). The combined peak stress (a) and peak strain energy density (b), are shifted from the individual peaks in the modes.	85
Figure 4-11. Simply supported rectangular plate with point force F at $x=fa$ and $y=fb$	86
Figure 4-12. Peak displacements and corresponding trace on plate in bending under harmonic load of 0.1 N amplitude, with frequency going from 0 to 100 Hz and located at $x=200.0$ mm and $y=90.0$ mm.....	88
Figure 4-13. Peak direct x, y components stress and Von Mises under harmonic load of 0.1 N amplitude, with frequency range from 0 to 100 Hz, located at $x=200.0$ mm and $y=90.0$ mm.....	89
Figure 4-14. (a) Von Mises envelope under single harmonic loading of 0.1 N amplitude, placed in the corner area $x=200.0$ mm, $y=90.0$ mm and with frequency solution range 0-100 Hz. (b) Top view [57].	90
Figure 4-15. (a) Strain energy density envelop for same loading condition as in Figure 4-14; (b) top view [57].	90
Figure 4-16. Bending beam modal strain energy density (SED) and resulting hotspots (red markers) for first three modes [24].	92
Figure 4-17. Static response in terms of strain energy density, SED, to a single point force applied at 1/10 of the beam dimension [24].	93

Figure 4-18. Frequency response peaks (dots) against bending beam predicted hotspots, represented by the shaded magenta areas and the static response band delimited by the parallel continuous lines [24].	93
Figure 4-19. Contingency table for hotspot prediction under static loading.	95
Figure 4-20. Bayesian parameters as a function of frequency for beam in bending in 3.1.2 [57].	96
Figure 5-1. Simulation flow diagram for the hotspot prediction algorithm using modes from component-mode synthesis, CMS.....	101
Figure 5-2. Hotspot prediction process implemented in MATLAB® with data from MSC Nastran® and for fatigue calculation with MSC Fatigue™.....	104
Figure 5-3. Thin rectangular plate, modelled in MSC Nastran®, detailing the location of a transversal unit load and the corner constraints obtained with rigid elements, RB2. Image generated in Patran®.	105
Figure 5-4. Mode threshold retentions of 0.1%, 0.2%, 0.4%, 1%, 5% and 10%, corresponds to model fraction respectively of 1% (a), 3% (b), 5% (c), 13% (d), 50% (e) and 76% (f). Images generated in Patran®.	107
Figure 5-5. Adams™ multibody system of the flexible plate and boundary constraints at rest position (a) and with vibrating stress countours during motion (b). Images generated in Adams/View™.	108
Figure 5-6. Case 1 response of first non-rigid modal coordinate (q_7) under sine sweep loading. Resonance is observed at the expected 15.7 Hz.	109
Figure 5-7. ROC diagram for Case 1, enforced motion [0-20 Hz] for 3 assumed levels of prevalence and the a priori filtering model fractions shown in Table 9.	110
Figure 5-8. Case 1 top damaged locations for different model fractions in hotspot prediction (HPA), compared with baseline result (topmost curve).....	111
Figure 5-9. Case 1 normalized collective damage index, $CDI\%$, at 0.1%, 1.0% and 5.0% model fraction obtained for a priori prediction algorithm (HPA), respectively with 1%, 3% and 5% of model retention.....	111

Figure 5-10. Case 1 response of first non-rigid modal coordinate ($q7$) to the harmonic loading at 10 Hz	112
Figure 5-11. ROC diagram for Case 2 comparing performance of a priori prediction and for different levels of prevalence.	113
Figure 5-12. Case 2 top damaged locations for different model fractions in hotspot prediction (HPA), compared with baseline result (topmost curve).	114
Figure 5-13. Case 2 normalized collective damage index, $CDI\%$, at 0.1%, 1.0% and 5.0% model fraction obtained for a priori prediction algorithm (HPA), respectively with 1%, 3% and 5% of model retention.	114
Figure 5-14. L-plate geometry showing supports and applied forces. Image generated in Patran®	115
Figure 5-15. Loading on top left corner comprises of 100 cycles at 50 N amplitude plus a single final cycle at 100 N.....	116
Figure 5-16. Loading on top right corner comprises 11 cycles at a 100 N amplitude..	117
Figure 5-17. Baseline unfiltered damage (log) distributed symmetrically across the plates. Image generated in Patran®	118
Figure 5-18. Two-pass filtered fatigue log of damage result for 6% model retention, visibly neglecting large contribution to the damage from the Top left loading. Image generated in Patran®	118
Figure 5-19. Fatigue result on a priori filtered model with 6% model retention. The results correctly capture the symmetry of the damage distribution (log scale). Image generated in Patran®	119
Figure 5-20. ROC diagram comparing hotspot prediction and two-pass for L-Plate (a) and perforated L-Plate (b), prevalence set at 3% with 6% retained model fraction. ..	120
Figure 5-21. Case 4, baseline log of damage distribution for perforated L-plate. Image generated in Patran®	120

Figure 5-22. Perforated L-plate damage distribution with two-pass (a) and a priori hotspot filtering (b). Images generated in Patran®.	121
Figure 5-23. Perforated L-plate damage value in top damaged locations: baseline, a priori hotspot prediction (HPA) and two-pass method (2-Pass).....	122
Figure 5-24. Test case 4, perforated L-plate collective damage index, <i>CDI</i> % at 0.1%, 1% and 3% comparing a priori algorithm (HPA) with two-pass on-line filtering method (2-Pass) at the same 3% model fraction.....	122
Figure 6-1. Fatigue life with Elements in order of decreasing damage for the single Aggressive Hillwork event, comparing unfiltered baseline to results after peak-valley filtering at 10% and 90% of maximum range [24].	130
Figure 6-2. Collective damage index, <i>CDI</i> %, at .1% and 10% mode fraction for unfiltered baseline analysis vs. different levels of peak-valley gating (PVX).....	130
Figure 6-3. Baseline normalized solution time according to Two-pass, Limits only and hotspot prediction (HPA).	131
Figure 6-4. Fatigue life vs. model fraction for Stress based hotspot at 65% from peak strain energy density filtering compared to alternative methods.....	132
Figure 6-5. Top 1% damaged locations, fatigue life vs. model fraction for Stress based hotspot filtering compared to alternative methods.	132
Figure 6-6. Fatigue life for top damaged elements represented in order of element ID. Boxed area points to missed hotspot [24].	133
Figure 6-7. Calculated critical elements (red shade) over predicted hotspots (dark wireframe). The insert close-up highlights a missed hotspot [24]. Patran® image.....	133
Figure 6-8. Duty cycle analysis: top damaged elements for the different acceleration method considered.....	135
Figure 6-9. Collective damage index, CDI, for All-Terrain Vehicle Duty Cycle case obtained at 0.1%, 1% and 3% model fraction, for different accelerated fatigue simulation methods.	137

Figure 6-10. Normalized collective damage index, CDI, for All-Terrain Vehicle Duty Cycle case obtained at 0.1%, 1% and 3% model fraction, for different accelerated fatigue simulation methods.....	137
Figure A-1. Simply supported beam in bending with harmonic force F at $x=fa$	154
Figure A-2. First normal mode at 18.822 Hz, for FE model comprising 32000 elements. Image generated in Patran®	157
Figure A-3. First normal mode at 18.822 Hz, for FE model comprising 32000 elements. Detail of the left multi point constraint (MPC) obtained with Nastran® RBE2 elements. Image generated in Patran®	157
Figure A-4. Simply supported rectangular plate with point force F at $x=fa$ and $y=fb$	157
Figure A-5. FE baseline model constituted of 9000 shell elements, "CQUAD4", in MSC Nastran® (C.1) with simply supported boundary conditions. Image generated in Patran®	163
Figure A-6. First six natural modes of FE baseline plate in bending as obtained with MSC Nastran® [57]. Images generated in Patran®	165
Figure A-7. Statically applied 0.1 N load centred at $x=210$ mm, $y=20$ mm, combined results of the analytical and FEM solutions for 2 sections, located respectively at $y=20$ and $y=30$. The Static FE and analytical solution overlap for both displacement (a) and strain energy density, SED, (b), [57]	166
Figure A-8. FE and analytical frequency response amplitude of direct stress y component, stress recovery location at $x=155$ mm and $y=26.7$ mm, under unit vertical harmonic loading at $x=155$ mm and $y=25$ mm [57]	167
Figure A-9. Static response in terms of displacements is nearly identical between 10 by 10 modal basis (100 modes) and 50 by 50 (2500 modes) – unit force positioned at $x=176.5$ mm and $y=3.18$ mm [57]	169
Figure A-10. Static response of strain x component showing no convergence up to 50 by 50 modal basis size (i.e. 2500 modes) [57].....	169

Figure A-11. Convergence rate of displacements, left (a), and stress, right (b), as function of the square root of the modal basis size; using the same total unit load with Dirac delta (first row), a finite small squared patch of 0.1 mm sides (middle row) and a squared patch of 1 mm sides (bottom row), [57].	170
Figure A-12. Dynamic response under 0.1 N harmonic load at 55.2 Hz, located at $x=155$ mm and $y=25$ mm, $\eta=0.1$. Max displacements (a), (c) and max stress components (b), (d) as function of square root of modal basis size. The convergence of the results in (c) and (d) is improved by a static correction basis comprising 100 by 100 static modes [57].....	172
Figure A-13. Effect of the static correction basis size with respectively 10 by 10 (a), 100 by 100 (b) and 1000 by 1000 modes (c), for the same loading conditions in Figure A-12 [57].....	173
Figure B-14. Multibody simulation model in commercial code Adams TM . Image generated in Adams/View TM	176
Figure B-15. Finite element model of the All-Terrain Vehicle frame with the 17 attachment points highlighted with their load distribution elements (RBE2). Images generated in Patran [®]	177
Figure B-16. Vertical spindle forces for event 5, Aggressive hillwork, describing respectively left-front (a), right-front (b), left-rear (c) and right-rear (d). Data source [109] , image generated in MSC Fatigue TM	180
Figure C-17. MSC Nastran [®] list of basic solution numbers and their description; the subset of solution used for this investigation is highlighted.	182

DECLARATION OF AUTHORSHIP

I, Marco Veltri, declare that this thesis and the work presented in it are my own and has been generated by me as the result of my own original research.

FEM Techniques for High Stress Prediction in Accelerated Fatigue Simulation

I confirm that:

1. This work was done wholly or mainly while in candidature for a research degree at this University;
2. Where any part of this thesis has previously been submitted for a degree or any other qualification at this University or any other institution, this has been clearly stated;
3. Where I have consulted the published work of others, this is always clearly attributed;
4. Where I have quoted from the work of others, the source is always given. With the exception of such quotations, this thesis is entirely my own work;
5. I have acknowledged all main sources of help;
6. Where the thesis is based on work done by myself jointly with others, I have made clear exactly what was done by others and what I have contributed myself;
7. Parts of this work have been published as:

M. Veltri, J. Zeischka, and N. S. Ferguson, "FEM-MBS techniques for stress concentration prediction and accelerated fatigue simulation," in *International Conference on Engineering Simulation: Effective Use and Best Practices, NAFEMS, Cheltenham, UK, 2008*.

M. Veltri, "FEM-MBS techniques for high stress prediction and accelerated simulation," in *International Conference on Accelerating the Future of CAE, NAFEMS, Oxford, UK, 2014*.

M. Veltri, "FEM Techniques for High Stress Detection in Accelerated Fatigue Simulation," in *XII International Conference on Recent Advances in Structural Dynamics, Southampton, UK, 2016*.

Signed:

Date:

Acknowledgements

I would like to express my utmost gratitude to my supervisor Dr Neil Ferguson for his support and guidance throughout the investigation. Neil combines rare professional skills with great interpersonal qualities, and always provided outstanding advice and recommendations. My thanks also go to the review committee, Dr Emiliano Rustighi and Professor Atul Bhaskar, for their fair comments and suggestions.

I would also like to thank Dr Neil Bishop for organizing the start of my research, as part of a US Air Force SBIR contract. Neil and his family provided wonderful support in my move from frantic Rome to the peaceful Surrey countryside. Likewise, my thanks and my admiration to Johann Zeischka, for being the inspiration behind the progression of my research towards topics and ideas that had been planted during our ground-breaking collaborations, first with Audi and later with Daimler Chrysler.

The All-Terrain Vehicle model is the result of an open collaboration between industry and academia led by the Fatigue Design & Evaluation Committee of the Society of Automotive Engineers. I wish to recognize the FD&E Committee of SAE for the value and spirit of such open collaboration. Likewise my thanks to the colleagues and friends at nCode, now part of HBM, who have strongly contributed to the All-Terrain Vehicle project. Special thanks go to Robert Cawte and Jeff Mentley for helping me locating some hard-to-find literature.

I would like to recognize MSC Software Corporation for their support through this investigation. The MSC UK office has been my second family ever since I moved to the UK. The support and encouragement that I have received from my colleagues is something that I will never forget, and that I can only hope one day to return. Special mention and gratitude goes to Dr Andrew Bell, Dr Arthur Hickson and Edwin De Vries.

I'm particularly grateful for the assistance provided by Ciaran on the run-up towards the final draft, and for the invaluable help I received from my father, Francesco, whose many years of professional writing have been of tremendous assistance. Lastly, I could not have reached this submission without the relentless support, care and love of my closest family members - my parents Franco and Carla, brothers Andrea and Arianna, my partner Monica and our precious Uma. I look forward to my life as a full time son, brother, uncle, partner, father and friend. I've got my work cut out again

Definitions and Abbreviations

0 Null matrix

2-Pass Two-pass online model filtering method

a Beam or plate dimension in x

AF Acceleration factor

AFS Accelerated fatigue simulation

ATV All-Terrain Vehicle

b Slope of S - N curve

b Beam or plate dimension in y

BS British Standard

c Number of loading channels

C Material constant in S - N curve

C Damping matrix

$\bar{\mathbf{C}}$ Damping matrix in \hat{N} -modes reduced modal space

CAE Computer assisted engineering

CB Craig-Bampton CMS method

CDI Collective Damage Index

$CDI_{\#}$ Collective damage index for set number of entities

$CDI_{\%}$ Collective damage index for a model fraction

CMS Component-mode synthesis

CPU Central processing unit

D Diagnostic event in hotspot detection

D Fatigue damage; flexural rigidity for plate in bending

D_i Fatigue damage contribution in cumulative damage rule

DOF Degree of freedom

D_s Steady state magnification factor

E Young's modulus

e Strain energy density for beam and plate in bending

e_m Modal strain energy density for mode m in beam in bending

e_{mn} Modal strain energy density for mode (m, n) in plate in bending

e_{ni} Modal strain energy density for mode n and element i (in FEM)

Eq. Equation

\mathbf{f} Vector of nodal forces representing externally applied loads

F Transverse concentrated load on beam or plate in bending

\mathbf{f}_0 Spatial portion of the loading \mathbf{f}

$\mathbf{f}_{0,i}$ Spatial portion of the loading vector \mathbf{f}_i

f_a, f_b Coordinates of concentrated force F

FE, FEM Finite elements method

\mathbf{f}_i Loading with spatial distribution $\mathbf{f}_{0,i}$ and time scaling $f_i(t)$

$f_i(t)$ Time dependent portion of loading \mathbf{f}_i

$f(t)$ Time dependent portion of loading \mathbf{f}

FPR False positive rate

h Beam or plate thickness

H Hypothesis event with probability $P(H)$

H' Complement event of H

HPA Hotspot prediction algorithm

\mathbf{I} Identity matrix

I Moment of cross sectional area

ID FE entity identification number (element or node)

k Number of residual vectors in CB augmented modal base

\mathbf{K} Stiffness matrix

$\bar{\mathbf{K}}$ Generalized stiffness matrix

K_f Fatigue notch factor

\mathbf{K}_i Stiffness matrix of the i^{th} FEM element

K_t Stress concentration factor

m Mode index for beams and plates in bending (x direction)

m, m_1, m_2 Material constant in S - N curve, reciprocal of slope b

\mathbf{M} Mass matrix

\bar{m} Mode truncation index for bending modes (x direction)

$\bar{\mathbf{M}}$ Generalized mass matrix

MAP Maximum absolute principal

Max_i Maximum value in time history i

MBD Multibody systems dynamics

MDOF Multiple-degree-of-freedom

Min_i Minimum value in time history i

MNF Modal neutral file used by AdamsTM

MPC Multi-point constraint in MSC Nastran[®]

m_t Number of normal modes after truncation

n Mode index in FE modelling and in plates in bending (y direction)

\bar{n} Mode truncation index for bending modes (y direction)

N Total number of DOF (FE) or number of cycles (fatigue)

\hat{N} Number of truncated modes

N_0 Statistical minimum of the fatigue life distribution

n_1, n_2 Number of cycles in sequences with stress range S_1, S_2

na Not applicable

Neg Number of negative conditions in diagnostic testing

No. Number

$Offset_k$ Stress offset for channel k in stress recovery formula

$Offset_n$ Stress offset for mode n in stress recovery formula

$P_k(t)$ Load history for channel k in stress recovery formula

Pos Number of positive conditions in diagnostic testing

PSD Power Spectral Density

PVX Peak and Valley extraction and gating

Q Eigenvectors of Craig-Bampton eigenvalue problem

q Modal coordinates vector

q̂ Modal coordinates vector after truncation

q* Modal coordinates of orthogonal basis (CB method)

q_j Modal coordinate for mode *j*

q_m, q_{mn}, q_n Modal coordinate for mode *m*, (*m, n*) and *n*

q_n Modal coordinates in component with fixed boundary normal
modes (CB method)

r Frequency ratio

r Number of element in FE component

R Loading cycle ratio of min and max principal stresses

RBE Rigid body element

RFC Rainflow cycle counting

ROC Receiver operating characteristics

s Number of static correction modes

S Nominal or remote stress

S₁, S₂ Stress range in test case load history sequence

S.D. Standard deviation

SDOF Single-Degree-of-Freedom (systems)

S_e Fatigue strength, stress threshold at infinite life

SED Strain energy density

S_{eq} equivalent stress leading to identical damage

SF_k Load scaling factor for channel k in stress recovery formula

SF_n Load scaling factor for mode n in stress recovery formula

SLOC Small-load-omitting criterion

$S-N$ Stress-Life method

$SRI, SRII$ Stress level at 1 cycle on $S-N$ curve

S_u Ultimate tensile strength

TPR True Positive Rate

u Displacement in x direction in beam and plate in bending

\mathbf{u} Nodal displacements vector

U Strain energy

$\hat{\mathbf{u}}$ Nodal displacement vector after modal truncation

$\tilde{\mathbf{u}}$ Nodal displacement vector with mode-acceleration method

\mathbf{u}_0 Static solution under load \mathbf{f}

\mathbf{u}_{0i} Static solution under single channel loading \mathbf{f}_{0i}

\mathbf{u}_b Boundary nodes DOF (CB method)

\mathbf{u}_i Internal nodes DOF (CB method)

U_i strain energy of the i^{th} element

U_m Strain energy for mode m in analytical beam in bending

U_{mn} Strain energy for mode (m, n) in analytical plate in bending

U_n Strain energy for eigenvector n

U_{ni} Strain energy for mode n and element i

$\ddot{\mathbf{u}}_{RB}$ Rigid body acceleration in inertia relief method

v Displacement in y direction in plate in bending

V Volume

V_i Element volume of the i^{th} element

VM Von Mises

w Transverse displacement in beam and plate in bending

W_m Mass normalized mode m for beam in bending

W_{mn} Mass normalized mode (m, n) for plate in bending

\mathbf{Z} Matrix of residual vectors

\mathbf{z}_k Residual vectors

Greek symbols

α Model fraction (%) used in $CDI\%$ index

$\gamma_{xy}, \gamma_{xz}, \gamma_{yz}$ Shear strains plate in bending

δ Dirac delta function

ΔK stress intensity functions in ΔK - N fatigue curves

ε Strain

ε_x Strain x component in beam and plate in bending

ε - N Strain life curve

ε_y Strain y component in plate in bending

η Structural damping coefficient

λ Eigenvalue

$\bar{\Lambda}$ Diagonal stiffness matrix in \hat{N} -modes reduced modal space

ν Poisson's ratio

ξ Modal damping coefficient

ρ Material density

$\sigma_{0,i,j,k}$ Stress influence coefficient i,j for load channel k

$\sigma_1, \sigma_2, \sigma_3$ Principal Stresses

σ_a Stress amplitude in fatigue cycle

σ_{ar} Fatigue equivalent stress

$\sigma_{Assessed}$ Assessed stress in FE entity prioritization

$\sigma_{e,ij}$ Stress tensor i,j components at element e

$\sigma_{e0,ij}$ Stress tensor i,j components at element e under unit load

$\sigma_{e0,x_i}, \sigma_{e0,y_i}$ Surface stress tensor direct components at element e under unit load

$\sigma_{e,x}, \sigma_{e,y}$ Surface stress tensor direct components at element e

σ_{ij} Stress tensor component

σ_m Mean stress in fatigue cycle

σ_{MAP} Maximum absolute principal stress

$\sigma_{VM,i}$ Von Mises stress for load channel i

σ_x Stress x component in beam and plate in bending

σ_y Stress y component in plate in bending

$\tau_{e,xy}$ Surface shear stress components at element e

τ_{e0,xy_i} Surface shear stress at element e under unit load

τ_{xy} Shear stress in plate in bending

ϕ Rotation angle in fatigue critical plane

Φ Modal basis

$\widehat{\Phi}$ Truncated modal basis

Φ_A Augmented modal basis

Φ_c Constraint modes in Craig-Bampton method

Φ_{CB} Craig-Bampton transformation matrix

Φ_{CB}^* Orthogonal Craig-Bampton transformation matrix

ϕ_j Mode shape vector j

Φ_n Fixed boundary modes in Craig-Bampton method

ϕ_n^* Mode shape vector n in orthogonal Craig-Bampton base

Ω Maximum excitation frequency

ω, ω_j Circular frequency

ω_m Undamped natural frequency for mode m

ω_{mn} Undamped natural frequency for mode with index (m, n) in
plate in bending

Chapter 1: Introduction

Computer assisted numerical modelling is an essential tool for fatigue life determination of complex mechanical systems. Yet, despite a much-increased affordability of ever more capable hardware and software resources, the heavy computational requirements combined with market time constraints are a continued challenge for structural durability engineers.

This research is motivated by the need to accelerate fatigue analysis of complex mechanical systems, characterized by large numerical models, long time integration intervals and dynamic response calculations. In such systems, the early detection of fatigue critical areas can drive an important simplification of the problem size, leading to a sensible reduction in solution time and to immediate and relevant cost savings.

The investigation focuses on the applicability and merits of accelerated simulation procedures aimed at the identification of a subset of critical regions, also known as hot-spots, to be determined *a priori*, that is prior to solving the time domain problem.

A proposed acceleration method is deemed particularly suitable during the initial design stages in heavy-duty durability computations of complex mechanical structures typical of the transport and general machinery industries.

1.1 Background to fatigue simulation of mechanical systems

All industrial structures and components, from transport to energy production or home appliances, are expected to be economically viable and to fulfil their service without failure. For mechanical systems subjected to repeated loading, dedicated analysis and testing campaigns are deployed in order to investigate and prevent the onset of fatigue failure. Despite the associated considerable computational burden, dynamic simulation combined with structural analysis and fatigue life prediction is a cost-effective alternative to experimental testing, especially during the pre-prototype design stages.

1.1.1 Early days of finite element modelling, fatigue and multibody dynamics simulation

Finite Elements (FE) simulation [1] is at the heart of both industrial and academic design of complex mechanical systems. Yet the proposition to analyse a full engineering assembly for its dynamic behaviour can be a daunting task, with the size of the numerical models (car, airplane, wind turbine etc.) and the length of the integration time histories requiring ever-increasing CPU, data storage and access time. A dynamic solution could be required for subsequent fatigue damage assessment especially to address areas of high stress concentration under time variable load.

Fatigue damage is microstructure degradation accumulated under cyclic or otherwise variable amplitude loading, typically with maximum stress considerably lower than material yield [2], [3]. The primary fatigue analysis methods, the Stress-Life ($S-N$) and the Strain-Life ($\varepsilon-N$), estimate the expected fatigue life by comparing stress or strain levels with cycles obtained during material testing. In computer based durability simulation such fatigue analysis can be seen as a post-processing step to quasi-static and dynamic simulations, whose objective is the resolution of a stress or strain time history for any given component [4].

The FE method is the evolutionary result of centuries of analytical approximations that encompassed Euler, Rayleigh, Ritz and Galerkin [5] but it was with the advent of computers assisted engineering, CAE, of the sixties, under the strong impulse of aerospace research, that FE could demonstrate its value and potential on industrial scale applications. What was mostly an academic subject [6] quickly became a modern fundamental industrial engineering computational tool [7].

A similar parallel development, again initially driven by space industry requirements, led to the development of the dynamics of multibody systems [8] or MBD, multibody dynamics [9], into an independent branch of mechanics [10]. The 1980s saw the emergence of multibody systems commercial solutions being capable to model, simulate and animate complete mechanical systems including large displacements and large rotations. During this time fatigue testing and analysis was also similarly advanced by modern testing hardware and computational capabilities, promoting the emergence of more accurate theories based on local strain methods as well as the appearance of the first general purpose fatigue analysis computer programs. In 1984 Landgraf and Conle

[11] outlined the many roles and trends of computer assisted durability in automotive structures, including servo-assisted material testing, structural analysis, data acquisition, damage analysis and life prediction. The authors reported an estimated 30% potential cost saving by just implementing already existing technology in fatigue fracture prevention. As fatigue simulation moved upfront in the design cycle, the modern philosophy of *durability by design* took the place of the traditional testing for durability approach [12].

1.1.2 Modern integrated CAE durability

Modern integration of FE, multibody systems and fatigue simulation began in mid-1980s, this time under the strong needs of a thriving and highly competitive ground transport industry. Most noticeably the use of FE modal flexibility in multibody simulation, given in a good résumé by Shabana [13], led to step advancements both in quality and efficiency of dynamic durability simulation. The Center for Computer Aided Design of the University of Iowa investigated the integration of FE, multibody and fatigue analysis tools, accounting for modal structural flexibility in both the multibody dynamics and FE stress recovery for fatigue [14] [15].

In 1991 Conle and Mousseau [16] reported an analytical study of the fatigue life of a full body chassis using multibody systems simulation in combination with proving ground experimental data. The purpose of the study was to replicate analytically what was done through experimental test; the computationally intense calculations with the 'large' 1500 elements model allowed for only short duration sections of the vehicle during the track test. Most topics and methods addressed by Conle et al. are still current today, including the unit loading method, solid surface 'skin' with very-thin-shell elements, biaxial stress assessment and automated critical plane selection. The authors correctly anticipated that advances in computational power and algorithm efficiency would have soon enabled much increased complexity. Indeed, with the inclusion of well-established component-mode synthesis techniques, CMS, such as the Craig-Bampton method by aerospace application [17], the initial rigid-body quasi-static approach was improved with the practical integration of flexible bodies, mode-acceleration corrections, integrated fatigue solutions via component-mode stress/strain superposition [18] and fully analytical loads, paving the way to the techniques commonly deployed today [19].

In 2000 Ambrogi et al. [20] combined FE and multibody simulation to described the important effect on fatigue life that can be attributed to flexibility even for components with high rigidity. In 2005 Arczczewski and Frączek [21] showed different options for stress recovery in combined FE and multibody systems calculation and quantitatively demonstrated a case with superior accuracy of modal and displacement based method over force-based approaches. In the same year, Braccesi and Cianetti [22] demonstrated the maturity of the CAE modelling methods for dynamic simulation of mechanical systems including flexible components. The durability process presented was applied to an industrial automotive case, fully based on commercially available software and validated against experimental results.

In 2007 Wannenburg [23] proposed a general framework for mapping all common numerical methods in durability assessment applicable to vehicle structural design.

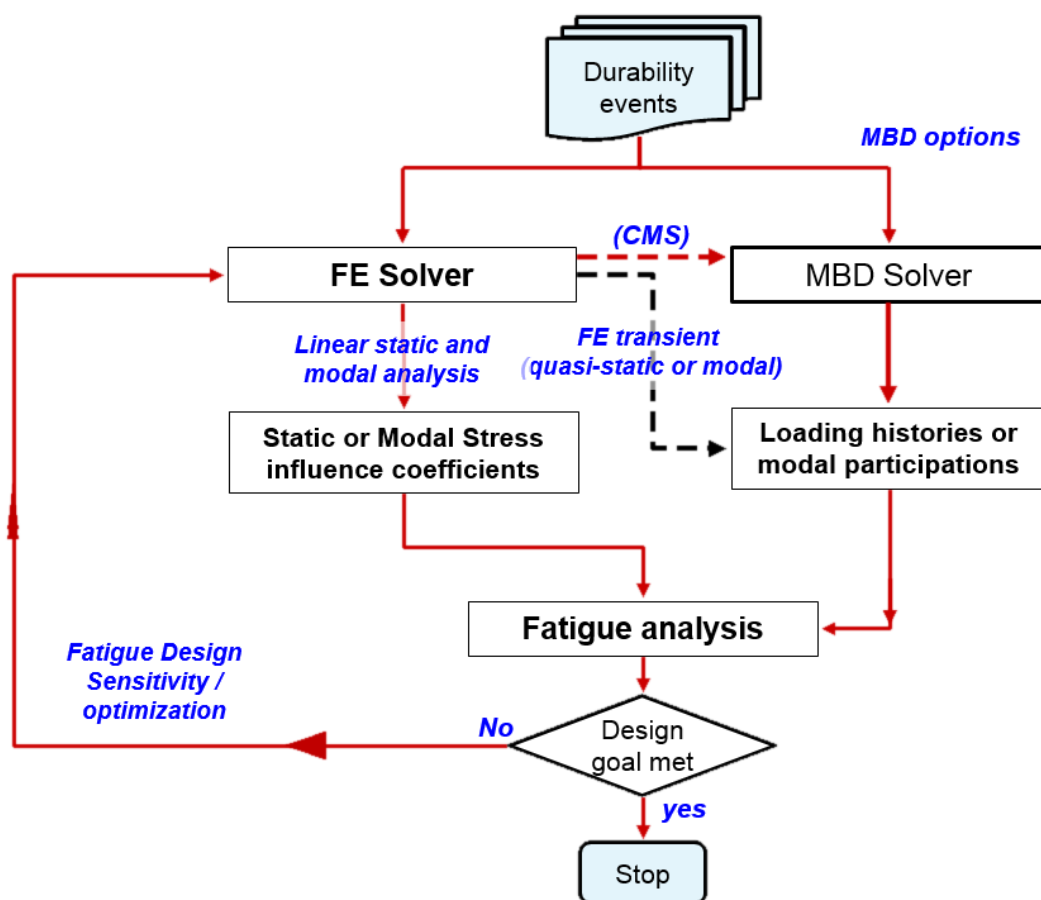


Figure 1-1. Durability design cycle based on FE (quasi-static and modal transient) or MBD, with options for flex bodies integration via component-mode synthesis CMS (2.1.3) [24].

1.1.3 Computational challenges in integrated durability

In this section, just as for the remaining of the thesis, the specific focus is towards the numerical challenges deriving from the size of the computational problem in fatigue simulation, rather than the quality of the data. The latter, of course, would remain as questionable as the simulation methods adopted for which dedicated literature is available.

Figure 1-1 presents a summary workflow of the common options in modern CAE time-based durability. The FE solver to the left side of the diagram is used to generate the influence coefficients from unit loading (quasi-static method) or the modal stresses (modal transient or CMS). Following the MBD solution path to the right of the diagram, the multibody solver can be efficiently deployed to provide the component loads even in long non-linear time transient events. Improved accuracy can be obtained with the inclusion of flexible components via CMS. In this case, the multibody solver directly calculates the component modal participations functions, leading to very efficient dynamic stress reconstruction directly in the fatigue solver.

Independent of the path chosen, the fatigue calculation at the bottom of Figure 1-1 requires stress or strain result recovery for all durability events. The whole process is repeated at each design cycle until fatigue design goals are met.

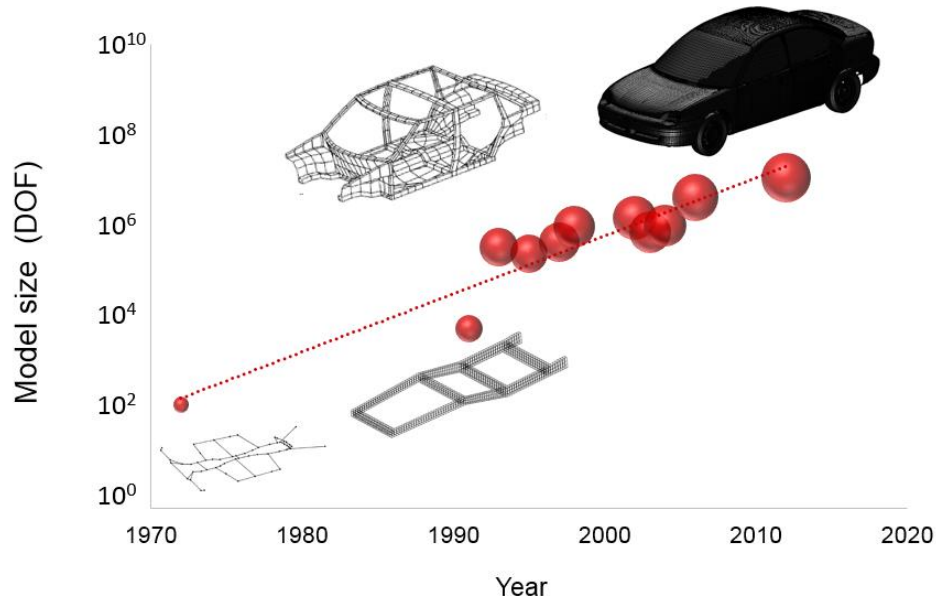


Figure 1-2. Evolution of FE model size and scope over time, sources [6],[16], [19], [22], [25]–[34] and LAPCAD Engineering.

Figure 1-2 shows the amazing progression of FE computational models in the automotive industry, from the few hundreds degrees of freedom of the early 1970s, to the tens of millions for present days. The large size of the numerical models combined with the multiple durability events determine that fatigue analysis is in practice only attainable at the cost of long processing times and/or by some degree of simplification.

From its inception to the present time, CAE fatigue calculation has been a compromise between accuracy and efficiency. The vehicle industry developed systematic routines and methods to reduce the numerical complexity, especially during ‘upfront durability’ at the early stages of design. Throughout the nineties successive authors [24], [25], [26], [36] [27], [32] described methods to limit the detailed fatigue life calculation to fewer critical areas and under selected critical events. If it became evident that all load case events need to be addressed [32], it was also understood that, in a structure characterized by many stress risers, connections and concentrated loads, only a small fraction of the model is expected to represent a fatigue concern. In the 1997 paper by Huang et al. [27] only 1% of the full vehicle body structure resulted in a Von Mises stress above 100MPa and only the top 100 of the 100,000 elements were selected as critical for fatigue.

Other authors took advantage of improved statistical methods for alternative frequency domain fatigue life prediction under stationary random loading [37]. In 1997 Dietz et al. [38] combined FE, multibody systems and fatigue to study railways bogies. They separated irregular single time transient events from stationary random operational loads deriving from track irregularities, for which linear system theory applies. Spectral densities inputs from track profiles and pre-calculation of stress load matrix led to fast calculation of stress covariance output matrix. Furthermore the same authors recognized the importance of identifying the most stressed locations for detailed fatigue analysis [39]:

“It is possible to perform modal stress calculations for all locations of a structure, but in most cases the resulting stress distributions will show locations which are heavily stressed under many different loading conditions, whereas other regions are almost unstressed therefore it is useful to perform modal stress calculations only for those critical locations”

Similarly, in 2005 Braccesi et al. [40] used component modal reduction in a linear state-space representation of the multibody system, leading to an efficient spectral estimation of the stress state. Within the linear assumptions and limited to stationary random processes, the evaluation of fatigue damage can be accurately performed for a generic system with flexible components using the Power Spectral Density matrix of element stress tensors.

Other modern authors advised regressing to simpler quasi-static methods if acceptable. In 2002 Haiba et al. [41] reviewed the life assessment techniques applied to dynamically loaded automotive components applicable to optimization algorithms including fatigue. Due to the complexity of dynamic and fatigue solutions, they recommended the use of quasi-static techniques when components operate substantially below their natural frequency. In 2006 Potukutchi et al. [31] described a method for obtaining a static load case correlating with potential durability critical areas and useful for fast design iterations in vehicle design. Aiming for fatigue simulation simplification in low production machines, in 2009 Wannenburg et al. [42], demonstrated possible applications for fatigue equivalent static loading in heavy vehicle design. In 2013 Lin of Chrysler Group [43] used d'Alembert's principle to convert experimentally acquired acceleration into additional operating load, with the aim to augment static stress with vibration stress without performing computationally intense dynamic analysis. In 2013 Rentalinen et al. [44] presented a fatigue approach based on FE sub-modelling and multibody systems analysis using quasi static stress recovery. In line with previous authors, Rentalinen remarked that:

“...even though computational capacity is increasing all the time, applying the finite element approach to a complex structure subject to dynamic multiaxial loading presents an overwhelming computational burden.”

Recently Braccesi et al. [45], again focusing on frequency domain life predictions, demonstrated that the exact spectral moments of the PSD functions matrix of element stress tensor are obtainable from only PSD functions matrix of its modal coordinates and from PSD functions matrix of inputs. For the cases presented the proposed simplification led to a speed-up of the standard computational time in excess of two orders of magnitude.

In summary, if current high computational power enables the use of FE models of virtually any required size, attempting to generate, store and process all results in durability solutions is often either unpractical or unattainable. Evidently, such considerations hold true across all industries deploying equivalent durability methods, including aerospace, general transport, offshore, machinery and wind energy. Furthermore, the problem under consideration is not a current limitation of hardware and software capacity. As Zu-Qing Qu in 2004 stated in his preface [46]:

“Although the computer speed and memory capacity continue to double every 18 months (Moore's law), the phenomenon that the demand of computer storage and speed will always exceed existing capabilities has been consistently demonstrated in finite element analysis during the past half century”

This statement holds true a decade later and, as shown by the trend in Figure 1-2, it is foreseeable that also in the future more computational power will simply lead to even more detailed modelling. The amount of data that is generated, stored, accessed and post-processed and the ensuing fatigue solution time constitute a steadily increasing burden. It is therefore even more necessary to reduce the problem size through modelling simplification.

1.2 Motivation

As will be detailed in a dedicated review in 2.2.10, the majority of academic research has focused on simulation acceleration by reduction of fatigue solution time, or *time editing*, with only a handful of references dedicated to prioritization and filtering of FE entities [38], [40], [44], [47], [48]. This is failing to address a major aspect in modern computational methods that is the trend towards ever increasing model sizes, often located on remote-access *cloud* storage. The typical 500 thousand degrees of freedom model of a vehicle full-frame of the late nineties [27] is currently upwards of 10 million [19]. Yet, regardless of the model size, only a small fraction of its surface/volume is expected to represent a fatigue risk [27], [39], [40].

In order to meet time and resources constraints, industry and commercial software developers often adopt simplification methods that are driven by empirical knowledge and require user judgment and intervention. Furthermore, in the literature reviewed no

evidence was found of a thorough comparative assessment between different acceleration techniques, nor of a tool to quantitatively estimate the possible error derived from the adopted simplifications. In summary, there is widespread usage of elimination techniques, assuming they will produce reliable results with beneficial effects, but the techniques are mostly empirical and unsupported by theory.

The investigation focuses on the applicability and merits of simulation procedures aimed at the early identification of a subset of critical regions, also known as hotspots, aiming to establish a framework for the assessment of fatigue simulation acceleration via elimination of low-stress entities, with particular focus on process automation and reliability.

1.3 Aims and objectives

The novel technique is based on two common conditions in industrial mechanical design:

- In a structure characterized by many stress risers, concentrated loads and boundary conditions, only a small fraction of the model is expected to represent a fatigue concern (a true hotspot).
- A higher range of stress, strain or strain energy density corresponds to a higher fatigue damage potential (a candidate fatigue hotspot).

Given the above, the further position is taken that, within certain measurable approximations, a sufficiently broad set of static correction and component modes can anticipate many areas of potential fatigue damage, the candidate hotspots, to be determined *a priori*, that is prior to solving the time domain problem, using threshold levels proportional to peak stress/strain dependent parameters (e.g. Von Mises stress or strain energy density).

After thorough investigation of currently available practices, the aim of this work is to develop and evaluate a process that combines off-the-shelf FE and multibody systems solutions with a purposely designed algorithm capable of accelerating fatigue simulations. In order for such an algorithm to provide practical value, it would need to allow some degree of automation and be controllable in terms of quantifiable efficiency (cost savings versus error or risks).

The fundamental questions addressed concern the applicability of the proposed process, the underlying assumptions and limitations, the influencing variables and conditions, the benefits and drawbacks compared to established practices and finally the expected accuracy that it might yield. All the computational and applied aspects are developed and demonstrated alongside the theory.

In summary the main objectives of this thesis are:

- Theoretical foundation and analysis of a priori identification of critical stress concentrations under time domain quasi-static and dynamic loads.
- Design and application of a novel predictive algorithm apt to simplify the handling of large time transient fatigue simulations without excessive detrimental impact on solution accuracy.
- Definition of measurable metrics of prediction value in terms of efficiency and error.
- Numerical validation and performance assessment from simple repeatable models to realistic industrial applications of increasing complexity.

Throughout this study the following common conditions and assumptions applicable to time domain durability of mechanical systems are maintained:

- Linear components (material and geometry), though non-linearity might be considered at system level (including large rotations, large displacements and follower forces)
- Lightly damped structures, typically with first few modes, with low modal density, dynamically excited.
- Metal fatigue analysis according to Stress-life or Strain-life theory, where linear damage summation rule is applied to variable amplitude events typical of medium to high cycle durability regime.

Furthermore, the method makes use of state-of-the-art FE, multibody systems and fatigue codes to resolve the stress histories and obtain the ensuing fatigue damage. The practice is mastered and used with critical objectiveness, constituting a tool within the method, rather than the primary aim of the research.

1.4 Structure & Organisation

The thesis consists of 7 chapters. Chapter 2 contains a review of the mathematical tools and theories used throughout the investigation, covering the relevant aspects of time based fatigue simulation of mechanical systems. The chapter ends with a critical assessment of commonly applied simplification practices in FE based fatigue simulation.

Chapter 3 reviews the hypotheses and limitations for accelerated simulation methods based on peak-valley elimination. A novel error classification is based on the identified four separate sources of approximations, for which dedicated performance metrics are proposed.

In chapter 4, simply supported beams and plates in bending provide a basic test environment to investigate the predictability of fatigue critical areas. The use of an efficient and repeatable parametric analysis provides a test of the hypotheses and limitations whilst uncovering prevalent trends and sensitivities. A method based on diagnosis testing is proposed as a means of assessing the predictability of fatigue critical areas.

In chapter 5, the investigation and procedures for a priori hotspot detection are developed and applied to time-based fatigue simulation via FE and multibody systems methods. The procedural components and workflow of this predictive technique are described and demonstrated on representative numerical models. The aim is to quantitatively test both the performance and dedicated metrics developed for accelerated fatigue simulation.

In Chapter 6, the method is applied to a realistic industrial cases. The durability problem is addressed according to industry standard and used to evaluate the performance and reliability of the prediction algorithm in a comparative assessment with alternative practices.

Chapter 7 provides a summary of the investigation and contributions to new knowledge, followed by recommendations for further investigation.

Chapter 2: Methods for fatigue simulation of mechanical systems

This chapter presents a review of the mathematical tools and theories used throughout the investigation. The relevant aspects of time based fatigue simulation of mechanical systems are introduced in two parts. Part A provides an overview of the common FE techniques deployed to the resolution of time transient simulations in mechanical systems, including considerations on modal reduction via component-mode synthesis and modal strain energy parameters. Part B covers the fundamentals of FE based fatigue methods. The chapter finishes with a classification and critical assessment of commonly applied practices in fatigue simulation acceleration.

2.1 Part A: Time based dynamic simulation of mechanical system

Finite Elements (FE) and Multibody Systems Dynamics (MBS or MBD) methods are widely deployed in industrial and academic simulation of complex mechanical systems. The multibody systems environment resolves the component loads originated by parts interaction under prescribed loads, motions and boundary conditions; the FE models are deployed to provide realistic stiffness to the deformable bodies and to recover detailed local stresses and strains histories. Often the final aim of the process is to perform fatigue and durability assessment for a number of components under prescribed variable events.

The general equation of motion for any given FE model [1] is

$$\mathbf{M}\ddot{\mathbf{u}} + \mathbf{C}\dot{\mathbf{u}} + \mathbf{K}\mathbf{u} = \mathbf{f} \quad (2.1)$$

where

- u** vector of nodal displacements,
- M** inertia matrix,
- C** viscous damping matrix,
- K** stiffness matrix,
- f** vector of nodal forces representing externally applied loads.

Although eq. 2.1 is not restricted to linear systems, in fatigue based durability the common assumption is that the problem is linear. This is because a medium to high number of repetitions is typically required, which, at least for metals, is not compatible with diffused material non-linearity and large deformations, as in creep for example. For the low to medium cycle regime this simplification is partly compensated by local plasticity approximated criteria, as described in paragraph 2.2.2. As for geometric non-linearity, arising from follower forces, large displacements and large rotations, such effects are more naturally captured in the multibody systems environment and will be tackled in a dedicated section.

2.1.1 Pseudostatic assumptions, unit loads and inertia relief

Although fatigue is based on time based analysis, the component under transient loading conditions might not be dynamically excited if the maximum excitation frequency is sufficiently low with respect to the natural modes of the system. In analogy to the *single-degree-of-freedom systems*, SDOF, the *frequency ratio* r is defined as [49]

$$r = \frac{\Omega}{\omega_m} . \quad (2.2)$$

In eq. (2.2) Ω indicates the maximum excitation frequency and ω_m is normally taken as first natural frequency of the *multiple-degree-of-freedom system*, MDOF, represented by (2.1). The steady state magnification factor for the first mode of a given system is defined by the ratio of the steady state amplitude over the static solution:

$$D_s(r) = \frac{1}{[(1-r^2)^2 + (2\xi r)^2]^{1/2}} , \quad (2.3)$$

with ξ the modal damping coefficient. Appendix A.1 and A.2 provide analytical examples of dynamic response obtained for a MDOF solved in the frequency domain.

2.1.1.1 Limits of pseudostatic approximation

The frequency domain solution of eq. (2.3) for realistic levels of structural damping (range 0.02 to 0.14 for metal and metal constructs [1]) leads to a determination of acceptable pseudo-static frequency response. As a rule of thumb, a frequency ratio r of 1/3 leads to a dynamic magnification of 1.12 which is within the expected approximations of FE modelling. However, if the object of the analysis is fatigue calculation, at this level of

magnification the power law relationship between stress and number of cycles (examples given in 2.2.7.1) could easily lead to errors in life determination up to 100%. In automotive applications, a safer upper frequency ratio limit of 1/5 has been suggested by some authors [29]. In practice, the dynamic magnification factor depends on the superposition of all modes and their damping coefficients, so the actual magnification factor could be sensibly higher, even for r below 1/5. In fact Anvari et al. [50] obtained 5% relative errors at frequency ratio close to 1/10.

Within the conditions and limits described above, the pseudostatic approach consists in approximating eq. (2.1) with

$$\mathbf{K}\mathbf{u} = \mathbf{f} \quad (2.4)$$

The pseudostatic response is therefore

$$\mathbf{u} = \mathbf{K}^{-1}\mathbf{f} \quad (2.5)$$

Separating the time dependency of the force $f(t)$ from the physical distribution \mathbf{f}_0 eq. (2.5) leads to an important simplification: the time transient response can be obtained simply scaling the static response $\mathbf{u}_0 = \mathbf{K}^{-1}\mathbf{f}_0$ by the time coefficient of the load.

$$\mathbf{u}(t) = \mathbf{K}^{-1}\mathbf{f}_0 f(t) = \mathbf{u}_0 f(t) \quad (2.6)$$

Often the load is distributed over multiple application points and directions, \mathbf{f}_i , each with its own time varying coefficient $f_i(t)$, so the total response is the superposition of the individual responses,

$$\mathbf{u}(t) = \sum_i \mathbf{K}^{-1}\mathbf{f}_{0i} f_i(t) = \sum_i \mathbf{u}_{0i} f_i(t) \quad \text{with } i = 1, 2, \dots, c \text{ loading channels} \quad (2.7)$$

2.1.1.2 Unit loading and stress influence coefficients

In many practical situations a loading point is split between its component's degrees of freedom, each representing a single location point and direction. The immediate example is a wheel spindle, where up to 6 loading components are defined, also termed loading channels. In such circumstance to help the general interpretation and the re-use of the data, the static response is normally obtained under the unit value of the loading, or otherwise pre-agreed constant numerical value [4]. The response to a unit loading represents the influence coefficients for the corresponding degree of freedom. Similarly,

the element stresses resulting from the deformation under unit loading are the stress influence coefficients $\sigma_{e0,ij}$. The components of the stress tensor at any element, $\sigma_{e,ij}(t)$, can be readily obtained by superposition of the stress influence coefficients, multiplied by the input forces. The latter operation can be conveniently operated directly during the fatigue run and selectively on the element of interest, typically on the model surface where the resulting in-plane stresses are:

$$\begin{aligned}\sigma_{e,x}(t) &= \sum_i \sigma_{e0,x_i} f_i(t) \\ \sigma_{e,y}(t) &= \sum_i \sigma_{e0,y_i} f_i(t) \\ \tau_{e,xy}(t) &= \sum_i \tau_{e0,xy_i} f_i(t)\end{aligned}\tag{2.8}$$

The evident advantage of eq. (2.7) is that the FE computational burden is limited to the static solutions $\mathbf{u}_{0,i}$ and to the element stress tensors of interest $\sigma_{e0,ij}$, which is one-off operation that is not dependent on the length of the required transient solution interval, so that virtually any time length can be addressed.

2.1.1.3 Inertia relief

The considerable computational benefit expressed by (2.7) implicitly assumes that the static equilibrium can be determined, but in the general case the model might not be fully constrained, or might even be completely free from constraints (e.g. flying airplane). In such cases the model would undergo rigid body motion in the unconstrained directions. To get around the problem, the common practise is to balance the applied load with the inertia loads corresponding exactly to the rigid body accelerations $\ddot{\mathbf{u}}_{RB}$ that would be generated by the unbalanced applied loads,

$$\mathbf{Ku} = \mathbf{f} - \mathbf{M}\ddot{\mathbf{u}}_{RB}\tag{2.9}$$

The practice is commonly referred to as *inertia relief*. The inertia loads on the right side of (2.9) consider only the rigid body motion, hence the contribution from deformation rate is neglected, in line with the hypothesis of low frequency ratio. The theoretical background is developed in analytical examples in Bisplinghoff et al. [51] and a practical description in FE applications can be found in specific solver manuals such as the Nastran® primer [52]. Kuo and Kelkar [26] described the typical use and approximations in the context of vehicle durability analysis; more recently Thipse [53] demonstrated a

methodology to overcome a potential pitfall in applying inertia relief in FE with load obtained from multibody systems analysis.

The widespread usage of the pseudostatic method is often due to its numerical advantages rather than the result of a careful assessment of the limitations and errors. However, the deployment of model reduction techniques and the recent integration of multibody systems and FE is gradually establishing dynamic transient as viable and cost effective, as described in the next section.

2.1.2 Dynamic solution with modal reduction techniques

A variety of model reduction techniques can be applied for efficient FE dynamic analysis and to integrate flexible components in multibody dynamic systems, where a small set of generalized coordinates replace a large number of physical coordinates. Besselink et al. [54] provide an overview of comparison of the common options from the combined field of structural dynamic, numerical mathematics and systems and control. The field of structural dynamics and fatigue is still dominated by modal reduction techniques, where the common foundation is in the mode-superposition method which is briefly outlined below.

Assuming unchanged force vibration harmonic motion, the undamped eq. (2.1) leads to an eigenvalue problem:

$$(\mathbf{K} - \omega_j^2 \mathbf{M}) \boldsymbol{\phi}_j = 0 \quad j = 1 \text{ to } N \quad (2.10)$$

where $\boldsymbol{\phi}_j$ is the mode shape vector, ω_j the corresponding eigenfrequency and N the total number of DOF in the system. It can be shown that the so defined mode shapes are orthogonal and constitute a linear independent set of N -dimensional vectors [49]. Therefore, any arbitrary system displacement in time can be expressed as a combination of the mass normalised mode shapes and scaling functions $q_j(t)$, the modal coordinates, through the modal expansion:

$$\mathbf{u}(t) = \sum_1^N \boldsymbol{\phi}_j q_j(t) = \boldsymbol{\Phi} \mathbf{q}(t) \quad (2.11)$$

The general equation of motion (2.1) transformed to the modal space takes a convenient decoupled form in absence of damping or imposing a diagonal damping matrix (typically modal damping). In practical problems the extraction of the normal modes is quite an

expensive operation for large systems so an approximate version of (2.11) is deployed instead. Modal truncation consists of neglecting the response of the highest modes and leads to a truncation error. In general, it is assumed that the response of the neglected modes tends to be static as long as their natural frequencies are high compared to the maximum excitation frequency. The common options are briefly outlined in the next section.

2.1.2.1 Mode-Displacement method

In ordinary *mode-displacement method* the summation at Eq. (2.11) is truncated at mode \hat{N} of the total modal space. Indicating with $\hat{\mathbf{q}}$ the modal coordinates after truncation,

$$\mathbf{u}(t) \simeq \hat{\mathbf{u}}(t) = \sum_1^{\hat{N}} \boldsymbol{\Phi}_j \mathbf{q}_j(t) = \hat{\boldsymbol{\Phi}} \hat{\mathbf{q}}(t) \quad (2.12)$$

In (2.12) typically $\hat{N} \ll N$, where the truncation is typically based on the frequency content of the loading, assuming that the modes dynamically excited would be the main contributors to the response. As remarked by Dickens et al. [55], such criterion only addresses the time dependent portion of the loadings $f_i(t)$ and ignores the spatial distribution $\mathbf{f}_{0,i}$. Even in the absence of dynamic response from higher modes, the truncation error will tend to zero only when the static response of the neglected modes tends to zero, which cannot be guaranteed a priori.

Figure 2-1 describes a typical frequency response in a given output quantity for a multiple degrees of freedom system. The top line represents the total response at all frequencies and is the superposition of a virtually infinite number of single degrees of freedom (modal decomposition). If only 3 modes are retained by the truncated modal basis (the *kept modes*), the dynamic response can be well represented within a reduced frequency range but the static contribution of the left over modes will be neglected. In fact, a much localized deformation imposed by external concentrated loads is likely to be significantly affected by the modal truncation, even for static loading.

In fatigue analysis localized deformations and the ensuing concentrated stresses are particularly relevant and must not be neglected. Appendix A.4.1 presents a study of the effects of modal truncation to solution convergence for plates in bending. The marked difference in rate of solution convergence between displacement and stress is demonstrated for different load patch sizes.

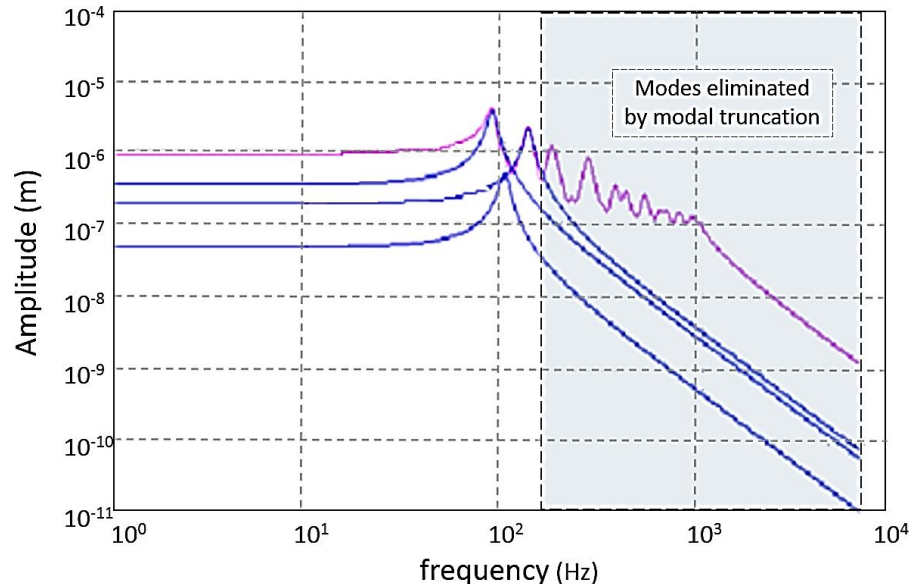


Figure 2-1. Effect of higher modes truncation to frequency domain response for an output quantity in MDOF systems [56],[57].

The techniques presented in the next section can sensibly improve both the static compatibility and the modal efficiency of the truncated solution.

2.1.2.2 Mode-Acceleration method

The mode-acceleration approximation technique ([1], [54]) is a computational variant of the static correction method allowing the inclusion of static response of the truncated modes without requiring their direct calculation. If the static response of the neglected modes is included in modal reduction (i.e. static correction) the truncation error will tend to zero as long as the response of such modes tends to be static.

The equation of motion (2.1) in the \hat{N} -modes reduced modal space is

$$\hat{\ddot{\mathbf{q}}}(t) + \bar{\mathbf{C}} \hat{\dot{\mathbf{q}}}(t) + \bar{\Lambda} \hat{\mathbf{q}}(t) = \hat{\Phi}^T \mathbf{f}(t) . \quad (2.13)$$

Rearranging to separate the modal coordinates gives

$$\hat{\mathbf{q}}(t) = \bar{\Lambda}^{-1} \hat{\Phi}^T \mathbf{f}(t) - \bar{\Lambda}^{-1} [\hat{\ddot{\mathbf{q}}}(t) + \bar{\mathbf{C}} \hat{\dot{\mathbf{q}}}(t)] \quad (2.14)$$

Using the modal superposition in Eq. (2.12)

$$\hat{\mathbf{u}}(t) = \hat{\Phi} \bar{\Lambda}^{-1} \hat{\Phi}^T \mathbf{f}(t) - \hat{\Phi} \bar{\Lambda}^{-1} [\hat{\ddot{\mathbf{q}}}(t) + \bar{\mathbf{C}} \hat{\dot{\mathbf{q}}}(t)] \quad (2.15)$$

The first term to the right in Eq. (2.15) is the pseudo-static response from the truncated modal basis. It could therefore take into account all modes [1], coinciding with Eq.(2.5). Substituting (2.5) in (2.15) leads to a better approximation $\tilde{\mathbf{u}}(t)$ of the dynamic response

$$\tilde{\mathbf{u}}(t) = \mathbf{K}^{-1}\mathbf{f}(t) - \hat{\Phi}\bar{\Lambda}^{-1}[\hat{\mathbf{q}}(t) + \bar{\mathbf{C}}\hat{\mathbf{q}}(t)]. \quad (2.16)$$

Compared to Eq. (2.12) of the mode-displacement method, the mode-acceleration solution in (2.16) provides the correct static solution whilst having the full dynamic response of the kept modes. Appendix A.4.2 presents the effect of the static correction for a thin plate in bending.

2.1.2.3 Residual flexibility

In chapter 2.1.2.2 it was shown how, in MDOF systems, the mode-acceleration approximation can ensure the static compatibility of any truncated modal basis and therefore improve the numerical efficiency of the kept modes (hence the name *mode acceleration*).

A practical alternative to mode-acceleration is the modal truncation augmentation [55]. Modal truncation augmentation consists of augmenting the modal basis with additional vectors, the *modal truncation vectors*, or alternatively *residual flexibility* [1] or *residual vectors* [33], obtained from the same approach given in mode-acceleration method.

Eq. (2.13) can be reorganized [1] as

$$\hat{\mathbf{q}}(t) + \bar{\mathbf{C}}\hat{\mathbf{q}}(t) = \hat{\Phi}^T\mathbf{f}(t) - \bar{\Lambda}\hat{\mathbf{q}}(t) \quad (2.17)$$

Replacing the factor in parenthesis to the right of Eq. (2.16) with the equivalent term in (2.17) leads to

$$\tilde{\mathbf{u}}(t) = \mathbf{K}^{-1}\mathbf{f}(t) - \hat{\Phi}\bar{\Lambda}^{-1}[\hat{\Phi}^T\mathbf{f}(t) - \bar{\Lambda}\hat{\mathbf{q}}(t)] = \hat{\Phi}\hat{\mathbf{q}}(t) + \mathbf{K}^{-1}\mathbf{f}(t) - \hat{\Phi}\bar{\Lambda}^{-1}\hat{\Phi}^T\mathbf{f}(t) \quad (2.18)$$

In this form, the modal response from the kept modes is now explicit in the first mode-displacement term; the second term is the static contribution from all modes; the last term is the static contribution from the kept modes. The difference between the last two terms is therefore the static contribution from the truncated modes and is referred to as the residual flexibility Φ_R :

$$\Phi_R = \mathbf{K}^{-1}\mathbf{f}(t) - \widehat{\Phi} \bar{\Lambda}^{-1} \widehat{\Phi}^T \mathbf{f}(t) \quad (2.19)$$

A set of k modal vectors \mathbf{Z} are formed considering mass orthogonal residual vectors obtained from applied loads reorganized through a reduced eigenvalue problem [55]. The resulting augmented modal basis is

$$\Phi_A = [\Phi_1 \dots \Phi_{\hat{N}} \mathbf{Z}_1 \dots \mathbf{Z}_k] \quad (2.20)$$

The residual vectors augment the modal basis so that the load paths are fully captured. Figure 2-2 shows an example of residual vector deformation under concentrated load that is not well captured by the lower frequency modes.

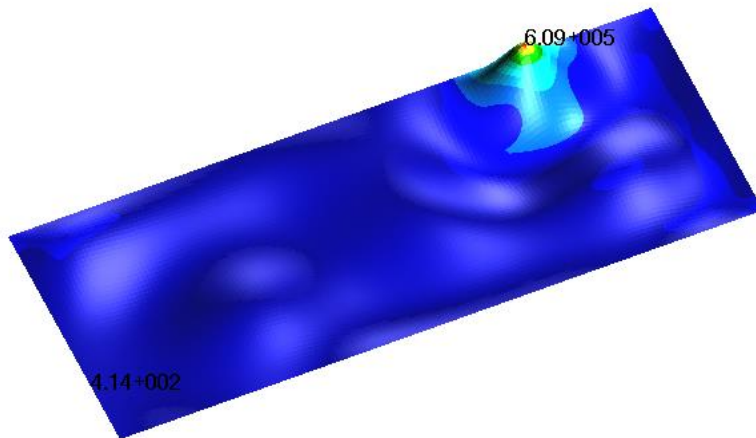


Figure 2-2. FE example of a residual vector for a simply supported plate under a concentrated point loading located near an edge (10 fixed normal modes retained) [57].

The technique can similarly be applied to other types of augmented modal basis, typically obtained via component-mode synthesis methods, as introduced in the next chapter.

2.1.3 Component-mode synthesis

Component-mode synthesis (CMS) is a widely applied technique for reducing the number of degrees of freedom in dynamically responsive systems. It is alternatively known as substructure analysis, superelements or building blocks technique [1].

With structures comprising multiple components joined together (as in a wing to a fuselage), perhaps with parts undergoing large relative motions with respect to one

another (e.g. control surfaces), it is not easy to define a single modal reduction basis capable of reproducing the system complexity. For such scenarios, sub-structuring techniques based on reduced components, such as CMS, are commonly deployed to increase both the efficiency and the accuracy of the solution.

2.1.3.1 Background and numerical benefits

De Klerk et al. [58] described the general mathematical framework of CMS in dynamic substructuring, which in turn is shown to have its mathematical roots in domain decomposition, that is the reduction of a complex mathematical field problem into its subdomains and their interface boundary solution (Schwarz approx. 1870).

In modern numerical terms the “domains” are substituted by numerical discretization and approximation via common techniques such as the Rayleigh-Ritz approach, boundary element techniques and the finite element method. De Klerk et al. [58] propose that such discretization should be considered a first level of discrete domain decomposition, where the FE nodes are the interface of a continuous problem solved by approximated field equations (shape functions). CMS can therefore be seen as a second level of domain decomposition, with a division of the FE discretized domain into substructures and a further approximation through a modal reduction technique.

CMS was first developed as a reduction technique in the early sixties. Hurty first outlined a method [59] based on 3 sets of modes, respectively rigid-body modes, *constraint modes*, equal in number to redundant constraints, and normal modes with fixed constraints. In 1968 the popular article by Craig and Bampton [17] treated all boundary degrees of freedom as redundant, avoiding the distinction between statically determinate and redundant modes. This lead to important practical simplifications, so that the Craig-Bampton approach is now widely recognized as the standard implementation for CMS. In 1971 MacNeal [60] illustrated all the classical variants of the Craig-Bampton method, according to the classification of the boundary in free, fixed or mixed condition. Furthermore, MacNeal identified a set of residual flexibility matrices, obtained through static analyses, apt to increase the accuracy and the efficiency of any CMS variant. This led to the widely applied practice to augment the modal basis with the *residual vectors* in order to satisfy the static completeness requirement. In 1985 Lu and Ma[61] showed that once the static completeness requirement is satisfied, the results using different static

modes are equivalent. In 2005 Arya, Henkel and Wilson [62] derived a generalized mixed boundary CMS formulation, Residual Flexibility Mixed-Boundary, which exactly reduces to Craig-Bampton for all-fixed boundary and to MacNeal for all-free boundary formulations. The method has been integrated in the 2004 version of the commercial code MSC Nastran® [33].

The article in 1997 by Huang et al. [27] demonstrated the potential for durability applications with numerical benefits deriving from stress recovery via CMS in FE modelling. The full potential for demanding time transient durability events is realized by combining CMS with multibody dynamics, the subject of a dedicated section.

In general terms, CMS modelling consists in dividing the FE structure into a number of sub-components, each defined by its boundary degrees of freedom and internal nodes. The physical degrees of freedoms within each component are reduced by virtue of modal substitution. The original structure is then re-assembled from all reduced components, essentially transforming the original large eigenvalue problem into several smaller problems.

Petyt [1] listed the following benefits :

- capacity to handle large and complex structure that would be unpractical to be analysed as a whole

- better control on local dynamic behaviour, for example eliminating local effects that are not relevant to the whole assembly dynamics, thus further improving the numerical efficiency

- allows subdividing and sharing a complex problem between multiple groups and projects, as each component/substructure can be prepared independently from the others.

For correct CMS deployment [54] one has to consider that the set of modal shapes used define a subspace of the complete solution and the need to converge to a sufficiently representative number of modes capable to provide accuracy in solution and full participation of the loads.

Once the technique has been sufficiently mastered, modal reduction is extremely advantageous also because:

- it preserves the dynamic behaviour (e.g. resonances, phases)
- it decouples the systems of equations
- element stress recovery for fatigue analysis can be selective both in time and in space.

The Craig-Bampton method, also known as the *superelements* method after the implementation in the general purpose code Nastran® [33], is a popular option to transfer reduced flexibility components from FE to multibody systems [8]. Due to the role in hotspot search algorithms, as clarified in chapter 5, some key concepts are presented in the next section. An application of Craig-Bampton is included in Appendix B.

2.1.3.2 The Craig-Bampton CMS method

Fixed interface CMS, better known as the *Craig-Bampton Method* [17], CB, consists in incrementing the truncated modal basis in Eq. (2.12) with deformation shapes from fixed interface constraint modes.

For any given component the following partitions can be introduced:

$$\mathbf{u} = \begin{Bmatrix} \mathbf{u}_b \\ \mathbf{u}_i \end{Bmatrix} = \begin{bmatrix} \mathbf{I} & \mathbf{0} \\ \boldsymbol{\Phi}_c & \boldsymbol{\Phi}_n \end{bmatrix} \begin{Bmatrix} \mathbf{u}_b \\ \mathbf{q}_n \end{Bmatrix} \quad (2.21)$$

Where:

- \mathbf{u}_b Boundary nodes DOF
- \mathbf{u}_i Internal nodes DOF
- $\boldsymbol{\Phi}_c$ Static mode shapes from unit displacement of boundary DOF (one at a time, with the remaining all null), also termed constraint modes.
- $\boldsymbol{\Phi}_n$ The set of n truncated natural mode shapes of the substructure obtained by fixing all boundary DOF
- \mathbf{q}_n Modal coordinates of component with fixed boundary normal modes
- \mathbf{I} Identity matrix
- $\mathbf{0}$ Null matrix

The constraint mode shapes $\boldsymbol{\Phi}_c$ are obtained by partitioning the stiffness matrix and solving the static equilibrium of \mathbf{u}_i to the enforced displacement of \mathbf{u}_b as shown in Eq. (2.22) and (2.23)

$$\begin{bmatrix} \mathbf{K}_{bb} & \mathbf{K}_{bi} \\ \mathbf{K}_{ib} & \mathbf{K}_{ii} \end{bmatrix} \begin{bmatrix} \mathbf{u}_b \\ \mathbf{u}_i \end{bmatrix} = \begin{bmatrix} \mathbf{f}_b \\ \mathbf{0} \end{bmatrix} \quad (2.22)$$

$$\mathbf{u}_i = -\mathbf{K}_{ii}^{-1} \mathbf{K}_{ib} \mathbf{u}_b = \boldsymbol{\Phi}_c \mathbf{u}_b \quad (2.23)$$

Eq. (2.23) expresses an approximated formulation for the internal DOFs as function of the selected boundary DOF and is also known as static condensation.

The transformation in 2.21 describes the *Craig-Bampton transformation matrix*:

$$\boldsymbol{\Phi}_{CB} = \begin{bmatrix} \mathbf{I} & \mathbf{0} \\ \boldsymbol{\Phi}_c & \boldsymbol{\Phi}_n \end{bmatrix} \quad (2.24)$$

The Craig-Bampton transformation matrix is used to derive the generalized Mass and Stiffness matrices

$$\bar{\mathbf{K}} = \begin{bmatrix} \mathbf{I} & \mathbf{0} \\ \boldsymbol{\Phi}_c & \boldsymbol{\Phi}_n \end{bmatrix}^T \begin{bmatrix} \mathbf{K}_{bb} & \mathbf{K}_{bi} \\ \mathbf{K}_{ib} & \mathbf{K}_{ii} \end{bmatrix} \begin{bmatrix} \mathbf{I} & \mathbf{0} \\ \boldsymbol{\Phi}_c & \boldsymbol{\Phi}_n \end{bmatrix} = \begin{bmatrix} \mathbf{K}_{cc} & \mathbf{0} \\ \mathbf{0} & \mathbf{K}_{nn} \end{bmatrix} \quad (2.25)$$

$$\bar{\mathbf{M}} = \begin{bmatrix} \mathbf{I} & \mathbf{0} \\ \boldsymbol{\Phi}_c & \boldsymbol{\Phi}_n \end{bmatrix}^T \begin{bmatrix} \mathbf{M}_{bb} & \mathbf{M}_{bi} \\ \mathbf{M}_{ib} & \mathbf{M}_{ii} \end{bmatrix} \begin{bmatrix} \mathbf{I} & \mathbf{0} \\ \boldsymbol{\Phi}_c & \boldsymbol{\Phi}_n \end{bmatrix} = \begin{bmatrix} \mathbf{M}_{cc} & \mathbf{M}_{cn} \\ \mathbf{M}_{nc} & \mathbf{M}_{nn} \end{bmatrix} \quad (2.26)$$

In essence, the fixed interface CMS combines two sets of modes in one augmented modal basis:

-*Fixed interface normal modes*: accounting for internal flexibility of the structure and ensuring dynamic behaviour is captured.

-*Constraint modes*: representing the attachments flexibility, obtained by fixing all boundaries and deforming one attachment degree of freedom by a unit displacement or rotation. The ensuing deformation in the structure represents a single constraint mode.

In order to fully capture the external conditions, there will be as many constraint modes as there are active load paths (constraint reactions or applied forces). The static mode shapes as defined above are capable of representing statically enforced displacements, including rigid body modes.

2.1.3.3 Modes Orthogonalization

The Craig-Bampton modes are not orthogonal with respect to the mass and stiffness matrices, as evidenced by the fact that their generalized mass and stiffness matrices in Eq. (2.25) and (2.26) are not diagonal.

The system of equation 2.1 can be recast in the generalized coordinates' space

$$\{\mathbf{q}\} = \begin{Bmatrix} \mathbf{u}_b \\ \mathbf{q}_n \end{Bmatrix}, \quad (2.27)$$

forming a new eigenvalue problem:

$$\bar{\mathbf{K}}\mathbf{q} = \lambda \bar{\mathbf{M}}\mathbf{q} \quad (2.28)$$

The eigenvectors satisfying (2.28) can be arranged in the matrix \mathbf{Q}

$$\{\mathbf{q}\} = [\mathbf{Q}]\{\mathbf{q}^*\}, \quad (2.29)$$

capable of transforming the initial Craig-Bampton modal basis into an equivalent orthogonal basis with modal coordinates \mathbf{q}^* :

$$\{\mathbf{u}\} = [\Phi_{CB}]\{\mathbf{q}\} = [\Phi_{CB}][\mathbf{Q}]\{\mathbf{q}^*\} = [\Phi_{CB}^*]\{\mathbf{q}^*\} \quad (2.30)$$

The orthogonal eigenvectors $[\Phi_{CB}^*]$ are not natural modes of the original system but of its Craig-Bampton mathematical representation. The low frequency modes and frequencies corresponds to the free-free natural modes, including rigid body modes. Higher frequency modes are influenced by the boundary stiffness and loose physical interpretation.

2.1.4 Alternative component modes

The Craig-Bampton method as presented in 2.1.3.2 is a common reduction method in FE based structural analysis, however equivalent methods based on alternative component modes are also used in selected applications [49][1].

Considering a generic definition of the component modes as *Ritz vectors* or *assumed modes*, to be used as modal basis to describe the displacements within a substructure, common components modes include:

Fixed-interface modes: the natural modes a component with clamped boundaries nodes, as for Φ_n presented in Eq. (2.21).

Free-interface modes: the natural modes of the free boundary component. The rigid body modes should not be considered free-interface modes but rather as a special combination of constraint modes.

Constraint modes: static deformation of a structure when a unit displacement is applied to one coordinate of a specified set of constraints, while all the remaining coordinates are fixed and the remaining degrees of freedom are force-free.

Static modes: the static shapes of a component under arbitrary loading at its boundary.

Residual modes: static response not captured by the kept modes under an assumed load pattern, as described in 2.1.2.3.

Rigid-body modes: the motion without deformation, comprising up to 6 independent modes. In practice the rigid-body modes are obtained by setting one designated rigid motion representative DOF to unity, with the rest of the designated rigid motion DOF set to zero and the rest of the modes free from forces. According to Craig et al. [49] the rigid-body modes are a special case of constraint modes, rather than zero frequency normal modes. In fact, they can be described as a linear combination of the constraint modes.

Attachment modes: similar in concept to the constraint modes except that they are defined per unit force at a designated DOF and without any constraint on the other degrees of freedom in the designated set, other than the rigid body motions. As the latter can be done in more than one way, the attachment modes are not uniquely defined.

Inertia Relief Attachment modes: IR refers to the process of applying to the component a self-equilibrated d'Alembert force system as described in 2.1.1.3. The IR attachment modes are obtained by using such forces to counterbalance the unit force at the designated DOF.

The above list is non-conclusive and there will be more options and as many CMS variants, as was briefly introduced in the literature review. For the purposes of this investigation, all the component modes could be representative of a particular energy transfer pattern, with the obvious exception of the rigid body modes, and could be therefore potential instruments in hotspot prediction techniques.

2.1.5 Flexible bodies via component-mode synthesis in multibody systems

As discussed, multibody systems analysis is traditionally deployed in a separate environment from FE, where the loads and dynamics at system level are dynamically integrated and ‘cascaded’ to the FE components for detailed local analysis. The separation of the 2 environments is not due to mathematical boundaries, but more the result of a difference in objectives. The FE formulation is typically well served by small displacements and small rotations which are reflected in simplified but very numerous element shape functions. The multibody systems dynamics code, on the other hand, not only has to be able to deal with large displacement and large rotations, but it is also expected to deal with general non-linear conditions and controls.

By virtue of component-mode synthesis, the multibody and FE equations can be coupled without losing precious local FE deformation details and avoiding overloading the multibody system of differential equations with excessive variables. In the floating frame of reference formulation [8] the global position of a point on a deformable body is the sum of body *reference* position and *elastic* (deformation) coordinates. The validity of linear superposition approximations is assumed only for the elastic coordinates (i.e. CMS generalized coordinates). The orthogonalization at 2.1.3.3 allows separation of rigid-body motion from elastic deformation.

A single multibody assembly could be composed of multiple flexible bodies, each with its own floating frame of reference and generalized coordinates. Figure 2-3 outlines a basic workflow for an integrated FE and multibody systems durability analysis. The FE analysis generates a component-mode synthesis reduced model, for each component of interest. The modal stresses associated to the component modes are stored in a result file while the reduced stiffness, mass and damping matrices are submitted to the multibody systems solver. The reduced component is included in the multibody assembly to form a collection of FE reduced parts, also known as flexible bodies, concentrated parameters components (e.g. mass, stiffness, damping), rigid body parts and boundary conditions. The ensuing system of Lagrange equations is solved for any required dynamic loading (i.e. fatigue event) and the relevant generalized coordinates are converted to stresses and strains through modal recovery.

Using multibody simulation alongside the FE code provides the additional benefit of easy integration and solution of systems and assemblies, and, crucially, it can account for all types of geometric non-linearity while still allowing the linear assumption at component level.

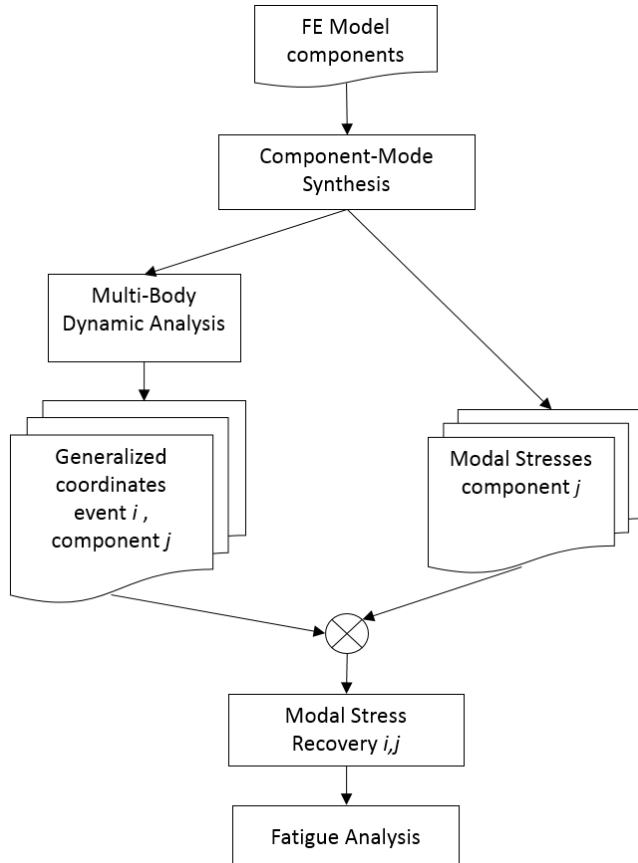


Figure 2-3. Durability workflow integrating FE and multibody simulation with flexible bodies.

2.2 Part B: Numerical methods and modelling in fatigue analysis

A complete overview of fatigue analysis is beyond the scope of this work. This section introduces the basic concepts and tools that are instrumental to the development and application of fatigue simulation acceleration techniques.

2.2.1 Background and definitions for fatigue analysis

Many globally accepted definitions and commonly applied fatigue methods can be conveniently obtained from the vast historical literature as well as International Standards such as the BS7608 [63] or Eurocodes [64].

By definition fatigue is [63]

“The damage of a structural part by the initiation and gradual propagation of a crack or cracks caused by repeated applications of stress”.

The history of fatigue is deep rooted in the experimental investigation in support to the industrial revolution of the 19th century. Schütz [65] presents a detailed chronology, starting from 1837 to the early 90s, and is an invaluable source of historical references and milestones. Fatigue technology developed around nominal stress theory, Wohler S-N curves, that completely ignored the physical local phenomena leading to the onset of fracture. The past century, aided by modern testing hardware and computational tools, saw the emergence of more accurate theories based on local strain such as Basquin and Morrow [2]. While Schütz looked with diffidence at the early appearances of fatigue software, “no replacement for experience of the fatigue expert”, the modern computational revolution determined a flourishing of efficient numerical methods that have adapted, extended and distributed a knowledge that was accumulated in nearly two centuries of applications.

Modern fatigue analysis can be performed with a variety of methods that reflect the different loading environments, material modelling, component geometry and type of failure. The primary fatigue analysis methods are the Stress-Life ($S-N$), the Strain-Life ($\varepsilon-N$) and the fracture mechanics or Crack-Propagation approach[2]. All methods have their foundation in the *similitude principle*: the fatigue behaviour of a test coupon can represent the behaviour of a real life component subjected to the same loading and environmental conditions. $S-N$ and $\varepsilon-N$ methods are the backbone of life assessments for most industrial applications, where the ultimate objective is the prediction of the time interval or the number of repetitions necessary to initiate a defect. The $S-N$ and $\varepsilon-N$ curves estimate the expected fatigue life by comparing stress or strain levels with cycles obtained during material testing. Expensive campaigns of experimental material testing are necessary to establish the relationship between the expected number of sustainable

cycles under a given level of stress (S - N curves) or strain (ε - N curves). The Military Handbook [66] provides an exhaustive range of material experimental data for most metals applied in aerospace.

The relationship between a cyclic stress level S and the expected number of cycles before failure N is well captured by a power law:

$$S^m N = C , \quad (2.31)$$

where C and m are material constants to be determined from experimental testing, e.g. via ASTM standards practices [67].

The relationship (2.31) is commonly described in terms of straight lines in bi-logarithmic axes system. Figure 2-4 shows an example of typical bilinear S - N curves, also termed Wöhler curves in honour of the famous German railway engineer who pioneered fatigue testing [65].

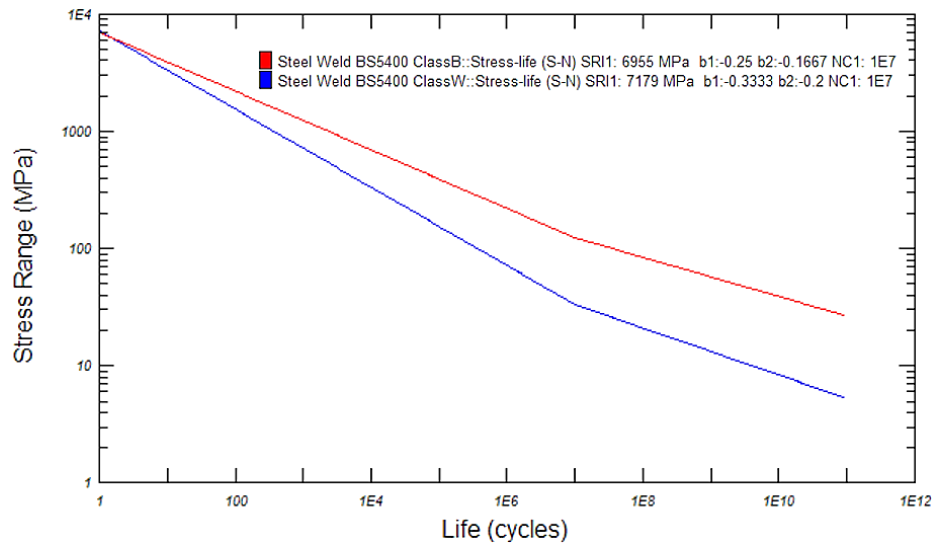


Figure 2-4. Steel Weld Stress-Life curves, best and worst classes according to BS7608 Code of Practice for fatigue Design and Assessment of Steel structures [63]; plot generated in MSC Fatigue™ [68].

Crack propagation methods are used either as an alternative or as a complement to S - N and ε - N methods in situations where some level of localized damage (cracking) is inevitable and tolerable. The object of the analysis in this case is normally to determine a safe inspection frequency interval and a critical crack size before repair or replacement is required [2] [69].

2.2.2 Local strain and energy modelling in fatigue

The calculation of the local plastic deformations that determine the onset and growth of a fatigue failure are challenging and expensive even for modern computational tools.

Several approximations based on elastic stress-strains and local energy criteria have been designed in order to provide a simplified solution near notches or areas of stress concentration.

The first and still very popular example is due to Neuber [70], where the “Neuber’s rule” equated the elastic strain energy to the product of local inelastic stresses and strains.

Seeger et al. [71] extended Neuber’s rule to nominal stresses beyond the limit of proportionality. Finally Molski and Glinka [72] devised a method based on equating local elastic and elasto-plastic strain energies. In 1985 Glinka[73] described the principle behind the equivalence of local elastic and plastic energy:

“In presence of localized plastic yielding the gross linear elastic behaviour of the material surrounding the notch also controls the deformations in the plastic zone. Thus, it can be concluded that the energy density W in the plastic zone is equal to that calculated on the basis of the elastic solution.”

In essence, the assumption in all these methods is that the local linear elastic strain energies are representative of the local non-linear behaviour of the plastic zone responsible for a crack initiation. This assumption limits the applicability of the method to cases in which the plastic zone is small in comparison to the surrounding elastic field.

Lagoda et al. [74][75][76] provide a good overview of the evolution of energy methods for fatigue, which are thought as particularly suitable for biaxial loading conditions. A fatigue algorithm based on an energy parameter capable of separating compression and tension load is demonstrated. Results from random uniaxial and biaxial calculations are within the acceptable factor of 3 compared to experimental values.

In 2007 Berto and Lazzarin [77][78] demonstrated the use of a the mean value of the Strain Energy Density (SED) over a control volume surrounding the highly stressed region in both notched and welded components. The main advantage of the mean value elastic strain energy density is that it can be determined by using relatively coarse meshes.

The experiences above testify to the close relationship between local linear strain energy density and the onset of fatigue damage, which will be assumed throughout this work.

2.2.3 Fatigue and finite element simulation

Bishop and Sherratt [4] can be credited with an early book completely dedicated to Finite Element based fatigue calculation. Fatigue simulation can be seen as a post-processing step to the Static and Dynamic simulations. With the deployment of FE based fatigue methods, a large part of the fatigue analyst's tasks has been shifted forward in the design cycle, long before any physical prototype is created.

Tang and others [79] describe a multidisciplinary Computer Assisted Engineering (CAE) environment aimed at integrated fatigue simulation via multiple solutions criteria.

Fatigue analysis can be performed with a variety of methods to reflect different loading environments and material modelling. Regardless of the approach the FE integrated methodology would include all the following components:

- Time history loading (or equivalent in frequency domain), possibly split between multiple channels, multiple events or load spectra.
- Stress (or strain) combination parameters.
- Rainflow cycle counting algorithms (or probability of rainflow ranges in PSD based methods).
- Experimental and empirical fatigue material data and material models to relate expected life to loading levels.
- Damage models cumulating fatigue damage accrued during a load cycle (e.g. Palmgren-Miner linear cumulative damage [63])

2.2.4 Time history loads

Traditionally the source of the time history would have been experimental tests or simple idealized mathematical formulae, but from the early nineties [16] to the modern days [22] the combination of FE and multibody systems simulation have gradually replaced a large part of physical test, so that is more common now to encounter semi-analytical or fully virtual loads. Whatever the source, the loads passed to the fatigue solver are immediately usable to resolve the stress tensors history through a superposition formula:

$$\sigma_{ij}(t) = \sum_k (P_k(t) SF_k + Offset_k) \sigma_{0,ij,k} \quad k = 1 \text{ to number of loads.} \quad (2.32)$$

Eq. (2.32) is a generalization of Eq. (2.8), where the $P_k(t)$ loads can be rescaled (SF_k factor) or offset and $\sigma_{0,ij,k}$ is the stress influence coefficient, possibly obtained via inertia relief.

In case of generalized coordinates, as in CMS, Eq. (2.32) takes the equivalent form:

$$\sigma_{ij}(t) = \sum_n (q_n(t) SF_n + Offset_n) \sigma_{modal,ij,n} \quad n = 1 \text{ to number of modes.} \quad (2.33)$$

In Eq. (2.33) $q_n(t)$ are the generalized coordinates and $\sigma_{modal,ij,n}$ are the modal stresses corresponding to the eigenvectors $[\Phi_{CB}^*]$ in 2.1.3.3.

The identical formalism in (2.32) and (2.33) leads to comparable computational burden, yet (2.33) crucially includes dynamic effects.

2.2.5 Stress-strain combination parameters

A combination parameter is required to compare the stress tensors of arbitrary complexity expressed by Eq. (2.32) or (2.33) to experimental material data. The fatigue test is normally performed under uniaxial conditions, where the stress tensor reduces to a scalar value. In stress analysis the popular choice of Von Mises equivalent stress (VM) is not directly applicable, partly due to the requirement to preserve the sign of the loading, partly due to the need to account for the main direction of load. In practice the Maximum Absolute Principal (MAP), the principal stress component with greater absolute value, is the most common option:

$$\sigma_{MAP} = \begin{cases} \sigma_1 \\ \sigma_3 & \text{if } |\sigma_3| > |\sigma_1| \end{cases} \quad (2.34)$$

In (2.34) σ_1 and σ_3 are the maximum and minimum principal stresses, implicitly indicating that the combination parameter retains the sign of the loading, so that the full range of compression-tension can be captured. A comparable Von Mises option, taking the sign of the σ_{MAP} , is referred to as *signed Von Mises*.

More elaborate combinations and fatigue solutions are required in case of change of direction of the maximum absolute principal or in presence of relevant contributions from the other principal stresses, a condition referred to as *multiaxility* [2]. One simple

alternative is the *uniaxial critical plane method* (graphically depicted in Figure 2-5), which is only applicable on the component free surface and considers the normal direct stress in planes normal to the surface. There will be a separate fatigue solution for each plane, so the solution time will be proportionally incremented by the chosen number of planes. For example, 18 calculations are required for 10 degrees increments of the critical plane rotation angle ϕ in Figure 2-5.

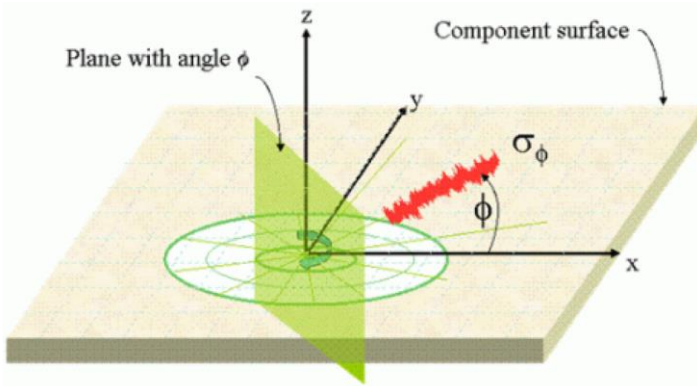


Figure 2-5. Resolution of normal stress to a critical plane; image from MSC Fatigue™ Theory Guide [68].

2.2.6 Rainflow Cycle counting

Experimental material test is normally generated with regular alternated loads, where knowledge of total range, from max to min and average stress value is capable of fully describing the load level as shown in Figure 2-6(a). The general definitions apply:

The stress range $\Delta\sigma$ is

$$\Delta\sigma = \sigma_{max} - \sigma_{min}, \quad (2.35)$$

the stress amplitude

$$\sigma_a = \frac{\sigma_{max} - \sigma_{min}}{2}, \quad (2.36)$$

and the mean stress

$$\sigma_m = \frac{\sigma_{max} + \sigma_{min}}{2} \quad (2.37)$$

In most practical cases the loads are variable amplitude with different levels or regularity or randomness depending on the application, as shown in Figure 2-6(b). Cycle counting

techniques have been used throughout history [2] with the aim to break-down any variable amplitude load into a collection of regular cycles fully described by Eq. (2.35-2.37). In 1968 Matsuishi and Endo [80] proposed a cycle counting method based on “falling rain” analogy; by extension all derived method are referred to as rainflow cycle counting methods, or RFC. Unlike its predecessors, RFC attempts to identify the closed hysteresis loops (i.e. fatigue cycles) induced by an arbitrary load functions, thus leading to more accurate estimations of the damage. Another important feature of RFC [81] is that signals with the same RFC are expected to produce the same damage, which is an important feature in signal reconstruction and experimental testing.

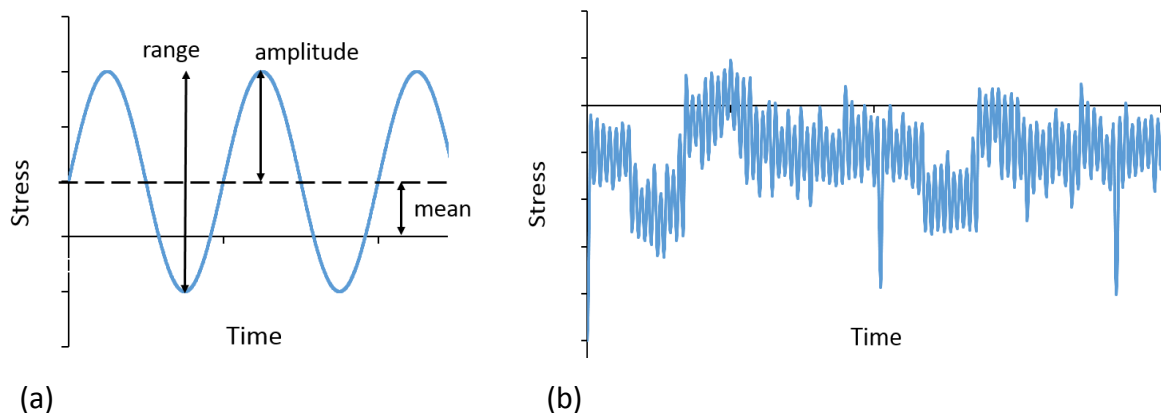


Figure 2-6. Regular cyclic signal (a) used for experimental test [2]; (b) excerpt of variable amplitude signal (uncalibrated) for a real life automotive suspension component [82].

The cycle counting techniques are best described through water analogies, from which it derives its original names. The *reservoir method* as described in the British Standards [63] is briefly outlined here. In Figure 2-7 an arbitrary signal (a) is reorganized so to start an end at his highest peak to constitute an imaginary water reservoir (b). The depth of the reservoir represents the largest outer hysteresis loop $\Delta\sigma_0$. As the water is drained from the absolute and relative minima, the “depth” and mean level of each residual water pocket is recursively recorded and represents the counted fatigue hysteresis cycles.

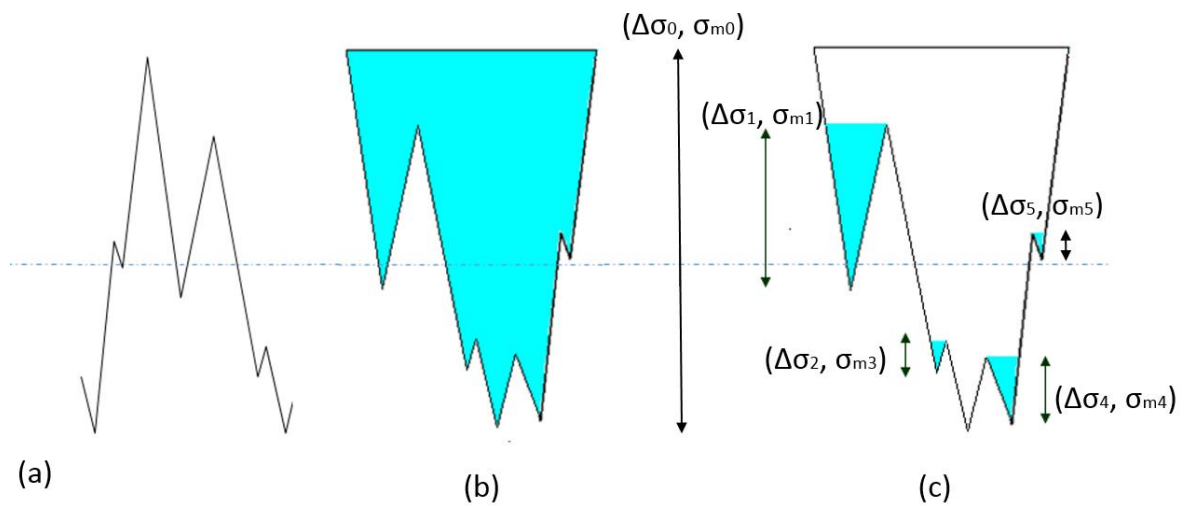


Figure 2-7. Rainflow cycle counting according to reservoir method [63].

The simple technique can be implemented in computer algorithms to address time histories of arbitrary complexity. The result is typically collected in a RFC matrix that can be inspected via 3D histograms such as in Figure 2-8.

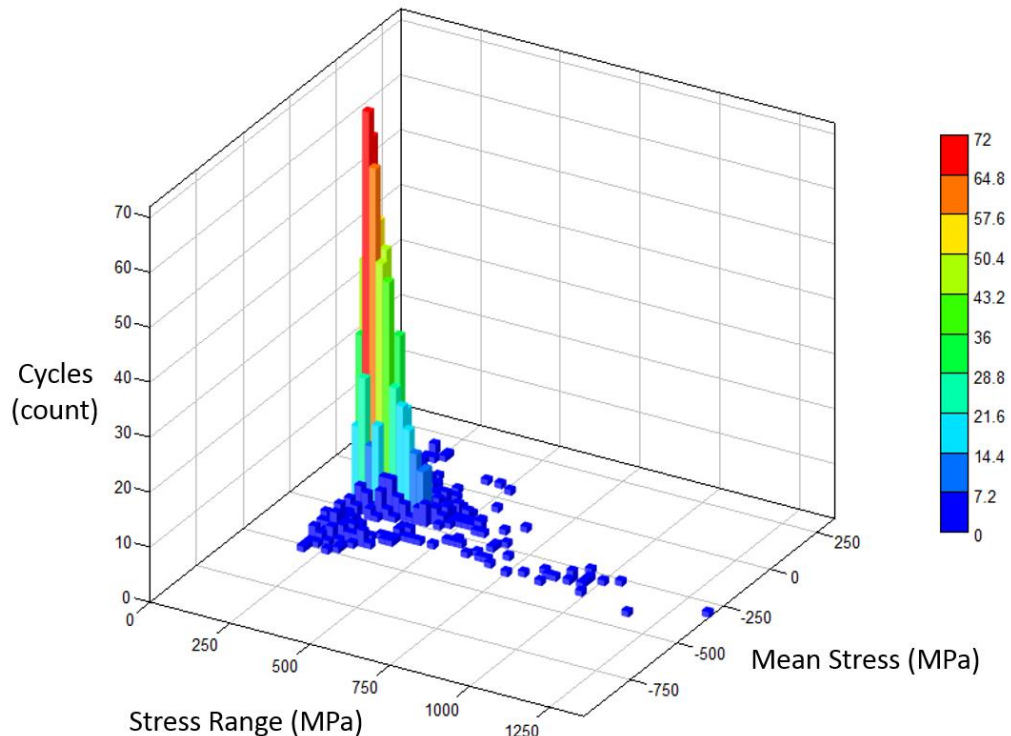


Figure 2-8. Rainflow cycle counting histogram for a representative automotive suspension signal in Figure 2-6(b) [82]; the range, mean and counted cycles refer to 2800 seconds of signal duration; rainflow algorithm and graphics from DesignLife™ [83].

2.2.7 Material fatigue models

A material fatigue model is a combination of analytical data and empirical rules that collectively aim to establish a similitude between the real life scenarios and the original experimental test. The analytical and empirical rules are used to include effects such as variable mean stress level, surface conditions, loading type, specimen size and any other relevant boundary and environmental conditions that might hamper the similitude. As anticipated in the introduction, the test data is collected according to either stress-life or strain-life model, which are now briefly described.

2.2.7.1 Stress-life model

The simple power law in (2.31) is commonly written in terms of straight lines in bi-logarithmic axes system, introducing the material constant b so that $m = -\frac{1}{b}$, eq. (2.31) is recast as

$$S^{-\frac{1}{b}} N = C, \quad (2.38)$$

taking the logarithm and isolating S leads to

$$\log S = b \log N - b \log C \quad (2.39)$$

In logarithmic axes Equation (2.39) represent a straight line with slope b . The constant C is related to the stress level at the interception with the y axis, *stress range intercept (SRI)*, by:

$$C = SRI^{-\frac{1}{b}} \quad (2.40)$$

Even though *SRI* represents the stress level corresponding to a life of 1 cycle, the *S-N* curve loses much of its accuracy beyond the yield stress range.

In practice the material data is best represented by two straight lines (Figure 2-9) so as to separate the high-cycle regime from the low-cycle regime. A fatigue strength parameter S_e can also be included to indicate the stress threshold to infinite life.

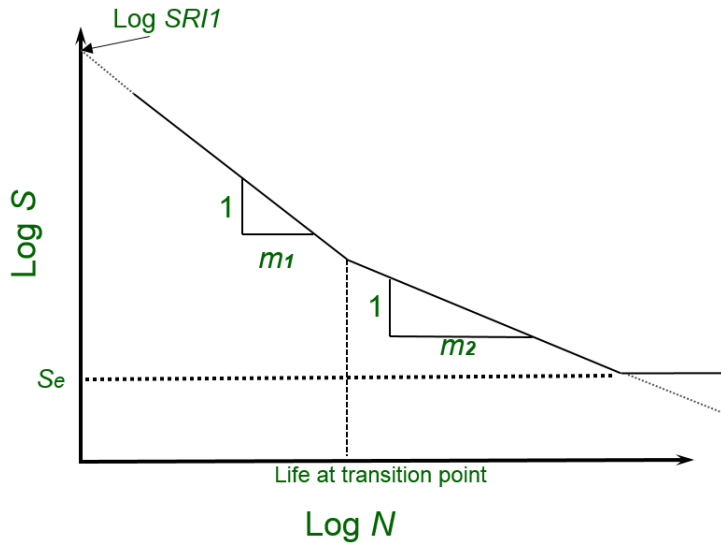


Figure 2-9. Bilinear S-N relationship in bi-logarithmic axes [63], [64].

2.2.7.2 Strain-life model

The strain life theory, (ε -N), is based on strain data monitoring during test, thus allowing one to extend test levels also beyond the linear elastic behaviour [2]. Without exposing the relevant mathematical complexity of the method, the essence is that the strain-life curve results from the sum of a plastic line, accounting for low cycle regimes, with the elastic line, accounting for high cycle regime, as depicted by the dotted lines in Figure 2-10(a). For linear stress-strain response the elastic line simply corresponds to the S-N method, so the S-N and ε -N method are in principle coinciding at high cycle regime. For medium to low-cycle regime, the ε -N is capable to consider the onset of plastic strain, which is not attainable with standard stress testing of the S-N method.

As plasticity is inherently nonlinear, it is worth clarifying that, albeit the ε -N method is compatible with computationally expensive nonlinear FE, the method is more commonly applied under standard linear assumptions. This apparent contradiction is justified by acknowledging that the induced metal plasticity is assumed to be confined to very small local areas. In other words, for the main part of the damage accumulation process the local plasticity is completely transparent to the global behaviour of the model, which will therefore remain linear. By extension, the further position is taken that [72]:

"in presence of localized plastic yielding the gross linear elastic behaviour of the material surrounding the notch also controls the deformations in the plastic zone... the energy

density W , in the plastic zone is equal to that calculated on the basis of the elastic solution".

The sentence is the justification for Neuber's rule[70] and similarly derived method [71].

The equivalence between elastic and plastic energy density is graphically presented in Figure 2-10(b), essentially expressing a conservation of local strain energy density during plastic yielding.

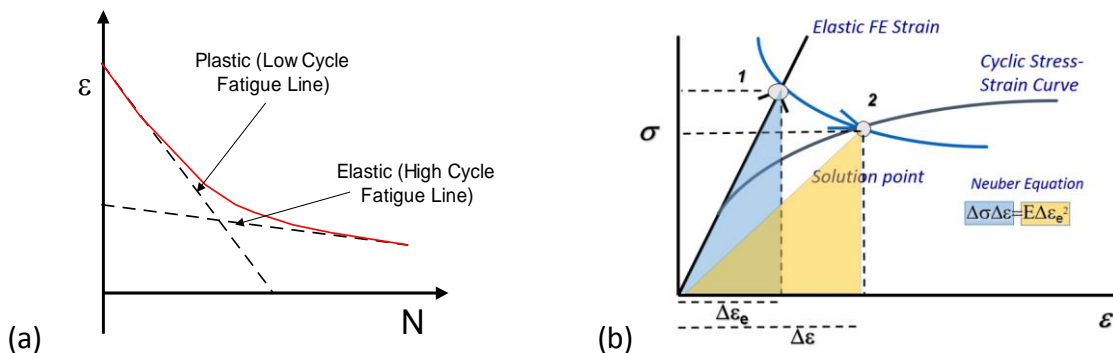


Figure 2-10. (a) Strain-life curve (continuous line) in bi-logarithmic axes [2]; (b) Neuber's correction rule to convert linear elastic strains into elastic-plastic strains while preserving the deformation energy [2]. Images from MSC Software Corporation [84].

2.2.7.3 Mean stress effect

The fatigue curves are normally obtained under the general conditions of fully reversed loading, with $\sigma_{min} = -\sigma_{max}$. This is normally referred to as stress ratio $R = -1$ according to the general formula

$$R = \frac{\sigma_{min}}{\sigma_{max}} \quad (2.41)$$

Other common testing stress ratio conditions are $R = 0$ and $R = 0.1$, where the loading is pulsating between near zero and the max value. In order to take into account of any other possible stress ratio condition, ranging from $R = -\infty$ to $R = 1$, the concept of equivalent stress generating identical damage at $R = -1$ is adopted. The simplest and most common $S-N$ option is over a century old and is known as the Goodman correction [2]:

$$\frac{\sigma_a}{\sigma_{ar}} + \frac{\sigma_m}{S_u} = 1, \quad (2.42)$$

where σ_{ar} is the equivalent stress and S_u is the material ultimate tensile strength. The equation (2.42) simply linearizes between the two extremes: $\sigma_m = 0$, where $\sigma_{ar} = \sigma_a$, and $\sigma_m = S_u$, where $\sigma_{ar} = 0$.

Over the past century, a number of options have been proposed both for S - N and for ε - N . In a recent publication Dowling [85] reviewed the most common options and demonstrated possible sources of inaccuracy.

2.2.7.4 Damage model

Fatigue failure could mean different things depending on the application, ranging from an invisible crack, to a fully separated component, so in fatigue analysis damage accumulation is described by a strictly non-physical damage parameter D , with possible value between zero, undamaged, and 1 for a failed component. For intermediate level of damage, the following hypothesis is made: taking S as the constant amplitude stress range and N , the corresponding expected total number of cycles as provided by the S - N curve, the damage accrued in each cycle is simply $1/N$. By extension the damage accrued after n cycles is expressed by the simple formula:

$$D = \frac{n}{N} . \quad (2.43)$$

As shown in 2.2.6, in variable amplitude loading an arbitrary stress history can be represented via multiple regular load levels S_i , each with its own cycle count n_i . The cumulative damage is then obtained as the sum of the damage contributions $D_i = n_i/N_i$, that is

$$D = \sum \frac{n_i}{N_i} \quad (2.44)$$

With failure assumed when $D = 1$.

The above rule was first proposed by Palmgren in 1924 and then developed by Miner in 1945 and is referred to as linear damage summation rule, Palmgren-Miner or simply Miner's rule. The rule makes the approximation that damage is accumulated linearly and that the order or the cycles does not affect the calculated damage. Having survived the test of time, the simple rule is known to be sufficiently reliable for most applications, with experimentally calculated D at failure ranging from 0.5 to 2 [2].

Figure 2-11 sums-up the main steps in the typical computer assisted fatigue process workflow. Clockwise starting from circled top-left corner, fatigue analysis begins as a post-processing exercise upon completion of FE stress or strain result recovery. The stress or strain time history is reduced to peaks and troughs and is passed through the rainflow cycle counting algorithm. Damage can be computed using the material model (a simple linear S-N curve in the image) from each pair of range-mean stress into the damage histogram. The total damage is accrued for each location according to the damage rule chosen. Once the process is repeated for each location, the collective results are normally visualized with standard FE post processing tools, like a fringe contour plot for example.

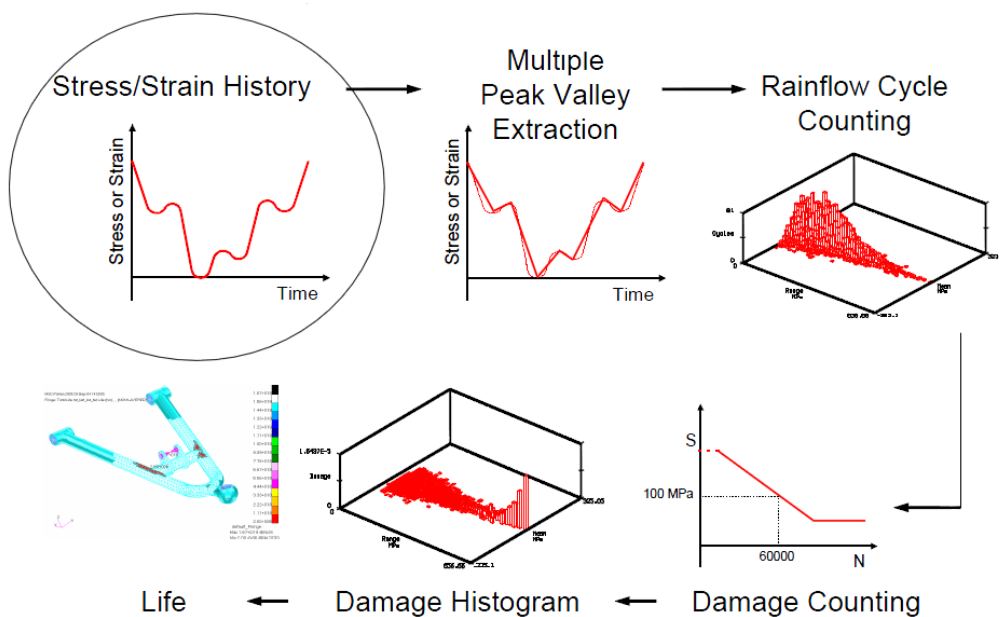


Figure 2-11. Fatigue workflow based on rainflow counting and S-N material description, from [56].

2.2.8 Fatigue stress concentrations, notching and welds.

In the context of FE, it is normally assumed that the modelling practices are sufficiently refined to assure “good quality” stress, however this is neither always possible (e.g. at discontinuity) nor necessary (e.g. a small cable threading hole). Even with current and future highly detailed modelling, there will always be need for mathematical abstraction in areas that have inherent manufacturing variability, such as welds, spot-welds or rivets. In such situations it is normally possible to identify a stress concentration factor K_t to

represent the effect of the notch on the nominal or remote stress S . The resulting maximum local stress is:

$$\sigma_{max} = K_t S \quad (2.45)$$

However, the so derived σ_{max} does not necessarily fit well the similitude principle with the experimental test, typically performed with unnotched coupons and uniform stress state. With the probability of fatigue failure being based on a weakest link principle [86], at equal stress levels it is logical to expect worse performances in uniformly stressed coupons. The formalization of this difference in performances is given by the fatigue notch factor K_f , capturing the effect of the notching on the fatigue strength alone:

$$K_f = \frac{S_e^{(unnotched)}}{S_e^{(notched)}} \quad (2.46)$$

The effects of the notching on S_e are assumed to propagate linearly in log scale, so that the rest of the fatigue curve is adapted to the new limit by pivoting the curve on the SRI to match the new fatigue limit at S_e .

When fatigue test results are not available, a number of theories based on geometrical and material consideration have been developed to derive K_f from K_t . Yao et al. [87] classified and compared the available theory according to average stress, fracture mechanics and stress field intensity models; the latter method resulting in consistently smaller errors. In practical FE modelling the relationship between K_f and K_t is still to be dealt manually on a case by case basis.

Welds could be seen a special case of notching with geometries that are repetitive in nature and have some degree of similarity in manufacturing, size and loading. Weld classification rules and the related weld classes are shared by all internationals standards [63], [64]. For more specific applications, such as thin sheet welds and spot welds used in automotive fabrications, the so called *structural stress* methods have been developed with the aim to avoid detailed modelling of the weldments while preserving the $S-N$ based logic. In 1995 Rupp et al. [88] proposed a spot weld $S-N$ method based on a simple beam representation and structural stress derived from the forces through the beam. Later, Henrysson [89] proposed an approach based on the same geometry but using stress intensity functions to generate $\Delta K-N$ fatigue curves. An equivalent structural stress

S-N approach targeting automotive seam welds was devised by Fermér and Svensson [90] at Volvo Car, with the weld “line” represented by a single inclined FE element. The recent book by Radaj et al. present a systematic survey of the multiple local approaches deployed for fatigue assessment of both spot and seam welds details. In 2006 [91] a comprehensive campaign on over 500 high strength steel spot-welds was carried out by a consortium of automotive industrial players and validated the structural stress methods. The result confirmed that spot-weld durability is largely driven by geometrical factors, just as it was the case with the weld classes from International Standards.

In essence, through the techniques described above, stress concentrations, joints or welds can be approached with a similar logic and method that is applied to the fatigue analysis of the base unnotched material.

2.2.9 Sources of variability and uncertainty in fatigue

A fatigue process can be schematically represented by 4 independent blocks:

- material parameters description (typically obtained through limited testing),
- manufacturing processes,
- loads (and the ensuing stresses) derived from customer usage,
- fatigue modelling.

For each block there are multiple sources of variability, such as the ultimate tensile strength or the fatigue limit of a material, as well as multiple uncertainties, e.g. choice of critical plane, representative customer usage, errors or approximations in the model.

As a consequence, any fatigue investigation is affected by both variability and uncertainty that can only be accounted for in statistical terms. Weibull’s aforementioned weakest link approach [86] yields the probability distribution that bears his name. Schijve [92] described and compared the 3-parameter Weibull distribution with the $\log(N)$ and 3-parameter $\log(N-N_0)$, with the two 3-parameter distributions outperforming the $\log(N)$; despite this result the $\log(N)$ distribution remains a popular option due to its simplicity and conservativeness at low probabilities. Schijve also reviewed the common independent sources of scatter in fatigue tests. The *S-N* curve is intrinsically derived from

statistical considerations so the curve represents a best fit (linear regression), however it is noteworthy that the scatter is not uniform along the regimes. As shown in Figure 2-12 a higher scatter is typically associated at the high cycle regimes due to the more complex mechanism of microcrack growth.

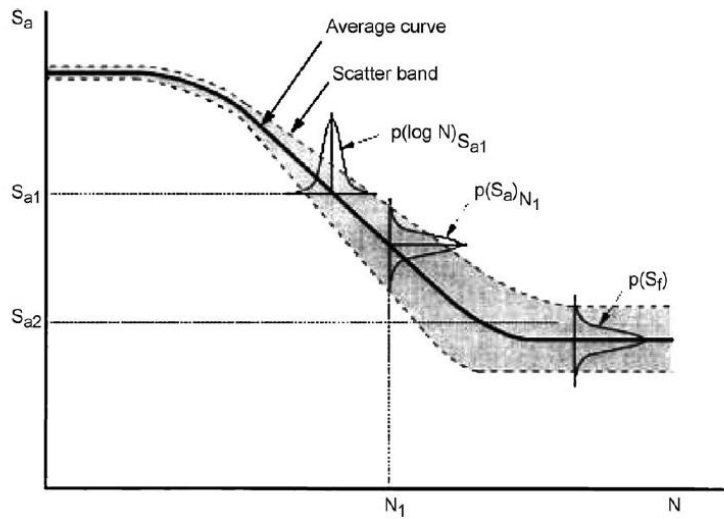


Figure 2-12. S-N curve showing different scatter bands in different regimes, from [92].

The limited knowledge and the need for a practical engineering approach require some simplification, so that any given S-N curve is describing the median (or 50% probability) and constant value deviation is typically used. For example, in Figure 2-13 the weld class F [63] is represented with scatter bands tolerance interval of +/- 2 standard error deviations.

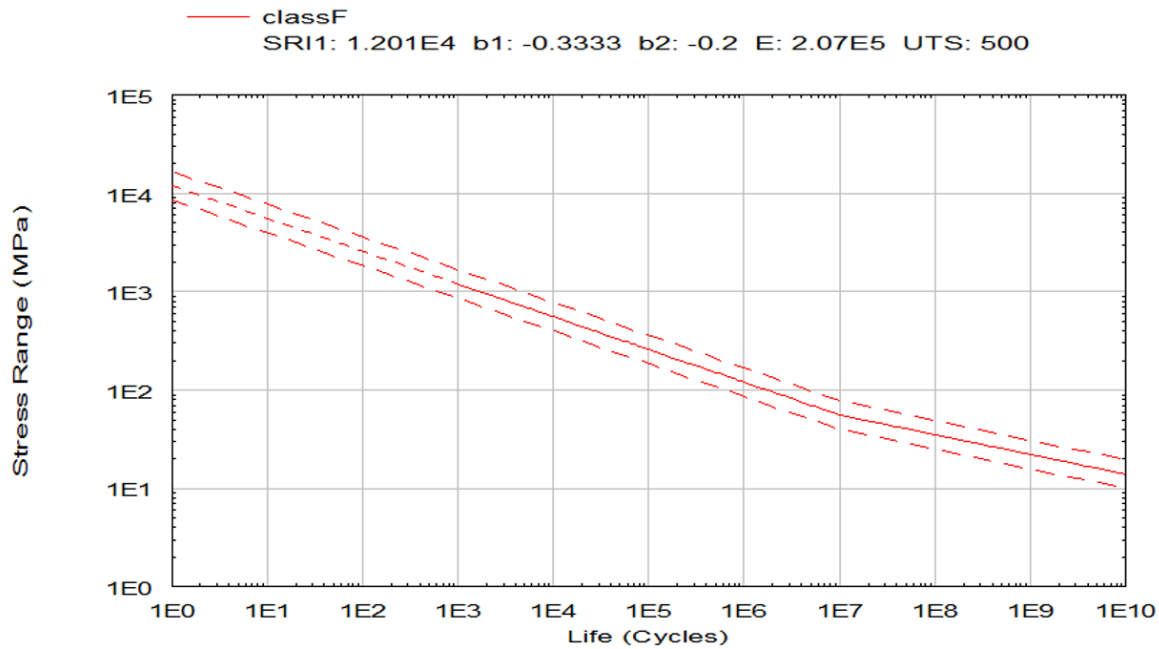


Figure 2-13. Stress-Life Weld class F curve [63] centred between a 2 standard deviation scatter bands; graphics in MSC Fatigue™ [68].

Statistical analysis is therefore deployed both to describe the fatigue properties, yielding tolerance or confidence limits, and to estimate a probability associated with a certain level of load. In a chapter dedicated to statistical aspects of fatigue [3] Stephens et al. describe how to quantify confidence through a factor k , the “one-sided tolerance limit factor”, taking into account probability of survival and a confidence level as a function of the sample size.

2.2.9.1 Bayesian framework and diagnosis testing

Although the Bayesian theory originated nearly as early as probability theory, provided that it builds upon the concept of conditional probability, its recognition and application as an alternative approach to the classical frequentist approach is relatively recent. Early applications in accelerated life test are described by Proschan et al. [93] in 1980. Research and applications in updated Bayesian probability are also common, especially in the field of health monitoring when the remaining useful life or the updated probability of crack propagation can help optimizing the inspection interval [94] and contribute to system reliability assessment [95]. This is still an open research field for fatigue simulation applications and more research and applications are foreseeable [96]. Simpler applications of Bayes’ rule are common in diagnosis testing, where it provides a means to

compare the accuracy and efficiency of different test procedures, as further detailed in the next paragraph.

Diagnosis testing is widely applied in machine learning and in the medical field as a method to identify the likelihood of a given post-test event (e.g. detection of illness) given an assumed pre-test probability of the event.

Assuming an hypothesis probability $P(H)$ for an event "H" (e.g. height of sea wave, onset of a disease, crack size) and given $P(D)$ the probability of a diagnostic event "D" (e.g. wave measurements, the presence of a hereditary gene, samples failed after inspection etc.), Bayes' rule states that:

$$P(H|D) = \frac{P(H)P(D|H)}{P(D)} \quad (2.47)$$

On the right side of equation (2.47), $P(D|H)$ is the expected *hit rate* or *success rate* of the predictive method offered by $P(D)$ and represents the events H that are correctly predicted by the events D.

On the left side of equation (2.47), $P(H|D)$ represents the *posterior probability* of correctly predicting event H given that event D is occurring. Normally this is expected to be an augmented probability with respect to the assumed $P(H)$ if D has any diagnostic power over H.

At the denominator of (2.47), considering H' the complement of H, so $P(H + H') = 1$, $P(D)$ can be partitioned in:

$$P(D) = P(H)P(D|H) + P(H')P(D|H') \quad (2.48)$$

$P(D|H')$ in equation (2.48) is the probability of a false positive identification and is a measure of the efficiency (or cost) of the prediction.

Diagnosis testing consists in testing the hypothesis H against evidence D. $P(D|H)$ is represented by the *true positive rate*, *TPR*, that is the number of *true positive conditions* results, *TP*, over the total number of positive conditions, *Pos*. Similarly, $P(D|H')$ is represented by the *false positive rate*, *FPR*, the number of *false positive conditions*, *FP*, over the total number of negative conditions, *Neg*.

The definitions above can be best interpreted via the *contingency table* in Figure 2-14, a simple mapping on the four possible outcomes of a diagnostic test.

		True condition		TPR=TP/Pos
		positive	negative	
Hypothesized condition	Yes	True Positives	False Positives	FPR=FP/Neg
	No	False Negatives	True Negatives	
		$Pos=TP+FN$		$Neg=FP+TN$

Figure 2-14. Contingency table in diagnostic testing with four possible classes.

Receiver operating characteristics, ROC, is a technique that was originally applied in radar signal detection as a binary classifier as function of receiver thresholds [97]. The ROC space is a two-dimensional graph in which the true positive rate is plotted on the Y axis against the false positive rate. The ROC diagrams can help in graphically visualizing and comparing results from contingency tables.

In this study the analogy is made between a medical test with dichotomous outcome (predicted illness or otherwise absence of illness) and fatigue damage prognosis (likely hotspot or otherwise safe area) according to the hotspot prediction technique.

2.2.10 Background to FE based accelerated fatigue simulation

Accelerated fatigue simulation, AFS, refers to the techniques generally aimed at improving the speed and efficiency of the fatigue simulation process. One of the early roles of fatigue simulation was to provide the numerical validation in support of experimental fatigue testing. Just as for experimental testing, the challenge in durability simulation is to convey the component lifetime usage (collected and extrapolated) into representative short duration events producing equivalent damage.

As FE and fatigue simulation moved forward in the industrial design process, accelerated fatigue simulation has been more specifically designed and applied to streamline the fatigue simulation design cycles, especially in the early phases of the design when

multiple iterations are expected. As broadly described in the introductory chapter, the challenge now becomes the sheer computational size of the problem to be submitted to the fatigue analysis.

Regardless of the CAE fatigue method of choice, the time necessary to run an ordinary fatigue simulation job is in a direct proportion with:

- The length and number of the loading events.
- The number of FE entities -nodes or elements- being analysed.

Therefore, accelerated fatigue simulation can either be applied via *time compression*, the time filtering to reduce the number of data points, or via *model filtering*, the identification of critical entities to reduce the model size.

2.2.10.1 Time compression techniques in fatigue simulation

Time compression techniques were initially developed for component accelerated fatigue testing. In 1973 Fuchs et al. [98] experienced that 90% of the loading only generated 10% of the calculated damage. They presented a computer algorithm called *ordered overall range* apt to eliminate smaller less damaging cycles. The method is based on a technique previously known as the *racetrack* method, due to the analogy of a racer cutting corners through gates [3]. In 1980 Socie and Artwohl [99] used strain life analytical damage estimates to eliminate up to 20% of the damage contributed by small cycles and reduced the total reversals by an order of magnitude. Analytical results compared well with prediction for the crack initiation life, however it was found that crack propagation was affected by the editing. In 1988 Heuler and Seeger proposed an allowable gating level at 50% of the endurance limit of the material under constant amplitude loading. In 1991 Hurd [100] proposed an accelerated simulation testing method based on energy content criterion for road data editing rather than fatigue damage. The durability experimental test compressed 100,000 simulated durability miles into a period of 15 days. In 1997 Caruso and Dasgupta [101] described the most commonly used analytical models for product life estimation and accelerated life testing. In 1999 Farrar et al. [102] classified the accelerated vibration techniques according to three types: testing for fewer cycles by scaling the loads, deletion of cycles with little damage potential and increasing the forcing frequency to reduce test time. In 2001 Yan et alias [103] investigated a small-load-

omitting criterion, SLOC, based on fatigue crack initiation threshold as proposed by Zheng [104].

Fatigue data editing, FDE, the elimination of less-damaging cycles via fatigue calculations at selected pick-up points, was recently investigated by Kadhim et al [105] in FE durability assessment showing a practical automotive example and the potential time saving. As previously noted by Farrar, Kadhim remarked that despite the wide acceptability of time editing practices, very limited research is available that is dedicated to FE simulation simplification.

The small-load-omitting criterion, can also be adapted to accelerated simulation, where the benefit of a numerical algorithm leads to further options and possibilities, as explained in the following paragraphs.

2.2.10.2 Peak-valley extraction and multiple-channel gating

The simulation model provides a simplified environment where many of the real-life effects are absent or simplified. Under the hypothesis of linear damage summation and using rainflow cycle counting procedures, the cycle sequencing order of the event is lost, along with the frequency content. In other words the loading path between relative peaks and troughs is deemed irrelevant and is discarded. *Peak-valley extraction*, PVX, refers to the editing of the time history where the intermediate time steps between relative peaks and troughs are removed from the signal. However, unlike experimental test, in most cases the simulated model is subjected to multiple coordinated loadings (or *channels*), this means that intermediate data between peaks have to be retained if they constitute a peak or a trough in any of the simultaneous signals.

The key steps of the peak-valley elimination process include:

- Identify peaks and valleys from each input signal.
- Retain only points corresponding to peaks and troughs across all channels, so to preserve the correct phase of the multiple signals.
- Optionally apply *racetrack* gating to the coordinated signals to introduce further filtering based for example on percentage of the max range.
- Provide to the fatigue solver a potentially much smaller portion of the original loading data.

In the simple example in Figure 2-15, peak-valley elimination reduces a single continuous time history to 9 turning points.

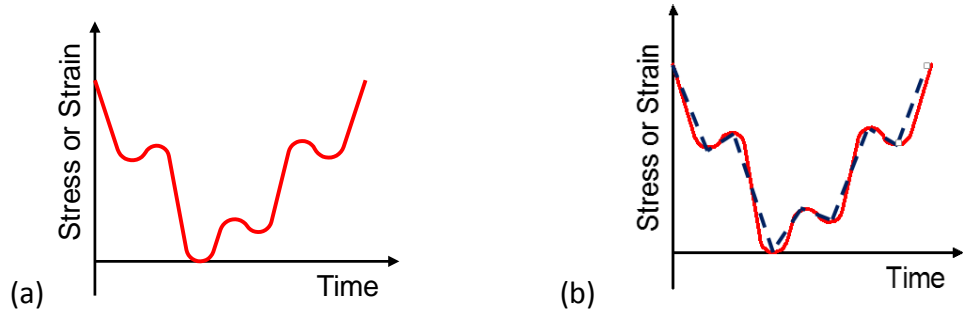


Figure 2-15. A continuous signal (a) is equivalent in term of fatigue damage to a signal represented by its turning points, dashed line (b), [56].

An optional gate level may be used to further eliminate lower range turning points: any range below a given gate threshold value is discarded. Figure 2-16 describes an application of multiple peak-valley on 3 channels sampled at 50 Hz. A gating level of 70% from peak range on the 3 channels, originally comprising 6001 points, Figure 2-16 (a), delivers a 95% reduction, down to 276 points, Figure 2-16 (b). The number of points and original phases are kept consistent during the editing.

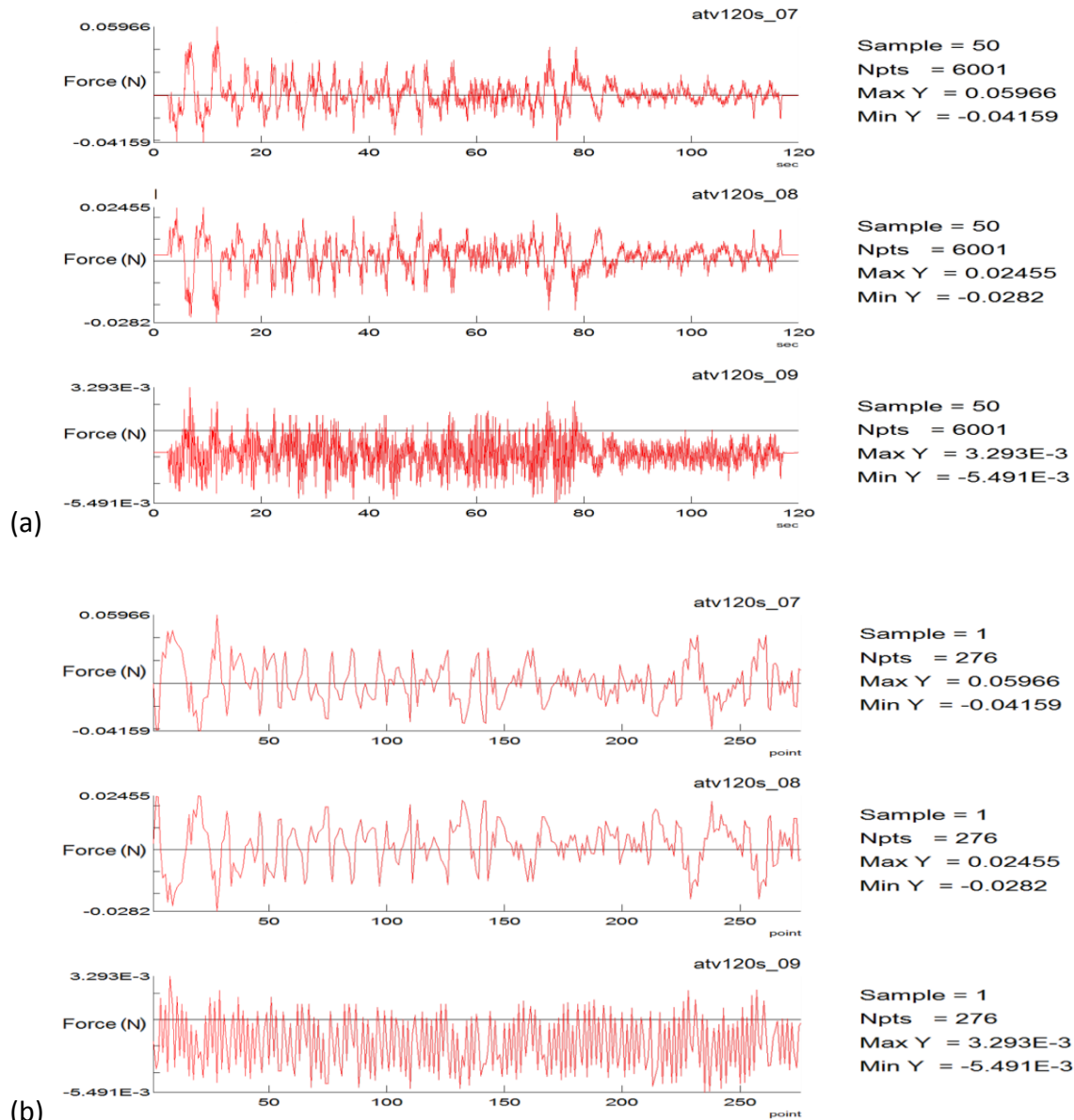


Figure 2-16. (a) Demonstration of multiple peak-valley application on 3 simultaneous channels. (b) A 70% gating on signal maximum range yields a 95% reduction in time history points. Peak-valley filtering and graphics in MSC Fatigue™ [68].

2.2.11 Acceleration via model filtering.

Possibly due to the applied nature of the requirement, most publications on the subject on model filtering are limited to industrial players and commercial software providers. Despite the high level of interest and the common usage of such practices, there is no public study with regard to their applicability and reliability and the analyst has to rely mostly on his own empirical experience.

In 1987 Conle [106] described simplified methods to determine critical, *hot spot*, element stress histories in complex multiaxial loading conditions. In 1993 Gopalakrishnan et al. [25] identified a limited set of fatigue critical areas based on peak loads and max stress ranges. Later Kuo and Kelkar [26] detailed a process for global durability analysis where critical areas identification is based on off-line stress influence coefficients. In 1997 Huang et al. [27] described an accelerated process for durability analysis based on FE methods; they used short peak-load events to prioritize entities based on Von Mises stress level distribution. Later, Dietz et al. [38][48] used quasi-static FE stress recovery with multibody systems determined loads to identify selected critical locations in a stress-load matrix, to be thereafter subjected to a detailed fatigue investigation. In 2001, Huang and Agrawal [107] patented a method of identifying critical elements in fatigue analysis based on Von Mises stress bounding and filtering modal coordinates' history. In 2005 Zeischka et al. [84] designed an automated framework for hotspot detection, dynamic and fatigue simulation in engine crankshafts; high numerical efficiency was obtained through *a priori* identification of critical sub-regions around bearing support areas. Also, in 2005 Braccesi et al. [40] described qualitative methods to rapidly identify the most stressed locations, before a full evaluation of fatigue damage. In the aforementioned 2013 paper, Rentalinen et al. [44] defined a detailed sub-model for selected critical details (e.g. welded connections) and performed stress recovery quasi-statically, using displacements obtained from dynamic simulation as boundary conditions.

In terms of standard industrial practices, all the commercial software assessed [68], [108], [83] include some form of automated controller to enforce both time and spatial reductions. As the majority of time based fatigue simulation practises are based on linear superposition, that is to say, static or modal, the applicable elimination criteria are also based on the same assumption. The commonly applied techniques for elimination of entities are described in more detail next, as they are used in comparative assessments throughout this investigation.

2.2.11.1 Entities elimination in static or modal superposition

A useful classification can be made between *online* and *offline* filtering. In Figure 2-17 the *online* methods are those applied during the FE or FE and multibody dynamics simulation

(MBD) by virtue of time based stress recovery, with the filtering process potentially being repeated with each durability event.

Conversely, *offline* methods don't use the time-history loads and can be applied independently, *a priori*, to the dynamic solution, with the filtering method executed only once across multiple events.

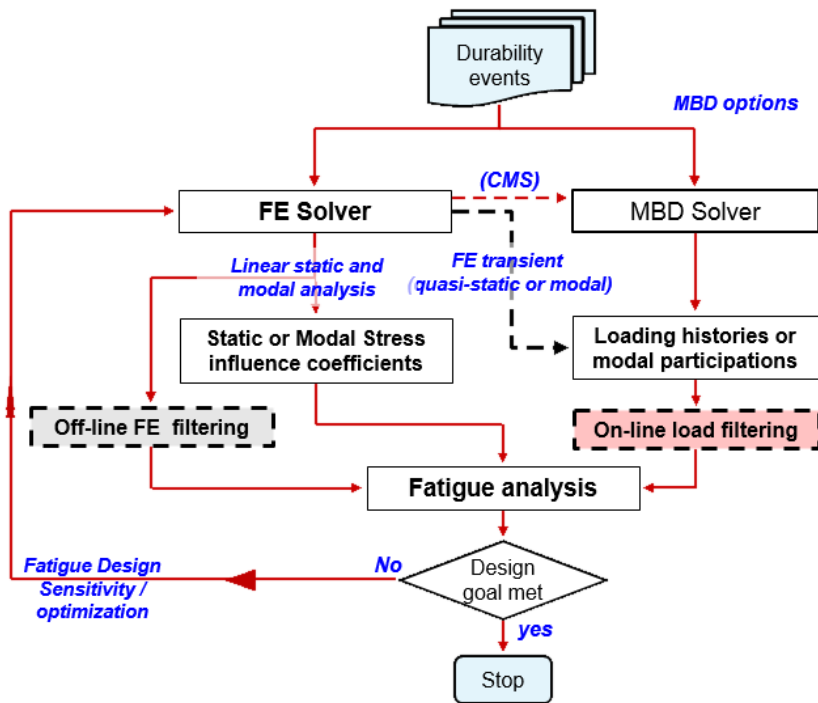


Figure 2-17. The CAE fatigue time based flow diagram with the inclusion of offline and online filtering.

Alongside the elimination algorithm, the estimated stress severity can be used to rank the analysis entities prior to performing a fatigue calculation. Ranking is used to ensure that the most damaging results are processed and eventually displayed first. This is a good practice to get fast feedback on a given durability event without having to wait for full analysis to be complete.

In nCode® based solvers [68], [83] the auto elimination % value , or alternatively the number of entities, can be specified to indicate the number of nodes/elements to be retained during the fatigue analysis. The entities eliminated will not produce any results.

On-line two-pass elimination

The online methods require that the full loading history is available and is organized in multiple *channels*. A loading channel is the time evolution at either a loading point (unit loading scaling in quasi-static method) or modal participation factor (modal superposition in modal transient).

The filtering method is then delivered via a two-step process, or *two-pass elimination* in [68] and [83]. A fast *first pass* fatigue calculation uses strong peak-valley time editing of the loading histories (e.g. 90% gating from peak-load) to compress the time data. Due to the omission of cumulative damage from edited smaller cycles, the simplified first pass solution is not valid for fatigue structural integrity assessment and is used only to provide a prioritization of the likely critical entities. In a *second pass* only the most critical entities from the previous prioritization step are submitted to a refined fatigue simulation using unfiltered or weakly filtered loading histories.

The *limits-only* elimination is an extreme first pass simplification using only the peak (Max_i) and trough (Min_i) in each individual loading channel. A simple limits-only approach is based on an *assessed Von Mises stress* defined at each FE entity in the model (element or node) as:

$$\sigma_{Assessed} = \sum_i (Max_i - Min_i) \sigma_{VM,i} \quad i = 1 \text{ to } c, \quad (2.49)$$

where c is the total number of loading channels and $\sigma_{VM,i}$ is the Von Mises stress at channel i obtained from static or modal influence coefficients. The assessed stress is not a true stress occurrence, given that the max and min values are not expected to happen simultaneously, but represents a stress range upper boundary inherent in the real load data.

A priori, off-line elimination

A priori, off-line, methods are essentially a one-off upfront filtering and sorting capability that is applied before running the quasi-static or modal transient events. The filtering is based purely on stress influence coefficients in Eq. (2.8), without the weighting from actual loads.

A simple implementation considers the element *assessed stress*, $\sigma_{assessed}$, as the summation of the Von Mises stress in each available load case:

$$\sigma_{assessed} = \sum_i \sigma_{VM,i} \quad i = 1 \text{ to } c. \quad (2.50)$$

During the filtering process, if $\sigma_{assessed}$ falls below a predetermined ratio the corresponding elements or nodes are eliminated from the subsequent fatigue calculation. Aside the inherent approximation, such a simple procedure is only applicable to a quasi-static method. In modal methods the Von Mises stress are not in a comparable scale and definition (2.54) loses significance. A variant of this approach, that is applicable equally to quasi-static and modal methods, constitutes the basis for the novel simulation acceleration technique which is the subject of chapter 5.

2.3 Summary

This chapter presented a review of the common numerical techniques deployed in time based dynamic and fatigue simulation of mechanical systems. The first part of the chapter (Part A) provided an overview of the common FE techniques deployed to the resolution of time transient simulations in mechanic systems, including useful considerations on modal reduction via component-mode synthesis and the integration with multibody systems. Component-mode synthesis based on Craig-Bampton method will play an important role in the investigation as a primary basis for hotspot prediction.

Part B covered the fundamentals of FE based fatigue methods. Attention was given to the commonality of the approach whether S - N or ε - N methods are applied to the base material or to component details and joints. The chapter terminates with an overview and classification of the commonly applied practices in accelerated fatigue simulation. An initial distinction is made between acceleration obtained via *time compression*, the time filtering to reduce the number of data points, or via *model filtering*, the identification of a subset of critical entities aimed at reducing the problem size.

A further useful classification is made between online and offline methods. The latter methods don't use the time-history loads and can be applied independently, *a priori*, to the dynamic solution. A method based on *a priori* hotspot identification is a primary focus of this investigation. The next chapter reviews the hypotheses, limitation and potential

errors deriving from accelerated fatigue simulation with the purpose of identifying applicable metrics and assessment tools.

Chapter 3: Model filtering in accelerated fatigue simulation

The background review in 2.2.10 presented multiple options in accelerated simulation. Industrial practice, however, favours a simple approach that has to be applicable to multiple loads, multiple locations and large amounts of data. Such requirements are met by the methods based on peak and valley extraction gating as described in 2.2.10.2 and 2.2.11.1. This chapter reviews the hypotheses and limitations for filtering methods based on peak and valley extraction. A novel error classification is based on four identified and separate sources of approximations, for which dedicated performance metrics are proposed.

3.1 Review of common assumptions in elimination based on peak-valley gating.

A distinction should be made between explicit and implicit assumptions made by the peak-valley method; the former relate to the applicability and scope of the algorithms implemented in the numerical model and can be rigorously met; the latter are accepted principles and guidelines that may have some level of variation depending on the industry and scope of application.

The following general assumptions are made with regard to the scope of this investigation:

- metal fatigue,
- linear deformation through pseudostatic or modal superposition, but with system's large displacements and geometric non-linearities tackled via multibody dynamics,
- variable amplitude loading captured via rainflow cycle counting techniques and assuming applicability of linear damage summation rule (damage accumulates linearly and there are no sequence effects).

The implicit assumptions are typically used to limit the scope to a subset of applications of interest. Given the focus on the time-based fatigue of mechanical systems typical of

general transport or industrial machinery, further assumptions are made to reduce the breadth of the numerical requirement:

- Lightly damped components, typically via proportional structural damping.
- Low modal density for the frequencies of interest (no acoustic or random vibration fatigue).
- Fabricated structures, typically made up of joints and welds, with multiple sources of stress risers, where only a small percentage of the whole model is expected to be of potential interest for fatigue.
- Realistic loads, so to exclude extreme variations, distributed in multiple points and collected in multiple events. Furthermore, a small proportion of the cyclic loads creates most of the damage. A typical expectation for a standard signal is that around 10% of the cycles generates 90% of the damage [98].

The last two assumptions are mandatory requirements without which efforts in accelerated fatigue simulation would be redundant.

Assuming the conditions above are all in principle acceptable, questions remain with regard to the acceptable threshold value required for small cycle elimination and the attendant benefits and risks. From a literature review, it appears that there is no single answer. This chapter compares the potential errors and benefits, and establishes some metrics that can be used for comparative assessment.

3.2 Treatment of errors in accelerated fatigue simulation

As previously described in 2.2.9, there are multiple sources of variability and uncertainty that affect any fatigue calculation. In terms of simulation these should also include the possibility of bad modelling practice or errors in determining the local deformations.

With the intention of isolating the effects specifically from accelerated fatigue simulation, all other sources of variability are ignored and good modelling practices are either assumed or demonstrated. As a direct consequence a non-accelerated fatigue simulation, the *baseline fatigue simulation*, will be taken as correct and all the errors will be calculated with respect to the baseline result.

The following four sources of accelerated simulation errors or, one might say, approximations, can be identified:

- Damage value differs from baseline - *Error-Type I*.
- Damage rank differs from baseline - *Error-Type II*.
- Fatigue critical entities are eliminated from calculation - *Error-Type III*.
- Non-critical entities are included in the fatigue calculation - *Error-Type IV*.

In the ensuing section the errors are further clarified and quantified with appropriate metrics. Given the applied nature of the method, it is useful to refer to a realistic test case as a demonstration workbench. In the next section a real case of an All-Terrain Vehicle is used for demonstrative purposes, but does not detract from a wider applicability of the definitions and methods that follow.

3.2.1 The All-Terrain Vehicle baseline test case

The FE and multibody simulation models of an Honda All-Terrain Vehicle, ATV, are the result of an open collaboration between industry and academia led by the Fatigue Design & Evaluation Committee of the Society of Automotive Engineers [109]. The vehicle in Figure 3-1 was the subject of a number of experimental and numerical investigations with the aim of developing a methodology for using computer simulation to predict structural fatigue life of automotive components [3]. The accessibility, relevance and completeness of the documentation made this model an ideal subject for academic theses and demonstrators [110]–[112]. An overview of the multibody assembly and the FE frame model is presented in Appendix B. Additional details with regard to the applicable durability schedule are presented in Chapter 6.



Figure 3-1. All-Terrain Vehicle before instrumentation [109].

The Multibody Dynamics model (Figure B-14 in Appendix) was generated in the commercial solver ADAMS™. The model includes a flexible frame generated via Craig-Bampton component-mode synthesis (2.1.3.2) [113] using the commercial FE solver MSC Nastran® [33].

The following section anticipates some of the fatigue calculations that are further discussed in chapter 6.

3.2.2 Approximations, errors and metrics in peak-valley filtering

In peak-valley extraction with gating, described in 2.2.10.2, the contribution from smaller load cycles might be dominant with respect to fewer high intensity loads [99], thus leading to a possible omission of important fatigue-critical entities.

It is useful to recognize that even an unfiltered peak-valley extraction can carry some degree of approximation when multiple concurrent channels are combined. Figure 3-2 shows an extreme example of such a situation with out-of-phase tension-compression and bending load histories, where the peak stress consistently appears at time points that are not relative peaks of the individual channels.

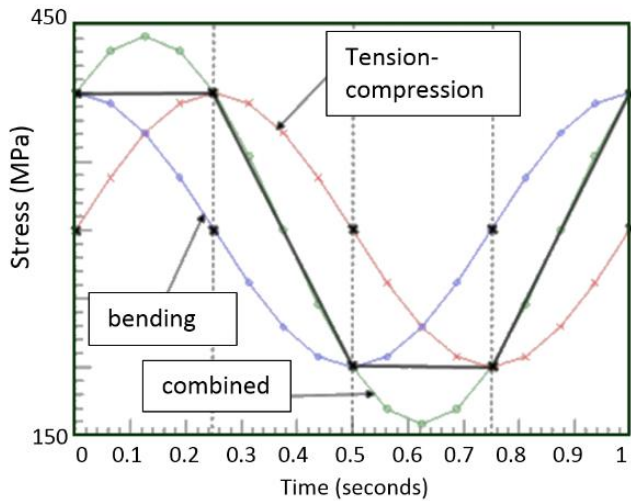


Figure 3-2. Example of combined loading where stress peaks occur at a time that is not a peak or valley in the isolated time histories [68].

3.2.3 Effects of damage value error, Error-Type I

Excluding special cases such as in Figure 3-2, common industrial experience is that peak-valley is representative of the loading. As smaller cycles have less relevance than higher ranges, according to the fatigue curve power law, simplification is possible at the cost of some approximation. This damage approximation error accrued as consequence of peak-valley filtering, is herein referenced to as *Error-Type I* ("I" Roman numeral).

The accelerated process can be described through selected events from the durability schedule of the All-Terrain Vehicle example (Appendix B.3). For *event-1* the original load data spans 768 seconds sampled at 204.8 Hz for a total of 157,360 data points. The load is applied to wheel spindles in the multibody simulation, with output steps at 100 Hz, resulting in 112 modal participation functions, each comprising 76800 points. Figure 3-3 shows the effect of different levels of peak-valley gating on the loadings. The horizontal axis presents the number of points in each of the 112 channels. At the far right the number of points drops by 20% at 10% gating; at the far left the drop is 82% at 80% gating. The vertical axis is the time stamp of the retained points. Without needing to look at the original loads, the constant slope indicates a regular distribution of cycle ranges with no risk of dismissing large damage contributions together with an acceleration factor that is proportional to the gating level. Noticeably, all gating levels

showed the same jump between 620s and 680s (near vertical slope), indicating an interval of low activity in the signal.

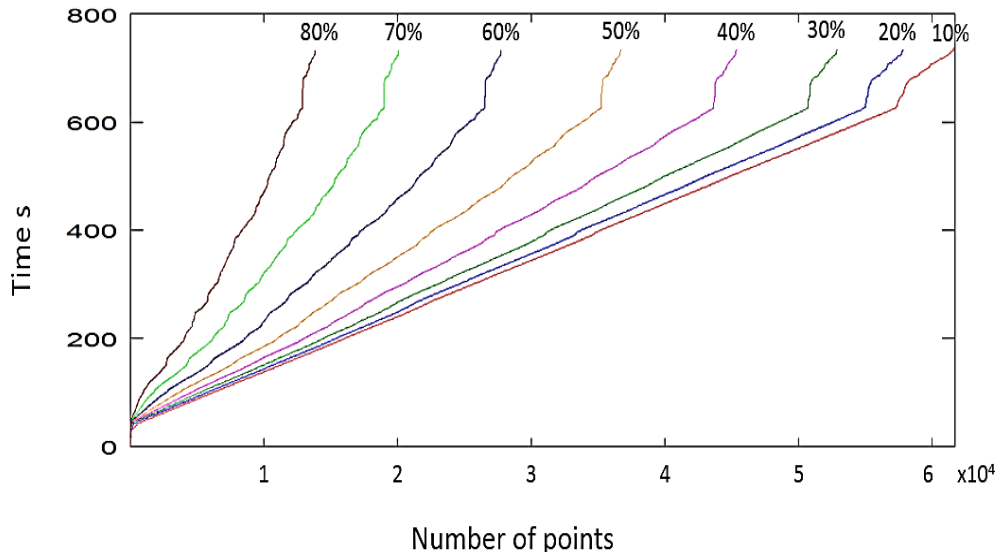


Figure 3-3. Effect of peak-valley with different filtering (% of peak) for the All-Terrain Vehicle *event-1*, with 112 simultaneous load channels, each with 157,000 points; peak-valley algorithm and graphics from MSC Fatigue™ [68].

Having looked at the effect of gating on the length of the signal, the level of gating that is acceptable (for example a level not affecting the damage calculation by more than 10%) will be examined next. As seen in the literature review, the gating level has been the subject of specific research and is case dependent. An alternative evidence-based approach is proposed in the section below.

3.2.3.1 Determination of small-load-omitting criterion

In Figure 3-4, the baseline run is compared with 10% and 90% gating respectively. The first 500 most damaged elements are presented in order of increasing life. It is observed that in the case of the 10% gating, the computed damage is identical to the baseline result, and yields a solution acceleration factor approximately equal to the ratio of points. Conversely, a 90% gating, beyond the few highly damage elements, shows a consistent drift in damage calculation with approximately an order of magnitude error, which is clearly unacceptable.

In essence, when anything other than small gating is applied to signal simplification, the total computed fatigue damage will be affected by an error, Error-Type I, which is normally assumed to be marginal, but that cannot be simply ignored outright.

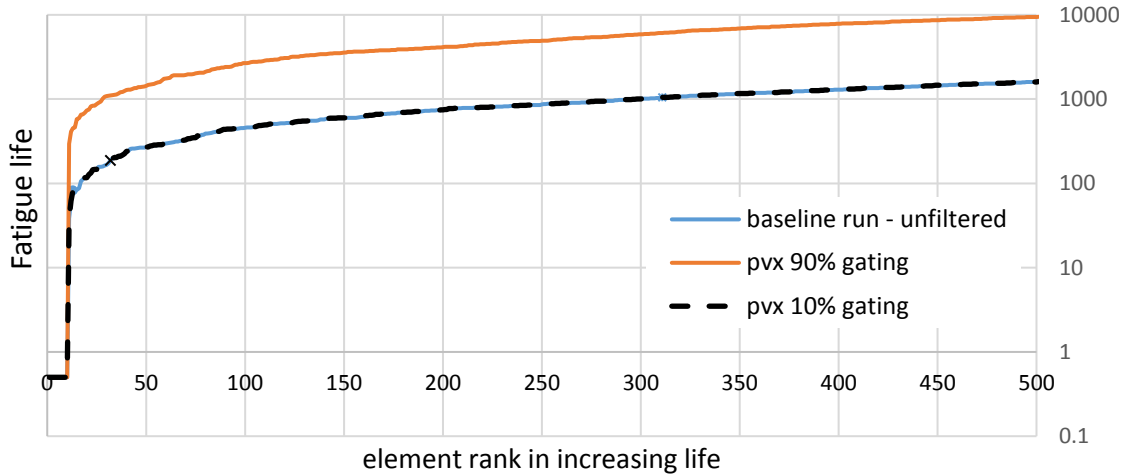


Figure 3-4. Fatigue life for the 500 most damaged elements in All-Terrain Vehicle event-5. The baseline reference result is compared to results at 10% and 90% gating levels [24].

In cases like Figure 3-4 one might wonder what level of gating might be safely applied without affecting the solution. The shape of the diagram suggests that one empirical way to circumvent the problem of the small-load-omitting threshold determination could be based on sampling. The process is as follows:

- Step 1: perform fatigue analysis with highly filtered loads, e.g. 90% gating, to estimate the top critical entities.
- Step 2: perform detailed analysis with full time histories on a few samples from the estimated most critical entities (say 10 to 100 locations).
- Step 3: perform a convergence study with increased levels of gating to determine the acceptable level of gating.

The rationale behind the proposed method is that the error from peak-valley approximation will tend to propagate evenly across the model, hence extracting a sample from relevant entities is a good indication of the effect of filtering. Considering that the

error might vary from location to location, it is important to introduce a specific metric to assist the analyst's decision.

3.2.3.2 Damage index metrics for Error-Type I

The area under the curves in Figure 3-5 represents the combined damage accumulation for the top damaged elements. To avoid mixing terms, this sum of cumulative damage will be referred to as the *collective damage index*, CDI . The collective damage index should be associated to either a number of entities, $CDI_{\#}$, or a model fraction, $CDI\%$. For example, the collective damage index of the top $\alpha\%$ most damage entities in the model is defined as:

$$CDI_{\alpha\%} = \sum_{k=1}^n D_k, \quad (3.1)$$

with n the number of elements in the $\alpha\%$ model fraction.

Figure 3-5 gives a graphical interpretation of the $CDI_{0.5\%}$ for the unfiltered baseline run.

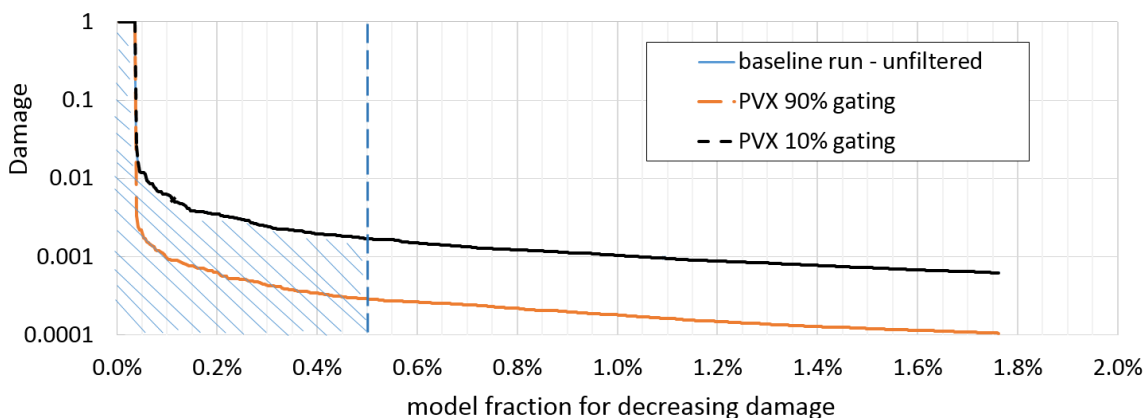


Figure 3-5. Fatigue damage for most damaged elements in All-Terrain Vehicle, event-5. The highlighted area represents the collective damage at 0.5% model fraction.

Results from a few tens or even hundreds of locations are sufficiently economical to obtain even when using full events data. Moreover, a convergence study with regard to the collective damage index, as well as derived quantities such as mean damage, average, standard deviation, can inform the user analyst about the exact level of filtering required for a given accuracy. The collective damage index will lead to a more robust and less

conservative assessment with respect to fixed a priori thresholds or single location calculations.

Comparing the collective damage calculated at different fraction levels can also give an indication of the fraction of the model contributing to the damage as shown in Figure 3-6. This could be used as a design variable in design optimization. In this case is useful to bear in mind that the damage value should be adjusted to the element surface size, in case of large variations in element mesh density.

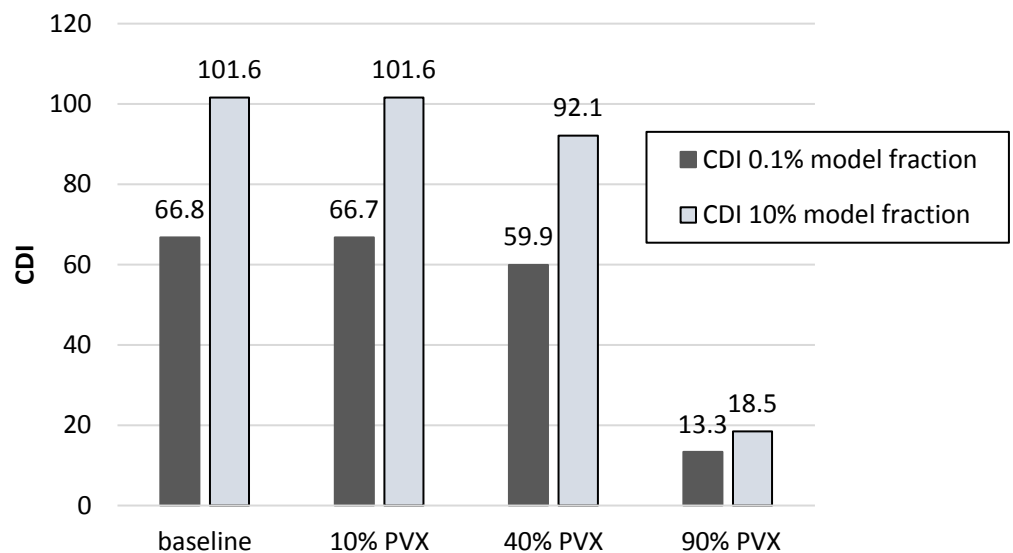


Figure 3-6. Convergence study of collective damage index, CDI, at 0.1% and 10% model fraction and for different levels of peak-valley filtering (PVX).

The operation described above would result in additional costs that can be estimated from the problem size or from similar tests and the benefits can be weighed against the costs. However, having performed a convergence study on one fatigue event does not necessarily guarantee that the same level of gating threshold will be applicable to other events unless some degree of problem similarity can be assumed.

3.2.4 Effects of damage ranking error, Error-Type II and III

As described in 2.2.11.1, a highly gated peak-valley filtering routine is used in two-pass processes to determine the critical locations. The rationale in this case is well explained by Figure 3-4 and Figure 3-5, where a 90% gating appears to have the same trend as the

life and damage in the unfiltered run. This is to say that, although the computed damage is not usable for life estimation, it can be used to rank the model in terms of critical locations.

Although the position above appears to be widely adopted in industrial practice, if not supported by analytical or physical evidence, it could lead to dramatic departures from reality. This is the case when, as a consequence of time history filtering, the severity ranking of the FE entities becomes ostensibly different from the reference baseline order. This ranking error, herein referred to as *Error-Type II*, directly affects the reliability of the whole two-pass accelerated fatigue process as some critical FE entities might be disregarded from the critical group and left behind. Neglecting fatigue-relevant entities is here referred to as *Error-Type III*, which is a direct measure of the reliability of the accelerated fatigue simulation process.

Once again this problem might be best clarified and illustrated using a result from the All-Terrain Vehicle test case. **Error! Reference source not found.** shows the differences between reference baseline ranking position and the predicted rank from peak-valley filtering with 90% gating.

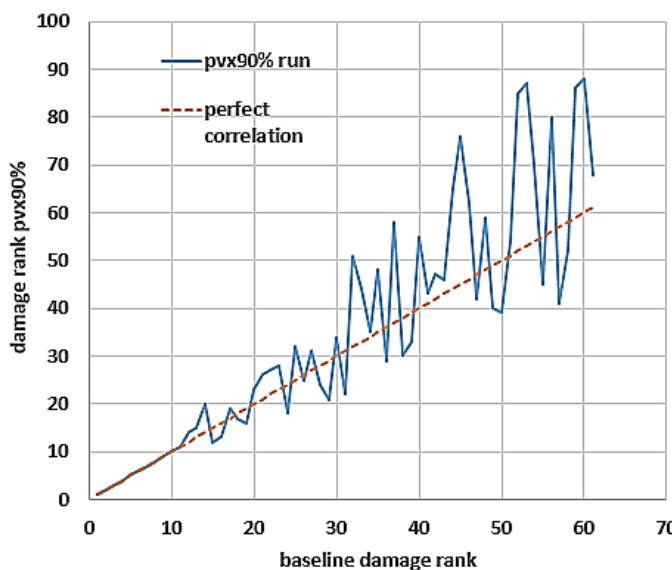


Figure 3-7. Element damage rank in peak-valley filtering with 90% gating (PVX 90%) vs. baseline damage rank [24].

Given that the position shift in damage rank is expected to increase as more entities are considered, the relative error in Figure 3-8 provides a more useful indication and is

expressed in terms of % position shift from target baseline results. A cursory reading of the table indicates that an error of the order of 100% (or a factor of two) can be expected in this case. As an example, in order to identify the top 1% critical entities using peak-valley gated at 90%, the analyst should retain at least 2% of the model.

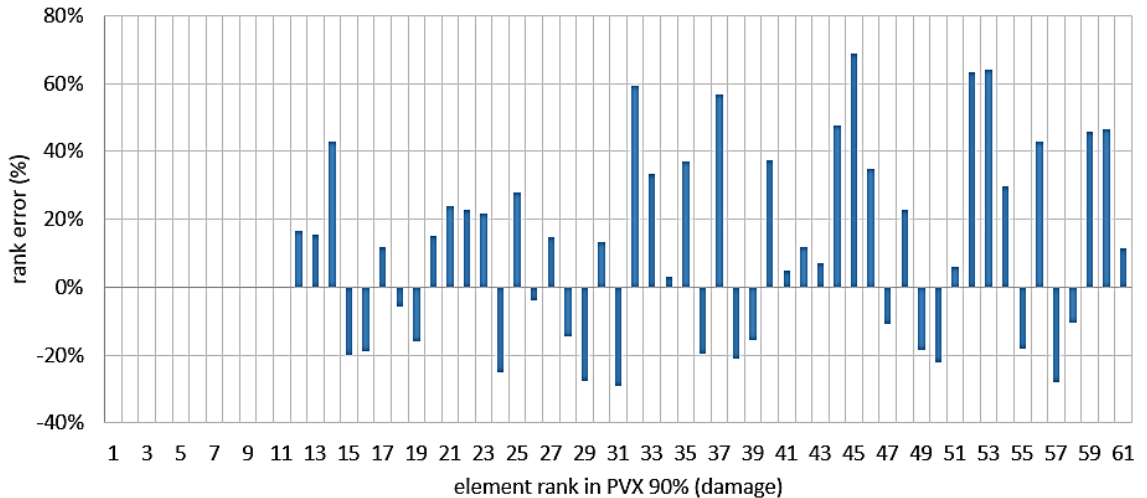


Figure 3-8. Critical element rank error % after peak-valley filtering with 90% gating (PVX 90%) [24].

Evidently, the complete ranking results can only be obtained *a posteriori* so they should either be a reference from previous knowledge or might be obtained through probabilistic sampling.

In summary, a convergence study on the effect of gating should be used to anticipate the effects of the filtering, however this might defeat the purpose of the process, which is to speed-up the analysis. A mitigation strategy for Error-Type III should then be to retain a larger group of entities trying to stay on the conservative side but without full assurance of capturing all critical locations.

3.2.5 False positives, Error-Type IV

A last typology of error, *Error-Type IV*, refers to the *false positives*, the entities that are retained by the filtering despite not being fatigue-critical. Rather than an error per se, Error-Type IV represents a potential source of inefficiency in the accelerated fatigue simulation routine. In multiple pass elimination methods such types of inefficiencies are minimized, however they could be relevant with highly gated filtering (*limits only* being the extreme case) and in combination with a conservative model fraction retention. In

such cases it might be worth assessing the efficiency of the method, alongside other sources of error, as described in the next section.

3.2.6 Metrics for reliability and efficiency, Error-Type III and IV

The most direct metric to assess the reliability of the hotspot estimation, represented by Error-Type III, is to consider the hit rate of the predicted hotspots with respect to the reference baseline hotspots. Likewise, a simple metric to measure the efficiency of the method, Error-Type IV, is to look at the ratio between the wrongly retained entities (false positives) and the total number of non-critical entities. These quantities were already encountered in 2.2.9.1 in the context of diagnosis testing where they are respectively defined as the *TPR* (true positive rate), and the *FPR* (false positive rate). In essence, the more complete approach that is proposed here is to look at the cost versus benefit comparison. This is, in fact, exactly what the contingency table in Figure 2-14 represents.

As will be clarified in chapter 4 and 5, the a priori methods are more likely to introduce non relevant entities as they only have indirect ways to control the number of retained entities. In this case the contingency table will be an extremely valuable tool in supporting the investigation of accelerated fatigue simulation practises and in establishing trade-off settings.

3.3 A priori filtering alternative to online accelerated fatigue simulation

This chapter is mostly dedicated to the assessment of online methods, as they represent the prevailing industrial practice in accelerated fatigue simulation. So far, references to a priori methods have been mostly indirect but they will be investigated in chapter 4 and 5. In anticipation of the arguments and topics that will be presented, some introductory comments are given here.

The list of hypotheses at the beginning of the chapter helped encapsulating the intended scope and applicability of the methods, some of which can only be truly assessed with hindsight. For example, the assumption that only a small percentage of the model was deemed of fatigue interest was well matched by the results in Figure 3-5, with 1% of the model spanning over 3 orders of magnitude of damage.

As much as all conditions and assumptions can be validated, the application and value of online methods is inextricably tied to availability and representativeness of the prescribed loads, as all the metrics are tied to a reference result, which is assumed correct and representative. Evidently in many cases this is far from a realistic assumption.

By contrast, the principle of a priori filtering is one in which expected areas of stress concentrations (or strain, or strain energy) are retained independently of loads' time history availability and therefore *offline* with respect to the dynamic calculation.

The a priori methods are essentially a one-off filtering and sorting capability that is applied before running the transient events (referring to diagram in Figure 2-17). The filtering can be based on peak stress thresholds obtained from statically applied loads and/or modal stresses obtained from modal analysis (performed offline). The aim is to eliminate low stress entities and prioritize the remaining critical entities (nodes or elements).

Such simple technique promises relevant benefits where multiple events and large models are concerned, however there is no detailed study with regard to the applicability and reliability in fatigue analysis and its application mostly relies on user experience and judgement. Consequently, the next chapter is dedicated to an investigation of the fundamental limits and assumptions in a priori filtering.

As a final remark, it is useful to mention explicitly that any reordering algorithm based on peak stress threshold might easily be invalidated by bad modelling practices and/or areas of high concentration of stress that might shield other meaningful parts of the model. Any automated procedure apt to identify critical areas would have to take into account such types of FE modelling occurrences. The 2008 US Patent filed by Breitfeldet al. at Daimler AG [114] describes the list of common FE modelling practices affecting the accuracy of the stress determination (e.g. overly stiff triangular elements, elements positioned near corner or edges or proximity to rigid elements). The authors detail a rule based methodology of general applicability (also referred to as *expert systems* approach) to automatically distinguish between representative stresses and stress concentrations merely resulting from FE modelling approximations. On this subject it is also significant to quote from the patent of Huang's et al. [107]:

“When using the methods known from the related art, it is left to the experience of an observer to evaluate the results of a finite element simulation, in particular the stresses in the finite elements. The related art provides no method that makes it possible to distinguish actual excess stresses from excess stresses resulting merely from the approximation of the model by finite elements.”

3.4 Summary

This chapter describes the underling hypotheses, limitations and potential errors in the application of accelerated fatigue simulation via peak-valley extraction and filtering (PVX).

Some key findings and original contributions are summarized below.

- A novel classification of the error types is based on the identified four separate sources of approximations: damage value, damage rank, hit rate, false positives.
- A proposed evidence-based approach for the assessment of acceptable levels of small load omission threshold, using a convergence study with increased levels of gating to control damage error (Error-Type I).
- A novel *collective damage index*, CDI, represents the combined damage accumulation for the top damaged elements. The collective damage index, as well as its derived quantities such as mean damage, average and standard deviation, can inform the user analyst about the exact level of filtering required for a given accuracy. The collective damage index leads to a more robust and less conservative assessment with respect to fixed a priori thresholds or single location calculations.
- The effect of peak-valley gating to the ranking error, Error-Type II, in turn affecting the reliability of the whole two-pass accelerated fatigue process when critical FE entities are disregarded from the analysis group (Error-Type III).

In essence, a complete set of specific metrics is proposed, aimed at targeting all potential errors and the sources of inefficiencies, thus establishing wider reaching terms of comparison than a simple simulation acceleration factor based on the elapsed solution time.

The last section of the chapter introduces the basic philosophy of the a priori approach as an alternative or complement to online methods. Table 1 provides a look-up summary and a qualitative comparison of accelerated fatigue simulation methods discussed.

Table 1. Qualitative comparison of selected methods in accelerated fatigue simulation

Acceleration method	Domain	AF (accel. factor)	Error type				Sensitivity	
			I (damage value)	II (damage rank)	III (1-true positive rate)	IV (false positives rate)	b (S-N curve slope)	Load type
PVX low gating	time	low	low	low	na	na	low	low
PVX high gating	time	high	high	medium	na	na	high	high
Extremes only	space	high	high	high	medium	medium	high	high
Two-pass method	space	high	low	low	low	low	high	high
A priori	space	high	low	na	medium	high	na	na

Chapter 4: A priori hotspot filtering for simply supported beams and plates in bending

In this chapter simply supported beams and plates in bending provide a basic test environment to investigate the predictability of fatigue critical areas. The use of an efficient and repeatable parametric analysis provides a test of the hypotheses and limitations whilst uncovering prevalent trends and sensitivities. A method based on diagnosis testing is proposed as a means of assessing the predictive capability of static and modal shapes.

4.1 Aims and scope of the analytical investigation

The aim of the investigation is to establish the conditions, favourable or unfavourable, in which the probable location of the highest damage can be anticipated before resolving the dynamic and fatigue problem. For these purposes, the classical beam and plate theory [115], [116] offers the simplest analytical solution, where the onset, evolution and sensitivities of fatigue hotspots can be investigated with repeatable parametric models.

Classical bending theory is applied to thin, uniform, simply supported straight beams and flat rectangular plates. The models don't aim to represent the full complexity of a typical fabricated assembly, however, they provide simplified conditions to test the assumptions applicable to time domain durability of mechanical systems, listed in paragraphs 3.1 and centred on linear superposition.

A further simplification is adopted with respect to the loadings, assumed to be discrete and concentrated (e.g. representing wheel spindles, joints, transmissions, actuators etc.). The analytical models presented here assume harmonic and concentrated loads, due to the computational advantage of the frequency domain, and considering that this simplification does not affect the general applicability to complex types of loading.

The parametric frequency domain solution, based on modal superposition, was coded in MATLAB® and compared with equivalent FE solutions. All FE analyses were performed using MSC Nastran® and Patran®. Appendix C provides further details on adopted software solutions and versions.

4.2 Hotspot patterns in beams in bending under harmonic loading

The beam is solved in the frequency domain for harmonic concentrated loads at any location. The subsequent distributions of stress and strain energy density are used to locate the true hotspots as a function of the frequency and the loading position.

The baseline simply supported beam model is outlined in Figure 4-1, with the parameters described in Table 2.

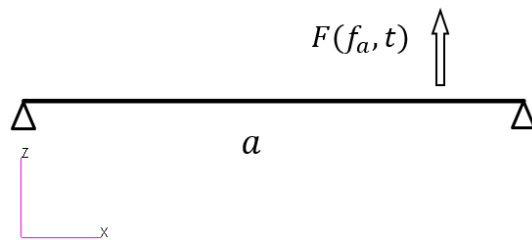


Figure 4-1. Simply supported beam in bending with harmonic force F at $x=f_a$.

Table 2. Parameters description for uniform beam in bending

Quantity	Description
a	length in x
b	section dimension in y
h	section dimension in z
I	moment of cross sectional area
ρ	mass per unit volume
E	Young's modulus
f_a	location of center of Force F
F	transverse force
η	proportional structural damping
$w(x)$	displacement in z direction

Appendix A.1 derives the closed form expressions used in the MATLAB® coding for displacement, strains, stresses and strain energy density. Some key definitions and equations are reported here for added clarity.

The mass normalized natural modes are given by:

$$W_m(x) = \sqrt{\frac{2}{\rho a b h}} \sin \frac{m \pi x}{a} \quad m = 1, 2, \dots \quad (4.1)$$

with m the mode order.

The modal expansion leads to the transverse displacement response:

$$w(x, t) = \sum_{m=1}^{\infty} W_m(x) q_m(t) \quad m = 1, 2, \dots, \quad (4.2)$$

where q_m are the steady state modal coordinates.

The resulting dynamic strains for a concentrated harmonic load positioned at f_a along the beam is:

$$\varepsilon_x = \sum_{m=1}^{\infty} \frac{2z}{\rho abh} \left(\frac{m\pi}{a} \right)^2 \sin \frac{m\pi x}{a} \sin \frac{m\pi f_a}{a} F e^{i\omega t} \frac{1}{\omega_m^2(1+i\eta) - \omega^2}, \quad (4.3)$$

where $\omega_m = m^2 \omega_1$ is the undamped natural frequency.

The stress and strain energy density $e(x, t)$ can be derived from (4.3) according to:

$$\sigma_x = E \varepsilon_x; \quad (4.4)$$

$$e(x, t) = \frac{1}{2} E \varepsilon_x^2 \quad (4.5)$$

A numerical evaluation of (4.3) demands that a modal truncation operates with an acceptable level of accuracy and convergence. Appendix A.4 addresses the solution sensitivity to factors affecting convergence and performance.

The stress distributions resulting from a force statically applied at any position f_a are determined from the truncated modal summation, and imposing a zero excitation frequency:

$$\sigma_x = \sum_{m=1}^{m=m_t} \frac{2zE}{\rho abh} \left(\frac{m\pi}{a} \right)^2 \sin \frac{m\pi x}{a} \sin \frac{m\pi f_a}{a} \frac{F}{\omega_m^2}. \quad (4.6)$$

In (4.6) and elsewhere the modal truncation number m_t is conservatively set to include the static contribution up to the first 400 modes (as described in A.4)

For selected dimensional examples the parameters of the chosen *baseline* model match the description in Table 3.

Table 3. Uniform beam parameters for baseline model

Quantity	Dimensions	Description
a	250 mm	length in x
b	0.5 mm	section dimension in y
h	0.5 mm	section dimension in z
ρ	7800 Kg/m ³	mass per unit volume
E	210 GPa	Young's modulus
f_a	25.0 mm	load application point

4.2.1 Static and dynamic response to a concentrated harmonic force

For a single harmonic loading, the maximum stress at each solution frequency, or equivalently the maximum strain energy density, directly corresponds to the most critical fatigue locations (hotspots). A complete description of the variation of hotspots location according to an arbitrarily placed harmonic load sweeping from zero to a defined maximum frequency is obtained. Figure 4-2 presents the normalized strain energy density of the baseline beam under a 0.01 N force located at 1/10 of the length ($f_a=25.0$ mm, structural damping $\eta=0.1$) for successive frequency responses between 0-100 Hz. The graph traces the location of strain energy density peaks as the harmonic loading increases in frequency starting from the static solution at $\omega=0$. Beyond the static solution shape, clear relative peaks correspond to the first resonance ω_1 at 18.9 Hz and the second resonance $4\omega_1$ at 75.3 Hz.

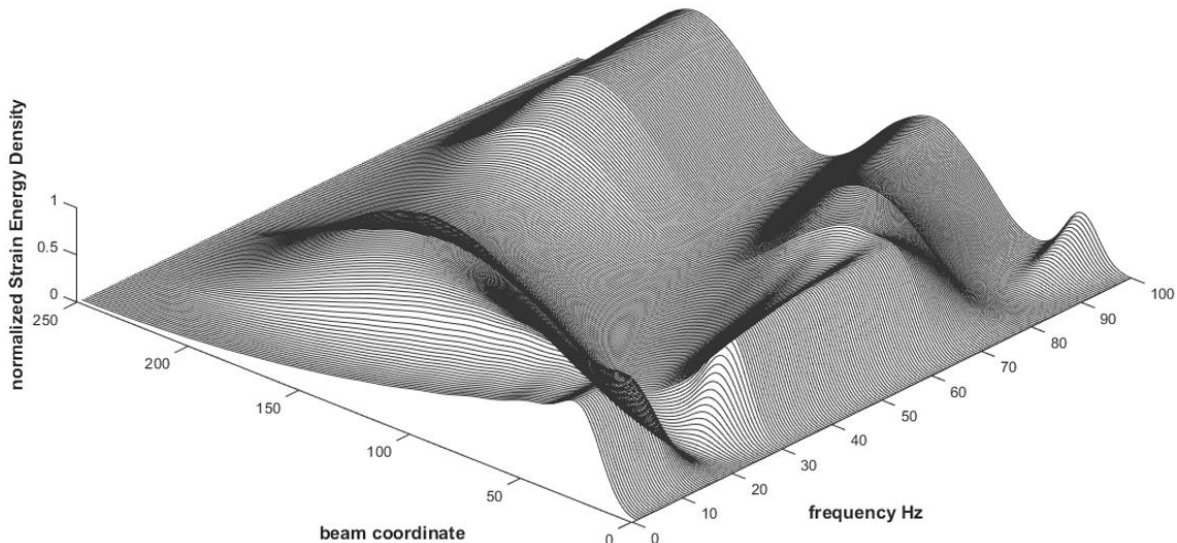


Figure 4-2. Normalized frequency response of strain energy density, force located at 1/10 of the length ($f_a=25.0$ mm, structural damping $\eta=0.1$).

In Figure 4-3 and Figure 4-4 the position of maximum stress amplitude is marked at each solution frequency, up to 200 Hz to include the third mode at 169.4 Hz. The resulting

hotspot pattern shows that, away from natural frequencies, the maxima tend to fall back to the static position at $1/10$ of the beam length. The locations of the peaks are approximately delimited by the tramlines at $x=0.08a$ and $x=0.22a$.

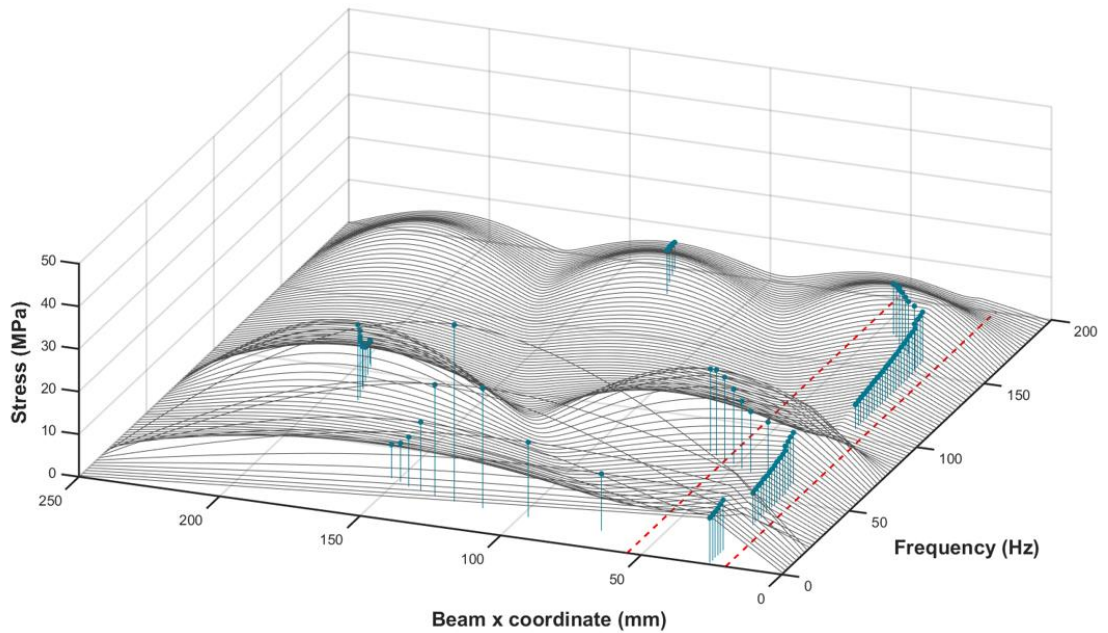


Figure 4-3. Beam stress frequency response for harmonic force of 0.01 N amplitude positioned at $1/10$ of beam length, structural damping $\eta=0.18$; the markers indicate the location of maximum stress amplitude [24].

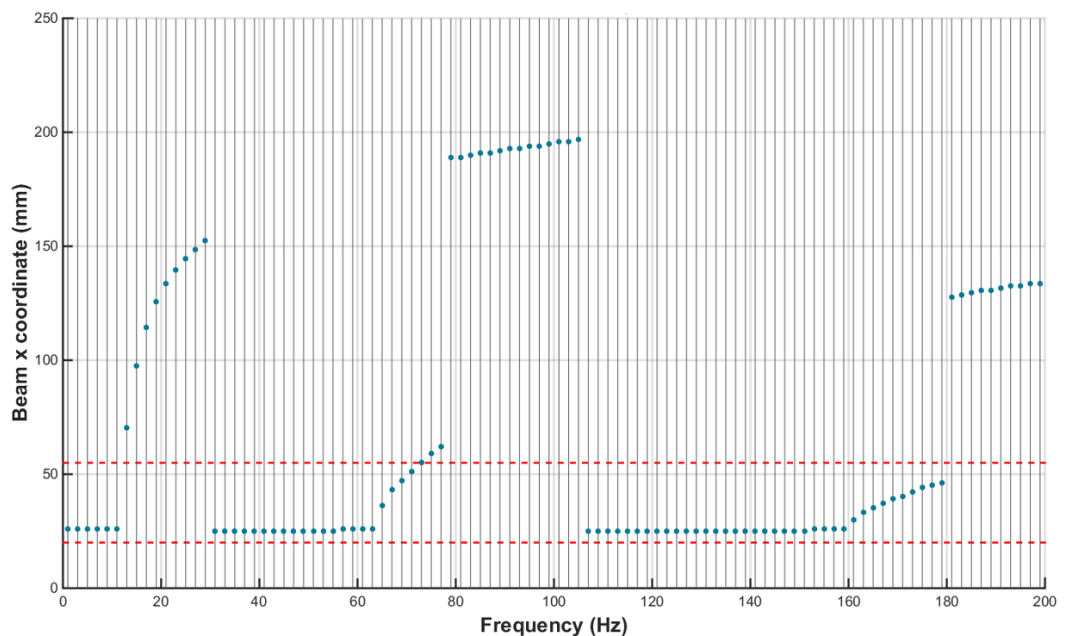


Figure 4-4. Top view of diagram in Figure 4-3, the circled markers identify the locations of maximum stress [24].

In Figure 4-5, due to symmetry, the reflected pattern of Figure 4-4 corresponds to a force symmetrically positioned at the other end the beam. In a more practical outworking of this simplified approach, this could be a schematic representation of a car rear or front axle, loaded independently to the left or to the right wheel hub.

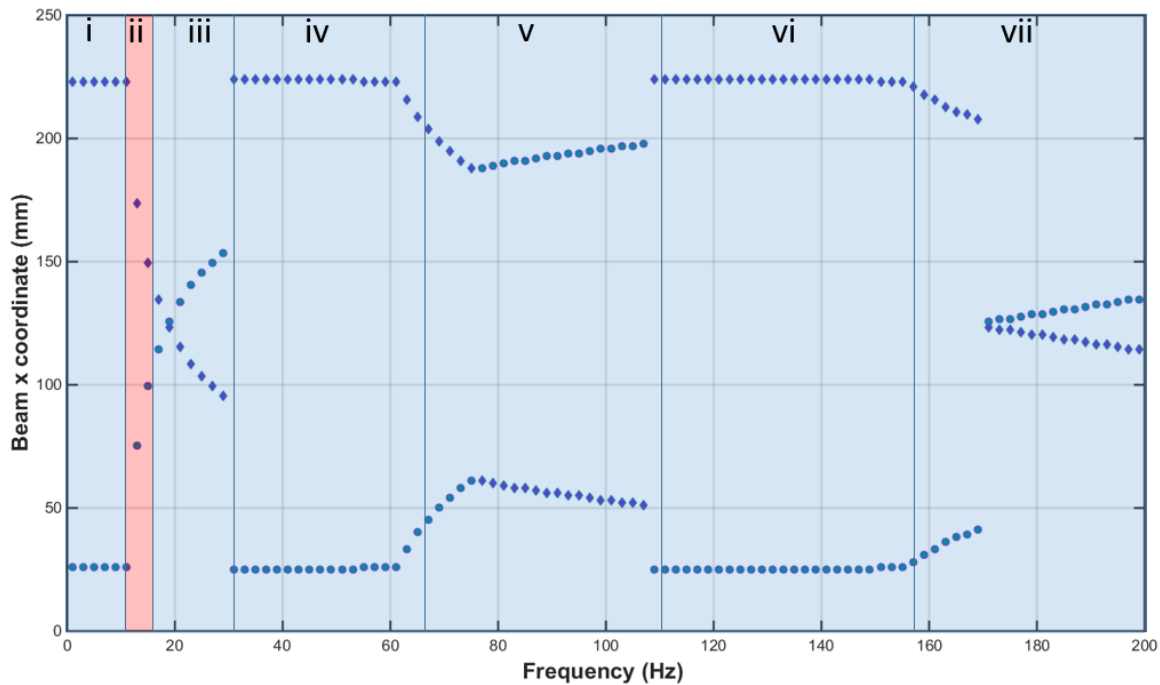


Figure 4-5. Combined maximum stress pattern for forces symmetrically positioned at 1/10 (circle markers) and 9/10 of beam length (diamond markers).

The results are susceptible to a qualitative interpretation based on the following frequency ranges:

- i. [0-10 Hz] The shape of the static response extends from zero to approximately half of the first natural frequency.
- ii. [10-15 Hz] Approaching the first natural frequency (18.9 Hz) the location of the peaks shift rapidly towards the first mode.
- iii. [15-30 Hz] Range of influence of the peak in the first mode; past the natural frequency the peaks move towards a peak location corresponding to the second mode shape.
- iv. [30-70 Hz] Peaks correspond to static response.
- v. [70-110 Hz] Second mode range of influence (75.3 Hz).
- vi. [110-155 Hz] Peaks correspond to a static response
- vii. [155-200 Hz] Third mode range of influence (169.4 Hz).

The above indicates that given the location of the single harmonic force, the peak stresses are highly predictable. Only for the small *transition range (ii)* between the static and first mode is the location of the hotspot less predictable, without knowing the excitation frequency beforehand.

The next sections are aimed at extending the initial results to a wider scope of conditions.

4.2.1.1 Influence of damping level on peak response distribution

The level of damping directly affects the width of the response half power band given approximately by $\eta\omega_m$ [49]. The effect of damping is demonstrated in Figure 4-6 for structural damping values between 0.0 and 0.40. Higher damping reduces the dynamic amplification and increases the half power band, so the peak response dwells longer in the static position and the transitions ranges are reduced. Conversely, a lower damping level appears to extend the transition ranges of the peak locations' uncertainty. The latter effect however would likely be less relevant compared to the dynamic amplification at or near the resonance frequency, given the power law relating fatigue damage and stress (2.2.7.1).

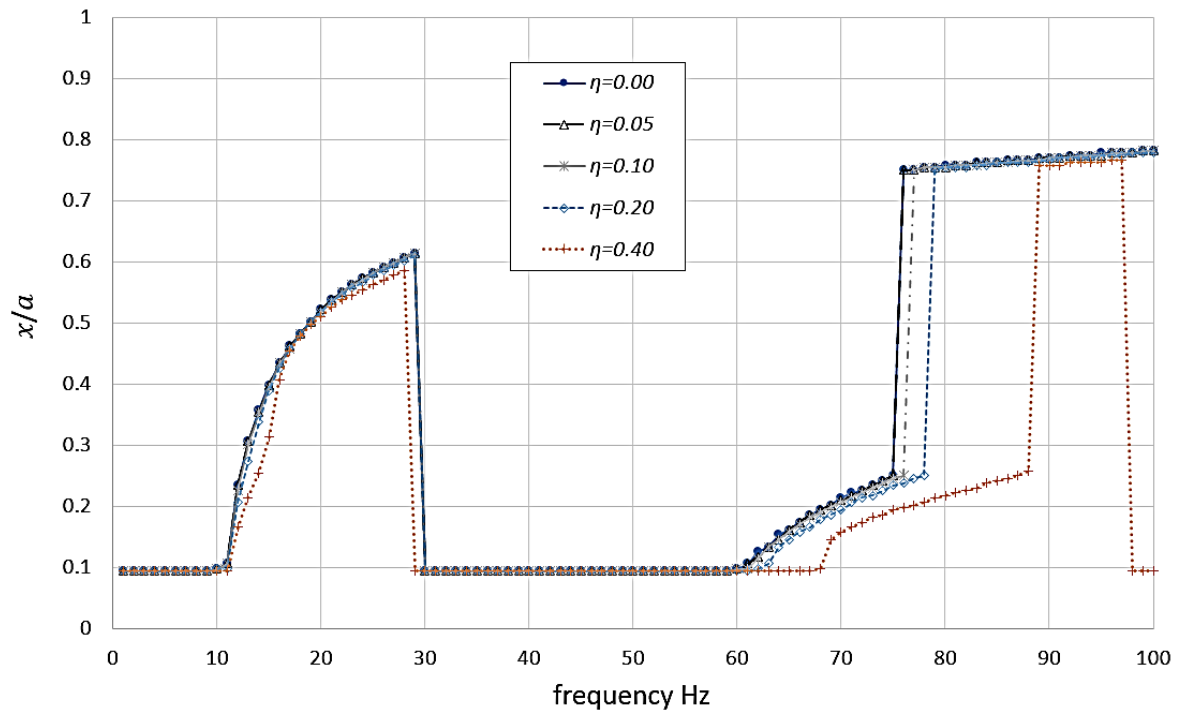


Figure 4-6. Location of peak response in the frequency range [0 – 100], the force is located at 1/10 of beam, with varying structural damping coefficient.

4.2.1.2 Effect of the position of the concentrated force

The location of the force does not change the general interpretation. Figure 4-7 shows the repeated results of 20 equally spaced forces, each individually applied. The transition ranges remain visible, with the forces applied on the peripheral sides of the beam (shaded areas) showing a larger shift per frequency increment.

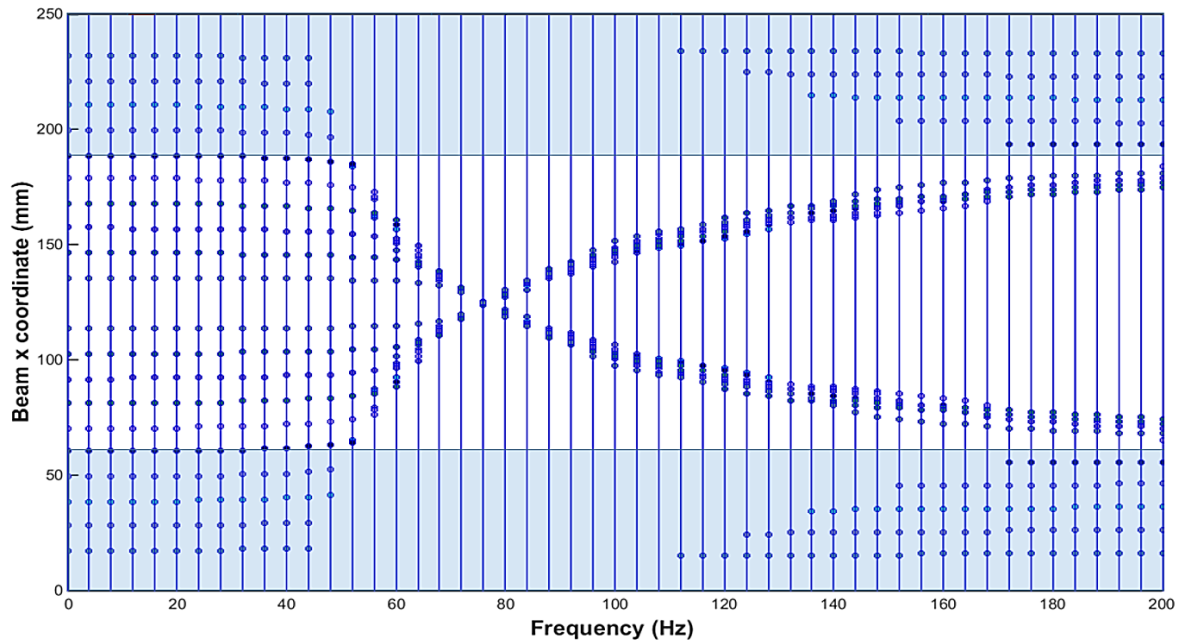


Figure 4-7. Maximum stress patterns for 20 individual forces applied at regular intervals along the beam axis. The shaded areas show a larger shift per frequency increment.

4.2.2 Static and dynamic response under simple combined excitations

Arbitrary combination of modal forces can result in virtually any shape that is compatible with the boundary conditions, according to Eq.4.3 or Eq. 4.6. However, many practical applications would typically be described by discrete distributions of localized forces that are likely to excite only the first few modes, either statically (e.g. with inertial loads) or dynamically. Selected combinations are briefly addressed below.

4.2.2.1 Pseudostatic response under combined concentrated forces

To simplify the problem, the focus is limited to the static response produced by two separate loading conditions. In a simply supported beam in bending, the peak bending stress corresponds to one of the two applied forces. The images in Figure 4-8 describe the

stress distribution resulting from two forces of equal intensity, 0.01 N, and sign (in-phase). A centrally located force, Force(I), is combined with Force(II) which, in turn, is shown to be located separately at 3 equally spaced positions along the beam half-length.

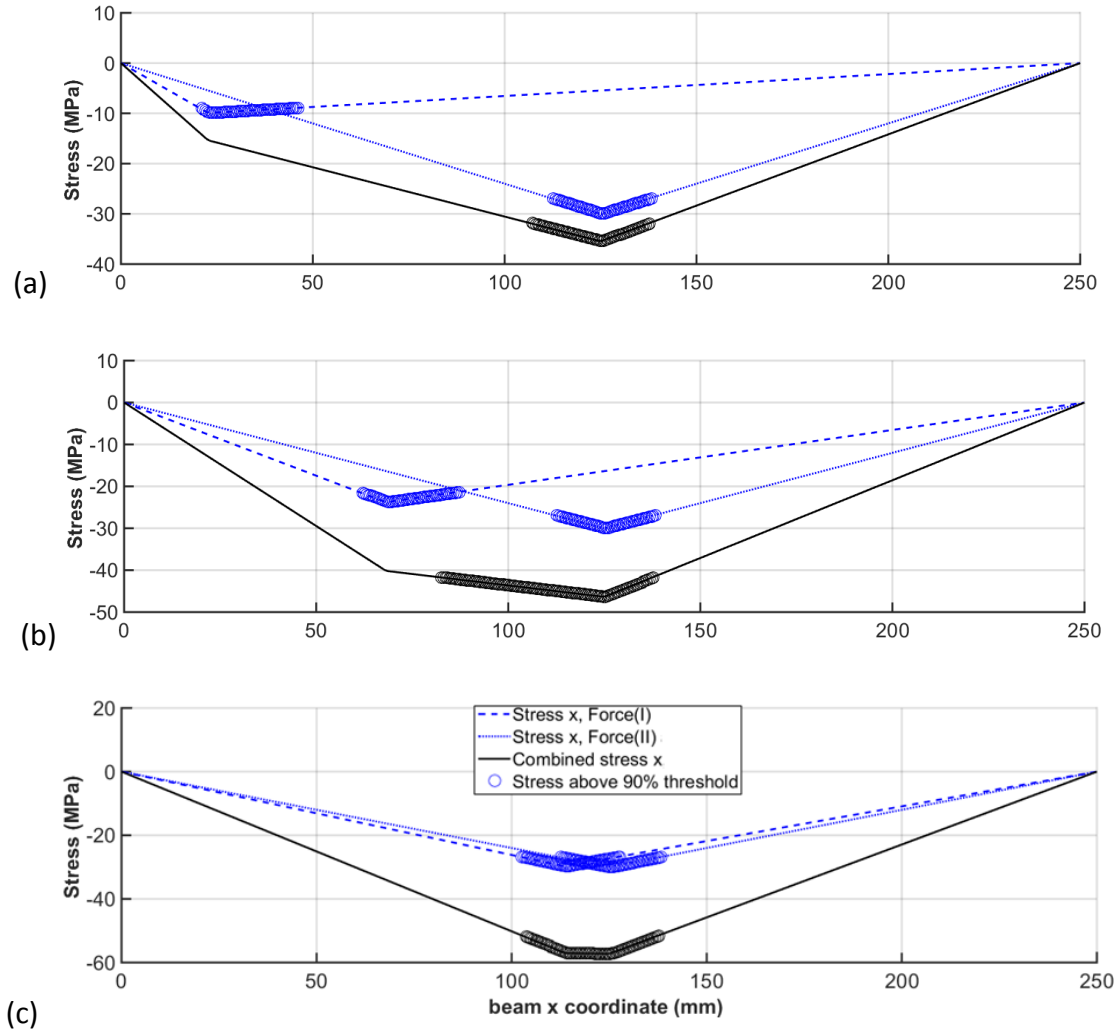


Figure 4-8. Bending stress from the combination of equal intensity 0.01 N forces, in phase. Force(I) is located respectively at 1/11 (a), 3/11 (b) and 5/11 (c) of the beam length, while Force(II) is kept at beam half-length.

Figure 4-9 repeats the case in Figure 4-8 but with forces in phase opposition. Excluding the near zero stress limit case of equal and opposing forces, in terms of response shape the sum of forces in phase opposition leads to less smeared peaks compared to the result shown for the in-phase case. Evidently, in terms of stress the in phase condition leads to more severe stresses.

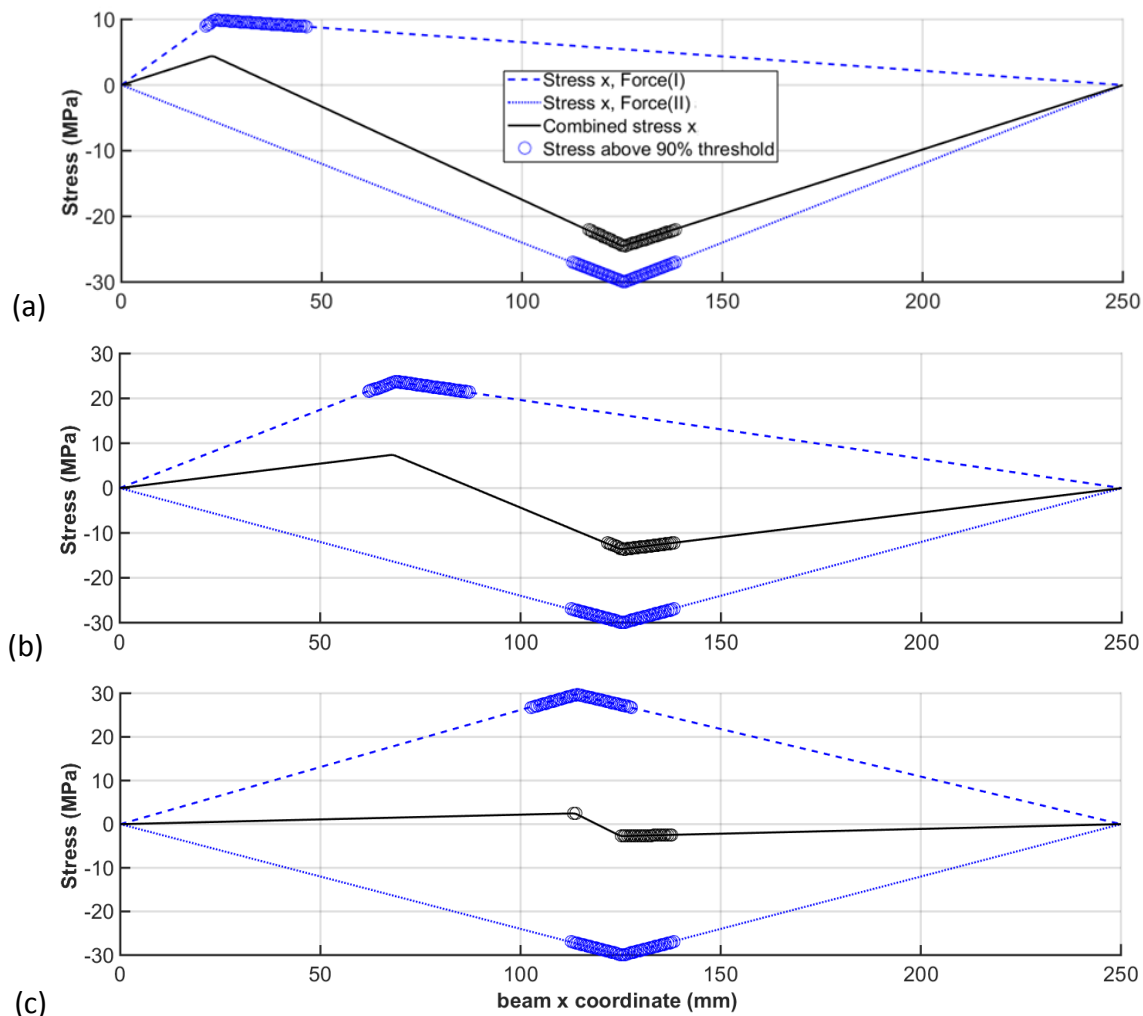


Figure 4-9. Bending stress from the combination of 0.01 N forces in opposite phase. Force(I) is located respectively at 1/11 (a), 3/11 (b) and 5/11 (c) of the beam length, while Force(II) is kept at beam half length.

In the general case of variable amplitude loads, Figure 4-8 and Figure 4-9 represent the two limit conditions between all possible phase combinations. In conditions where phase is equally probable the case of forces in-phase would lead to a maximum combined stress and a corresponding higher fatigue damage contribution.

4.2.2.2 Effect of multiple excitation frequencies

A combination of multiple harmonic components could result in shifting the peak stress locations between the individual component response peaks. As a schematic example, Figure 4-10 represents the response resulting from a particular combination of mode 1 and mode 2. The resulting peak stress (a) and peak strain energy density (b), are shifted from the individual peaks in the modes.

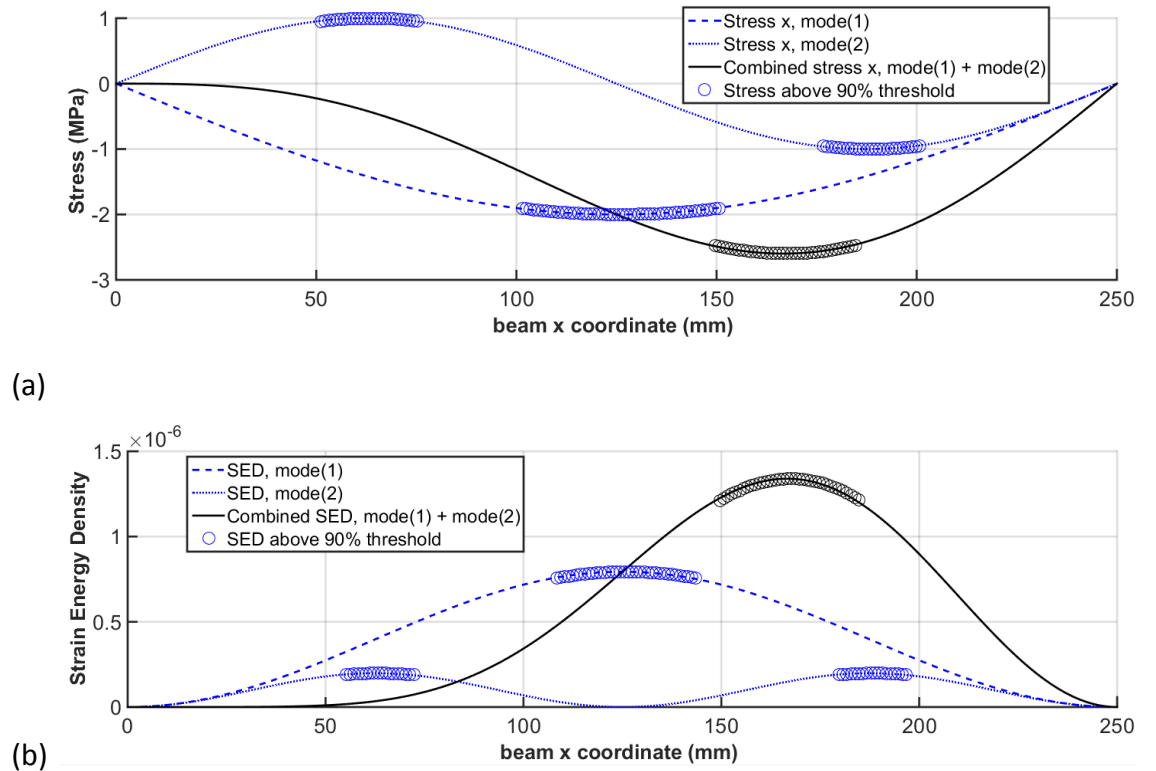


Figure 4-10. Response from a combination of mode 1 and mode 2 in terms of stress (a) and strain energy density (b). The combined peak stress (a) and peak strain energy density (b), are shifted from the individual peaks in the modes.

4.2.3 Stress concentrations from geometrical features

The effect on fatigue life of stress concentrations and notches has been described in section 2.2.8. Although the uniform beam in bending does not represent local geometrical details, an arbitrarily located fatigue notch factor K_f (representative of a small hole for example) could shift the location of the peak stress, irrespective of the loading point or excitation mode. An a priori hotspot prediction approach should anticipate such occurrences around selected geometric features.

4.3 Harmonic response of simply supported plates in bending

Classical plate theory essentially adds a dimension to the beam in bending. Although the plate will respond in a similar manner as the beam, the surface reflects the intended target geometry in hotspot prediction applications, leading the extension to FE models of general scope.

Once again the simplification of concentrated harmonic forces is made and the solution is presented in the frequency domain. The applicable equations are developed in A.2; some key equations and definitions are included here for clarity.

The uniform rectangular plate is shown in Figure 4-11, with parameters given in Table 4.

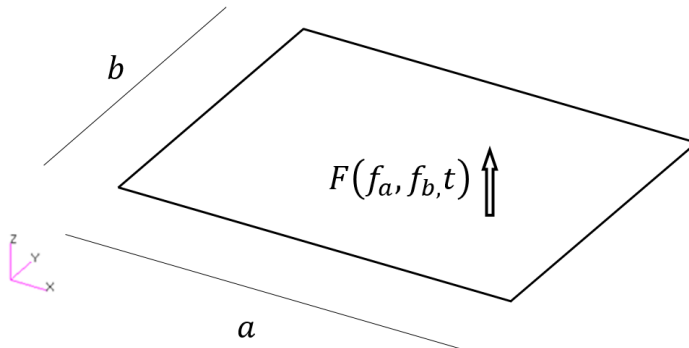


Figure 4-11. Simply supported rectangular plate with point force F at $x=f_a$ and $y=f_b$.

Table 4. Parameters for uniform plate in bending

quantity	description
a	length x
b	length y
h	plate thickness
ρ	mass per unit volume
D	$\frac{Eh^3}{12(1-\nu^2)}$ flexural rigidity
F	transverse load
f_a	load location coordinate on x axis
f_b	load location coordinate on y axis
η	proportional structural damping
$w(x, y)$	displacement in z direction

The mass normalized natural modes satisfying the boundary conditions are:

$$W_{mn}(x, y) = \frac{2}{\sqrt{\rho abh}} \sin \frac{m\pi x}{a} \sin \frac{n\pi y}{b} \quad m, n = 1, 2, \dots, \quad (4.7)$$

with corresponding natural frequencies:

$$\omega_{mn} = \pi^2 \sqrt{\frac{D}{\rho h}} \left[\left(\frac{m}{a} \right)^2 + \left(\frac{n}{b} \right)^2 \right] \quad m, n = 1, 2, \dots \quad (4.8)$$

Considering harmonic loading $F(t) = F e^{i\omega t}$, and η , as the constant structural damping parameter, the steady state modal coordinates q_{mn} are given by :

$$q_{mn}(t) = \frac{2}{\sqrt{\rho a b h}} \sin \frac{m\pi f_a}{a} \sin \frac{n\pi f_b}{b} F e^{i\omega t} \frac{1}{\omega_{mn}^2 (1+i\eta) - \omega^2} \quad (4.9)$$

Summing all modal contributions in the modal expansion results in the transverse response at any (x, y) location:

$$w(x, y, t) = \sum_{m=1}^{\infty} \sum_{n=1}^{\infty} W_{mn}(x, y) q_{mn}(t) , \quad (4.10)$$

Showing the dependency on the application force Eq. (4.10) becomes:

$$w(x, y, f_a, f_b, t) = \frac{4}{\rho a b h} \sum_{m=1}^{\infty} \sum_{n=1}^{\infty} \sin \frac{m\pi x}{a} \sin \frac{n\pi y}{b} \sin \frac{m\pi f_a}{a} \sin \frac{n\pi f_b}{b} F e^{i\omega t} \frac{1}{\omega_{mn}^2 (1+i\eta) - \omega^2} \quad (4.11)$$

The ensuing expressions for the strain, stress and strain energy density derived applying classical thin plate theory in appendix A.2.

4.3.1 Hotspot patterns under harmonic loading

A baseline numerical model with parameters given in Table 5 is subject to several sine-sweep force excitations randomly positioned over the surface, with the aim of investigating patterns and trends for hotspot locations. Similar to the hotspot patterns previously presented for the beam, the location of the maxima in the displacement, stress and strain energy density can be traced at any frequency solution point. For visualization purposes the results can be represented as a 3D orbit of any quantity of interest as the load frequency increases.

Table 5. Parameters for baseline plate model

quantity	dimensions	description
a	250 mm	length in x
b	100 mm	length in y
h	0.2 mm	plate thickness
ρ	7800 Kg/m ³	mass per unit volume
E	210 GPa	Young's modulus
D	153.85 N·mm	flexural rigidity
f_a	200.0 mm	load coordinate on x axis
f_b	90.0 mm	load coordinate on y axis
η	0.1	proportional structural damping

Figure 4-12 shows the orbit generated by tracing the plate location (x, y plane) and maximum displacement value (vertical dimension). The plate is subject to an harmonic load of 0.1 N amplitude applied at coordinates $x=200.0$ mm, $y=90.0$ mm and with frequency increasing from 0 to 100 Hz. Figure 4-13 presents direct and equivalent Von Mises [117] stress components for the same case.

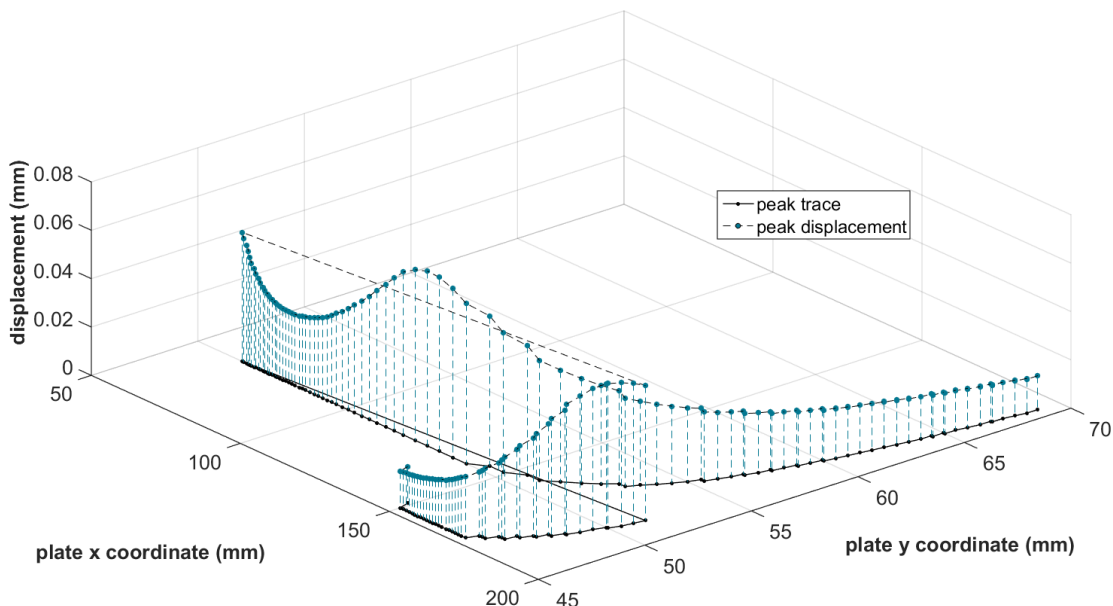


Figure 4-12. Peak displacements and corresponding trace on plate in bending under harmonic load of 0.1 N amplitude, with frequency going from 0 to 100 Hz and located at $x=200.0$ mm and $y=90.0$ mm.

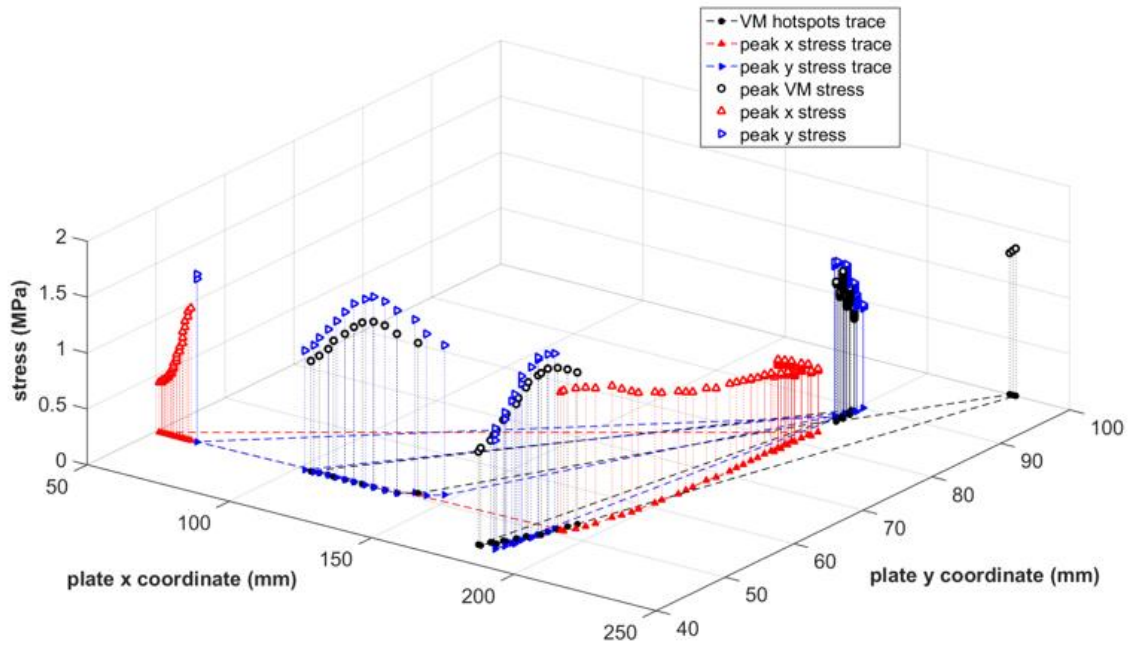


Figure 4-13. Peak direct x , y components stress and Von Mises under harmonic load of 0.1 N amplitude, with frequency range from 0 to 100 Hz, located at $x=200.0$ mm and $y=90.0$ mm.

The orbits plots are susceptible to a similar interpretation given for peak pattern of the beam in bending (4.2.1). For the case in Figure 4-13, with 0.1 N force located at $x=200.0$ mm and $y=90.0$ mm, the stress peaks move from the static location towards a central location $x=125.0$ mm, $y=50.0$ mm dominated by the first mode (resonance at 57.2 Hz) and then onto areas dominated by the second mode (resonance at 80.9 Hz). The resulting peak position is less predictable only for short frequency ranges represented by the straight lines, where rapid positional shifts in peak response are observed.

Evidently, the tracking of multiple stress components and/or multiple locations with such orbit plots is not easily interpretable. As a simplification, the envelope plot of a single combination parameters such as Von Mises stress or strain energy density, as defined in A.2.1, can give a qualitative description of the hotspot patterns. Figure 4-14 and Figure 4-15 present the Von Mises and strain energy density envelope for the whole frequency history from 0 to 100 Hz, subject to an harmonic force of amplitude 0.1 N, applied to the same coordinates $x=200.0$ mm, $y=90.0$ mm. The images provide visual insight into the relative severity for each frequency solution point for a constant amplitude load. Aside from the expected modal peaks and troughs, local effects corresponding to the loading

position dominate the low frequencies range, as expressed by stress concentration patch centred on the load application point in Figure 4-14(b) and Figure 4-15(b)

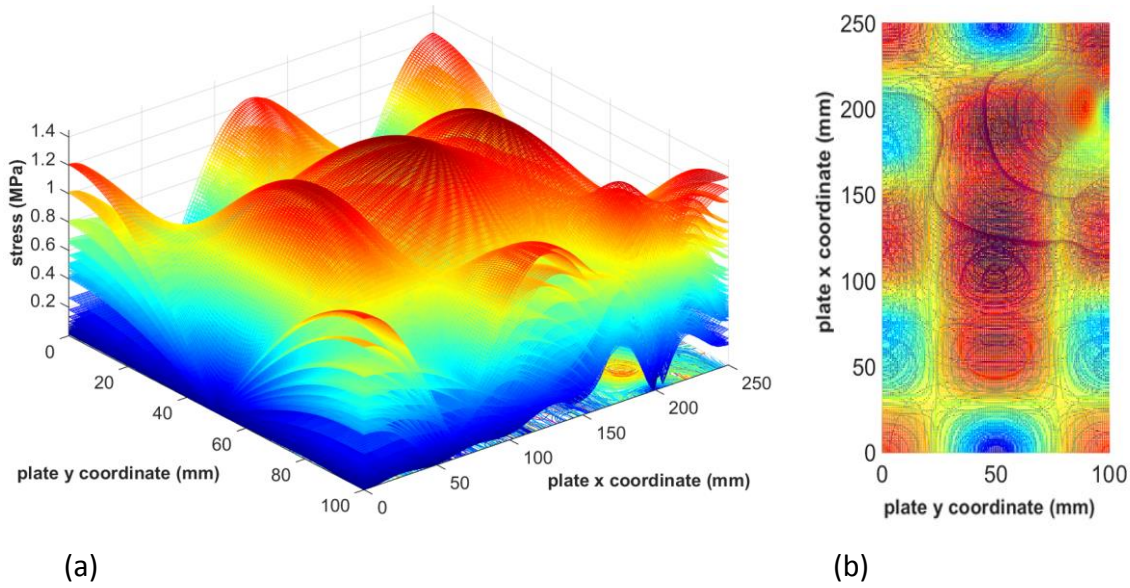


Figure 4-14. (a) Von Mises envelope under single harmonic loading of 0.1 N amplitude, placed in the corner area $x=200.0$ mm, $y=90.0$ mm and with frequency solution range 0-100 Hz. (b) Top view [57].

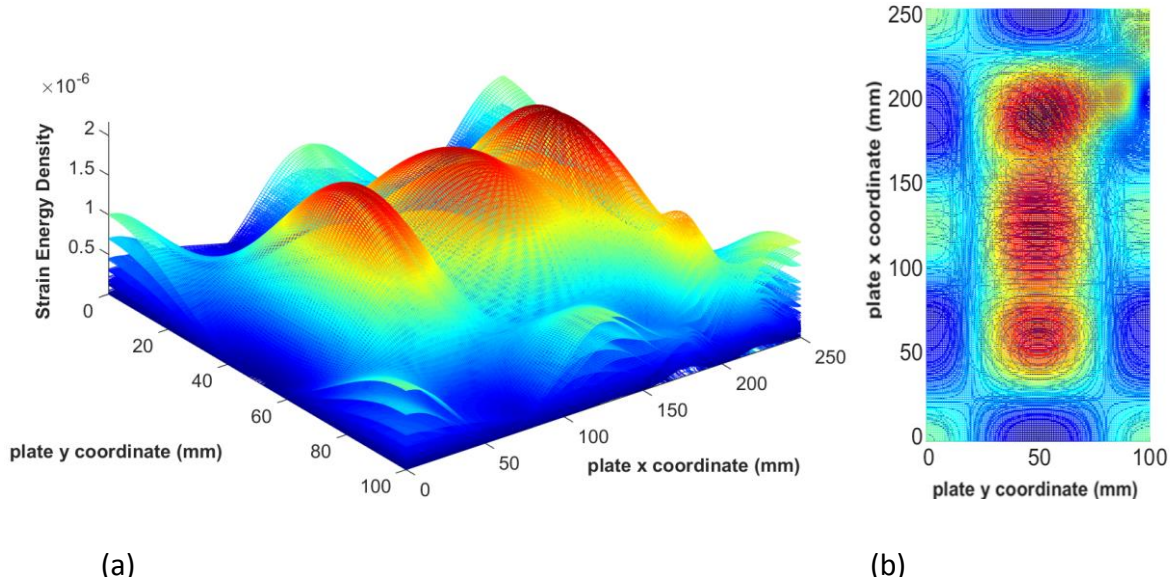


Figure 4-15. (a) Strain energy density envelop for same loading condition as in Figure 4-14; (b) top view [57].

4.4 Predictability of hotspots in beams and plates in bending

The principle of a priori hotspot filtering, is one in which expected areas of stress concentration (or strain, or strain energy) are retained independently of the knowledge of the time variation of the applied loads.

In the simplest case of a single harmonic loading, presented in 4.2.1, given the location of the force, the peak stresses are highly predictable for most frequency ranges. Yet, the response in transition ranges approaching natural frequencies are less predictable.

The Fourier series represented by Equation (4.6), supports the intuitive understanding that it is not possible to anticipate the hotspot location under loading conditions of arbitrary complexity. However, such conditions may not constitute a significantly practical condition, especially under the common, limiting assumptions stated in paragraph 4.1.

With arbitrary loading conditions, and limiting to the cases of interest of high dynamic amplification typical of lightly damped structure, the system response will tend to favour load paths that are predictable, over more extreme combinations. The presence of stress concentrations will provide additional predictability derived from the stress multipliers, and its power-law regulated effects to the fatigue damage.

In summary, an a priori filtering technique carries a risk of neglecting fatigue critical entities, Error-Type III in 3.2.4, deriving from a combination of responses. The approach is therefore to control the margin of error. The next section provides an example application of the a priori technique, demonstrating the proposed metrics to account for reliability and efficiency of the acceleration method.

4.5 Hotspots prediction for a beam in bending with concentrated harmonic force

The simpler case of single concentrated harmonic force load is used to develop the initial concepts and steps for a priori hotspot prediction. The true hotspots distributions obtained applying Bernoulli-Euler theory in 4.2.1 are compared with the predicted hotspots obtained with a simple a priori algorithm implemented in MATLAB®.

4.5.1 A priori hotspots candidates

A general process for the a priori identification of the beam hotspot locations can be described as follows:

1. Obtain m modes of interest based on a specified frequency cut-off that is related to the expected maximum loading frequency.
2. Calculate s static solution modes in response to F_i load patterns for $i=1$ to s
3. For each $m+s$ (modal and static) solution, retain beam sections based on the pre-set threshold value of a derived result (e.g. Von Mises stress or strain energy density).
4. Merge the predicted $m+s$ hotspot regions into the reduced analysis group.

As a first step, Figure 4-16 shows the normalized modal strain energy density distribution for the first 3 modes, assuming frequencies of interest up to 200 Hz. The critical areas to be retained (shown with red line markers) correspond to beam locations with a strain energy density above a pre-set threshold limit, in this case 90%, with respect to the normalized peak energy (indicated by blue markers).

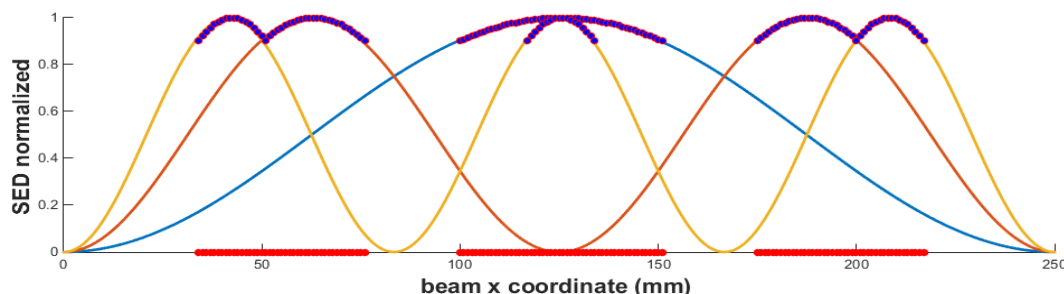


Figure 4-16. Bending beam modal strain energy density (SED) and resulting hotspots (red markers) for first three modes [24].

For the second step, the critical areas resulting from a single force statically applied at a location f_a are determined from the truncated modal summation imposing null excitation frequency. Figure 4-17 represents the static response to a single point force arbitrarily applied at 1/10 of the distance along the beam. The resulting blue filled markers indicate strain energy density levels above the 90% threshold.

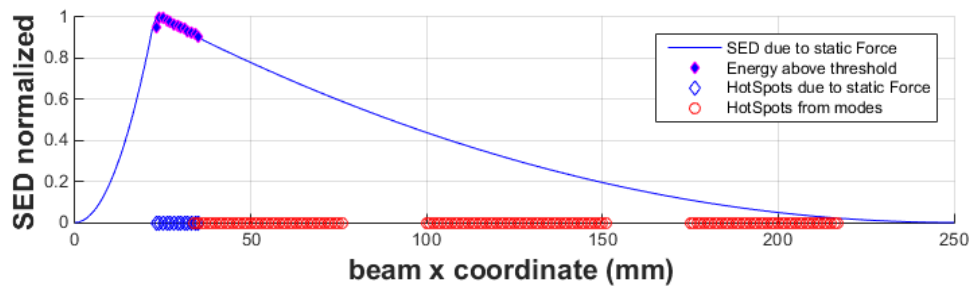


Figure 4-17. Static response in terms of strain energy density, SED, to a single point force applied at 1/10 of the beam dimension [24].

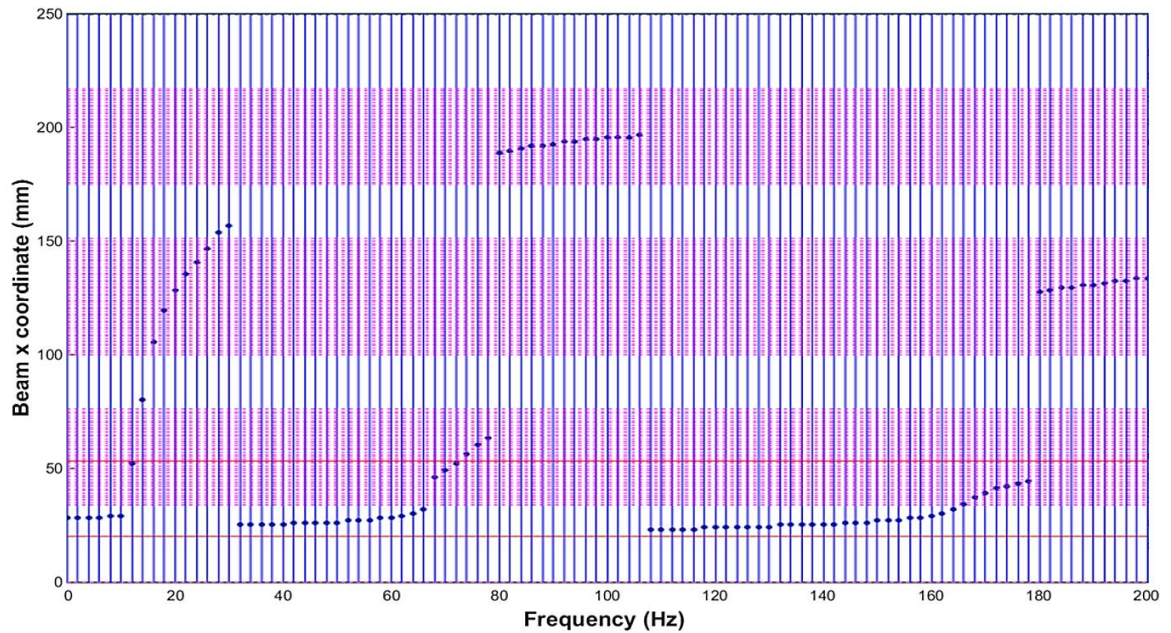


Figure 4-18. Frequency response peaks (dots) against bending beam predicted hotspots, represented by the shaded magenta areas and the static response band delimited by the parallel continuous lines [24].

In Figure 4-18 the calculated hotspots as a function of frequency are superimposed onto the consolidated modal hotspots (shaded magenta areas) and onto the static response band (area delimited by the parallel continuous lines), suggesting that the peak hotspot areas can be predicted accurately for this example. The next section provides a means for a more rigorous and usable quantification of the prediction quality.

4.5.2 Hotspot prediction metrics via diagnostic test

Considering the inherent approximations of the proposed methodology, a quantification of the prediction quality is only attainable in statistical terms. As anticipated in 3.2.6, the

definition of *TPR* (true positive rate), and the *FPR* (false positive rate) in diagnosis testing techniques, as introduced in 2.2.9.1, provide valid means to compare the reliability and the efficiency of a hotspot prediction technique.

For this purpose, a discrete set of 250 solution locations was evenly distributed across the component. The application of diagnosis testing can best be described with a medical analogy shown in Table 6. The discrete solution locations are equivalent to the patients' population, the onset of fatigue damage represents the "disease" and the hotspot prediction algorithm is the diagnostic tool used to detect the onset of the disease.

Table 6. Analogy between fatigue hotspot prediction and disease diagnosis testing

Definition	Medical description	Hotspot prediction algorithm
	Patient	Discrete solution point on beam
	Population	Numerical beam model
Prevalence	Probability of diseases appearing in population	Expected fraction of numerical model presenting relevant fatigue damage
True Positive Rate (<i>TPR</i>) (hit rate)	Probability of positive diagnosis in a patient with a disease	Expected fraction of hotspot predicted solution locations that are truly fatigue critical
False Positive Rate (<i>FPR</i>)	Probability of positive diagnosis in a patient without disease	Expected fraction of hotspot predicted solution locations that are not fatigue critical (false alarm)

The definitions above are tested with the beam example described in the previous section. The beam comprised 250 locations and the statistical measure is obtained as a function of loading frequency. The prevalence for this test is conservatively set to 25 entities (10%) of the model at each solution frequency. At a chosen strain energy density threshold of 90% peak value, the hotspot filtering retains 147 locations (59%) of the model.

		Hotspot Evidence (Frequency response)		
		positive	negative	
Hotspot Predictor (First 3 modes + static vector)	Yes	24 (True Positive)	123 (False Positives)	$TPR=TP/Pos=0.96$
	No	1 (False Negatives)	102 (True Negatives)	$FPR=FP/Neg=0.54$
		$Pos=TP+FN=25$		$Neg=FP+TN=225$

Figure 4-19. Contingency table for hotspot prediction under static loading.

In an initial hotspot performance assessment, the contingency table introduced at 2.2.9.1 can be obtained at each solution frequency. In Figure 4-19 the contingency table is formed for the static solution. In Figure 4-20 the relevant statistical measures are plotted against excitation frequency.

The reliability of the prediction is directly expressed by the success rate (TPR) which is typically high, except for selected frequencies falling in between modes. The amount of false positives (FPR) gives an indication of the efficiency of the calculation. The ratio of TPR and FPR , the *likelihood ratio*, combines both reliability and efficiency in a single parameter and represents the usefulness or *diagnostic capacity* of the prediction method. A likelihood ratio close to unity indicates no prediction capability, implying an equal probability to detect a true hotspot but also to make a false prediction.

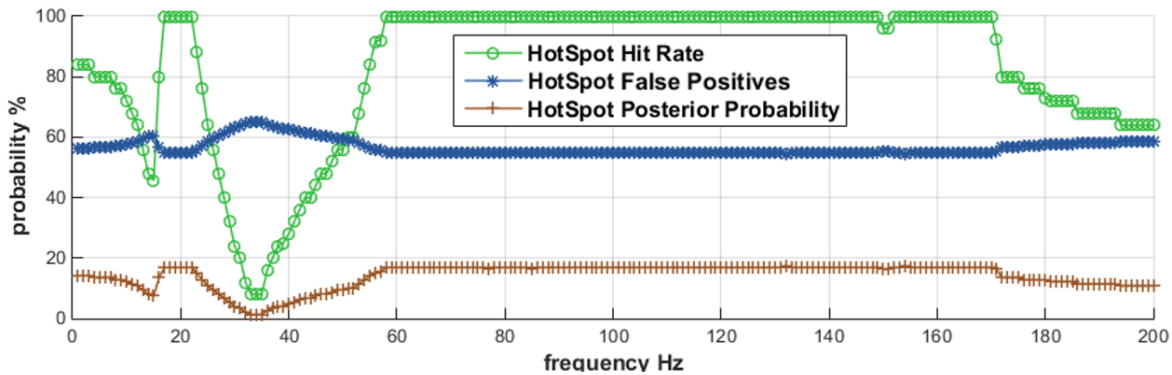


Figure 4-20. Bayesian parameters as a function of frequency for beam in bending in 3.1.2 [57].

A reliable prediction is one in which all critical hotspots have been identified, regardless of the amount of false positives, the latter being relevant to the efficiency and practical value of the method. Clearly, the preference is to obtain a reliable prediction at the lowest solution cost (lowest false positive rate).

In the next chapter an accelerated fatigue simulation process based on a priori hotspot prediction is formalized in the context of a FE driven durability analysis.

4.6 Summary and conclusions

The onset and predictability of fatigue critical areas was investigated for simply supported beams and plates in bending. The classic beam and plate theory does not aim to represent the full complexity of a realistic fabricated assembly, but it provides a simplified environment to investigate conditions that are present in many models of interest, such as lightly damped structures, discrete concentrated loads, pseudostatic or dynamic behaviour typically involving the first low frequency modes.

The principle of a priori hotspot filtering is to retain expected areas of stress concentration (or strain, or strain energy) irrespectively of the knowledge concerning the history of the applied loads. Even for the simple case of a single applied force, the investigation so far has presented combinations of loading frequency and forcing locations which can significantly decrease the predictability of the most critical locations. Likewise, certain combinations of loads and excitation frequency can shift the position away from the maxima in the response due to the individual loads. However, such

hypothetical conditions may not always constitute a significant practical occurrence, especially under the common limiting assumptions.

Given the risk of neglecting fatigue critical entities, a filtering technique based on this a priori method has to control the margin of error. The statistical measures expressed in a contingency table are proposed as a valid means to assess and quantify the reliability and the efficiency of the prediction method.

A reliable prediction is one in which all critical hotspots have been identified, regardless of the amount of false positives, the latter being relevant to the efficiency and practical value of the method.

Chapter 5: Development of a priori hotspot prediction algorithms in FE based fatigue simulation

In this chapter, the investigation and procedures for a priori hotspot detection are developed and applied to time-based fatigue simulation via FE and multibody systems methods. The procedural components and workflow of this predictive technique are described and demonstrated on representative numerical models. The aim is to quantitatively test both the performance and the dedicated metrics developed for accelerated fatigue simulation.

5.1 A priori accelerated fatigue simulation in FE framework

The principle of a priori filtering is one in which expected areas of stress concentrations (or strain or strain energy) are retained independently of the knowledge of the applied loads' time history and therefore offline with respect to the numerically expensive dynamic calculations. Such an approach would be particularly useful where multiple events and large models are concerned, however, the attendant risks and advantages are not easily anticipated and its application mostly relies on user experience and judgement.

Chapter 4 was dedicated to the investigation of the fundamental limits and assumptions in a priori filtering. Although the hotspot locations are not generally fully predictable without a localized stress recovery and fatigue assessment, under common conditions, the locations of many critical areas are expected to reflect both individually statically applied loads and the natural vibration modes. Moreover, the presence of multiple identifiable stress raisers, typical of any realistic fabricated structure, is expected to further contribute towards isolating the areas of interest.

In this chapter the procedures for a priori hotspot detection that have been explored via analytical models are extended to FE structures representative of a wider complexity. Consequently, a new proposed metric for the efficient evaluation and quantification of accelerated fatigue simulation, AFS, as anticipated in 4.5.2, is refined and adapted to the FE framework. The metrics are demonstrated and tested on successive examples.

5.2 Hotspot prediction applied to FE processes

In chapter 2, Figure 2-17 described the schematic workflow of quasi-static or modal transient analyses typical of industrial durability design cycles. The a priori filtering algorithm is an offline and independent step to generate stress influence coefficients. The filtering procedure replicates the same steps presented in 4.5.1 for identification of the hotspot candidate in the analytical case.

The a priori filtering is based on peak stress thresholds obtained from statically applied loads or modal stresses, with the aim to eliminate low stress entities and prioritize the remaining critical FE entities (nodes or elements).

The concept of an augmented modal basis is used here to indicate the combination of static and component modes, with the aim of considering all possible sources of stress concentration via multiple modes of energy transfer. As seen for the analytical case, a sufficiently broad set of modes is one that considers all load application points, constraints and inertial modes that are likely to be excited based on the position and frequency of the excitation. In the limiting case of quasi-static analysis, the method could be based on the influence coefficients obtained under unit loads and inertia relief conditions, as described in 2.1.1. For the general case, section 2.1.2 listed several alternative mode shape representations under the collective definition of component modes; including normal modes, fixed and free boundary modes and attachment modes.

In this study, component-mode synthesis, CMS, with the Craig-Bampton method, CB, is proposed as a primary choice for hotspot prediction due to its widespread acceptance within the FE community and to its capacity to easily combine energy transfer patterns from applied loads (constraint modes) with the internal dynamics (fixed boundary modes) in one simple modal result file description. Although CMS is not exclusively used in conjunction with multibody systems, the integrated FE and multibody simulation approach is an ideal target for the accelerated fatigue process.

5.2.1 Hotspot prediction algorithm workflow

Figure 5-1 describes the conceptual workflow of the proposed hotspot detection algorithm. As a first step the CMS modes, or equivalent assumed modes, are provided by

the chosen FE solver. As described in 2.1.2 and 2.1.3 this is often a standard part of the dynamic solution, irrespectively of the fatigue calculation.

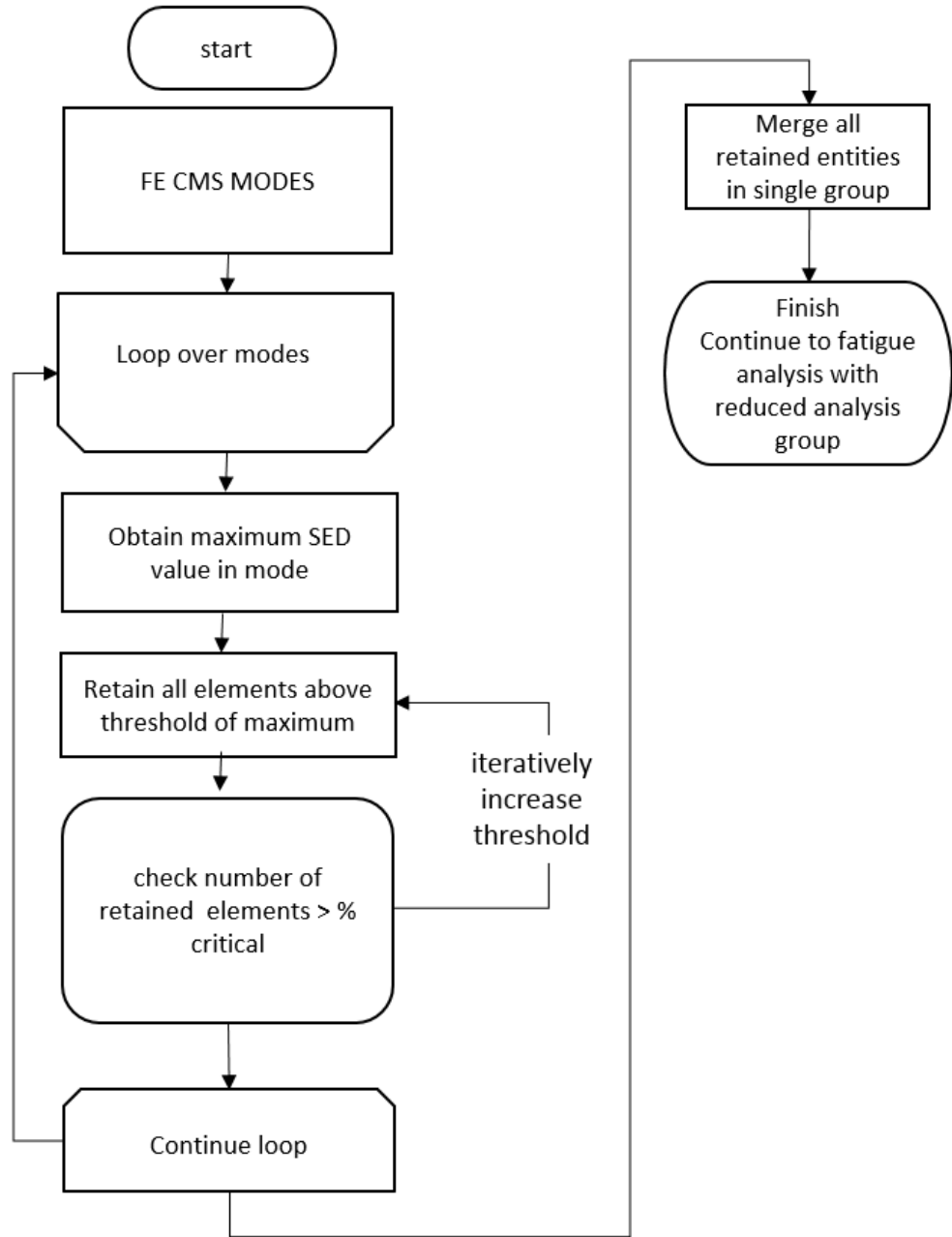


Figure 5-1. Simulation flow diagram for the hotspot prediction algorithm using modes from component-mode synthesis, CMS.

The areas for potential fatigue damage (the candidate hotspots) are identified using threshold levels relative to a peak parameter (e.g. Von Mises stress or strain energy density). The use of an unsigned, derived scalar measure of the stress tensor is necessary in order to avoid the unnecessary, further complications of components and directions.

Once the identification and filtering process in each mode has concluded, the retained entities are merged into a reduced set and passed-on to continue the fatigue process.

In the chart of Figure 5-1, to drive the entity filtering process, the method uses the level of strain energy density as a simple scalar parameter capable of representing the local deformation driving the fatigue damage. Although in principle Von Mises stress and strain energy density could be equally valid, the latter is representative of the total deformation energy and has been more directly linked to the onset of fatigue failure, as outlined by the literature survey in 2.2.2. On the practical side, in FE simulation, strain energy density has the additional advantage of representing the total element deformation in a single value at the centroid, thus avoiding having to consider multiple layered results typical of commonly used shell elements. Finally, the strain energy density integrated over an enclosed set of elements is representative of a collective deformation energy flowing through the local region.

The definitions of strain energy and modal strain energy density are derived in Appendix D in the context of FE modelling. The following section provides an outline with selected definitions.

5.2.2 Element modal strain energy density

The modal strain energy definitions summarized here are applicable to multi degree of freedom systems represented by FE methods via modal reduction techniques, with

- r total number of FE elements for the selected reduced component,
- $U_i(t)$ strain energy of the i^{th} element,
- U_{ni} element modal strain energy for the i^{th} element and n^{th} mode.

Considering \mathbf{K}_i the stiffness matrix of the i^{th} element and assuming an application of Craig-Bampton CMS or equivalent leading to $[\Phi_{CB}^*]$ augmented, orthonormalized component modes, (2.1.3.3), the element modal strain energy for i^{th} element, n^{th} mode is given by

$$U_{ni} = \frac{1}{2} \{\Phi_n^*\}^T [\mathbf{K}_i] \{\Phi_n^*\}. \quad (5.1)$$

Where \mathbf{K}_i in (5.1) is opportunely zero-padded in order to match the rows of $\{\boldsymbol{\phi}_n^*\}$.

The implicit dependency of U_{ni} on the element size, can be readily eliminated by dividing by the element volume V_i ,

$$e_{ni} = \frac{U_{ni}}{V_i}. \quad (5.2)$$

Unlike the time dependent strain energy, $U_i(t)$, obtainable after the full solution of the dynamic problem, the modal strain energy U_{ni} and modal strain energy density e_{ni} are calculated *a priori* by solving an eigenvector problem.

5.3 Implementation of a priori algorithm in MATLAB® with commercial FE codes

The hotspot procedure was implemented in the MATLAB® programming environment and using the MSC Nastran® FE solver. Figure 5-2 describes the main steps. Initially, the MSC Nastran® modal reduction (solution 103 as described in appendix C.1), provides the component modes for a given finite element spatial discretisation. Successive application of MATLAB® routines collect the model information and cycle through the modal load cases, as previously described in Figure 5-1. A separate “driver” file provides the controlling values, such as the energy threshold or maximum percentage of elements to be retained in each mode. The resulting retained elements in each mode are merged into single or multiple groups. The resulting groups are exported to the Patran® post-processing environment and later used in the integrated fatigue solver MSC Fatigue™.

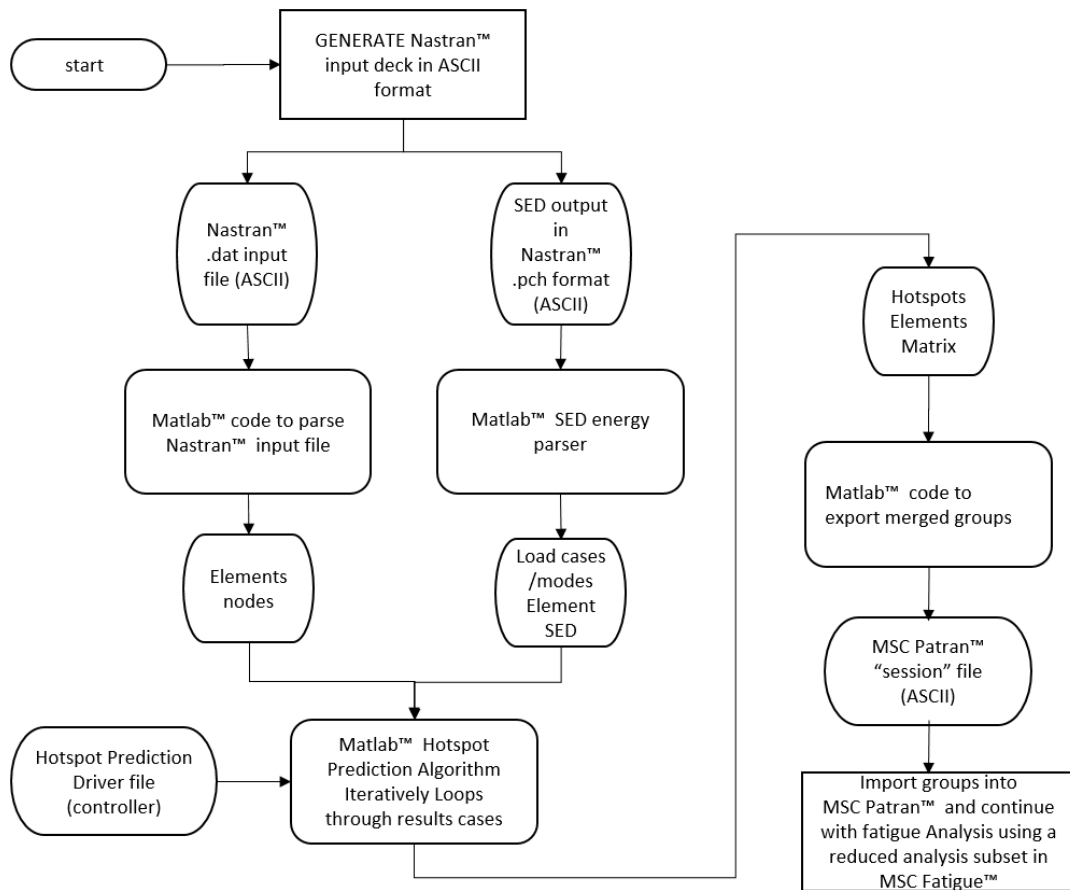


Figure 5-2. Hotspot prediction process implemented in MATLAB® with data from MSC Nastran® and for fatigue calculation with MSC Fatigue™.

5.4 Application to thin plate in bending

The geometry of the analytical baseline plate of the previous chapter is represented with an MSC Nastran® model comprising 9000 shell elements. A comparison with the analytical equivalent is included in appendix A.3. In this case a shell supporting a membrane, bending and shear stiffness response has been adopted, however the method is applicable irrespective of the formulation used.

In order to replicate the typical discrete constraints schematization of FE modelling, the simple supports are concentrated in areas around the four corners, using a web of rigid elements, (RBE2 in Nastran® terminology), distributing the reaction across 3 rows of elements.

The Craig-Bampton method is deployed selecting the 4 corners as boundary nodes, resulting in 6 x 4 constraint modes. A unit concentrated force is applied at a location near

a corner, as shown in Figure 5-3, for the purpose of generating a corresponding residual vector (2.1.2.3). The remaining component modes consist of 10 fixed boundary modes and 6 residual vectors originating from free-body inertial motion, for a total for 41 Craig-Bampton modes. Table 7 compares the first 14 fixed boundary modes with the Craig-Bampton modes after orthogonalization.

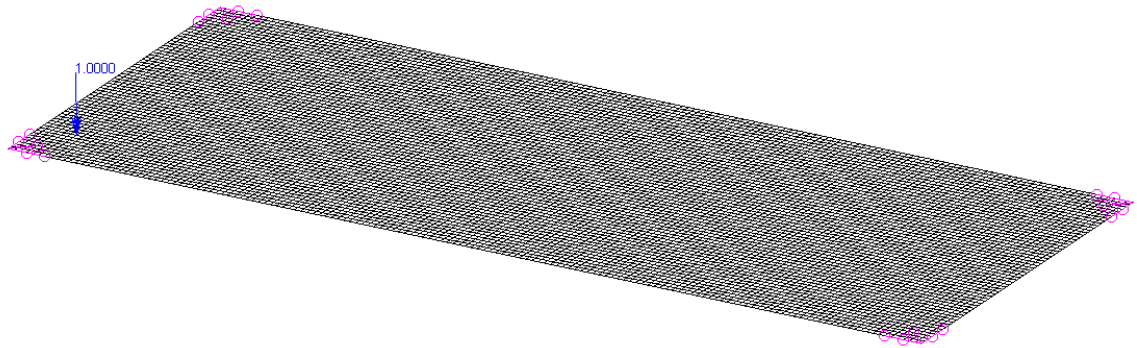


Figure 5-3. Thin rectangular plate, modelled in MSC Nastran®, detailing the location of a transversal unit load and the corner constraints obtained with rigid elements, RB2. Image generated in Patran®.

Table 7. Fixed boundary and Craig-Bampton (CB) modes of rectangular plate

Mode No.	Fixed boundary modes	CB modes after orthonormalization
1	15.76	0.00
2	34.95	0.00
3	44.34	0.00
4	77.46	0.00
5	83.53	0.01
6	119.82	0.01
7	125.72	17.15
8	131.79	26.42
9	156.34	47.68
10	173.78	56.71
11	227.45	93.23
12	268.98	96.43
13	294.70	112.20
14	561.16	123.11
15	4897.47	144.23
16	7170.56	158.13
17	9159.83	161.60

5.4.1 Baseline fatigue analysis

The *baseline* high fidelity analysis is defined as the reference fatigue simulation process where no accelerated fatigue simplification is enforced. For the baseline analysis the unfiltered plate model is submitted to a standard uniaxial S-N analysis in MSC Fatigue™, assuming linear damage summation rule, rainflow cycle counting and the maximum absolute principal as stress combination parameter (2.2.5). The baseline fatigue analysis settings are summarized in Table 8.

Table 8. Summary of main fatigue analysis settings for baseline analysis

Baseline fatigue analysis settings	
Method	S-N
FE result location	9000 x 2 Elements (top and bottom layer)
S-N fatigue dataset	Steel BS7608 Class F
Tensor Type	Stress
Stress units	MPa
Stress combination parameter	Maximum Absolute Principal
Mean stress correction	Goodman

5.4.2 A priori hotspot prediction

The hotspot search algorithm, 5.2.1, loops through the 41 Craig-Bampton modes and selects entities according to the fixed threshold. Successive trials with varying level of percentage model retention in each mode, respectively 0.1%, 0.2%, 0.4%, 1%, 5% and 10%, lead to the element groups shown to a model retention of respectively 1% in Figure 5-4 (a), 3% (b), 5% (c), 13% (d), 50% (e) and 76% (f).

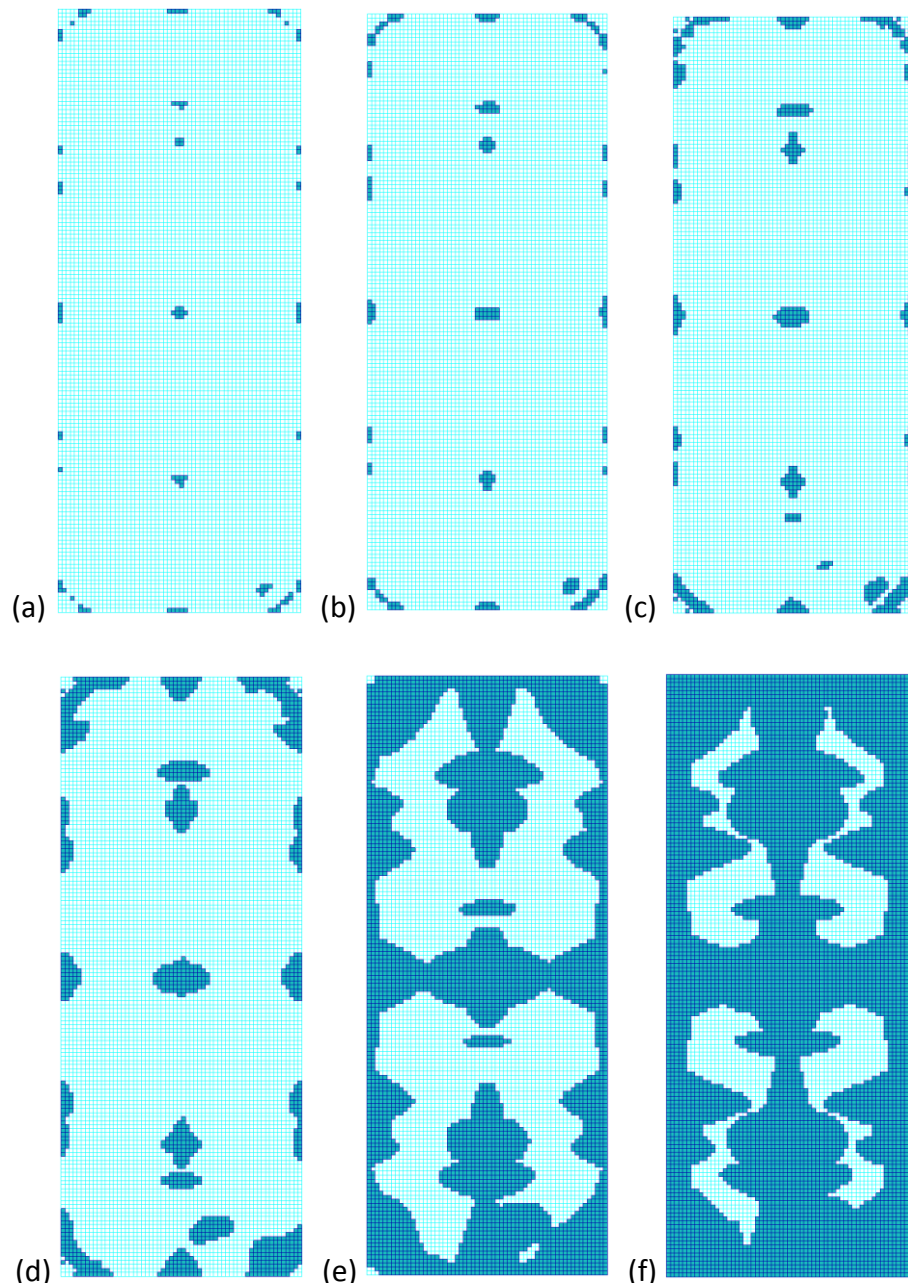


Figure 5-4. Mode threshold retentions of 0.1%, 0.2%, 0.4%, 1%, 5% and 10%, corresponds to model fraction respectively of 1% (a), 3% (b), 5% (c), 13% (d), 50% (e) and 76% (f). Images generated in Patran®.

5.4.3 Multibody system of a dynamically responsive plate

Although the component in this case is also the whole system, the multibody solver Adams™ was used for the convenience in running transient problems, and also with the intention of demonstrating the applicability of the process to systems of arbitrary complexity.

Adams™ imports the modal neutral file (MNF as described in appendix C.3), containing the reduced mathematical model of the plate generated by MSC Nastran®. A modal damping model is adopted with 4% of critical damping.

Hinged constraints (spherical joints constraining only translations) or clamps (all 6 DOF fixed) are used, depending on the case. Similarly, different types of loading, static or dynamic were investigated, using both enforced motions and applied forces. Selected cases are reported in the following section.

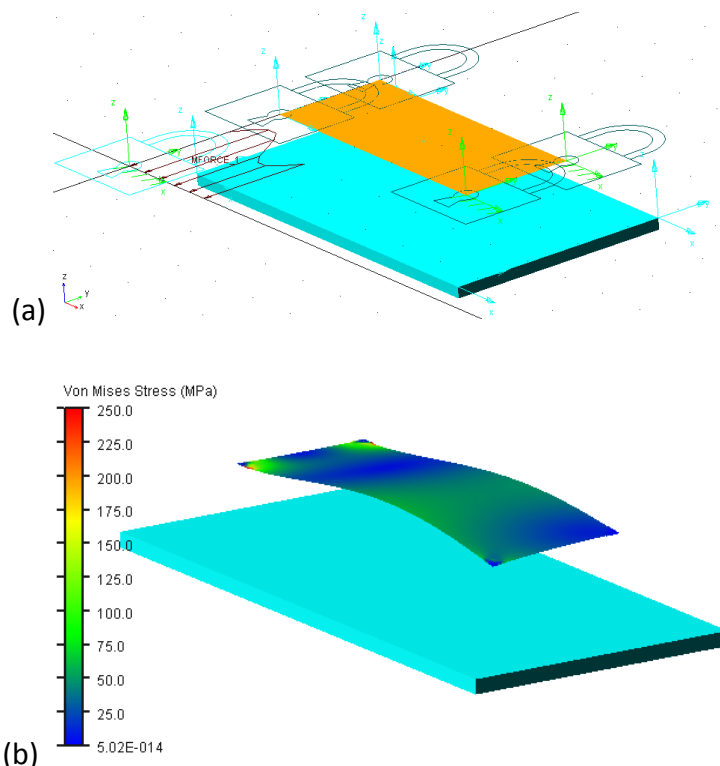


Figure 5-5. Adams™ multibody system of the flexible plate and boundary constraints at rest position (a) and with vibrating stress countours during motion (b). Images generated in Adams/View™.

5.4.4 Results for selected loading and boundary conditions

Test Case 1 – Base motion sweeping from 0 to 20 Hz in 20 seconds

The plate is clamped via four corners directly onto the rigid base (representing a shaker table) with no intermediate compliance. The rigid base is excited with enforced vertical motion starting from 0 Hz and gradually increasing to 20 Hz in 20 s, using continuous increments. The excitation covers the first resonance at 15.7 Hz, as shown with the response of the first non-rigid modal coordinate, q_7 in Figure 5-6.

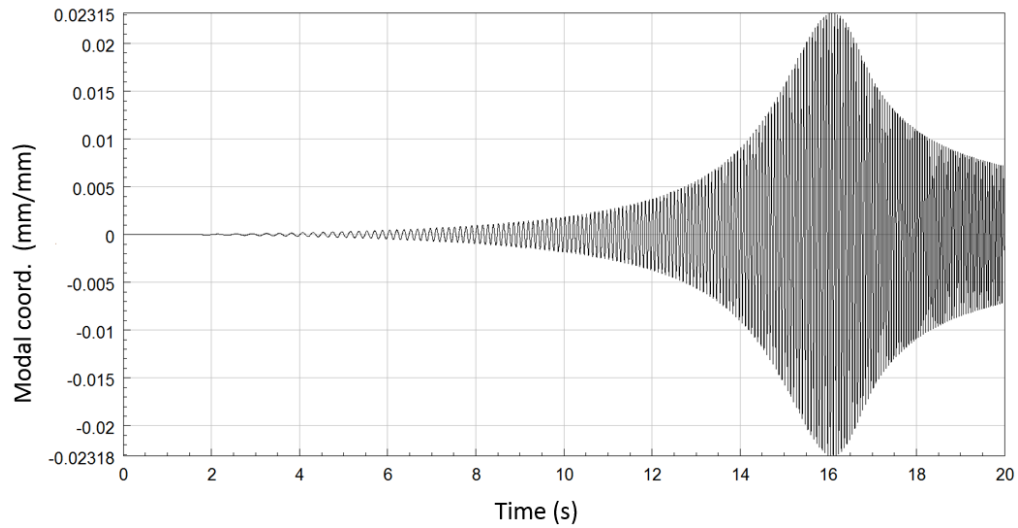


Figure 5-6. Case 1 response of first non-rigid modal coordinate (q_7) under sine sweep loading. Resonance is observed at the expected 15.7 Hz.

Table 9 presents the results of the diagnostic test in the form of contingency tables for 3 levels of assumed prevalence and 6 different model fractions resulting from varying the a priori filtering thresholds.

Table 9. Case 1 contingency tables at different prevalence values and for different a priori hotspot prediction model fractions

		retained model fraction in hotspot prediction					
		1%	3%	5%	13%	50%	76%
prior % (prevalence)		true positive rate (TPR)					
	1%	0.22	0.50	0.81	1.00	1.00	1.00
	2%	0.12	0.28	0.50	0.91	1.00	1.00
	3%	0.13	0.25	0.42	0.80	1.00	1.00
prior % (prevalence)		false positive rate (FPR)					
	1%	0.009	0.020	0.043	0.117	0.493	0.754
	2%	0.009	0.020	0.042	0.110	0.487	0.752
	3%	0.008	0.018	0.040	0.105	0.482	0.749
prior % (prevalence)		likelihood ratio (TPR/FPR)					
	1%	23.86	24.48	18.72	8.53	2.03	1.33
	2%	12.55	13.84	11.95	8.22	2.05	1.33
	3%	15.93	13.83	10.68	7.60	2.07	1.33
prior % (prevalence)		posterior probability					
	1%	0.17	0.14	0.11	0.07	0.02	0.01
	2%	0.20	0.18	0.15	0.10	0.04	0.03
	3%	0.20	0.18	0.15	0.11	0.05	0.04

The receiver operating characteristics, ROC diagram, in Figure 5-7 provides an immediate graphical interpretation of the contingency tables collected in Table 9. For a given minimum TPR threshold (e.g. 60%), the upper and leftmost point, corresponding to the highest likelihood ratio at 18.72 (highlighted in Table 9) provides the best accuracy (*TPR*) for a given cost (*FPR*). The identified point, corresponding to the best possible diagnostic outcome, was obtained with 5% model retention for an assumed 1% prevalence.

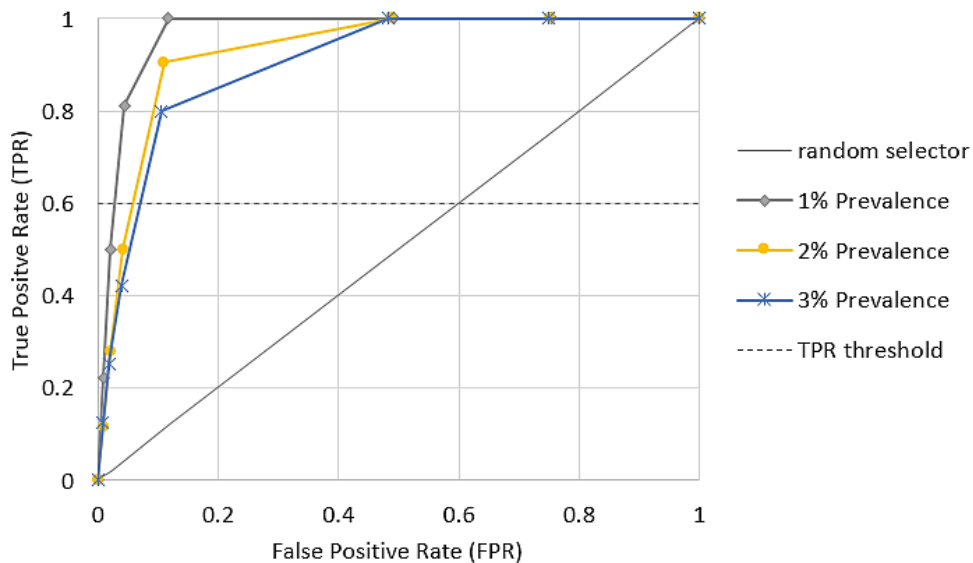


Figure 5-7. ROC diagram for Case 1, enforced motion [0-20 Hz] for 3 assumed levels of prevalence and the a priori filtering model fractions shown in Table 9.

The diagrams in Figure 5-8 present the most critical locations detected with different hotspot model fractions and in comparison to the reference baseline result. The corresponding collective damage index, CDI, histogram in Figure 5-9 precisely quantifies the effect of the model filtering on the total cumulated damage. The *CDI%* values are normalized with the baseline results respectively at 0.1%, 1% and 5% model fraction.

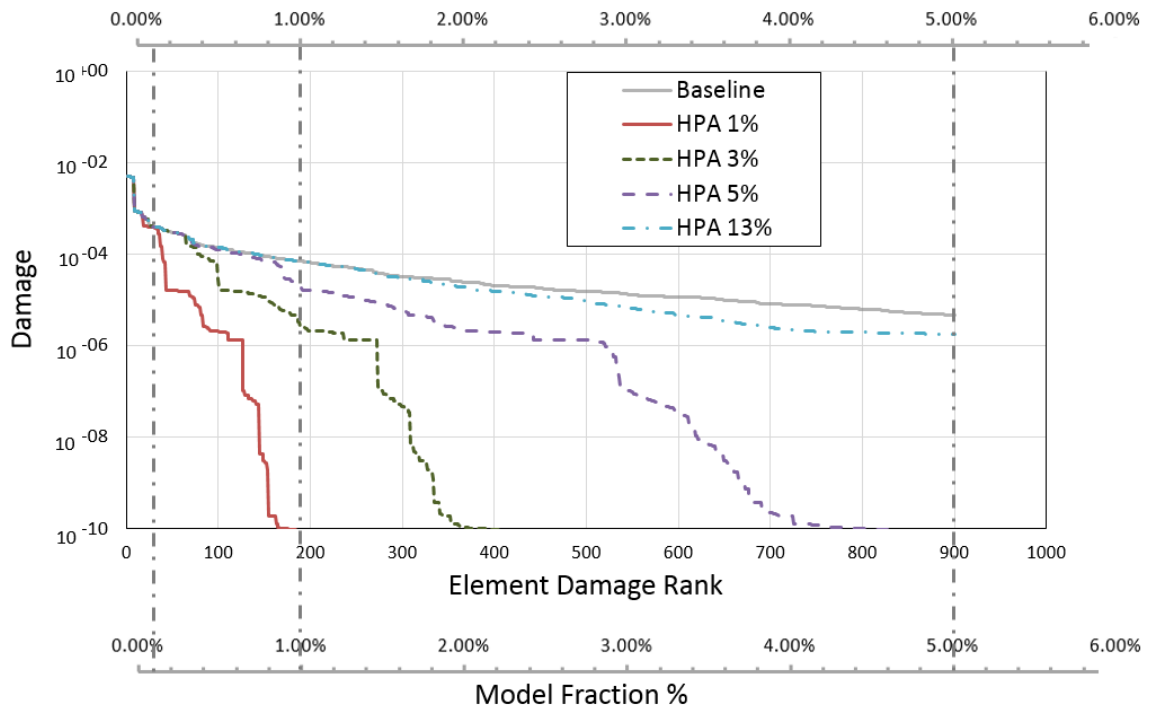


Figure 5-8. Case 1 top damaged locations for different model fractions in hotspot prediction (HPA), compared with baseline result (topmost curve).

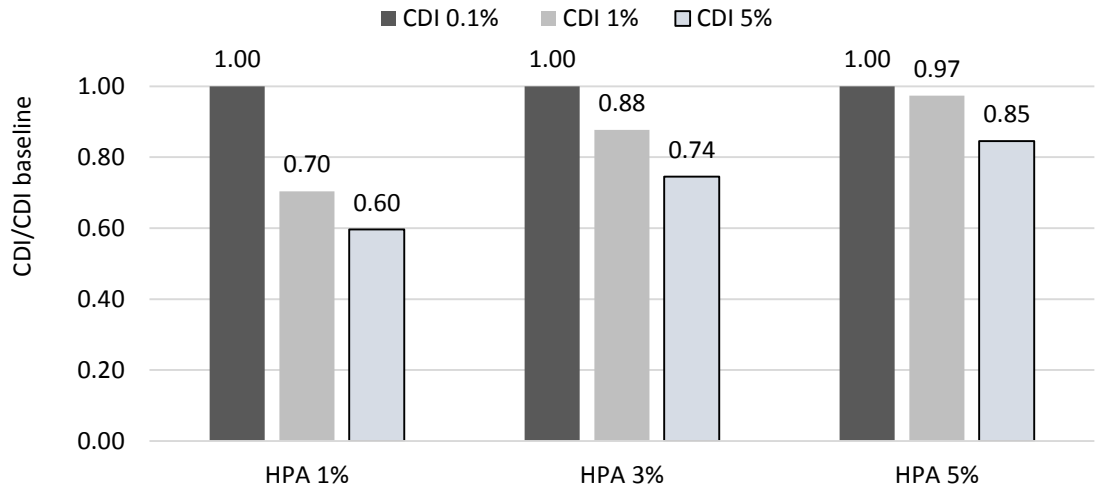


Figure 5-9. Case 1 normalized collective damage index, $CDI\%$, at 0.1%, 1.0% and 5.0% model fraction obtained for a priori prediction algorithm (HPA), respectively with 1%, 3% and 5% of model retention.

Test Case 2 – Dynamic response for 1N harmonic force at 10 Hz

The same model in Case 1 is subjected to a transversal 1N harmonic point load, applied as shown in Figure 5-3, with a frequency of 10 Hz. The frequency and position of the loading are chosen to approximate the hotspot conditions observed in the transition area

between the static shape and the first modal response, as discussed in 4.2.1. Figure 5-10 shows the response of the first non-rigid modal coordinate q_7 .

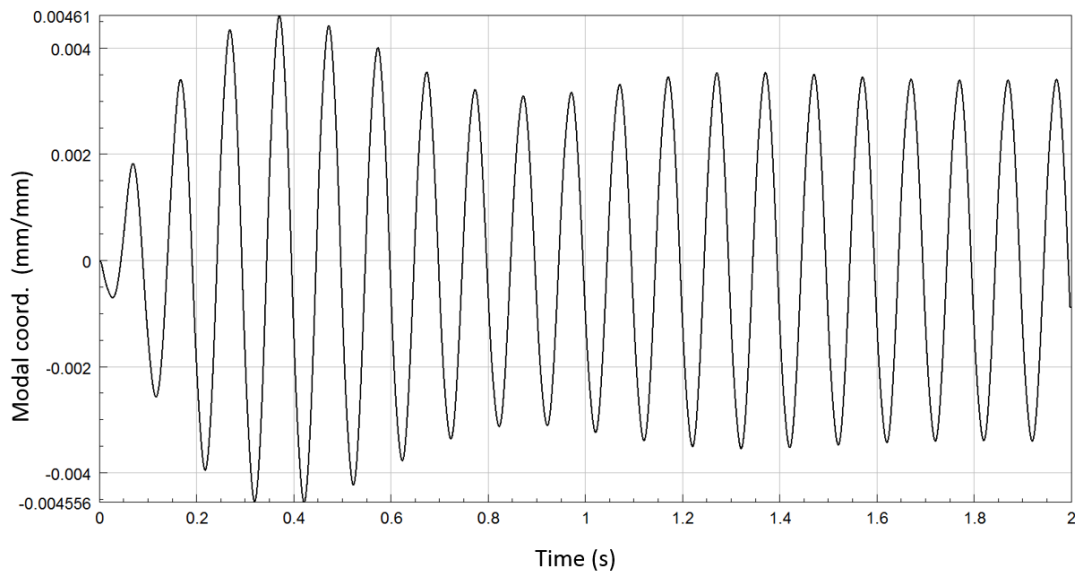


Figure 5-10. Case 1 response of first non-rigid modal coordinate (q_7) to the harmonic loading at 10 Hz.

Table 10. Case 2 contingency tables at different fatigue damage prevalence values and with increasing model fractions in a priori hotspot prediction

		Hotspot prediction retained model fraction %					
		1%	3%	5%	13%	50%	76%
prior % (prevalence)		true positive rate (TPR)					
	1%	0.19	0.36	0.57	0.94	1.00	1.00
	2%	0.12	0.22	0.38	0.66	1.00	1.00
	3%	0.08	0.15	0.26	0.46	0.81	0.93
prior % (prevalence)		false positive rate (FPR)					
	1%	0.010	0.022	0.046	0.118	0.492	0.754
	2%	0.009	0.021	0.044	0.115	0.487	0.751
	3%	0.009	0.021	0.045	0.116	0.488	0.751
prior % (prevalence)		likelihood ratio (TPR/FPR)					
	1%	19.57	16.25	12.38	8.01	2.10	1.37
	2%	12.55	10.48	8.52	5.69	2.08	1.36
	3%	8.28	7.13	5.82	3.93	1.65	1.24
prior % (prevalence)		posterior probability					
	1%	0.17	0.14	0.11	0.07	0.02	0.01
	2%	0.20	0.18	0.15	0.10	0.04	0.03
	3%	0.20	0.18	0.15	0.11	0.05	0.04

The ROC diagram in Figure 5-11 indicates that the best performances are, again, those obtained with 5% model retention for an assumed 1% prevalence, however in this case both the accuracy and efficiency of the prediction appear significantly lower compared to Case 1. Here again the CDI results, Figure 5-12, provide a more exact quantification of the effect of the model filtering on the total cumulated damage.

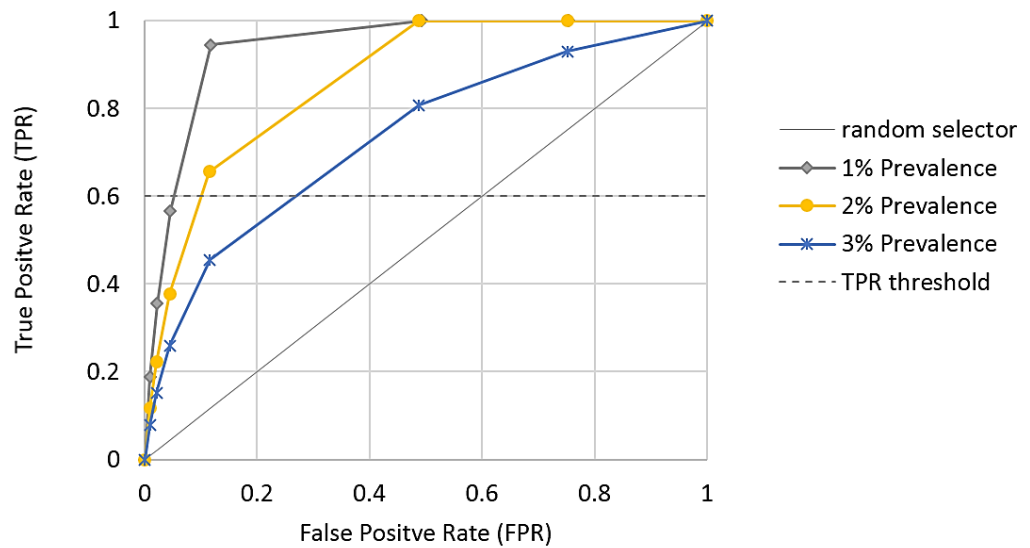


Figure 5-11. ROC diagram for Case 2 comparing performance of a priori prediction and for different levels of prevalence.

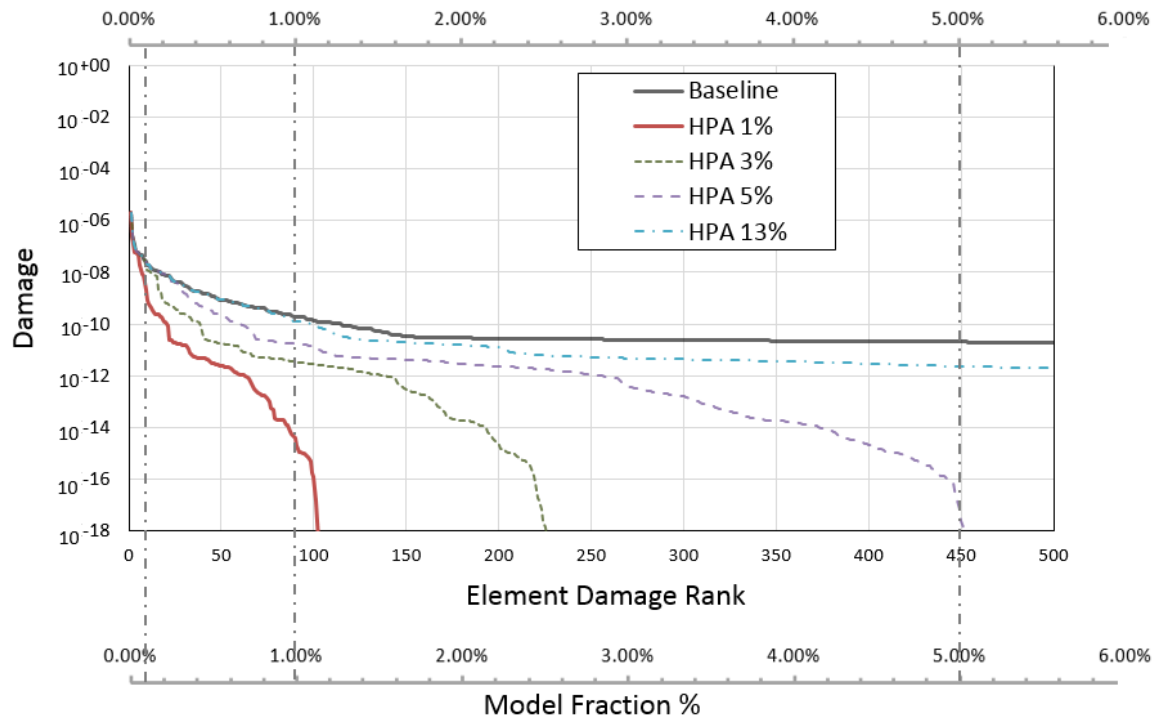


Figure 5-12. Case 2 top damaged locations for different model fractions in hotspot prediction (HPA), compared with baseline result (topmost curve).

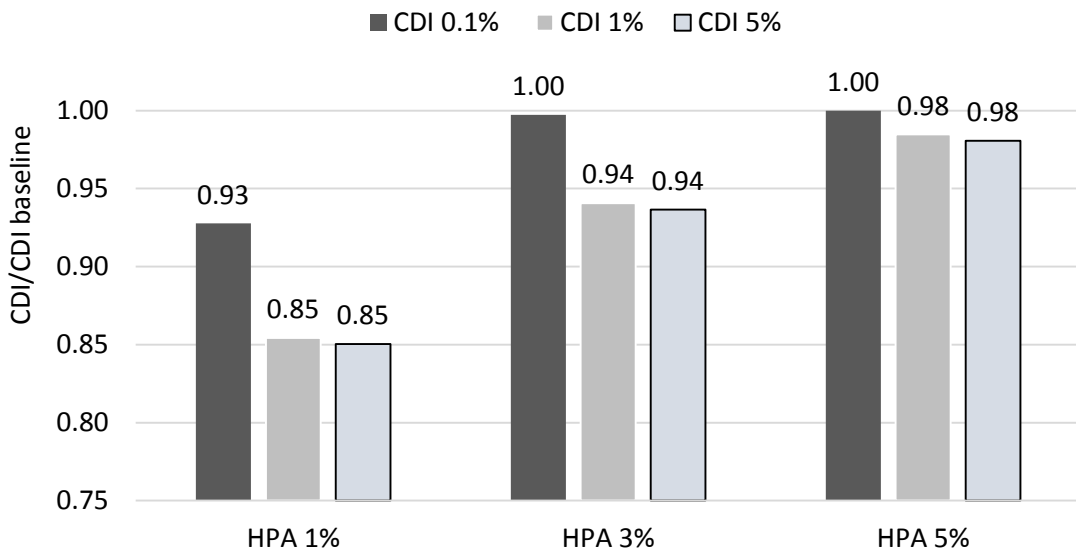


Figure 5-13. Case 2 normalized collective damage index, $CDI\%$, at 0.1%, 1.0% and 5.0% model fraction obtained for a priori prediction algorithm (HPA), respectively with 1%, 3% and 5% of model retention.

5.5 Application to thin L-plates in pseudostatic superposition of two corner forces

Test Case 3 – Pseudostatic response to equivalent damage forces

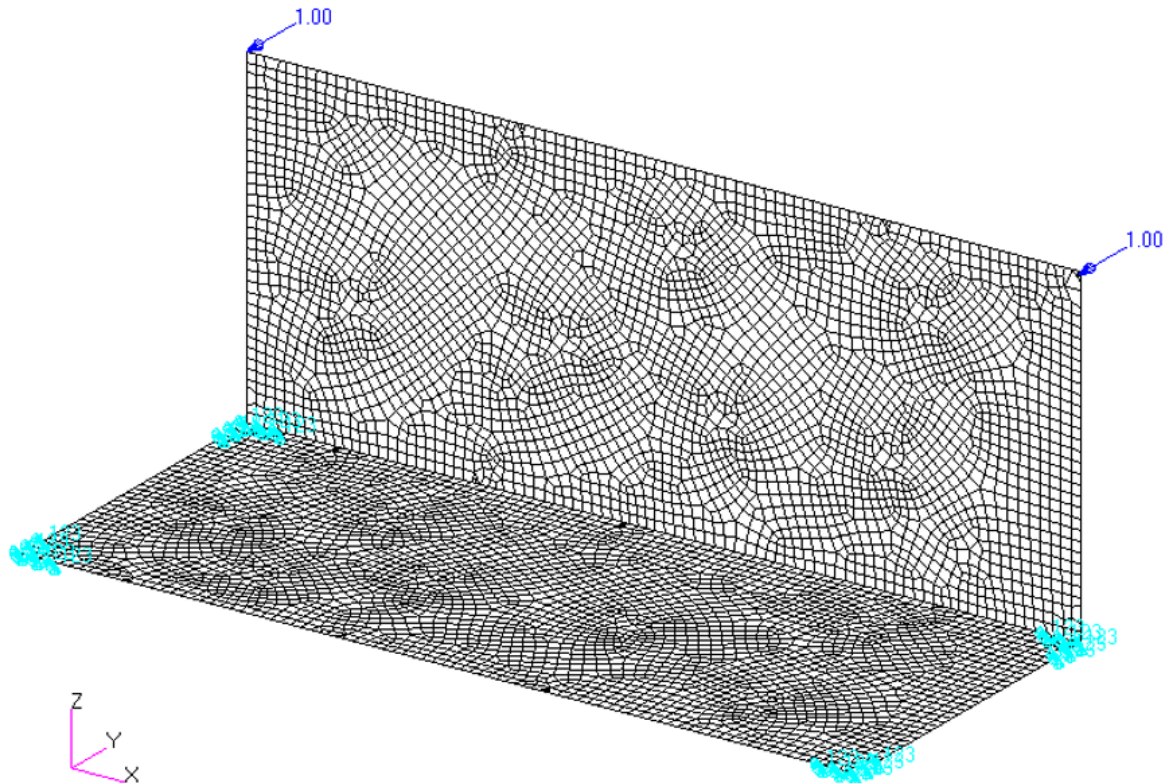


Figure 5-14. L-plate geometry showing supports and applied forces. Image generated in Patran®.

The example of the L-plate in Figure 5-14 is purposely crafted to demonstrate the simple conditions where the result of a traditional two-pass method might be affected by considerable error.

The base plate is clamped and the vertical top-left and top-right corners are simultaneously loaded with time histories represented respectively by Figure 5-15 and Figure 5-16. The loadings are crafted so as to produce identical damage when individually applied. This condition is easily obtained for the common linear or bilinear S-N curves, such as the weld curve used for this example (Figure 2-13). Recalling the power relationship between stress and cycles introduced in Eq. (2.31):

$$S^m N = C, \quad (5.3)$$

the equivalent stress of a sequence of n_1 cycles, at stress range S_1 , leading to the identical damage by a single application of the load is

$$S_{eq} = (n_1)^{1/m} S_1 \quad (5.4)$$

Proceeding similarly for a sequence of n_2 loads at stress range S_2 :

$$S_{eq} = (n_2)^{1/m} S_2 \quad (5.5)$$

The two described loadings produce identical equivalent damage when their respective equivalent stress coincide, leading to:

$$S_2 = \left(\frac{n_1}{n_2}\right)^{1/m} S_1 \quad (5.6)$$

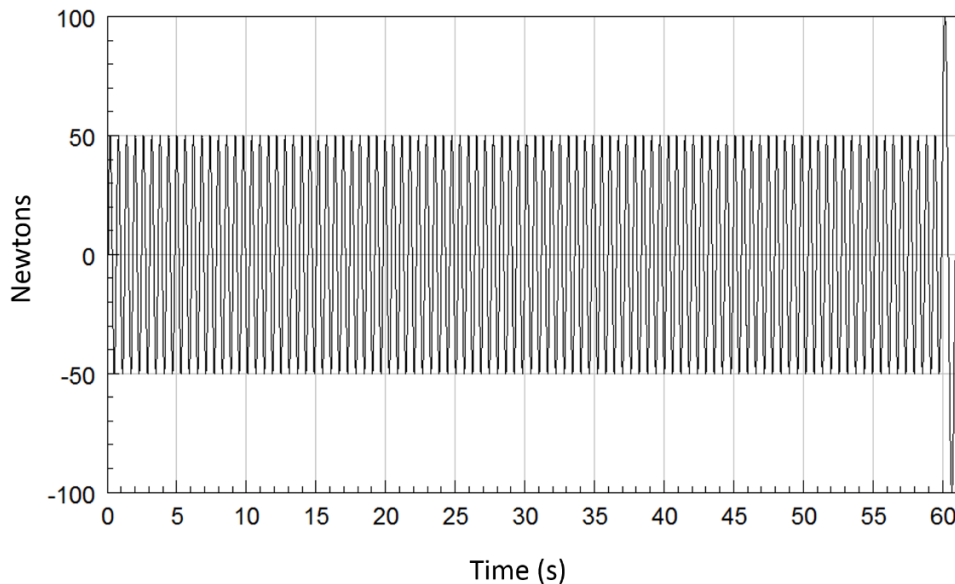


Figure 5-15. Loading on top left corner comprises of 100 cycles at 50 N amplitude plus a single final cycle at 100 N.

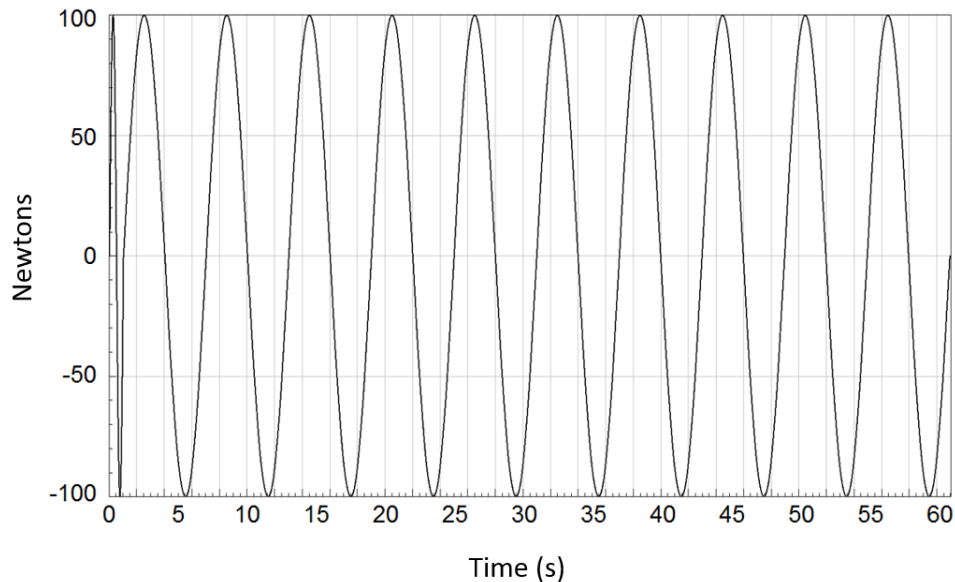


Figure 5-16. Loading on top right corner comprises 11 cycles at a 100 N amplitude.

The result from a baseline unfiltered fatigue run, Figure 5-17, confirms that the damage is distributed symmetrically across the plates. In the same prescribed conditions, however, the accelerated fatigue simulation based on a two-pass filtering method, even with a conservative peak-valley gate at 50% of loading, results in the very different distribution shown in Figure 5-18. This evident error is due to the single larger cycle affecting the peak-valley threshold filtering. As consequence of this load “bias” towards the largest peak, a large part of the repetitions from the top left corner are discarded by the peak-valley threshold. Ultimately, the first pass fatigue analysis dismisses some of the most damaged areas from the left side of the plate.

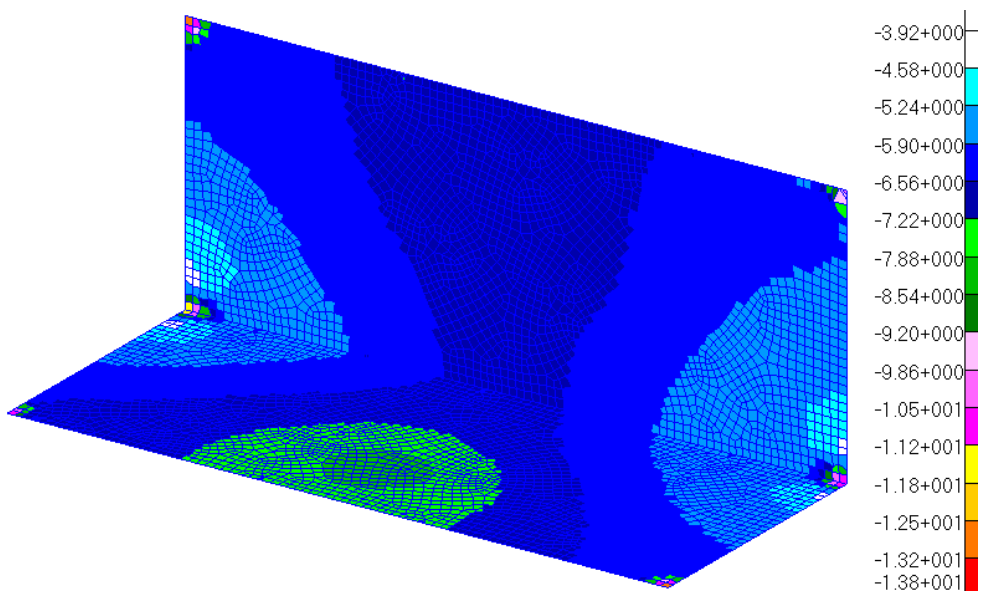


Figure 5-17. Baseline unfiltered damage (log) distributed symmetrically across the plates. Image generated in Patran®.

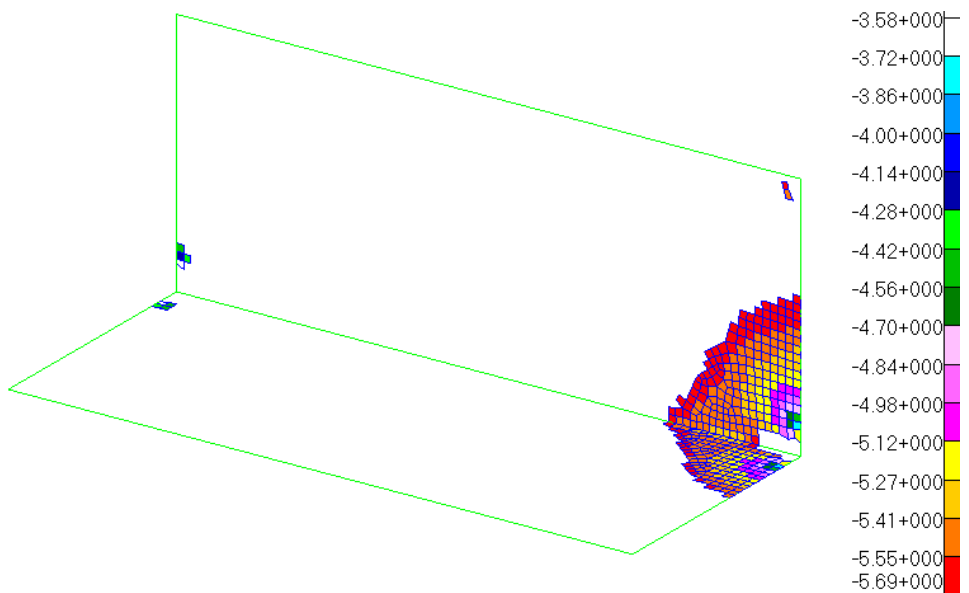


Figure 5-18. Two-pass filtered fatigue log of damage result for 6% model retention, visibly neglecting large contribution to the damage from the Top left loading. Image generated in Patran®.

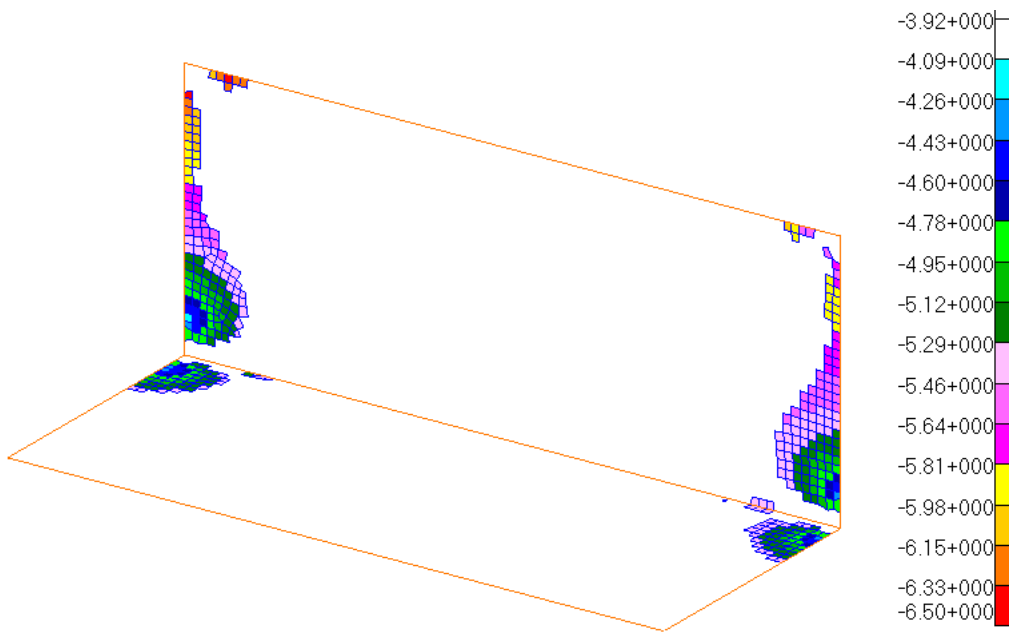


Figure 5-19. Fatigue result on a priori filtered model with 6% model retention.

The results correctly capture the symmetry of the damage distribution (log scale). Image generated in Patran®.

Once again, the qualitative effect described in Figure 5-18 and Figure 5-19 can be precisely quantified by the proposed new metrics in terms of contingency tables (Table 11), ROC diagrams (Figure 5-20) and collective damage index, CDI, values.

Table 11. Contingency tables comparing a priori hotspot prediction, HPA, and two-pass accelerated fatigue simulation in L-plates

	L-plate		Perforated L-plate	
	HPA	Two-pass	HPA	Two-pass
		6%		
<i>prior % (prevalence)</i>		<i>true positive rate (TPR)</i>		
1%	0.98	0.50	1.00	0.50
2%	0.99	0.48	1.00	0.49
3%	0.98	0.48	0.99	0.49
<i>prior % (prevalence)</i>		<i>false positive rate (FPR)</i>		
1%	0.048	0.053	0.049	0.054
2%	0.038	0.049	0.039	0.049
3%	0.029	0.044	0.029	0.045
<i>prior % (prevalence)</i>		<i>likelihood ratio (TPR/FPR)</i>		
1%	20.57	9.49	20.57	9.32
2%	26.08	9.91	25.77	9.90
3%	34.17	10.79	34.17	11.02
<i>prior % (prevalence)</i>		<i>posterior probability</i>		
1%	0.17	0.09	0.17	0.09
2%	0.35	0.17	0.34	0.17
3%	0.51	0.25	0.51	0.25

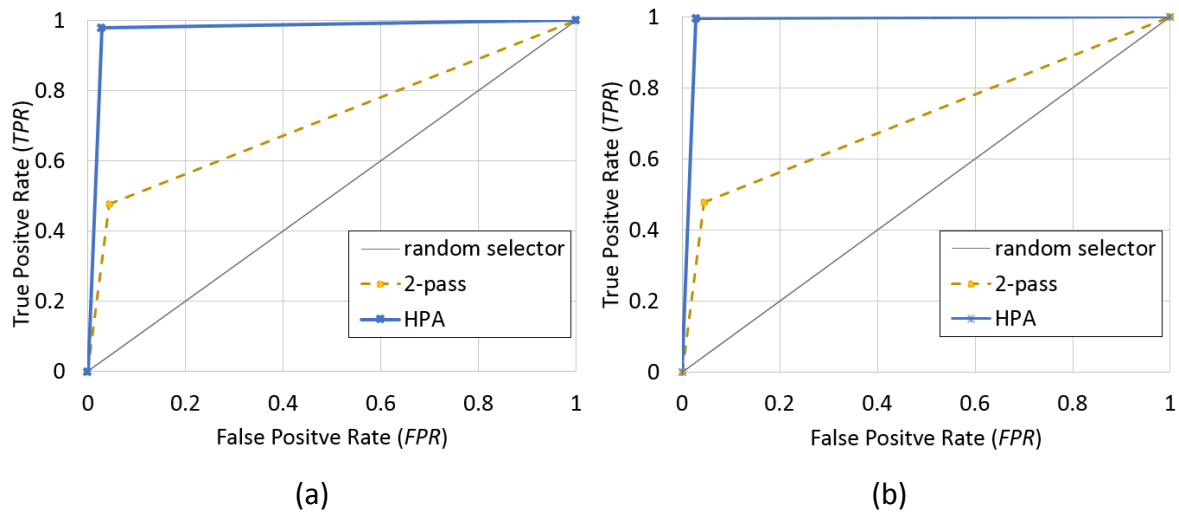


Figure 5-20. ROC diagram comparing hotspot prediction and two-pass for L-Plate (a) and perforated L-Plate (b), prevalence set at 3% with 6% retained model fraction.

Test Case 4 – Pseudostatic response to equivalent damage forces on a perforated L-Plate

A perforated L-plate is obtained by removing selected elements from the model used in Case 3. The baseline results are shown in Figure 5-21.

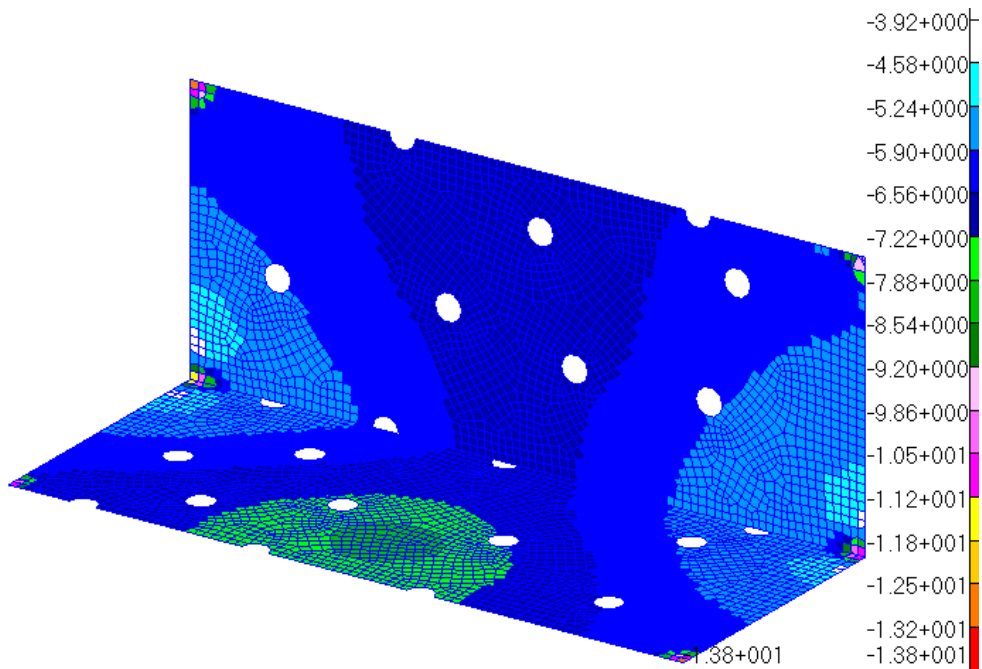


Figure 5-21. Case 4, baseline log of damage distribution for perforated L-plate.
Image generated in Patran®.

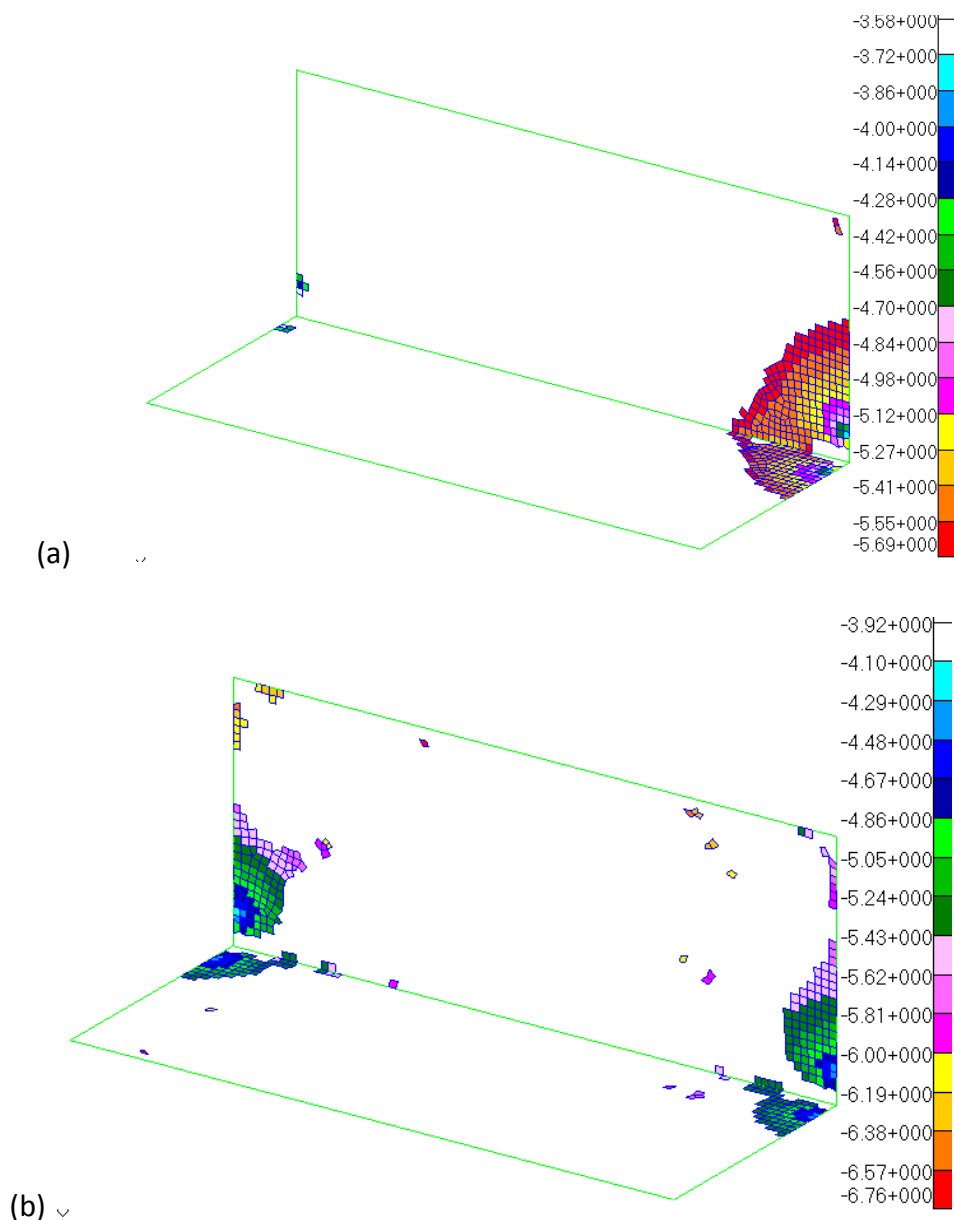


Figure 5-22. Perforated L-plate damage distribution with two-pass (a) and a priori hotspot filtering (b). Images generated in Patran®.

As it was to be expected, the two-pass filtering method is again affected by load “bias” error, as demonstrated by the asymmetric damage distribution in Figure 5-22(a). Conversely, the a priori hotspot filtering, Figure 5-22(b), correctly captures the symmetric damage distribution observed for the baseline results in Figure 5-21. In Figure 5-23 the baseline top damaged locations are compared to the a priori hotspot prediction and two-pass method, both obtained at the same 3% model retention. Figure 5-20(b) and Table 11 provide the precise metrics for quantification of efficiency and accuracy, also in comparison with the L-plate in Case 3.

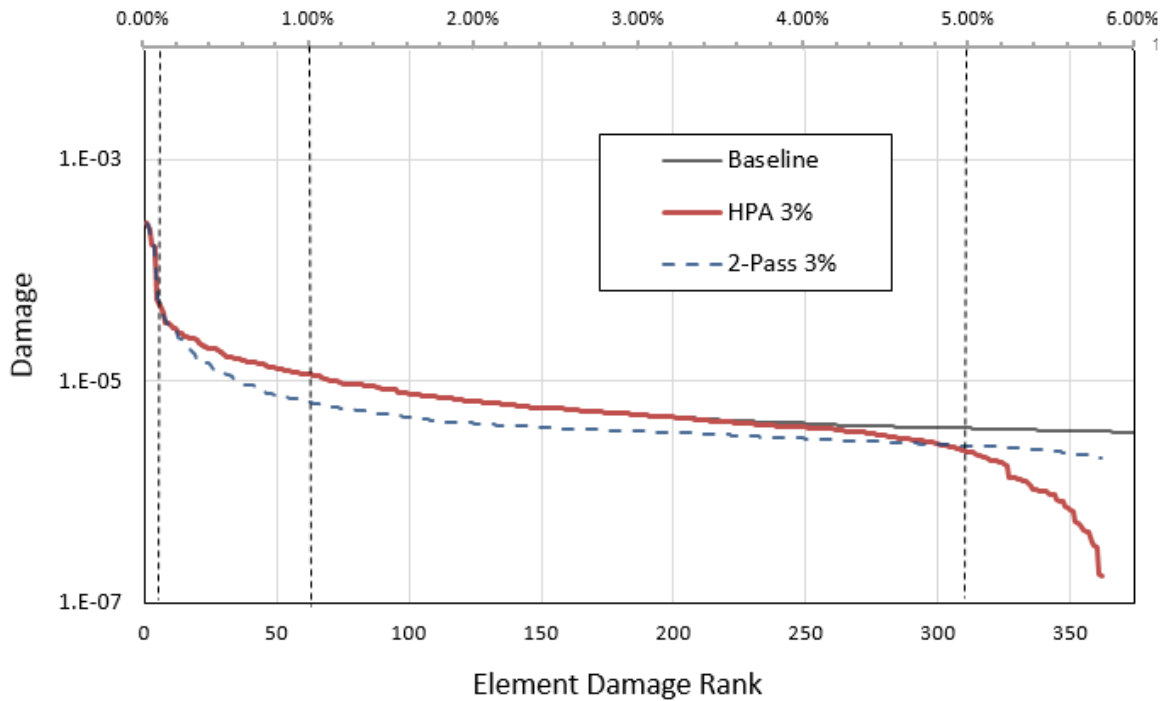


Figure 5-23. Perforated L-plate damage value in top damaged locations: baseline, a priori hotspot prediction (HPA) and two-pass method (2-Pass).

The actual impact on the neglected total damage is best represented by the collective damage index in Figure 5-24. In Table 12 extended statistics, such as mean and average damage provide additional depth to the proposed accelerated fatigue simulation metrics.

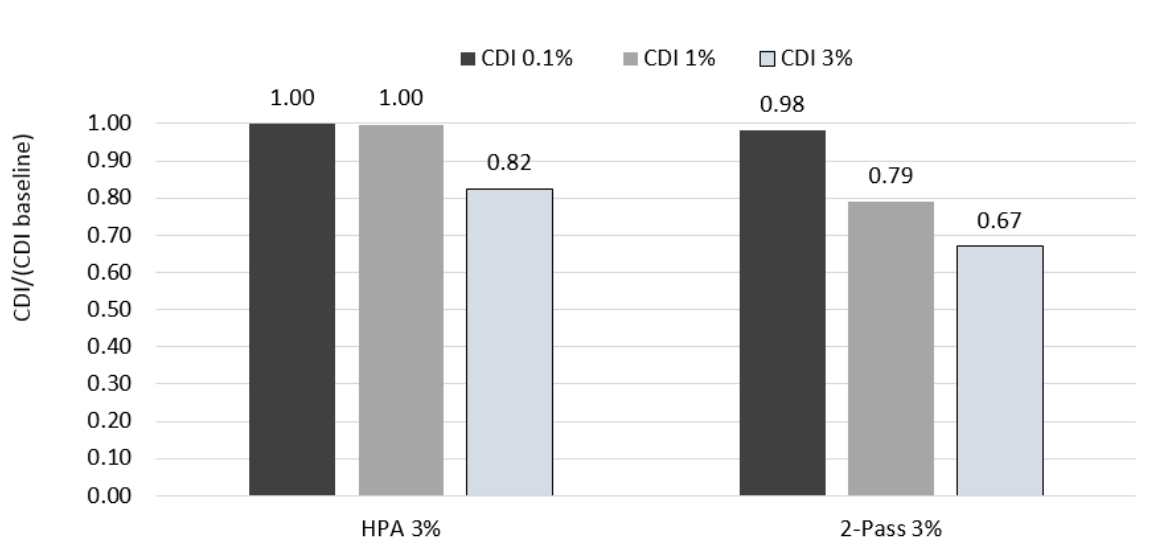


Figure 5-24. Test case 4, perforated L-plate collective damage index, $CDI\%$ at 0.1%, 1% and 3% comparing a priori algorithm (HPA) with two-pass on-line filtering method (2-Pass) at the same 3% model fraction.

Table 12. Extended CDI statistics for case 4, perforated L-plate, comparing baseline results with a priori prediction (HPA) and two-pass method (2-Pass)

	Baseline	HPA 3%	2-Pass 3%
CDI 0.1%	1.29×10^{-3}	1.29×10^{-3}	1.27×10^{-3}
average damage	7.18×10^{-5}	7.16×10^{-5}	7.05×10^{-5}
max damage	2.65×10^{-4}	2.65×10^{-4}	2.65×10^{-4}
S.D. damage	7.83×10^{-5}	7.82×10^{-5}	7.90×10^{-5}
CDI 1.0%	2.84×10^{-3}	2.83×10^{-3}	2.24×10^{-3}
average damage	1.58×10^{-5}	1.57×10^{-5}	1.24×10^{-5}
max damage	2.65×10^{-4}	2.65×10^{-4}	2.65×10^{-4}
S.D. damage	3.08×10^{-5}	3.08×10^{-5}	3.12×10^{-5}
CDI 3.0%	4.16×10^{-3}	3.43×10^{-3}	2.79×10^{-3}
average damage	7.71×10^{-6}	6.35×10^{-6}	5.17×10^{-6}
max damage	2.65×10^{-4}	2.65×10^{-4}	2.65×10^{-4}
S.D. damage	1.87×10^{-5}	1.90×10^{-5}	1.88×10^{-5}
CDI 5.0%	4.99×10^{-3}	3.43×10^{-3}	2.79×10^{-3}
average damage	5.55×10^{-6}	3.81×10^{-6}	3.10×10^{-6}
max damage	2.65×10^{-4}	2.65×10^{-4}	2.65×10^{-4}
S.D. damage	1.47×10^{-5}	1.50×10^{-5}	1.48×10^{-5}

5.6 Observations for Test Cases 1-4

For both case 1 and 2 the performances of the a priori prediction was satisfactory, with case 2 leading to the anticipated lower efficiency. With a single applied load a considerable portion of the predicted hotspots will be remote from stress concentrations, with negative affect on the efficiency, especially in comparison with online methods.

The proposed collective damage index, CDI, statistics can precisely quantify the impact on the accrued damage deriving from the filtering approximation. At a low $CDI_{0.1\%}$ the observed approximation was generally minimal, suggesting that, if only a few highly damaged locations are required (e.g. early design cycles), the a priori HPA method can be safely applied and could lead to important cost savings. Conversely, with the intention to capture a 1% model fraction (of damage *prevalence*), the CDI result might indicate that at least 3% of model retention should be considered.

Cases 3 and 4 were crafted specifically to exemplify the possible adverse effect of peak-valley gating in certain loading combinations, where fewer load spikes can obscure a high number of damaging cycles.

Such load spikes may be an actual occurrence (pot hole, carb strike, unusual landing etc.) or they could be a hard-to-detect signal acquisition error. Whether the spike is real or not, the results of the online methods are “biased” by its presence, with consequential potential errors in damage ranking and prioritization.

By contrast, the a priori approach is insensitive to the loading and, as shown in Figure 5-19, the same 6% of model fraction used for accelerated fatigue with two-pass method, led to the correct damage distribution.

Test Case 4 was designed to investigate the effect on a priori prediction of randomly distributed stress concentrations around geometrical features. The preliminary result showed a potential improvement in terms of *TPR* (hit rate) but a negative effect on the overall efficiency due to the increase in *FPR* (false discoveries).

Lastly, the greater efficiency of the a priori method for Case 3 and 4 is due to the selective choice of static shapes, rather than the full set of Craig-Bampton modes. This result indicates a possible opportunity to improve the efficiency of the method, perhaps at the cost of a reduced process automation.

5.7 Chapter summary and conclusions

In this chapter the procedures for a priori hotspot detection, first explored in Chapter 4 via simple analytical models, are extended to FE structures representative of a general complexity.

The proposed a priori model filtering is formalized and coded in a MATLAB[®] routine, in combination with the off-the-shelf FE solutions. The process is generally applicable to FE-based fatigue analysis using the pseudostatic and modal superposition approaches, where the Craig-Bampton method is proposed as a primary basis for hotspot prediction. Although component-mode synthesis is not exclusively used in conjunction with multibody systems dynamics, the integrated FE and multibody simulation is an ideal target for the accelerated fatigue process.

The designed metrics for efficient evaluation and quantification of accelerated fatigue simulation performances, anticipated in 4.5.2, are adapted and applied to the FE environment.

The a priori prediction is initially tested with the familiar rectangular plate, dynamically excited via base motion. For the second case, the frequency and position of a concentrated loading are chosen to approximate the hotspot conditions observed in the transition area between the static shape and the first modal response, as discussed in 4.2.1. In both cases the performances of the a priori prediction was satisfactory, however the simplicity of the loading negatively affects the efficiency of the discoveries, as indicated by a relatively high false positive rate (*FPR*).

The results of different filtering settings have been successfully assessed by the proposed metrics. The contingency tables used in diagnostic tests, with the accompanying receiver operating characteristics, ROC diagrams, provide direct and simple means of quantifying and comparing the efficiency and the accuracy of any accelerated fatigue simulation method based on model elimination. Different thresholds of model elimination, under variable assumed fatigue damage prevalence, can be inspected and compared.

Case 3 and 4 investigated the realistic conditions where a priori identification performs decisively better than traditional online methods. The possible occurrence of the described scenario, an isolated load spike obscuring relevant parts of the signal, should be carefully considered in a robust accelerated fatigue simulation process, perhaps suggesting to combine the benefits of a priori and online filtering.

The simple geometries investigated provided an ideal test bench for the validation of the performance metrics. However in order to investigate further the merits and opportunities for the application of a priori filtering, a more realistic scenario is required. Such is the case presented in the next chapter.

Chapter 6: Fatigue simulation acceleration test cases

The concepts and methods developed in chapter 5 are applied to a real-life industrial cases of medium complexity. The durability problem is addressed according to industry standards and used to evaluate the performance and reliability of the prediction algorithm in a comparative assessment with alternative practices. A combined FE, multibody systems and fatigue simulation of an All-Terrain Vehicle is addressed in detail in order to explain and compare different solution acceleration techniques. The novel performance assessment tools and dedicated hotspot visualization techniques are proposed as a way to quickly and efficiently compare the different acceleration methods.

6.1 All-Terrain Vehicle fatigue analysis

As anticipated in paragraph 3.1 simulation acceleration technique is tested in the common restrictive conditions typical of vehicle durability. These are characterized by multiple stress risers, localized loads and constraints and with only few, low frequency, low modal density, natural modes that are dynamically excited.

The All-Terrain Vehicle model and its experimentally acquired loadings, introduced in 3.2.1, are well representative of a real-life commercial automotive simulation, yet the smaller complexity of the model makes its use and process demonstration far more accessible and practical. The All-Terrain Vehicle project represents an ideal initial workbench to demonstrate and compare accelerated fatigue simulation reduction techniques.

In this chapter representative events are dynamically solved and the relevant stress histories are used in the ensuing fatigue calculations. A detailed description durability schedule is included in Appendix B.3.

6.1.1 Baseline simulations

The *baseline* high fidelity analysis is defined as the reference fatigue simulation process where no accelerated fatigue simplification is enforced. The 112 solution time histories are considered in full and the vehicle frame is submitted to a standard *S-N* solver using common solution practices based on linear damage summation and rainflow cycle

counting. A uniaxial critical plane method (2.2.5) is chosen as combination parameter and the local direct surface stress is calculated at 10 degree critical plane rotation increments, resulting in 18 full fatigue calculations for each FE location.

The tubular frame is welded together, with the joints representing a natural weakness for fatigue. In order to make the assessment more realistic, an average strength weld class [63] is assigned to the model, resulting in added conservativeness in any non-welded area. All the fatigue calculations are performed with the established commercial code MSC Fatigue™ [68] based on nCode® DTLIB™ solver library [118] using methods and settings that are commonly available in all commercial fatigue solvers. The baseline Fatigue analysis settings are summarized in Table 13.

Table 13. All-Terrain Vehicle baseline fatigue analysis settings

Baseline fatigue analysis settings	
Method	<i>S-N</i>
FE result location	28433 Elements (top and bottom layer)
<i>S-N</i> fatigue dataset	Steel BS7608 Class F
Tensor Type	Stress
Stress units	Mpa
Stress combination parameter	Surface critical plane solutions (18 angles)
Mean stress correction	Goodman

6.2 Single event accelerated fatigue methods

The single event comprising 580 seconds of *Aggressive Hillwork* run, AH600, is investigated. The common concepts and practices for fatigue simulation acceleration are described in chapter 2.2.10 and demonstrated in chapter 3. The speed and accuracy performances of the proposed a priori hotspot algorithm are compared with common multiple-pass methods (2.2.11). Hereafter the relevant variations of the methods with applicable parameters are briefly introduced and demonstrated.

6.2.1 Peak-valley and *first pass* fatigue analysis

As described in 2.2.10.2, peak-valley valley gating is a simple and convenient way to eliminate less damaging parts of the loading signal. The gating can be defined in terms of a percent threshold to peak value and is applied simultaneously on each loading channel.

Table 14 provides a summary of the problem size and the solution time reductions

obtained for the *Aggressive Hillwork* event. The high fidelity unfiltered run is compared with runs of respectively 10% and 90% peak-valley gating.

Table 14. Solution time acceleration for single *Aggressive Hillwork* event with peak-valley gating respectively at 10% and 90% of maximum range

number of FE entities	No. of channels	peak-valley (% range gating)	channel size (points)	solution elapsed time (s)	normalized Solution time
28433 x 2	118	0.0%	290,000	3827	1.00
28433 x 2	118	10%	108,692	1010	0.28
28433 x 2	118	90%	4,812	53	0.01

The diagram in Figure 6-1 presents the top 500 damaged element in a baseline and unfiltered analysis are compared with equivalent peak-valley analyses with gating respectively at 90% and 10% of maximum range. A monotonic growth is obtained by ordering the result locations in order of increasing life. No discernible difference is observed between the 10% peak-valley and the original unfiltered results, whilst the life estimation for the 90% gating analysis is overestimated by a factor that is approximately a constant shift in logarithmic scale. The latter filtering error is an example of *Error-Type I* according to the classification proposed in 3.2.3.

The collective damage index histograms in Figure 6-2 provide a precise quantification of the approximation resulting from peak-valley filtering for a given model fraction.

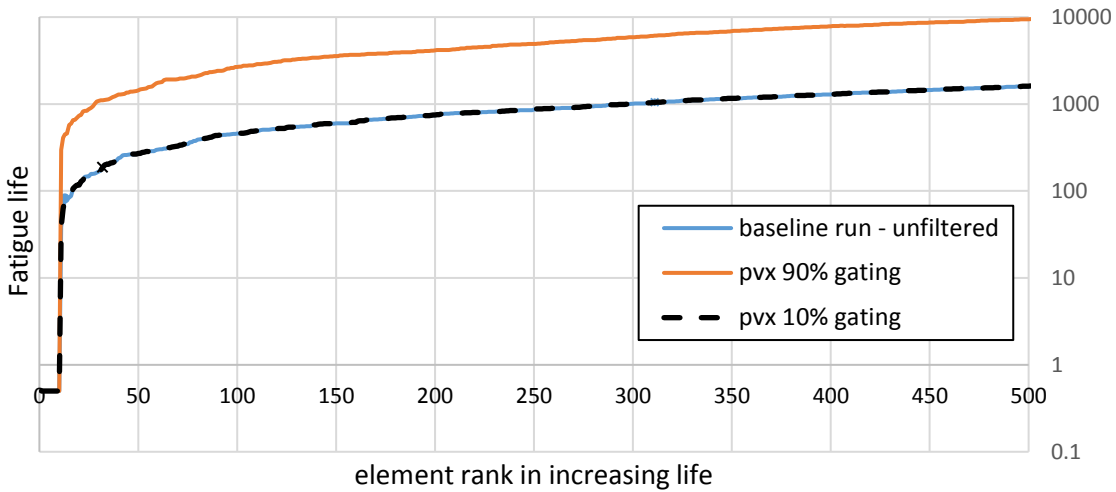


Figure 6-1. Fatigue life with Elements in order of decreasing damage for the single Aggressive Hillwork event, comparing unfiltered baseline to results after peak-valley filtering at 10% and 90% of maximum range [24].

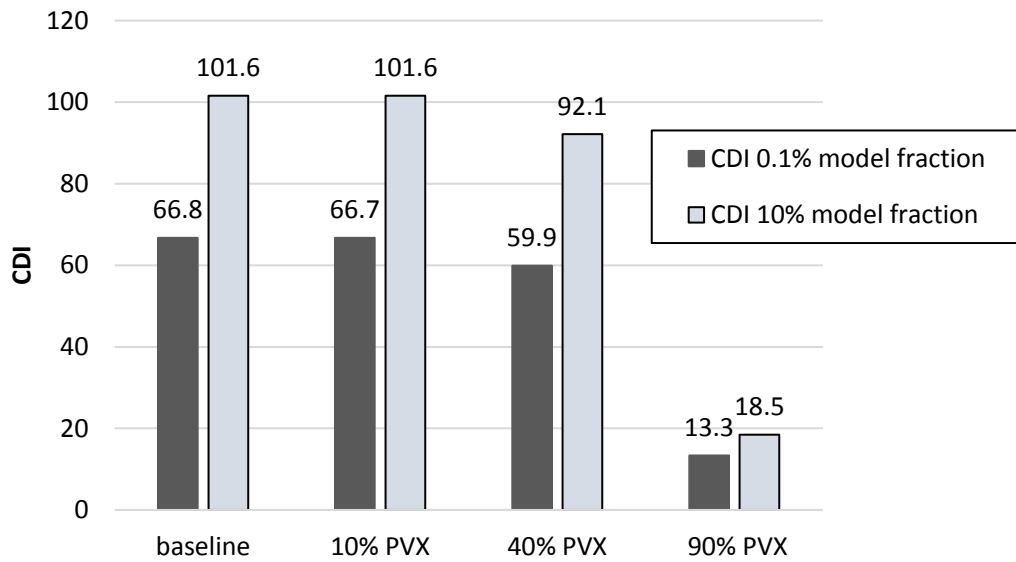


Figure 6-2. Collective damage index, $CDI\%$, at .1% and 10% mode fraction for unfiltered baseline analysis vs. different levels of peak-valley gating (PVX).

In summary, a low 10% gating yields a considerable solution acceleration (72% reduction in solution time) with virtually absence of error. A higher 90% gating reduces drastically the time signal, resulting in an extremely fast solution (99% reduction in solution time) but sensibly underestimates the fatigue damage (*Error-Type I*).

6.2.2 Accelerated fatigue methods comparison

The speed and accuracy performances of the proposed a priori hotspot algorithm are compared with common multiple-pass methods (2.2.11). In Figure 6-3 the solution run time is normalized according to a baseline run obtained in absence of any entity filtering. The hotspot acceleration factor is demonstrated for strain energy density (SED) threshold values of 65% and 80%, resulting in 5.3% and 2.7% model fractions. For the chosen single event the solution acceleration is simply determined by the model fraction retained by the filtering method, hence the a priori filtering at 5.3% and 2.7% are just behind the top performers at 1% model retention. With multiple events the efficiency of the two-step approaches is expected to decrease, as each event requires its own incremental first pass search. By contrast the a priori filtering, based on a one-off hotspot search, is insensitive to the number of events to be processed.

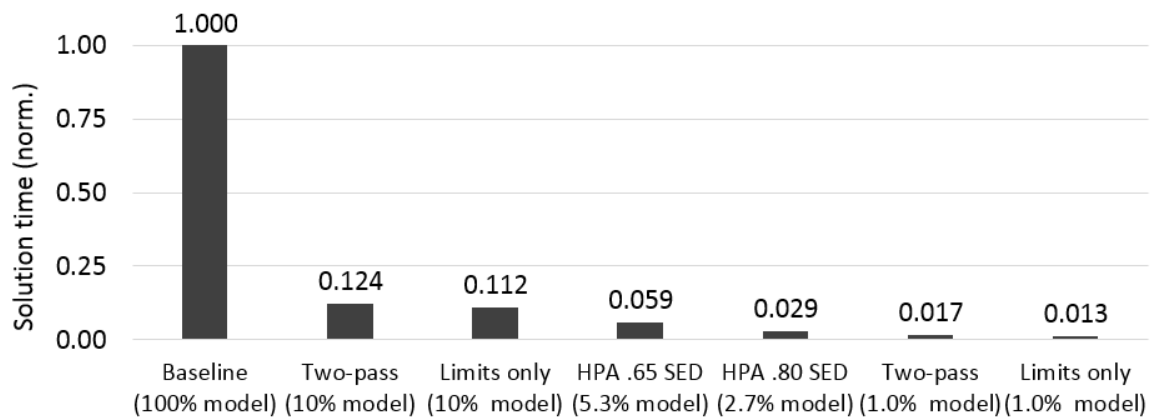


Figure 6-3. Baseline normalized solution time according to Two-pass, Limits only and hotspot prediction (HPA).

Figure 6-4 shows the results of the hotspot algorithm in comparison to the common solution acceleration techniques. The a priori hotspot method (continuous red line) shows an improved capacity to identify critical region compared to *limits only* with 1% retention, but worse than any other methods presented.

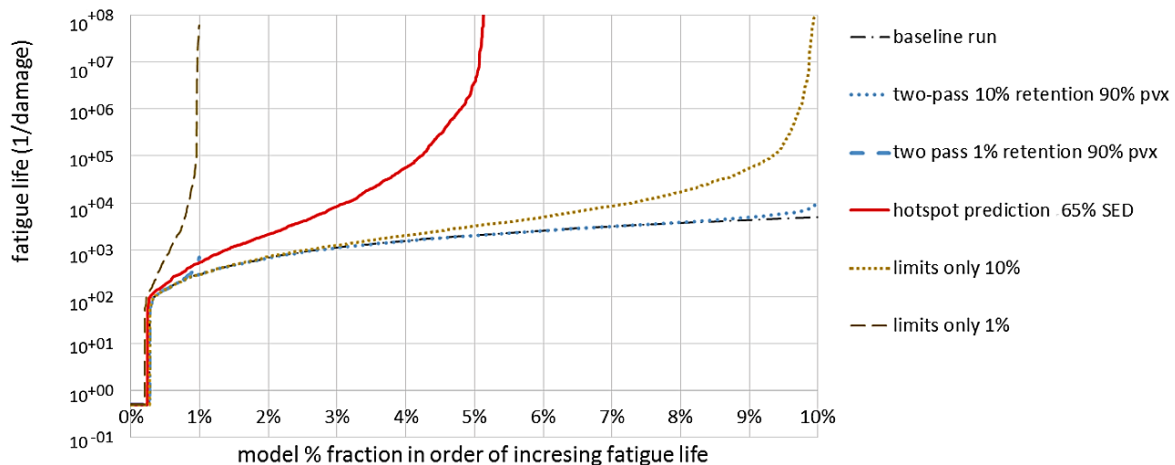


Figure 6-4. Fatigue life vs. model fraction for Stress based hotspot at 65% from peak strain energy density filtering compared to alternative methods.

A close observation of the highest damage locations (top 1% in Figure 6-5) reveals that a few top damaged locations, including some with life below 1 repetition, appear to have been missed by the hotspot algorithm. Despite the improvement over the 1% *limits only* method, a closer investigation to the reason behind the missed locations is required.

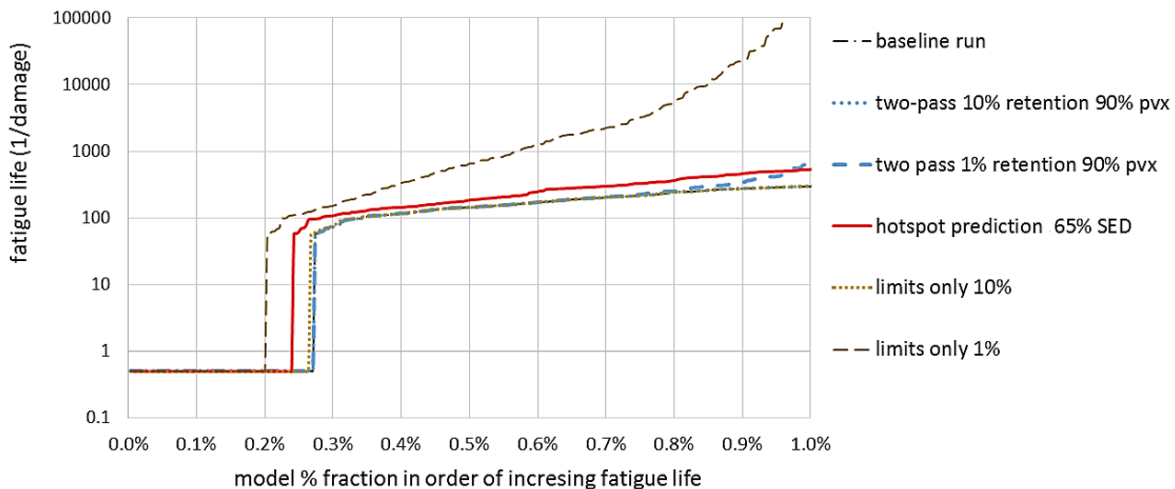


Figure 6-5. Top 1% damaged locations, fatigue life vs. model fraction for Stress based hotspot filtering compared to alternative methods.

In Figure 6-6 the fatigue life of the most damaged elements is presented in order of element ID number. Due to the customary contiguity of FE elements with progressive numbering, the image represents the hotspots areas as vertical clusters. Comparing the unfiltered baseline and HPA fatigue results indicates one critical area (boxed area in Figure 6-6) that is clearly missed. The missed area can be retraced on the FE geometrical

model in Figure 6-7, where the baseline calculated critical areas (shaded elements) are presented alongside the predicted hotspots (dark wireframe elements). The insert close-up image in Figure 6-7 describe the missed hotspot, an area remote from the attachment points and possibly escaped due to the approximation of the hotspot filtering criterion.

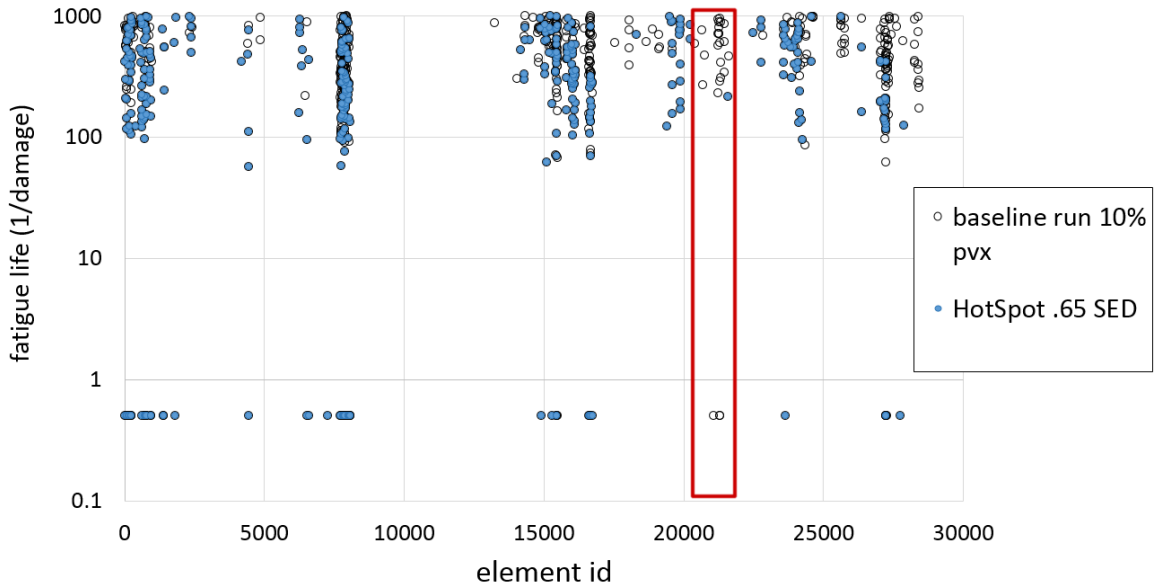


Figure 6-6. Fatigue life for top damaged elements represented in order of element ID. Boxed area points to missed hotspot [24].

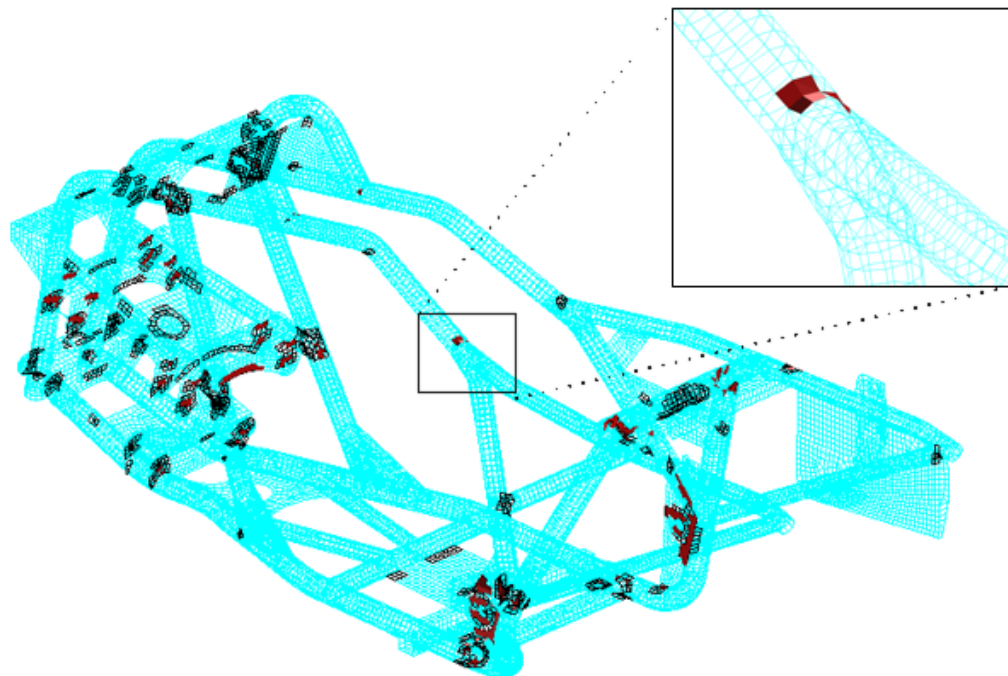


Figure 6-7. Calculated critical elements (red shade) over predicted hotspots (dark wireframe). The insert close-up highlights a missed hotspot [24]. Patran® image.

In Table 15 the strain energy density, SED, thresholds at 65% and 80% are tested against a hotspot prior prevalence of 1%, 2% and 3%. For all cases the increased posterior probability and high likelihood ratio are indicative of the positive diagnostic capacity of the prediction method. Solutions with greater hit rate are preferable, however the higher hit rate is reached at the expenses of the efficiency (false positive rate). For comparable levels of hit rate, the likelihood ratio provides an indicative measure of the computational costs associated to the prediction thus providing a useful term for quality comparison.

Table 15. Hotspot prediction assessment via contingency tables with varying assumed prevalence for Aggressive Hillwork event [24]

Case	prevalence (prior prob.)	SED % (filter)	P(D) (hit rate)	P(D H) (post. prob.)	P(H D)	P(D H') (false pos. rate)	$\frac{P(D H)}{P(D H')}$ (likelihood ratio)
AH600-A	.01	65%	.053	.70	.13	.046	15.03
AH600-B	.02	65%	.053	.52	.20	.043	12.00
AH600-C	.03	65%	.053	.49	.28	.039	12.61
AH600-D	.01	80%	.027	.45	.17	.023	19.98
AH600-E	.02	80%	.027	.35	.26	.020	17.33
AH600-F	.03	80%	.027	.29	.32	.019	15.48

6.3 Duty cycle accelerated fatigue methods comparison

A duty cycle analysis comprising 6 main events from the events schedule (appendix B.3, Table 28) is performed with the aim to check the accelerated fatigue simulation performances in a more computational demanding environment. The six events, chosen through load pre-screening, are presented in Table 16 alongside their respective number of passes per fatigue life.

Table 16. Fatigue durability schedule for duty cycle simulation [109]

event number	description	passes per life
1	Low speed loop	100
4	Hillwork with snow	60
5	Aggressive hillwork	60
11	Bump course 2 CW	70
17	Recreational run	100
19	Flat off-road CCW	175

Figure 6-8 presents the top damaged elements for different acceleration methods, comparing limits only, two-pass and hotspot prediction algorithm. The retained model fraction for the limits only and two-pass method is arbitrarily set at 5% and 1% of the model. The hotspot retained model fraction is shown at 5.3% and 2.7%, resulting from strain energy density (SED) thresholds values respectively of 65% and 80%.

From this qualitative assessment, as seen for the single event, the a priori hotspot method appear to shows an improved capacity to identify critical region compared to *limits only* with 1% retention, but worse than the two-pass method.

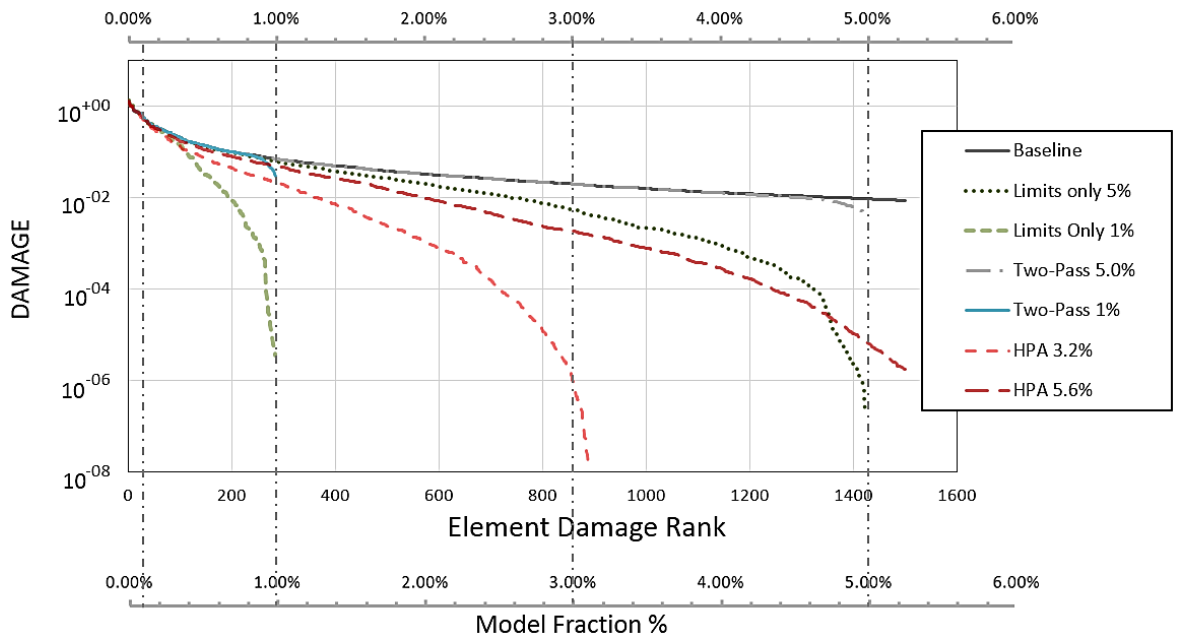


Figure 6-8. Duty cycle analysis: top damaged elements for the different acceleration method considered.

In Table 17 the contingency tables for the acceleration method considered in Figure 6-8 are listed for 3 levels of assumed prior prevalence. The contingency tables provide a precise quantification of the respective performances both in terms of capability to detect hotspots (true positive rate) and in the associated efficiency (false positive rate).

Table 17. Contingency tables for duty cycle analysis comparing limits only, two-pass and hotspot prediction algorithm (HPA)

	Limits only	Limits only	Two-pass	Two-pass	HPA	HPA
	<i>retained model fraction %</i>					
	5.0%	1.0%	5.0%	1.0%	3.2%	5.6%
<i>prior % (prevalence)</i>		<i>true positive rate (TPR)</i>				
1%	0.91	0.44	1.00	0.90	0.53	0.76
2%	0.76	0.26	1.00	0.50	0.40	0.62
3%	0.68	0.20	1.00	0.33	0.34	0.54
<i>prior % (prevalence)</i>		<i>false positive rate (FPR)</i>				
1%	0.041	0.006	0.040	0.001	0.027	0.049
2%	0.035	0.005	0.031	0.000	0.024	0.045
3%	0.031	0.004	0.021	0.000	0.022	0.041
<i>prior % (prevalence)</i>		<i>likelihood ratio (TPR/FPR)</i>				
1%	22.07	77.92	24.74	943.44	19.82	15.53
2%	21.58	51.81	32.76	6904.79	16.61	13.74
3%	22.08	47.52	48.47	Infinite	15.69	12.98
<i>prior % (prevalence)</i>		<i>posterior probability</i>				
1%	0.18	0.44	0.20	0.91	0.17	0.14
2%	0.31	0.51	0.40	0.99	0.25	0.22
3%	0.41	0.60	0.60	1.00	0.33	0.29

The quantitative picture is further improved by the collective damage indexes in Figure 6-9 and normalized CDI index in Figure 6-10. The *CDI%* value gives an exact measure of importance of the neglected hotspots, which in turn might be attributed a different weight depending on the design cycle phase.

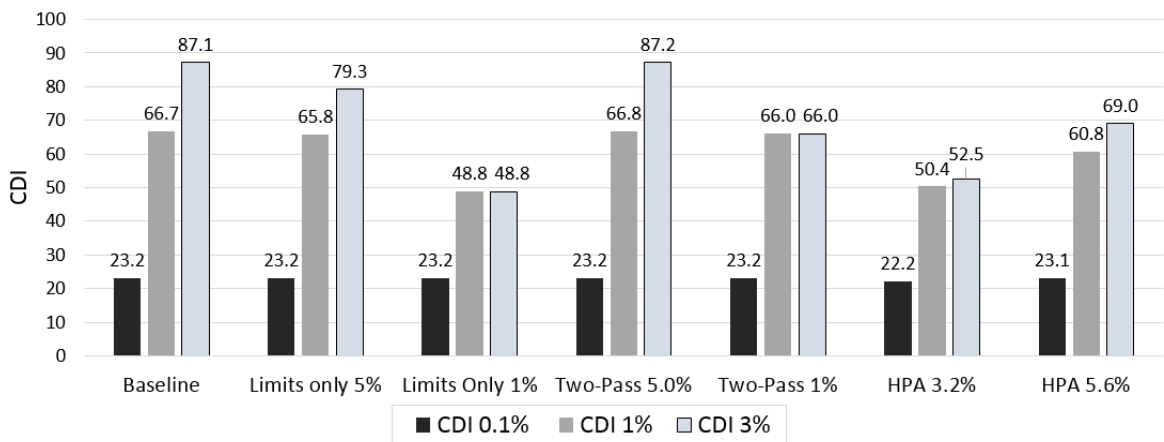


Figure 6-9. Collective damage index, CDI, for All-Terrain Vehicle Duty Cycle case obtained at 0.1%, 1% and 3% model fraction, for different accelerated fatigue simulation methods.

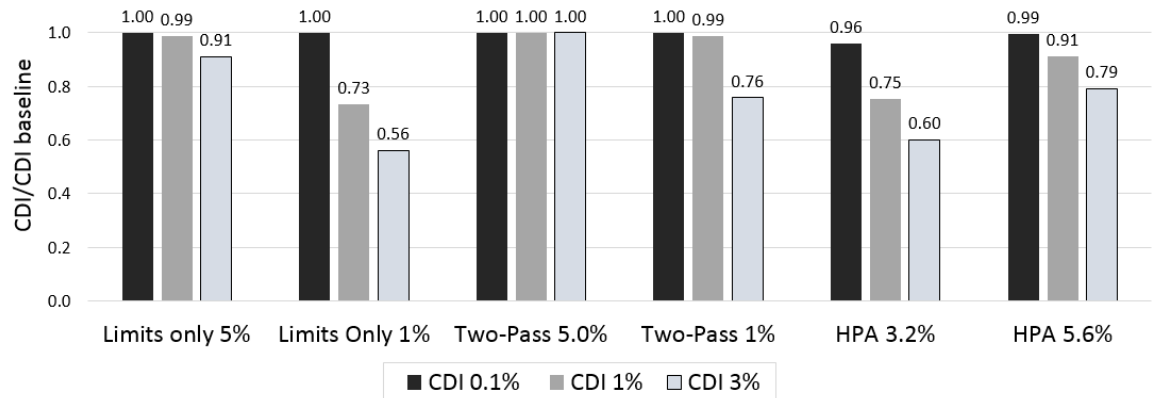


Figure 6-10. Normalized collective damage index, CDI, for All-Terrain Vehicle Duty Cycle case obtained at 0.1%, 1% and 3% model fraction, for different accelerated fatigue simulation methods.

Lastly, additional insight can be obtained extracting damage statistics related to the collective damage index calculation, as reported in Table 18. The additional parameters, such as the average and maximum damage could be used to improve the robustness of automated procedures, as in the case of optimization algorithms.

Table 18. All-Terrain Vehicle collective damage index, CDI, statistics for duty cycle analysis

	Baseline	Limits Only		Two-Pass		HPA	
	retained model fraction %						
	100%	5.0%	1.0%	5.0%	1.0%	3.2%	5.6%
CDI 0.1%	23.18	23.18	23.18	23.18	23.18	22.21	23.06
average damage	0.83	0.83	0.83	0.83	0.83	0.79	0.82
max damage	1.29	1.29	1.29	1.29	1.29	1.29	1.29
S.D. damage	0.19	0.19	0.19	0.19	0.19	0.21	0.20
CDI 1.0%	66.74	65.80	48.85	66.76	66.00	50.37	60.82
average damage	0.24	0.23	0.17	0.24	0.23	0.18	0.21
max damage	1.29	1.29	1.29	1.29	1.29	1.29	1.29
S.D. damage	0.23	0.23	0.26	0.23	0.23	0.24	0.24
CDI 3.0%	87.15	79.30	48.85	87.17	66.00	52.48	69.04
average damage	0.10	0.09	0.06	0.10	0.08	0.06	0.08
max damage	1.29	1.29	1.29	1.29	1.29	1.29	1.29
S.D. damage	0.16	0.17	0.17	0.16	0.17	0.16	0.17
CDI 5.0%	94.65	80.10	48.85	94.33	66.00	52.48	69.32
average damage	0.07	0.06	0.03	0.07	0.05	0.04	0.05
max damage	1.29	1.29	1.29	1.29	1.29	1.29	1.29
S.D. damage	0.13	0.14	0.13	0.13	0.14	0.13	0.13
CDI 100.0%	105.82	80.10	48.85	94.33	66.00	52.48	69.32
average damage	0.004	0.003	0.002	0.003	0.002	0.002	0.002
max damage	1.29	1.29	1.29	1.29	1.29	1.29	1.29
S.D. damage	0.03	0.03	0.03	0.03	0.03	0.03	0.03

6.4 Summary and conclusions

An All-Terrain Vehicle simulation test case provides the necessary complexity needed to evaluate the performances of the method in a realistic industrial environment and in comparison with established practices. Both a single event and multiple events cases, duty-cycle in automotive terminology, are addressed.

The effectiveness and significance of the proposed accelerated simulation metrics are successfully demonstrated for this realistic industrial application.

The results of different filtering settings have been successfully assessed by the proposed metrics. The contingency tables used in diagnostic tests, provide direct and simple means of quantifying and comparing the efficiency and the accuracy of the accelerated fatigue simulation method.

The proposed collective damage index, CDI, statistics can precisely quantify the impact on the accrued damage deriving from the filtering approximation. The $CDI\%$ value gives an exact measure of importance of the neglected hotspots, which in turn might be attributed a different weight depending on the design cycle phase. The additional parameters, such as the average and maximum damage could be used to improve the robustness of automated procedures, as in optimization algorithms.

For the case considered, the solution acceleration is mostly determined by the model fraction retained by the filtering method, hence the a priori filtering is not particularly advantageous with respect of the top performer two-pass method. However, as described with targeted examples in chapter 5, this is highly case dependent. Moreover, with multiple events, or in recursive optimization loops, the efficiency of the two-step approaches is expected to decrease, as each event requires its own incremental first pass search. By contrast the a priori filtering, based on a one-off hotspot search, is insensitive to the number of events to be processed. In these conditions, the a priori technique could lead to potential benefits, especially in the early phases of the durability design cycle, where uncertainties are higher.

Chapter 7: Conclusions

7.1 Summary

This thesis has been dedicated to the investigation of accelerated fatigue simulation techniques by means of model filtering, with the aim of assisting the solution of large numerical fatigue problems typical of industrial mechanical structures. Perhaps due to the applied nature of the topic, the available research is limited and the fatigue analyst may resource to simplification criteria that are based on experience, and without better indication with regard to the risks and benefits of the applicable procedure. Yet, large interests and values are at stake, considering the risk of a design recall or the possibility of accelerating the design cycle leading to immediate cost benefits.

With the aim of designing and exploring the applicability and merits of a novel a priori filtering method, the field of investigation has been re-organized and structured with

- acceleration methods classification;
- definition of error types;
- design and testing of the applicable metrics and related indexes;
- dedicated graphical and tabulated representations assisting with the presentation and interpretation of the results.

The collective deployment of the presented tools and practices constitute a framework where present or future variants of accelerated fatigue simulation methods can be investigated and compared.

The investigation focused on the applicability and merits of accelerated simulation procedures aimed at the fast identification of a subset of critical regions, also known as hotspots. The work presents the theory and a numerical validation study in support to a novel method for the identification of fatigue hotspots, to be determined prior to entering the time domain problem.

The a priori method is essentially a one-off filtering and sorting capability that is applied before running the transient events. The filtering can be based on peak stress thresholds obtained from statically applied loads and/or modal stresses obtained from modal

analysis (performed offline with respect to the dynamic simulation). The aim is to eliminate low stress areas and prioritize the remaining critical locations.

An original statistical assessment of risks and benefits in fatigue simulation acceleration provides the means for damage prediction quantification and comparison.

The proposed a priori technique is inherently more approximate than traditional on-line filtering methods, however it could lead to potential benefit in time saving, especially in early phases of the durability design, with demanding optimization cycles, or as a complement to traditional filtering to increase robustness in uncertain loading scenarios.

Selected industries (e.g. transport, aero, energy etc.) could immediately deploy some of the proposed techniques for the purpose of determining the best strategy between accuracy and computational costs, or simply to better assess the risk and error margin deriving from accelerated fatigue simulation.

7.2 Key findings

7.2.1 Simulation acceleration errors and metrics

The investigation addressed the general underlying hypotheses, limitations and potential errors in the application of accelerated fatigue simulation.

The novel classification of the error types is based on the identified four separate sources of approximations: damage value, damage rank, hit rate and false positives, respectively termed Error-Type I through IV.

A complete set of specific metrics is proposed, aimed at targeting all potential errors and sources of inefficiencies, thus establishing wider reaching terms of comparison than a simple simulation acceleration factor based on the elapsed solution time.

Considering the inherent unknowns and approximations in the filtering methodology, a quantification of the prediction quality is only attainable in statistical terms. In this study the analogy is made between a medical test with dichotomous outcome (predicted illness or otherwise absence of illness) and fatigue damage prognosis (likely hotspot or otherwise safe area) according to the hotspot prediction technique.

The reliability of the prediction can be directly expressed by the success rate (*true positive rate* or *TPR*). Likewise the rate of false positives (*FPR*) gives an indication of the efficiency of the calculation. Finally the ratio of *TPR* and *FPR*, the *likelihood ratio*, combines both reliability and efficiency in a single parameter and represents the usefulness or *diagnostic capacity* of the prediction method.

A novel *collective damage index*, CDI, represents the combined damage accumulation for the top damaged elements. The collective damage index, as well as its derived quantities such as max damage, average and standard deviation, can inform the user analyst about the exact level of filtering required for a given accuracy. The collective damage index leads to a more robust and less conservative assessment with respect to fixed a priori thresholds or single location calculations.

7.2.2 Analytical models of beams and plates in bending

The onset and predictability of fatigue critical areas was investigated for simply supported beams and plates in bending.

In the simplest case of a single harmonic loading, given the location of the force, the peak stresses are highly predictable for most frequency ranges. Yet, the response in narrow transition ranges approaching natural frequencies are less predictable. Likewise, certain combinations of loads and excitation frequency can shift the position away from the maxima in the response due to the individual loads. However, under common loading conditions, and limiting to the cases of interest of high dynamic amplification typical of lightly damped structures, the system response will tend to favour load paths that are predictable, over more extreme combinations. The presence of stress concentrations will provide additional predictability derived from the stress multipliers, and its power-law regulated effects to the fatigue damage.

The a priori filtering technique carries a risk of neglecting fatigue critical entities, Error-Type III, deriving from a combination of responses. The approach is therefore to control the margin of error through dedicated error metrics.

The statistical measures expressed in a contingency table provide valid means to assess and quantify the reliability and the efficiency of the prediction method.

A reliable prediction is one in which all critical hotspots have been identified, regardless of the amount of false positives, the latter being relevant to the efficiency and practical value of the method.

7.2.3 FE simulation of thin plates

The proposed a priori model filtering is formalized and coded in MATLAB® programming environment, in combination with the off-the-shelf FE solutions. The process is generally applicable to FE-based fatigue analysis using the pseudostatic and modal superposition approaches, where the Craig-Bampton method is proposed as a primary basis for hotspot prediction. Although component-mode synthesis is not exclusively used in conjunction with multibody systems dynamics, the integrated FE and multibody simulation is an ideal target for the accelerated fatigue process.

The a priori prediction is initially tested with the familiar rectangular plate, dynamically excited via base motion. In a second case, the frequency and position of a concentrated load are chosen to approximate the hotspot conditions observed in the transition area between the static response and the first natural mode. In both cases the performances of the a priori prediction was satisfactory, however the simplicity of the modelling and loading negatively affects the efficiency of the discoveries, as indicated by a relatively high false positive rate (*FPR*).

The results of different filtering settings have been successfully assessed by the proposed metrics. The contingency tables used in diagnostic tests, with the accompanying *receiver operating characteristics diagrams*, ROC space, provide direct and simple means of quantifying and comparing the efficiency and the accuracy of any accelerated fatigue simulation method. Different thresholds of model elimination, under variable assumed fatigue damage prevalence, can be inspected and compared.

The proposed collective damage index, CDI, statistics can precisely quantify the impact on the accrued damage deriving from the filtering approximation. At a low $CDI_{0.1\%}$ the observed approximation was generally minimal, suggesting that if only a few highly damaged locations are required (e.g. early design cycles) the a priori hotspot prediction method can be safely applied. Conversely, with the intention to capture a 1% model

fraction (of damage *prevalence*), the CDI result might indicate that at least 3% of model retention should be considered.

7.2.4 FE simulation of thin L-plates

The L-plates in Test Case 3 and 4, were crafted specifically to exemplify the possible adverse effect of peak-valley gating in certain loading combinations, where fewer load spikes can obscure a high number of damaging cycles. Such load spikes may be an actual test occurrence (pot hole, carb strike, unusual landing etc.) or they could be a hard-to-detect signal acquisition error.

Whether the load spike is real or not, the results of the online methods are “biased” by its presence, with consequential potential errors in damage ranking and prioritization. In such realistic conditions the a priori identification performs decisively better than traditional online methods. The possible occurrence of the described scenario, an isolated load spike obscuring relevant parts of the signal, should be carefully considered in a robust accelerated fatigue simulation process, perhaps suggesting to combine the benefits of a priori and online filtering.

Test Case 4, a perforated L-plate, was designed to investigate the effect on a priori prediction of randomly distributed stress concentrations around geometrical features. This preliminary result showed a potential improvement in terms of *TPR* (hit rate) but a negative effect on the overall efficiency due to the increase in *FPR* (false discoveries) with many stress riser not constituting an actual fatigue threat.

7.2.5 All-Terrain Vehicle single and duty-cycle simulation

An All-Terrain Vehicle simulation test case provides the necessary complexity needed to evaluate the performances of the method in a realistic industrial environment and in comparison with established practices. Both a single event and a multiple events cases, duty-cycle in automotive terminology, are addressed.

The effectiveness and significance of the proposed accelerated simulation metrics are successfully demonstrated also for these realistic industrial applications.

The proposed collective damage index, CDI, statistics can precisely quantify the impact on the accrued damage deriving from the filtering approximation. The additional parameters, such as the average and maximum damage can be used to improve the robustness of automated procedures, as in the case of optimization algorithms.

The investigation observed that in conditions of well-defined and reliable loads, the accelerated simulation based on two-pass method led to better overall performances.

For the case considered the solution acceleration is mostly determined by the model fraction retained by the filtering method, hence the *a priori* filtering is not particularly advantageous with respect of the top performer two-pass method. However, as demonstrated with targeted examples in chapter 5, this is highly case dependent. With multiple events, or in recursive optimization loops, the efficiency of the two-step approaches is expected to decrease, as each event requires its own incremental first pass search. By contrast the *a priori* filtering, based on a one-off hotspot search, is insensitive to the number of events to be processed.

7.3 Key Contributions to new knowledge

The main original contribution is the design and application of a novel hotspot prediction algorithm based on automatic reduction in physically representative critical subgroups, or hotspots, by virtue of *a priori* screening of critical areas using local parameters extracted from static and modal vectors.

Principal characteristics of the proposed novel prediction method are the automatic *a priori* screening approach, i.e. prior to solve the transient problem, the model organization in physically representative hotspot sub-regions, the use of modal strain energy density thresholds as means of identifying the regions, the quantification assessment in determining accuracy and efficiency of the method as well as the sensitivity to key parameters affecting the prediction.

Accordingly, the research also provided a general framework applicable to the assessment of prediction accuracy and efficiency for similar current and future fatigue simulation acceleration methods or, equivalently, to the assessment of numerical prediction against experimental evidence.

In relation to the prediction method, the original contributions can be organized in the following groups:

- A general framework applicable to the assessment of prediction accuracy and efficiency for similar current and future fatigue simulation acceleration methods
- A novel classification of the error types is based on the identified four separate sources of approximations: damage value, damage rank, hit rate, false positives.
- A novel *collective damage index*, CDI, representing the collective damage accumulation for the top damaged elements, leading to a more robust and less conservative assessment of the filtering thresholds.
- Demonstration of the proposed a priori method starting from simple repeatable analytical models, progressing to schematic FE examples and culminating with full-scale applications.
- Design and application of diagnostic testing techniques, based on contingency tables and receiver operating characteristics diagrams, dedicated to the description of the relationship between solution acceleration, prediction error bounds and efficiency.

Additional minor original contributions in other areas include:

- Classification and mapping of the known fatigue simulation acceleration practices.
- Investigation of the effect of small-load-omission criterion (gating) on element damage order error.
- An evidenced-based approach for the assessment of acceptable levels of small load omission thresholds, using convergence study with increased levels of gating to control damage error.
- Static and dynamic numerical implementations of Euler-Bernoulli (beam in bending) and Kirchhoff-Love (plate in bending) theories, including static correction, correlation with FE modelling, demonstrating a different convergence ratio in displacement and stresses-strains, with sensitivity to modal truncation, load patch size and damping.

7.4 Areas for research continuation

The investigation covered one particular technique, the a priori hotspot prediction, for which the effects and risks were not fully understood. Although some useful conclusions

could be drawn with regard to its potential use and applicability, other avenues of possible research have been identified and may be considered of interest both for academic or industrial applications.

7.4.1 A priori prediction with Bayesian update

A Bayesian framework allows to formalize the problem of hotspot detection in accelerated fatigue techniques.

In this investigation the criteria for identification of hotspot locations was based on a simple dichotomous statistical event (hotspot or not) which could be represented with simple Bernoulli probability function for each component mode.

In an updated Bayesian framework, the prior probability, so far treated as a fixed prevalence, could now be updated with sampling from very limited portions of the load data. Such approach would potentially overcome the latent risk of load bias affecting two-pass methods, while simultaneously improve the efficiency of the a priori retention.

Furthermore, in a Bayesian framework the prior probability can also be used to convey, with consistent mathematical rigour, any additional prior knowledge or risk factor related to the position of interest (weld, corner, fillet, corrosive environment etc.).

7.4.2 Accelerated fatigue simulation with hybrid online-offline filtering

The investigation observed that in conditions of well-defined and reliable loads, the accelerated simulation based on two-pass method generally led to better performances. Yet the a priori logic could lead to further incremental acceleration by using the high *specificity*, (defined as $1-FPR$), capable of eliminating considerable portion of the model that are very unlikely to develop fatigue damage. An investigation into the combined effect of a priori and online might possibly lead to much improved performances while minimizing the risk of missing fatigue hotspots (false negatives).

7.4.3 Accelerated fatigue simulation based on load sampling

An assessment on the quality of the hotspot identification can only be done once a reference result is known. When reference results are not known, assumptions are inevitably made with regard to the applicable filtering method and threshold. This means

that posterior error consistency checks should follow the prediction. If the errors are excessive, the analysis should be repeated with more conservative settings.

One possible alternative is to operate a statistical sampling on both the available loads and the model, to provide an estimate of the error. A similar procedure was described in the present study for the determination of an acceptable lower gate in load filtering. However, this approach could also be used for the estimation of any other of the proposed metrics.

7.4.4 Other industrial applications for collective damage index

Comparing the collective damage index, CDI, calculated at different model fraction levels can give an indication of the fraction of the model contributing to the damage, as shown in chapter 3, Figure 3-6. The CDI could be used as a design variable in design optimization to drive automatic and robust design changes.

7.5 Closing remarks

The list of hypotheses at the beginning of the chapter 3 helped encapsulating the intended scope and applicability of the solution acceleration methods. Some of the hypotheses however can only be fully assessed with hindsight, as for example, the assumption that only a small percentage of the model is deemed of fatigue interest.

As much as all conditions and assumptions can be validated, the application and value of traditional *online* accelerated simulation methods is inextricably tied to availability and representativeness of the prescribed loads, as all the metrics are tied to a reference result, which is assumed correct and relevant. Evidently in many cases this could be far from a realistic assumption.

Such concerns would be particularly relevant where multiple events and large models are involved, when the attendant risks and advantages are not easily anticipated and solution acceleration application mostly relies on user experience and judgement.

By contrast, the principle of a priori filtering is one in which expected areas of stress concentrations (or strain, or strain energy) are retained independently of loads' time history availability (but load application point and type is assumed known) and therefore

offline with respect to the dynamic calculation, thus representing a useful complement if not an alternative to traditional methods.

The investigation covered one particular technique of *a priori* hotspot prediction, for which the application effects and inherent risks were not fully understood. Although some useful conclusions could be drawn with regard to its potential use and applicability, more research and especially more applications would allow to capture alternative usage scenario. Likewise, other avenues of possible research have been identified and may be considered of interest both for academic or industrial applications.

Appendices

Appendix A Analytical and FE solutions of simply supported plates and beams in bending

An analytical solution of thin, uniform simply supported straight beams and rectangular plates, subject to a concentrated force, is based on modal superposition [115] [116]. An original parametric frequency domain solution algorithm was written and executed in MATLAB® programming environment using the geometry and fundamental equations described in the following sections. The fundamental equations and the relevant stress and strain modal quantities are derived in appendix A.1 (simply supported beams) and A.2 (simply supported plates).

In appendix A.3 a selected analytical baseline validation model is compared against corresponding detailed FE models in order to establish the correctness and efficiency of both the analytical and numerical solutions.

Appendix A.4 addresses the solution sensitivity to factors affecting solution convergence and efficiency. The latter aspects are normally in antithesis and therefore need to be considered in detail before the model can be used with confidence. Increasing the number of retained solution modes proportionally affects the solution time, therefore a strong emphasis is given to the solution sensitivity on modal basis size in order to find the best compromise between efficiency and accuracy.

Table 19. Parameters description for uniform beam in bending

Quantity	Description
a	length in x
b	section dimension in y
h	section dimension in z
I	moment of cross sectional area
ρ	mass per unit volume
E	Young's modulus
F	transverse force
f_a	location of force F
η	proportional structural damping
$w(x)$	displacement in z direction

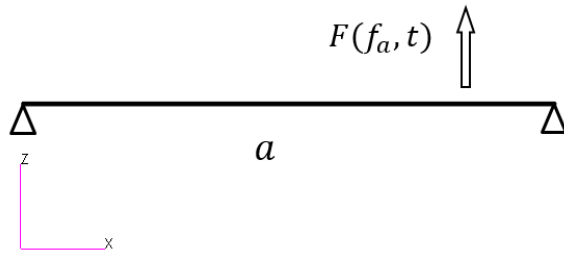


Figure A-1. Simply supported beam in bending with harmonic force F at $x=f_a$.

A.1 Bernoulli-Euler beam formulation and modal energy density definition

For the simply supported beam in bending in Figure A-1 the mass normalized modes are given by

$$W_m(x) = \sqrt{\frac{2}{\rho abh}} \sin \frac{m\pi x}{a} \quad m = 1, 2, \dots, \quad (\text{A.1})$$

and the corresponding natural frequencies are

$$\omega_m = \sqrt{\frac{EI}{\rho bh}} \left[\left(\frac{m\pi}{a} \right)^2 \right]^{1/2} \quad m = 1, 2, \dots. \quad (\text{A.2})$$

Considering u the displacement parallel to the unstretched middle axis, the strain x component is

$$\varepsilon_x = \frac{\partial u}{\partial x} = -z \frac{\partial^2 w}{\partial x^2} \quad (\text{A.3})$$

The modal strain energy density per beam unit length for mode m simplifies to

$$e_m(x) = \frac{EI}{\rho abh} \left(\frac{m\pi}{a} \right)^4 \left(\sin \frac{m\pi x}{a} \right)^2 \quad (\text{A.4})$$

Integrating (A.4) along the length of the beam leads to the expected total modal energy for mode m , assuming mass normalized modes, with natural modes (A.1), that is:

$$U_m = \frac{1}{2} \left\{ \sqrt{\frac{EI}{\rho bh}} \left[\left(\frac{m\pi}{a} \right)^2 \right] \right\}^2 = \frac{1}{2} \omega_m^2 \quad (\text{A.5})$$

Applying a time varying force at an arbitrary location, the resulting generalized force $N_m(t)$ is:

$$N_m(t) = \int_0^a W_m(x) F(x, t) dx \quad (A.6)$$

Assuming a point force via Dirac delta function $F(x, t) = F(t)\delta(x - f_a)$, equation (A.6) simplifies to

$$N_m(t) = F(t) \sqrt{\frac{2}{\rho abh}} \sin \frac{m\pi f_a}{a} \quad (A.7)$$

In equation (A.4), considering harmonic loading $F(t) = Fe^{i\omega t}$, and introducing η , constant proportional structural damping, the steady state modal coordinates q_m are obtained by convolution integral leading to

$$q_m(t) = \sqrt{\frac{2}{\rho abh}} \sin \frac{m\pi f_a}{a} Fe^{i\omega t} \frac{1}{\omega_m^2(1+i\eta) - \omega^2} \quad (A.8)$$

Summing all modal contributions in a modal expansion leads to the vertical response:

$$w(x, t) = \sum_{m=1}^{\infty} W_m(x) q_m(t) \quad (A.9)$$

Showing the dependency on application force (A.9) becomes:

$$w(x, f_a, t) = \frac{2}{\rho abh} \sum_{m=1}^{\infty} \sin \frac{m\pi x}{a} \sin \frac{m\pi f_a}{a} Fe^{i\omega t} \frac{1}{\omega_m^2(1+i\eta) - \omega^2}$$

The bending strains and stresses for a concentrated harmonic force applied at f_a are given by:

$$u = -z \frac{\partial w}{\partial x} \quad (A.10)$$

$$\varepsilon_x = \frac{\partial u}{\partial x} = \sum_{m=1}^{\infty} \frac{2z}{\rho abh} \left(\frac{m\pi}{a} \right)^2 \sin \frac{m\pi x}{a} \sin \frac{m\pi f_a}{a} Fe^{i\omega t} \frac{1}{\omega_m^2(1+i\eta) - \omega^2} \quad (A.11)$$

$$\sigma_x = E \varepsilon_x \quad (A.12)$$

The critical areas resulting from a force statically applied at position f_a are determined from the truncated modal summation and imposing a null frequency in eq. (A.11):

$$\sigma_x = \sum_{m=1}^{m=m_t} \frac{2zE}{\rho abh} \left(\frac{m\pi}{a} \right)^2 \sin \frac{m\pi x}{a} \sin \frac{m\pi f_a}{a} \frac{F}{\omega_m^2}, \quad (A.13)$$

where the modal truncation value m_t is obtained from convergence studies detailed in appendix A.4.

A.1.1 Beam in bending analytical and FE modal validation

The bending beam modes are checked against FE models. The chosen validation *baseline* model matches the description in Table 20.

Table 20. Uniform beam parameters for baseline model

quantity	dimension	description
a	250 mm	length in x
b	0.5 mm	section dimension in y
h	0.5 mm	section dimension in z
ρ	7800 Kg/m ³	mass per unit volume
E	210 GPa	Young's modulus
f_a	25.0 mm	load application point

In Table 21 the first 10 flexural modes of the baseline model are compared with 2 equivalent FE models constructed respectively with 4000 and 32000 solid elements (Nastran® CHEXA8 with 8 nodes). The frequencies are perfectly matched even with a relatively coarse model Figure A-2 depicts the first mode obtained with the refined 32K elements model. Figure A-3 shows a close up of the left support obtained with rigid multi point constraint in Nastran®, otherwise known as RBE2 rigid multi-point constraints, to ensure the beam endings rotate rigidly on the simple support.

Table 21. Uniform beam in bending, analytical and FE natural frequencies

Mode No.	Analytical (Hz)	MSC Nastran® (Hz) 4000 elements	% error	MSC Nastran® (Hz) 32000 elements	% error
1	18.823	18.823	0.001%	18.822	0.001%
2	75.291	75.289	0.002%	75.289	0.002%
3	169.404	169.396	0.005%	169.396	0.005%
4	301.163	301.137	0.009%	301.136	0.009%
5	470.567	470.504	0.013%	470.502	0.014%
6	677.617	677.486	0.019%	677.482	0.020%
7	922.312	922.070	0.026%	922.062	0.027%
8	1204.652	1204.240	0.034%	1204.227	0.035%
9	1524.638	1523.978	0.043%	1523.957	0.045%
10	1882.269	1881.263	0.053%	1881.231	0.055%

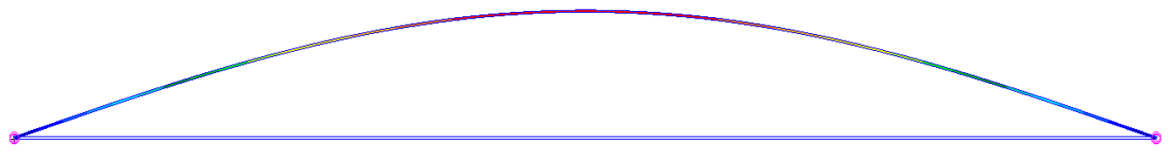


Figure A-2. First normal mode at 18.822 Hz, for FE model comprising 32000 elements. Image generated in Patran®.

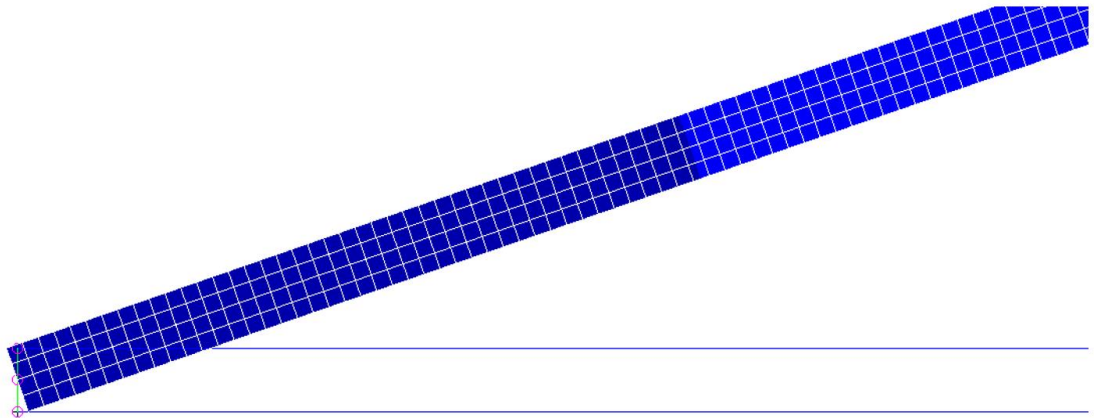


Figure A-3. First normal mode at 18.822 Hz, for FE model comprising 32000 elements. Detail of the left multi point constraint (MPC) obtained with Nastran® RBE2 elements. Image generated in Patran®.

A.2 Kirchhoff formulation for plate in bending and modal energy density definition

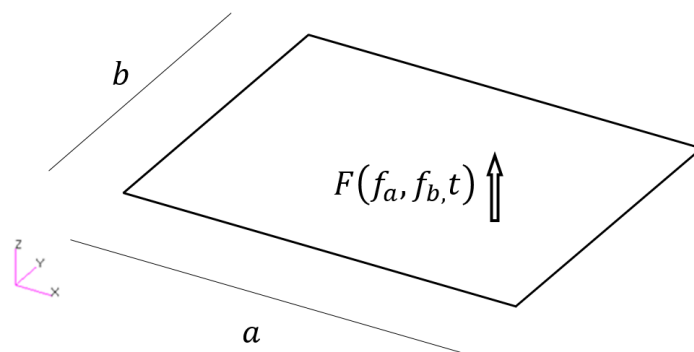


Figure A-4. Simply supported rectangular plate with point force F at $x=f_a$ and $y=f_b$.

Table 22. Uniform plate parametric geometry and physical properties

quantity	description
a	length x
b	length y
h	plate thickness
ρ	mass per unit volume
D	$\frac{Eh^3}{12(1-\nu^2)}$ flexural rigidity
F	transverse load
f_a	load location coordinate on x axis
f_b	load location coordinate on y axis
η	proportional structural damping
$w(x, y)$	displacement in z direction

The bending strain energy for the uniform plate in Figure A-4 is derived using classical thin plate theory [49], [116].

Considering the uniform rectangular plate in Figure A-4, with the properties described in Table 22. The mass normalized natural modes satisfying the boundary conditions are

$$W_{mn}(x, y) = \frac{2}{\sqrt{\rho abh}} \sin \frac{m\pi x}{a} \sin \frac{n\pi y}{b} \quad m, n = 1, 2, \dots, \quad (\text{A.14})$$

with corresponding natural frequencies of

$$\omega_{mn} = \pi^2 \sqrt{\frac{D}{\rho h}} \left[\left(\frac{m}{a} \right)^2 + \left(\frac{n}{b} \right)^2 \right] \quad m, n = 1, 2, \dots. \quad (\text{A.15})$$

Applying a time varying force, the generalized force N_{mn} is:

$$N_{mn}(t) = \int_0^a \int_0^b w_{mn}(x, y) F(x, y, t) dx dy \quad (\text{A.16})$$

Assuming a point force via Dirac delta function $F(x, y, t) = F(t) \delta(x - f_a)(y - f_b)$, equation (A.16) simplifies to:

$$N_{mn}(t) = \frac{2F(t)}{\sqrt{\rho abh}} \sin \frac{m\pi f_a}{a} \sin \frac{n\pi f_b}{b} \quad (\text{A.17})$$

In equation (A.17), considering harmonic loading $F(t) = F e^{i\omega t}$, and introducing η , constant structural damping, the steady state modal coordinates q_{mn} are obtained by the convolution integral leading to

$$q_{mn}(t) = \frac{2}{\sqrt{\rho abh}} \sin \frac{m\pi f_a}{a} \sin \frac{n\pi f_b}{b} F e^{i\omega t} \frac{1}{\omega_{mn}^2 (1+i\eta) - \omega^2} \quad (\text{A.18})$$

Summing all modal contributions in this modal expansion results in the vertical response at any (x, y) location as:

$$w(x, y, t) = \sum_{m=1}^{\infty} \sum_{n=1}^{\infty} W_{mn}(x, y) q_{mn}(t) , \quad (A.19)$$

Showing the dependency on the application force equation (A.19) becomes:

$$w(x, y, f_a, f_b, t) = \frac{4}{\rho a b h} \sum_{m=1}^{\infty} \sum_{n=1}^{\infty} \sin \frac{m \pi x}{a} \sin \frac{n \pi y}{b} \sin \frac{m \pi f_a}{a} \sin \frac{n \pi f_b}{b} F e^{i \omega t} \frac{1}{\omega_{mn}^2 (1 + i \eta) - \omega^2} \quad (\text{A.20})$$

The displacement parallel to the unstretched middle surface are

$$u(x, y, z) = -z \frac{\partial w}{\partial x}; \quad (\text{A.21})$$

$$v(x, y, z) = -z \frac{\partial w}{\partial y}.$$

The strain components are

$$\varepsilon_x = \frac{\partial u}{\partial x} = -z \frac{\partial^2 w}{\partial x^2};$$

$$\varepsilon_y = \frac{\partial v}{\partial x} = -z \frac{\partial^2 w}{\partial y^2}; \quad (\text{A.22})$$

$$\gamma_{xy} = \frac{\partial u}{\partial y} + \frac{\partial v}{\partial x} = -2z \frac{\partial^2 w}{\partial x \partial y};$$

$$\gamma_{xz} = \frac{\partial u}{\partial z} + \frac{\partial w}{\partial x} = 0, \quad \gamma_{yz} = \frac{\partial v}{\partial z} + \frac{\partial w}{\partial y} = 0.$$

Differentiating the vertical displacements in Eq. (A.20) and substituting in Eq. (A.22) leads to

$$\varepsilon_x = \sum_{m=1}^{\infty} \sum_{n=1}^{\infty} \frac{4z}{\rho abh} \left(\frac{m\pi}{a} \right)^2 \sin \frac{m\pi x}{a} \sin \frac{n\pi y}{b} \sin \frac{m\pi f_a}{a} \sin \frac{n\pi f_b}{b} F e^{i\omega t} \frac{1}{\omega_{mn}^2(1+i\eta) - \omega^2};$$

(A.23)

$$\varepsilon_y = \sum_{m=1}^{\infty} \sum_{n=1}^{\infty} \frac{4z}{\rho abh} \left(\frac{m\pi}{b} \right)^2 \sin \frac{m\pi x}{a} \sin \frac{n\pi y}{b} \sin \frac{m\pi f_a}{a} \sin \frac{n\pi f_b}{b} F e^{i\omega t} \frac{1}{\omega_{mn}^2 (1+i\eta) - \omega^2};$$

(A.24)

$$\gamma_{xy} = \sum_{m=1}^{\infty} \sum_{n=1}^{\infty} -\frac{8z}{\rho abh} \frac{mn\pi^2}{ab} \cos \frac{m\pi x}{a} \cos \frac{n\pi y}{b} \sin \frac{m\pi f_a}{a} \sin \frac{n\pi f_b}{b} F e^{i\omega t} \frac{1}{\omega_{mn}^2 (1+i\eta) - \omega^2}.$$

(A.25)

The bending stresses for an isotropic thin plate are obtained by using inverse *Navier* equations:

$$\sigma_x = -\frac{Ez}{1-\nu^2} \left[\frac{\partial^2 w}{\partial x^2} + \nu \frac{\partial^2 w}{\partial y^2} \right];$$

(A.26)

$$\sigma_y = -\frac{Ez}{1-\nu^2} \left[\frac{\partial^2 w}{\partial y^2} + \nu \frac{\partial^2 w}{\partial x^2} \right];$$

(A.27)

$$\tau_{xy} = -\frac{Ez}{1+\nu} \frac{\partial^2 w}{\partial x \partial y}.$$

(A.28)

The full expressions of the stress tensor follow naturally from equations (A.26-A.28) and are omitted here for brevity.

A.2.1 Modal strain energy density

The total deformation energy is the volume integral

$$U(t) = \frac{1}{2} \int_V (\sigma_x \varepsilon_x + \sigma_y \varepsilon_y + \tau_{xy} \gamma_{xy}) dV$$

(A.29)

For the bending plate considered, using relations (A.23-A.28), equation (A.29) becomes:

$$U(t) = \frac{1}{2} \int_V \left\{ \frac{Ez^2}{1-\nu^2} \left[\frac{\partial^2 w}{\partial x^2} + \nu \frac{\partial^2 w}{\partial y^2} \right] \frac{\partial^2 w}{\partial x^2} + \frac{Ez^2}{1-\nu^2} \left[\frac{\partial^2 w}{\partial y^2} + \nu \frac{\partial^2 w}{\partial x^2} \right] \frac{\partial^2 w}{\partial y^2} + 2 \frac{Ez^2}{1+\nu} \left[\frac{\partial^2 w}{\partial x \partial y} \right]^2 \right\} dV$$

(A.30)

Performing through the thickness integration $\int_{-h/2}^{h/2} dz$, equation (A.30) reduces to a surface integral

$$U(t) = \frac{1}{2} \iint_A \frac{h^3}{12} \left\{ \frac{E}{1-\nu^2} \left[\frac{\partial^2 w}{\partial x^2} + \nu \frac{\partial^2 w}{\partial y^2} \right] \frac{\partial^2 w}{\partial x^2} + \frac{E}{1-\nu^2} \left[\frac{\partial^2 w}{\partial y^2} + \nu \frac{\partial^2 w}{\partial x^2} \right] \frac{\partial^2 w}{\partial y^2} + 2 \frac{E}{1+\nu} \left[\frac{\partial^2 w}{\partial x \partial y} \right]^2 \right\} dx dy$$

(A.31)

Grouping the flexural rigidity term $\frac{Eh^3}{12(1-\nu^2)}$ leads to the form shown by Timoshenko [115]

$$\begin{aligned}
U(t) &= \frac{D}{2} \iint_A \left\{ \left[\frac{\partial^2 w}{\partial x^2} + \nu \frac{\partial^2 w}{\partial y^2} \right] \frac{\partial^2 w}{\partial x^2} + \left[\frac{\partial^2 w}{\partial y^2} + \nu \frac{\partial^2 w}{\partial x^2} \right] \frac{\partial^2 w}{\partial y^2} + 2(1-\nu) \left[\frac{\partial^2 w}{\partial x \partial y} \right]^2 \right\} dx dy \\
&= \frac{D}{2} \iint_A \left\{ \left[\frac{\partial^2 w}{\partial x^2} \right]^2 + \left[\frac{\partial^2 w}{\partial y^2} \right]^2 + 2\nu \frac{\partial^2 w}{\partial x^2} \frac{\partial^2 w}{\partial y^2} + 2(1-\nu) \left[\frac{\partial^2 w}{\partial x \partial y} \right]^2 \right\} dx dy
\end{aligned} \tag{A.32}$$

Eq. A.32 can alternatively be grouped in:

$$U(t) = \frac{D}{2} \iint_A \left\{ \left[\frac{\partial^2 w}{\partial x^2} + \frac{\partial^2 w}{\partial y^2} \right]^2 - 2(1-\nu) \left[\left[\frac{\partial^2 w}{\partial x^2} \frac{\partial^2 w}{\partial y^2} \right] - \left[\frac{\partial^2 w}{\partial x \partial y} \right]^2 \right] \right\} dx dy \tag{A.33}$$

Considering the strain energy of a small elemental surface (dx, dy), equation (A.33) leads to the definition of surface strain energy density:

$$e(x, y, t) = \frac{D}{2} \left\{ \left[\frac{\partial^2 w}{\partial x^2} + \frac{\partial^2 w}{\partial y^2} \right]^2 - 2(1-\nu) \left[\left[\frac{\partial^2 w}{\partial x^2} \frac{\partial^2 w}{\partial y^2} \right] - \left[\frac{\partial^2 w}{\partial x \partial y} \right]^2 \right] \right\} \tag{A.34}$$

Here is noted explicitly that equation (A.34) defines a surface strain energy density as the thickness integration was included in Eq. (A.31). Moreover, in line with the symmetric behaviour of the bending theory considered, the energy density represents both top and bottom layers.

The time independent modal strain energy terms e_{mn} can be obtained by inserting in equation (A.34) the deformation imposed by each modal shape $W_{mn}(x, y)$ as expressed in Eq. (A.14):

$$\begin{aligned}
e_{mn}(x, y) &= \frac{D}{2} \left\{ \left[\frac{2}{\sqrt{\rho abh}} \left(\frac{m\pi}{a} \right)^2 \sin \frac{m\pi x}{a} \sin \frac{n\pi y}{b} + \frac{2}{\sqrt{\rho abh}} \left(\frac{n\pi}{b} \right)^2 \sin \frac{m\pi x}{a} \sin \frac{n\pi y}{b} \right]^2 \right. \\
&\quad \left. - 2(1-\nu) \left[\frac{4}{\rho abh} \left(\frac{mn\pi^2}{ab} \right)^2 \left(\sin \frac{m\pi x}{a} \sin \frac{n\pi y}{b} \right)^2 - \frac{4}{\rho abh} \left(\frac{mn\pi^2}{ab} \right)^2 \left(\cos \frac{m\pi x}{a} \cos \frac{n\pi y}{b} \right)^2 \right] \right\}
\end{aligned} \tag{A.35}$$

Grouping common terms leads to:

$$\begin{aligned}
e_{mn}(x, y) &= \frac{D}{2} \frac{4\pi^4}{\rho abh} \left\{ \left[\left(\frac{m}{a} \right)^2 + \left(\frac{n}{b} \right)^2 \right]^2 \left(\sin \frac{m\pi x}{a} \sin \frac{n\pi y}{b} \right)^2 \right. \\
&\quad \left. - 2(1-\nu) \left(\frac{mn}{ab} \right)^2 \left[\sin^2 \left(\frac{m\pi x}{a} \right) \sin^2 \left(\frac{n\pi y}{b} \right) - \cos^2 \left(\frac{m\pi x}{a} \right) \cos^2 \left(\frac{n\pi y}{b} \right) \right] \right\}
\end{aligned} \tag{A.36}$$

Equation (A.36) represents the modal strain energy density of the continuous bending plate, taking the equivalent role of e_{ni} used for discrete systems in appendix D.2.

Integrating e_{mn} across the plate leads to the total strain energy in mode (m, n) as:

$$\begin{aligned}
 U_{mn} &= \iint_A e_{mn}(x, y) dx dy = \\
 &= \frac{D}{2} \frac{4\pi^4}{\rho abh} \left\{ \left[\left(\frac{m}{a} \right)^2 + \left(\frac{n}{b} \right)^2 \right]^2 \left(\frac{ab}{4} \right) - 2(1 - \nu) \left(\frac{mn}{ab} \right)^2 \left[\frac{ab}{4} - \frac{ab}{4} \right] \right\} \\
 &= \frac{D}{2} \frac{4\pi^4}{\rho abh} \left\{ \left[\left(\frac{m}{a} \right)^2 + \left(\frac{n}{b} \right)^2 \right]^2 \left(\frac{ab}{4} \right) \right\} = \frac{D}{2} \frac{\pi^4}{\rho h} \left\{ \left[\left(\frac{m}{a} \right)^2 + \left(\frac{n}{b} \right)^2 \right]^2 \right\} \tag{A.37}
 \end{aligned}$$

Grouping the term representing ω_{mn} as defined in Eq. (A.14), leads to the expected expression of total modal energy with mass normalized eigenvectors

$$U_{mn} = \frac{1}{2} \left\{ \pi^2 \sqrt{\frac{D}{\rho h}} \left[\left(\frac{m}{a} \right)^2 + \left(\frac{n}{b} \right)^2 \right] \right\}^2 = \frac{1}{2} \omega_{mn}^2 \tag{A.38}$$

The modal strain energy U_{mn} is the continuum equivalent of $U_n = \frac{1}{2} \omega_n^2$ used for discrete systems in appendix D.2. The total deformation energy in the system can be written as the sum of the contributions from each mode:

$$U(t) = \sum_{mn} U_{mn} q_{mn}^2(t) \tag{A.39}$$

It is worth noticing explicitly that the energy conservation expressed by (A.39) is not valid for sub-portion of the plate. In fact, writing (A.34) in terms of modal contributions yields mutual energy terms between modes due to the quadratic factors that are eliminated by virtue of eigenvectors orthogonality only when integrated across the full surface, yielding (A.39). If integration is not extended to the whole surface this simplification is not applicable and therefore considering the elementary surface (dx, dy) :

$$e(x, y, t) \neq \sum_{mn} e_{mn}(x, y) q_{mn}^2(t) \tag{A.40}$$

A.3 Analytical and FE validation of simply supported plates in bending

The equations presented in A.1 and A.2 are purposely coded in a frequency domain parametric solution algorithm in a MATLAB® software environment.

A baseline validation model using the parameters shown in Table 23 is initially compared against a corresponding detailed FE model comprising 9000 shell elements (Figure A-5) in

order to establish the correctness and efficiency of both the analytical and numerical solutions.

All FE analyses are performed using MSC Nastran®, version 2012. Postprocessing is performed in Patran® and MATLAB®. Appendix C provides a brief overview of the adopted software solutions.

Table 23. Parameters for baseline plate model

quantity	dimensions	description
a	250 mm	length in x
b	100 mm	length in y
h	0.2 mm	plate thickness
ρ	7800 Kg/m ³	mass per unit volume
E	210 GPa	Young's modulus
D	153.85 N·mm	flexural rigidity
η	0.1	proportional structural damping

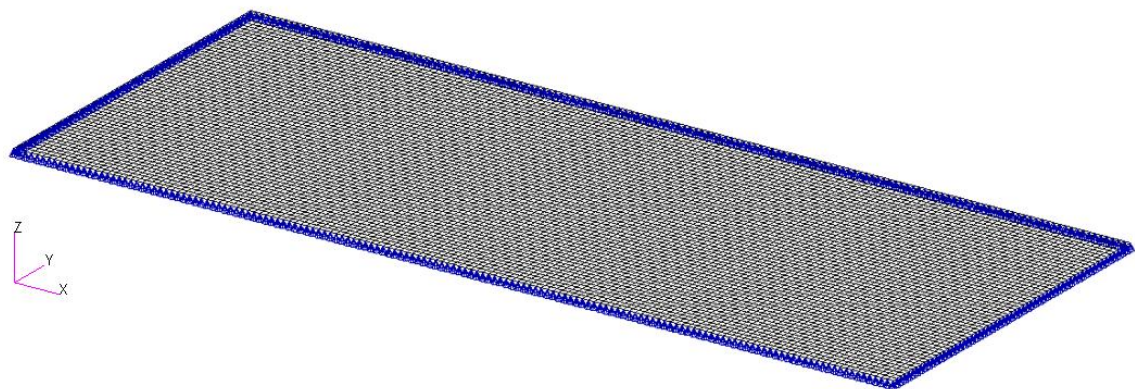


Figure A-5. FE baseline model constituted of 9000 shell elements, “CQUAD4”, in MSC Nastran® (C.1) with simply supported boundary conditions. Image generated in Patran®.

The validation study covered the following aspects:

- Eigenvalues and Eigenvectors.
- Static and dynamic correlation using concentrated and distributed forces.
- Sensitivity to:
 - Modal basis size;
 - Concentrated Dirac delta force vs. force distributed over a small patch;
 - Damping and Frequency range;

- Loading Point.
- Improved solution efficiency through static correction (analytical) and residual vectors (FE).

The last bullet point is noteworthy, since the parametric analytical model was developed with the aim of providing a fast and accurate tool capable of automatically iterating through a large number of solutions. The static correction is effectively recovering the static response for a set of truncated modes, with the effect of enhancing the efficiency of the few retained solution modes.

A.3.1 FE and analytical modes

The modes calculated analytically compare very well with the FE calculation. An additional FE variant is considered to evaluate the limited effect of shear and membrane stiffness. The resulting natural frequencies for the first 10 modes are listed in Table 24, with the first 6 modes as calculated in FE shown in Figure A-6.

Table 24. Baseline simply supported plate, Analytical and FE natural frequencies [57]

Mode No.	<i>m</i>	<i>n</i>	Analytical (Hz) (Meirovitch [116])	MSC Nastran® (Hz) (bending, shear and membrane)	% error	MSC Nastran® (Hz) (bending only)	% error
1	1	1	57.221	57.202	0.033	57.208	0.023
2	2	1	80.899	80.839	0.075	80.855	0.055
3	3	1	120.362	120.252	0.092	120.277	0.071
4	4	1	175.611	175.443	0.096	175.478	0.077
5	2	2	205.208	205.164	0.021	205.176	0.016
6	2	2	228.886	228.731	0.068	228.780	0.055
7	1	1	248.844	246.410	0.095	246.451	0.079
8	2	2	268.349	268.021	0.122	268.075	0.102
9	2	2	323.597	323.047	0.170	323.128	0.145
10	1	1	333.463	333.150	0.094	333.200	0.079

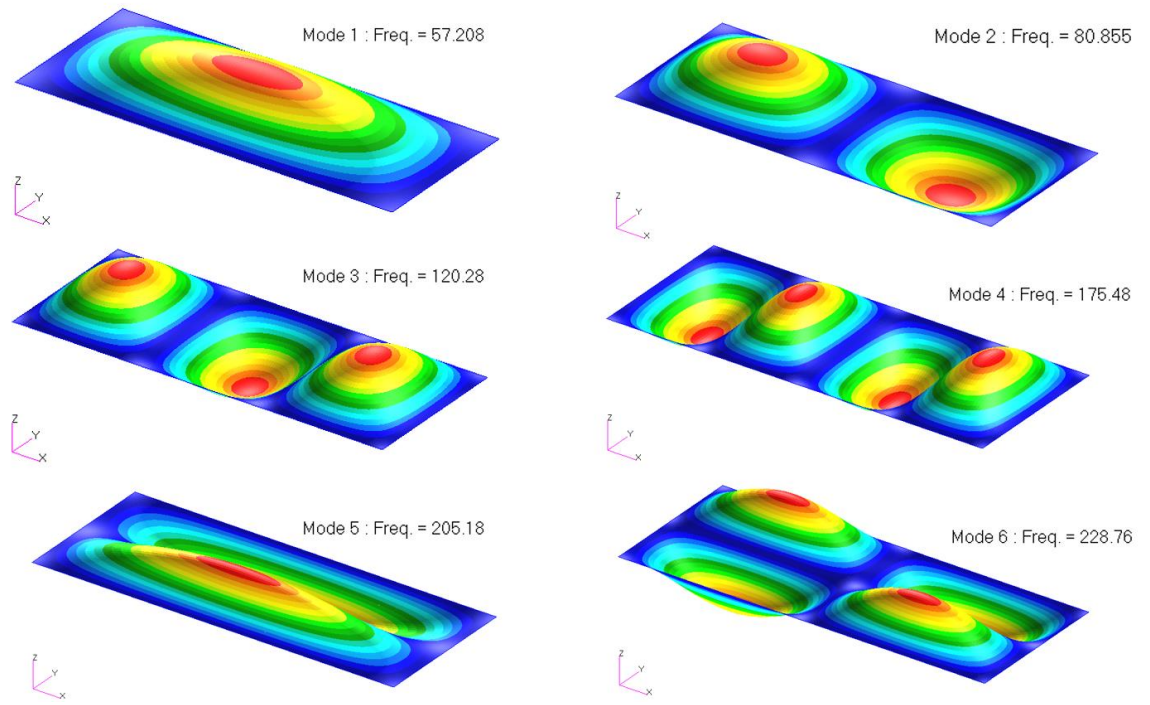


Figure A-6. First six natural modes of FE baseline plate in bending as obtained with MSC Nastran® [57]. Images generated in Patran®.

A.3.2 **Statically applied concentrated force**

The analytical and FE models are subjected to a static 0.1 N vertical load distributed over a 10 by 10 mm area centred at $x=210$ mm, $y=20$ mm. The analytical model is based on 100 by 100 modal basis. The FE model is solved in Nastran® via stiffness matrix inversion method.

Figure A-7 shows the combined results of the analytical and FE solutions for 2 sections, located respectively at $y=20$ and $y=30$. Both the displacements in Figure A-7(a) and the strain energy density in Figure A-7(b) provide an excellent match.

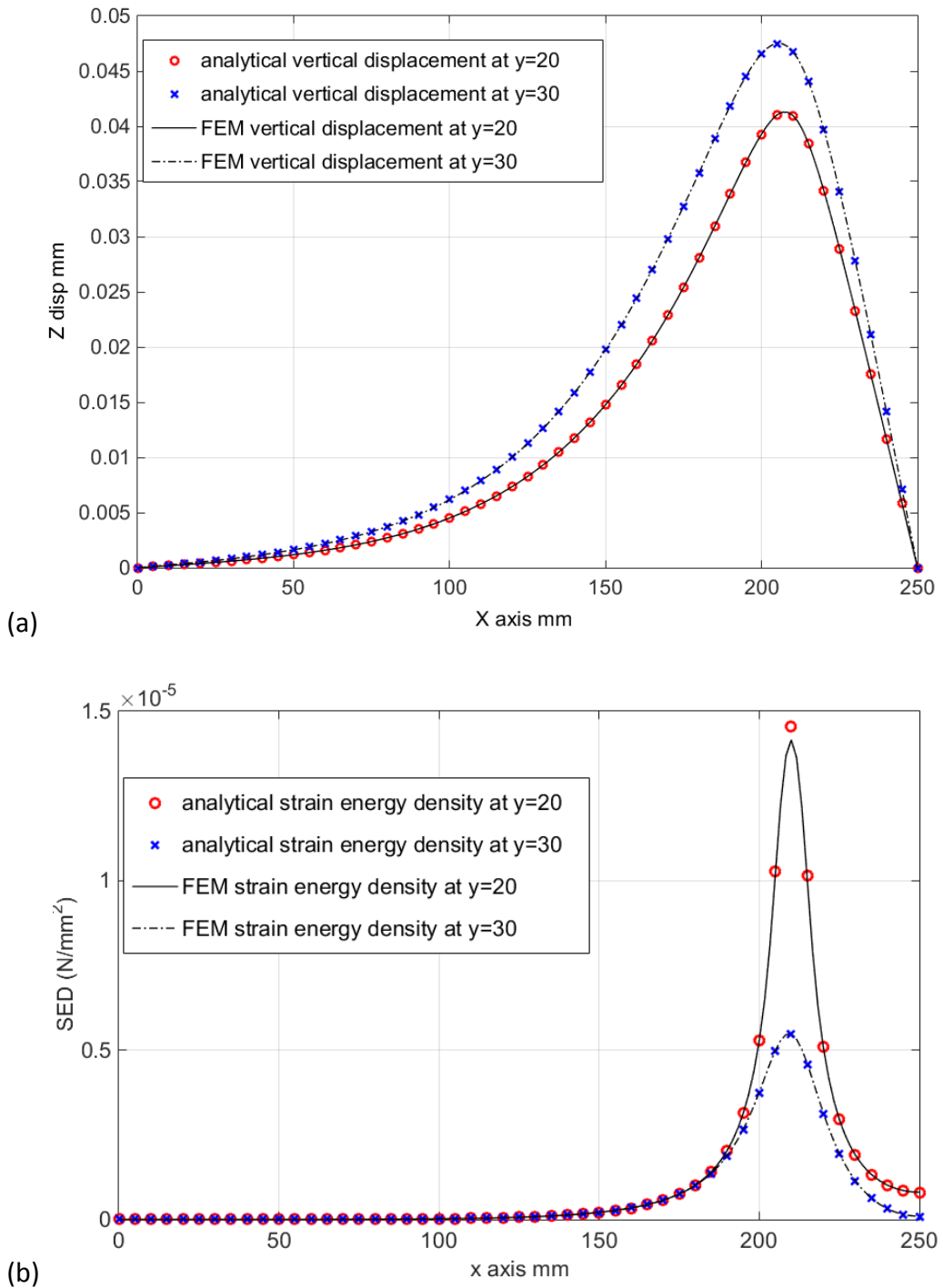


Figure A-7. Statically applied 0.1 N load centred at $x=210$ mm, $y=20$ mm, combined results of the analytical and FEM solutions for 2 sections, located respectively at $y=20$ and $y=30$. The Static FE and analytical solution overlap for both displacement (a) and strain energy density, SED, (b), [57].

A.3.3 Harmonic response to single applied force

An analytical frequency response is obtained under a unit, 1 N, vertical harmonic loading arbitrarily placed on the plate at $x=155$ mm and $y=25$ mm. The frequency response solution is calculated at regular 1 Hz increments from 0 to 300 Hz, with:

- $\eta = 0.10$ structural damping
- $\bar{m} = 2000$ modal truncation in x ;
- $\bar{n} = 2000$ modal truncation in y .

Figure A-8 shows the amplitude frequency response at the highest stress recovery position. The analytical response is compared with the corresponding MSC Nastran® results, the latter using the direct matrix inversion method in order to remove any approximation deriving from modal truncation.

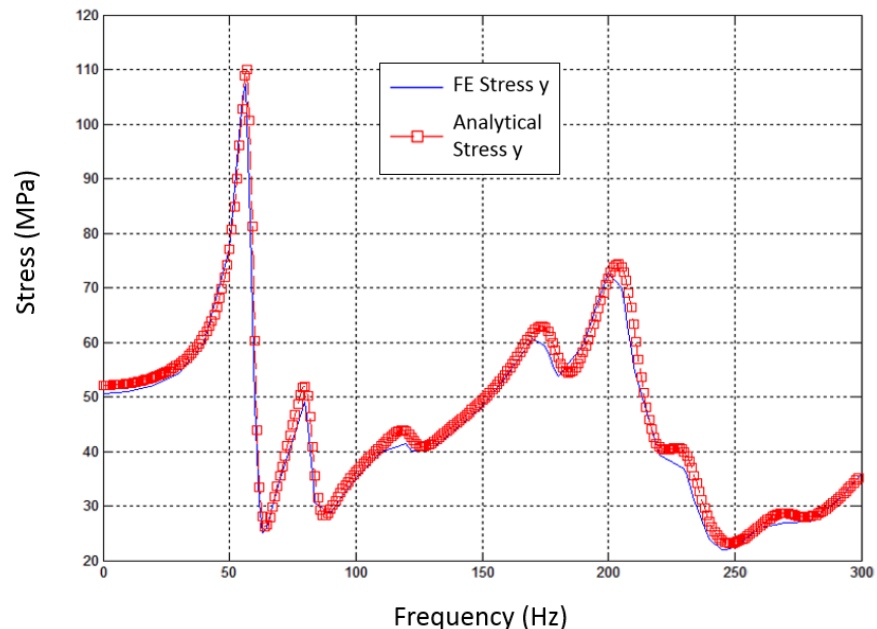


Figure A-8. FE and analytical frequency response amplitude of direct stress y component, stress recovery location at $x=155$ mm and $y=26.7$ mm, under unit vertical harmonic loading at $x=155$ mm and $y=25$ mm [57].

A.4 Solution sensitivities and performances

The previous sections provided a validation of the dynamic and static behaviour of the analytical solution as coded in MATLAB®. This section addresses the solution sensitivity to factors affecting convergence and performance. Such aspects are normally discussed in

antithesis and therefore need to be considered in detail before the numerical model can be used with confidence.

The numerical model specification throughout the sensitivity studies is based on fully parametric analytical models and random seeding of force location to allow unbiased exploration.

A.4.1 Sensitivity to modal basis truncation and load patch size

Increasing the number of retained solution modes proportionally affects the solution time. Therefore, a strong emphasis needs to be given to the sensitivity due to the modal basis size, in order to find the best compromise between efficiency and accuracy.

In seeking solution convergence, consideration is given to the output entity of interest. Deformations are relatively easy to capture with few modes, but stresses or strains, being a second order derivative, require a more refined modal basis.

Figure A-9 shows an example of the static displacement in normalized contour plot, resulting from different modal bases. The unit Dirac delta force was randomly positioned at $x=176.5$ mm and $y=3.18$ mm. The maximum displacement is correctly captured with a 10 by 10 modal basis (100 modes); using a 50 by 50 modal basis (2500 modes) only affects the solution by less than 1%.

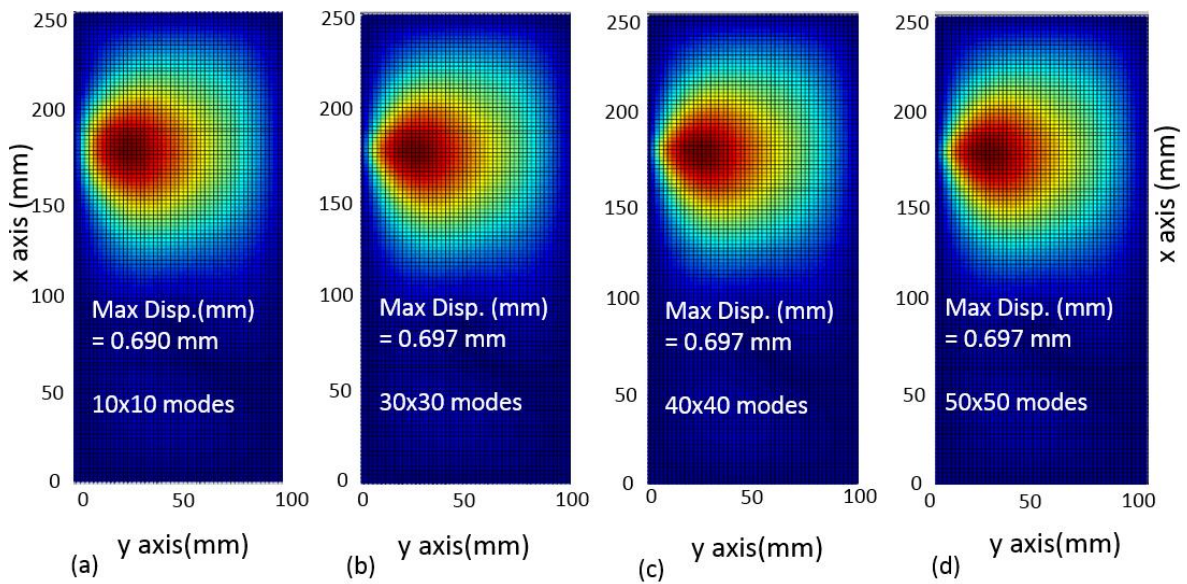


Figure A-9. Static response in terms of displacements is nearly identical between 10 by 10 modal basis (100 modes) and 50 by 50 (2500 modes) – unit force positioned at $x=176.5$ mm and $y=3.18$ mm [57].

Conversely, Figure A-10 shows that, for the same case, the strain x component does not converge, even when a relatively large 50 by 50 modal basis is adopted.

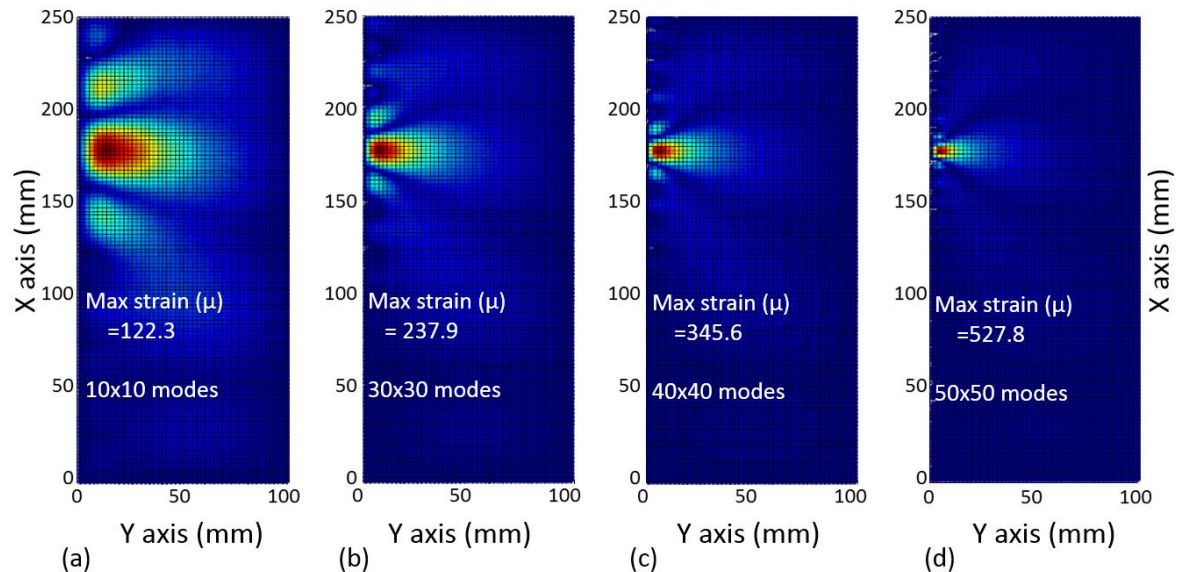


Figure A-10. Static response of strain x component showing no convergence up to 50 by 50 modal basis size (i.e. 2500 modes) [57].

The lack of convergence for the strain x component is due to the idealized concentrated force that is enforcing a local mathematical discontinuity.

Figure A-11 describes the convergence rate of the square root of modal basis size using the same total load going from Dirac delta (first row), a finite small squared patch of 0.1 mm sides (middle row) and finally a squared patch of 1 mm sides (bottom row). The harmonic load of 0.1 N is located at $x=155$ mm and $y=25$ mm. The results show:

- no convergence of stress and strain components with Dirac delta force (first row of images)
- Slow convergence with square patch force of 0.1 mm side (second row),
- Fast convergence with square patch of 1 mm side (third row).

The result is in line with similar issues affecting FE results with concentrated loads and provide guidance on the acceptable boundaries and level of accuracy attainable by the combination of patch size and modal base. The next section will establish ways to improve the accuracy of a much smaller modal bases.

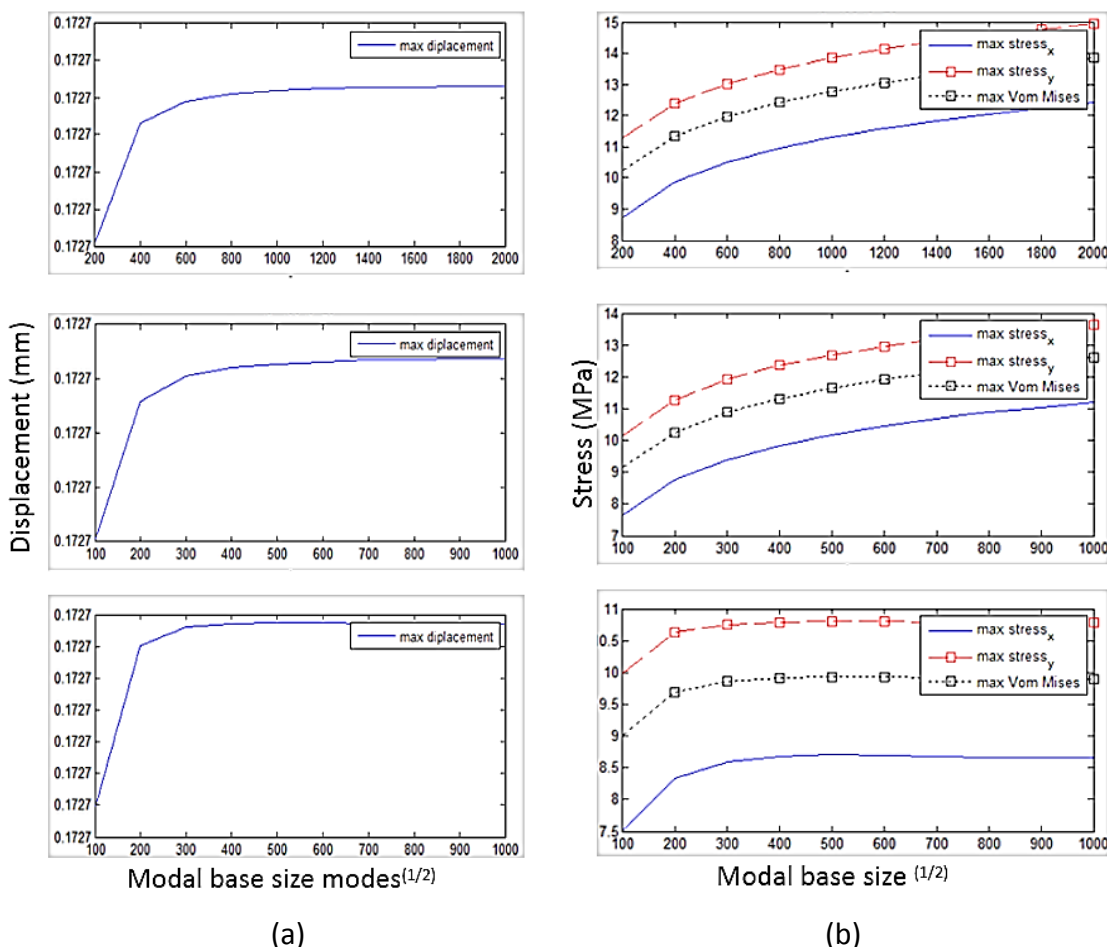


Figure A-11. Convergence rate of displacements, left (a), and stress, right (b), as function of the square root of the modal basis size; using the same total unit

load with Dirac delta (first row), a finite small squared patch of 0.1 mm sides (middle row) and a squared patch of 1 mm sides (bottom row), [57].

A.4.2 Static correction convergence study for plate in bending

With the analytical solution, the static contribution of the eliminated modes can be conveniently calculated beforehand as it does not depend on the frequency of the load. The static correction is obtained from equation (A.20) by considering $\omega=0$ and $\eta=0$ and only using modes not already included in the truncated modal basis \bar{m} by \bar{n} :

$$w(x, y, t) = \frac{4}{\rho abh} \sum_{m=\bar{m}+1}^{\infty} \sum_{n=1}^{\infty} \sin \frac{m\pi x}{a} \sin \frac{n\pi y}{b} \sin \frac{m\pi f_a}{a} \sin \frac{n\pi f_b}{b} F e^{i\omega t} \frac{1}{\omega_{mn}^2} \\ + \frac{4}{\rho abh} \sum_{m=1}^{\infty} \sum_{n=\bar{n}+1}^{\infty} \sin \frac{m\pi x}{a} \sin \frac{n\pi y}{b} \sin \frac{m\pi f_a}{a} \sin \frac{n\pi f_b}{b} F e^{i\omega t} \frac{1}{\omega_{mn}^2} \quad (\text{A.41})$$

The pre-calculated *static correction* in Eq. (A.41) is added to the dynamic solution, as demonstrated in the next examples.

Figure A-12 describes the dynamic response convergence rate for displacement and stresses as function of the square root of the modal basis size. The harmonic load of 0.1 N is again located at $x=155$ mm and $y=25$ mm and with structural damping $\eta = 0.10$, as in the model in A.3.3. The investigation is carried for a single harmonic frequency at 55.2 Hz, that is 2 Hz below the first natural frequency.

In Figure A-12 (a) and (b) the max displacement and stress results are obtained in absence of static correction. Conversely, the results in Figure A-12 (c) and (d) use a static correction comprising 100 by 100 static modes, with the static correction contribution reported along the total response.

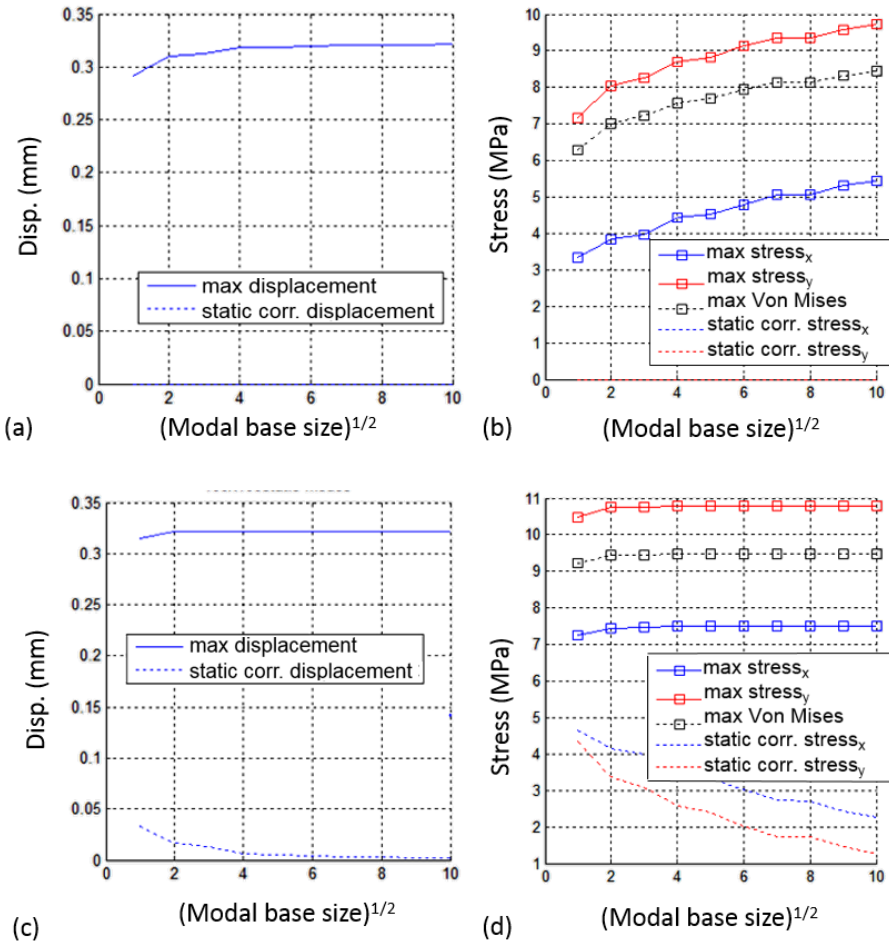


Figure A-12. Dynamic response under 0.1 N harmonic load at 55.2 Hz, located at $x=155$ mm and $y=25$ mm, $\eta=0.1$. Max displacements (a), (c) and max stress components (b), (d) as function of square root of modal basis size. The convergence of the results in (c) and (d) is improved by a static correction basis comprising 100 by 100 static modes [57]

Having established the role and the need for static modes, the sensitivity plots in Figure A-13 provide an indication of the effect of increasing the size of the static correction basis. Comparing the results of a static correction with a 10 by 10 modal basis, Figure A-13 (a), to a correction using 100 by 100 modes, Figure A-13(b), shows a variation close to 10% for the stress components. However a static correction based on 1000 by 1000 modes only affects the results by further 0.3% for the case considered, as shown in Figure A-13 (c).

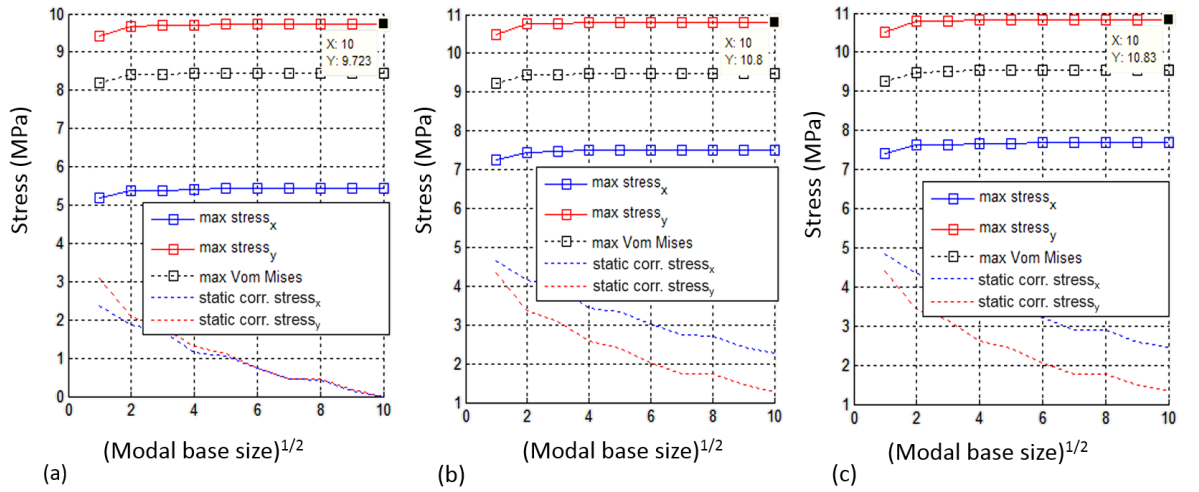


Figure A-13. Effect of the static correction basis size with respectively 10 by 10 (a), 100 by 100 (b) and 1000 by 1000 modes (c), for the same loading conditions in Figure A-12 [57].

In summary, for the problem under consideration, good convergence is established combining the necessary dynamic modes, based on frequency ratio $r = \frac{\Omega}{\omega_m}$ (as described in 2.1.1), with a static correction basis with around 100 by 100 modes. A considerably smaller static correction modal basis size (approximately 20 by 20) could be deployed for fast processing at the cost of reduced accuracy.

Appendix B Craig-Bampton method application to an All-Terrain Vehicle model

B.1 Background

The multibody simulation and FE models of an Honda All-Terrain Vehicle, ATV, in Figure B-14 and Figure B-15, are the result of an open collaboration between industry and academia led by the Fatigue Design & Evaluation Committee of the Society of Automotive Engineers [109].

The Honda All-Terrain Vehicle in was the subject of a number of experimental and numerical investigations with the aim of developing a methodology for using computer simulation to predict structural fatigue life of automotive components [112]. The applied methodology follows the methods demonstrated by Conle and Mousseau [16] in the early nineties. The accessibility, relevance and completeness of the documentation make this model an ideal subject for academic theses and demonstrators [119]. In 2002 Markale [112] and Kulkarni [111] focussed on the development of a multibody dynamics model in commercial code AutoSim™, capable of predicting the dynamic loads acting on the frame of the vehicle. Shenoy [110] combined stresses from unit loads and time histories from multibody dynamics to obtain a stress distribution on the vehicle's frame.

B.2 Model description

In 2001 Ge Wang et al. generated an initial multibody model in Adams™ (appendix C.3) [120]. The model included a flexible frame [113] originally build by Cameron Nelson and Greg Fialek in ANSYS® for the Fatigue Design & Evaluation Committee of the Society of Automotive Engineers [110].

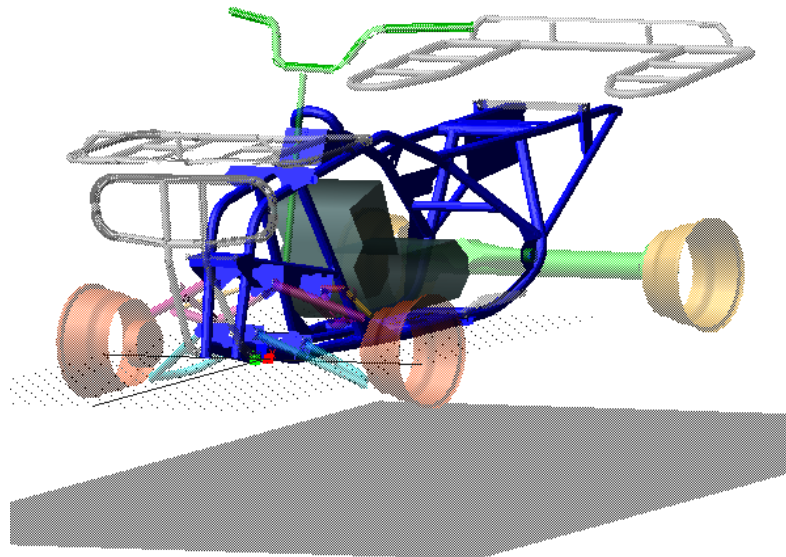


Figure B-14. Multibody simulation model in commercial code Adams™. Image generated in Adams/View™.

The flexible frame in Figure B-15 is represented in the MBD model via Craig-Bampton component-mode synthesis (chapter 2.1.3) using the commercial FE solver MSC Nastran® [33]. A summary of the multibody assembly is presented in Table 25.

Table 25. Summary of All-Terrain Vehicle multibody model

Entity type	number
Total DOF	128
Moving Parts	34
Flexible Bodies	1
Spherical Joints	6
Fixed Joints	22
Hooke Joints	2

A summary of the FE vehicle frame model shown Figure B-15 and its corresponding component-mode synthesis description is listed in Table 26.

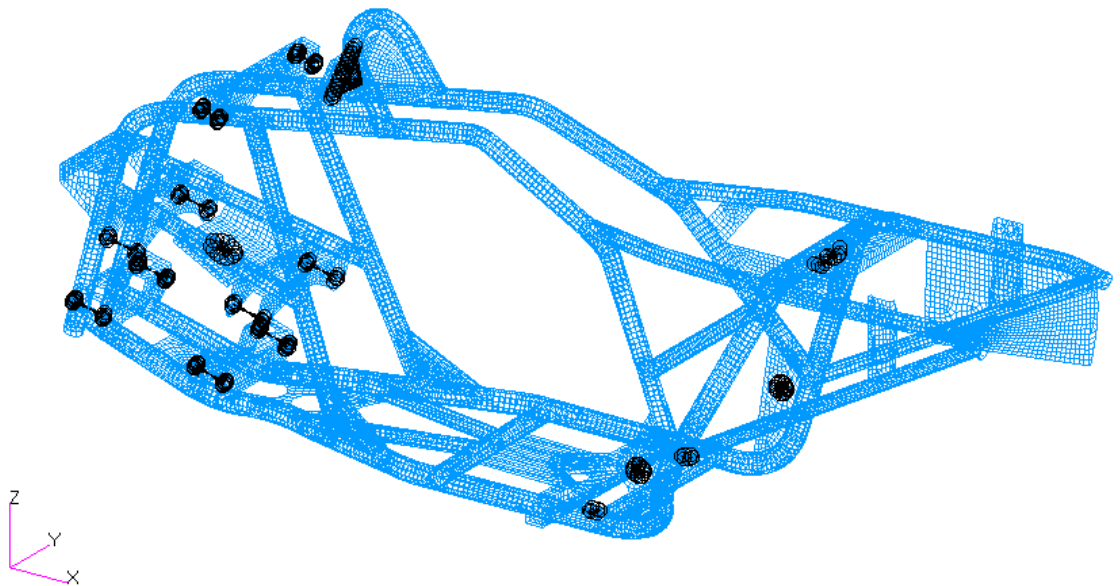


Figure B-15. Finite element model of the All-Terrain Vehicle frame with the 17 attachment points highlighted with their load distribution elements (RBE2).
Images generated in Patran®.

Table 26. All-Terrain Vehicle frame, FE model and CMS description

FE entity type	Number of entities	free-free modes	constraint modes	residual vectors	Total output channels (modes)
Shells	28433	10	102	6	118
Nodes	24986				

The frame is connected to the multibody assembly by 17 attachment points, each carrying 6 DOF. The geometric attachment points are treated as a local distributed connection using the characteristic web elements, RBE2 in Nastran® terminology. In Figure B-15, the 17 RBE2 connections are highlighted as a darker web of elements.

The attachment points resulted in a total of 102 attachment modes to be added to 10 fixed boundary normal modes, as explained in 2.1.3.2. The total number of degrees of freedom, or Craig-Bampton modes, is 118, including 6 residual vectors resulting from inertial acceleration.

The columns in Table 27 detail the frequency of the first fixed boundary modes alongside the Craig-Bampton modes. The latter column presents 6 rows of null frequencies representing 6 rigid body modes, followed by frequencies that correspond approximately to a free-free condition.

Table 27. First fixed boundary and Craig-Bampton (CB) modes

Mode No.	fixed boundary modes frequency Hz	CB modes frequency Hz
1	94.87	0.00
2	129.06	0.00
3	205.26	0.00
4	245.48	0.00
5	249.74	0.00
6	264.20	0.00
7	269.21	85.18
8	292.55	111.72
9	313.62	122.80
10	362.96	129.12

B.3 Durability events schedule

A fatigue durability schedule defines a number of events and repetitions representative of customer usage, alternatively termed *fatigue duty-cycle*. Each event has a predefined set of repetitions, equivalent to multiple “passes” on a test track sections. The fatigue structural integrity of any proposed design is measured in terms of the fatigue damage accumulated through the whole duty-cycle.

The actual durability schedule for the All-Terrain Vehicle model comprises of the 21 events. The events and their expected lifetime occurrences are listed in Table 28.

Table 28. Full fatigue durability schedule for the All-Terrain Vehicle simulation [109]

event number	description	passes per life
1	Low speed loop	100
2	Grave lot	100
3	Hillwork	60
4	Hillwork with snow	60
5	Aggressive hillwork	60
6	Farm vocation	120
7	Farm vocation 2	110
8	Bump course	100
9	Staggered bumps	65
10	Staggered bumps 2	65
11	Bump course 2 CW	70
12	Bump course 2 CCW	70
13	High speed transport	75
14	ISO track 2	100
15	Ditch crossing	25
16	Ditch crossing 2	25
17	Recreational run	100
18	Flat off-road CW	150
19	Flat off-road CCW	175
20	Bump course 3	90
21	Jumps	10

A dedicated experimental data acquisition exercise was conducted by a team of the SAE Fatigue Design & Evaluation Committee [109] [112], for which the acquisition technique was the subject of independent research. In brief, the vehicle was instrumented with wheel force transducers and driven around the test track and open fields, recording the relevant events' load data. The acquired rotating wheel forces were converted into the wheel spindle loads to be applied directly onto the multibody model. Figure B-16 shows an example of 4 vertical forces (left-front, right-front, left-rear and right-rear respectively) for event 5, Aggressive hillwork, in Table 28. The data was acquired at 204.8 Hz, for a total of 580 seconds resulting in 120,000 data points per loading channel. The size and type of

the acquired data is representative of any modern ground vehicle design, thus constituting a real-life benchmark useful in assessing and comparing the performances of fatigue simulation methods.

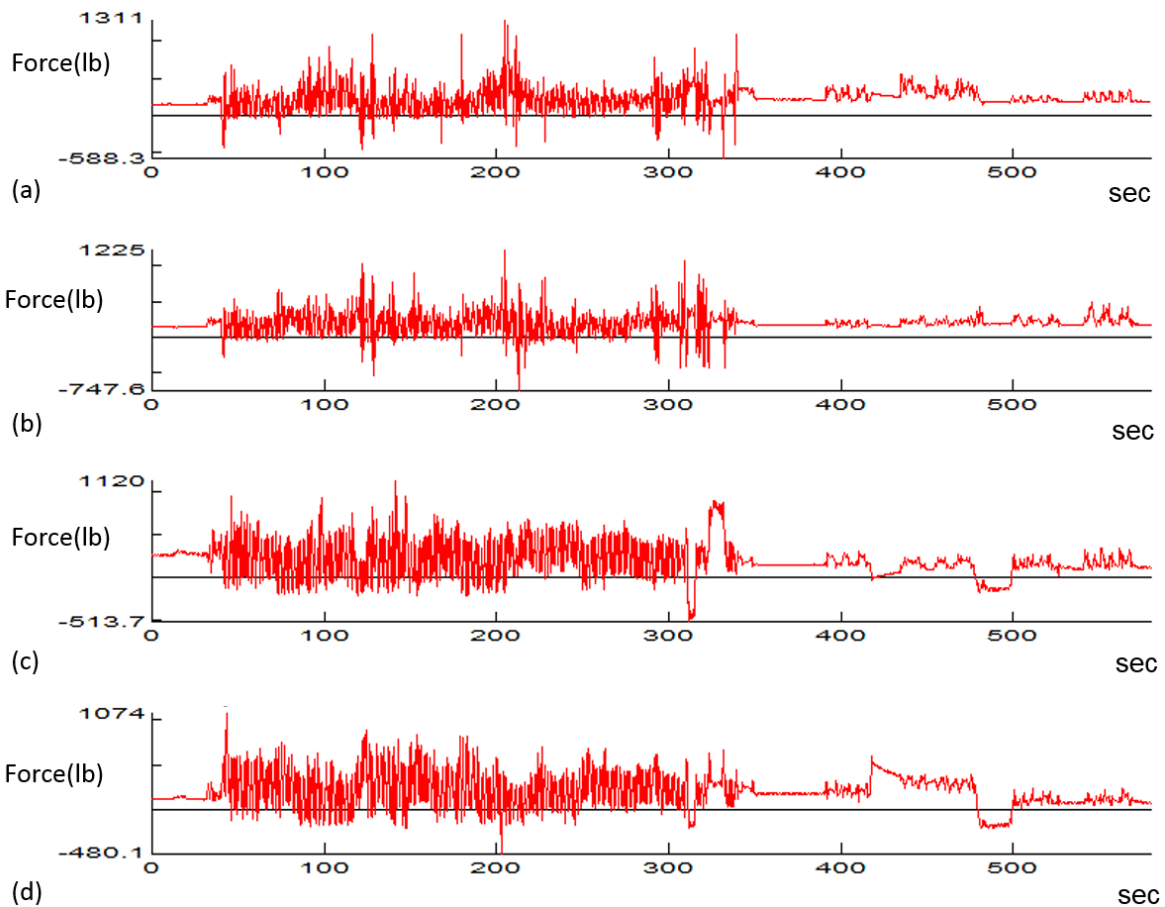


Figure B-16. Vertical spindle forces for event 5, Aggressive hillwork, describing respectively left-front (a), right-front (b), left-rear (c) and right-rear (d). Data source [109], image generated in MSC Fatigue™.

Appendix C Engineering software tools and versions

Contemporary numerical simulation applied to mechanical design makes wide usage of all virtual prototyping domains: FEM, multibody systems dynamics and fatigue. Each virtual tool has algorithms developed and optimised to efficiently prepare and solve the specific domain task.

A brief description of the software tools used in this research will follow. The process defined in this investigation is not limited to the software tools used herein. Rather, the benefits discussed may be discovered with any similarly capable set of software tools.

C.1 FE pre and post processing

Patran® geometry and FE modelling has become a standard design tool for modern digital model creation; adaptive and high quality FE-meshes can be readily created with a variety of tools.

MSC Nastran® is a well-established solution in both Aerospace and Automotive industries. The solver offers multiple solution sequences, each associated with unique *SOL* number code, ranging from linear static to non-linear explicit and covering both time and frequency domain. Figure C-17 lists some basic solution numbers and provides a brief description; the subset of solutions used for this investigation is highlighted. For the component-mode synthesis method deployed for this investigation, MSC Nastran® performs a modal reduction and orthonormalization according to the Craig-Bampton method; MSC Nastran® also includes options for residual vectors as a standard feature. For component-mode synthesis in combination with the multibody solver Adams™, MSC Nastran® provides a dedicated capability to export reduced models in neutral format, the modal neutral file (MNF). Aside the generalized mass and stiffness matrices, optionally the MNF format can include the generalized damping matrix and prescribed modal loads.

SOL Number	SOL Name	Description
101	SESTATIC	Statics with options: Linear steady state heat transfer. Alternate reduction. Inertia relief.
103	SEMODES	Normal modes.
105	SEBUCKL	Buckling with options: Satic analysis. Alternate reduction. Inertia relief.
106	NLSTATIC	Nonlinear or linear statics.
107	SEDCEIG	Direct complex eigenvalues.
108	SEDFREQ	Direct frequency response
109	SEDTRAN	Direct transient response.
110	SEMCEIG	Modal complex eigenvalues
111	SEMFREQ	Modal frequency response.
112	SEMTRAN	Modal transient response.

Figure C-17. MSC Nastran® list of basic solution numbers and their description;
the subset of solution used for this investigation is highlighted.

C.2 FE based fatigue solvers

MSC Fatigue™ is an FE tool capable of performing a variety of analyses in the field of fatigue and durability. The basic operations include an S - N (stress-life) and ε - N (strain-life) with a linear damage summation rule, rainflow cycle counting and mean stress correction effects. Aside the fatigue solvers, the software embeds signal filtering capabilities, such as multiple peak-valley with gating, and simulation acceleration options, such as limits-only and two-pass methods.

C.3 Multibody systems dynamics

Adams™ is a motion simulation solution for analysing the complex behaviour of mechanical assemblies. Adams/View™, the graphical interface to the solver, allows easy assembly of articulated mechanisms by virtue of a library of joints and constraints. Once the virtual prototype is complete, Adams™ checks the model and then solves second order simultaneous equations to obtain kinematic, static, quasi-static and dynamic behaviour. Results are viewable as graph, data plots, reports or animations. Typically, the resulting loads created from Adams™ simulation studies will provide loading conditions to FE programs. The Adams™ solver can embed FE modal reduced flexible bodies via dedicated file format, the modal neutral file (MNF). Several FE commercial solvers embed

a capability to export a model according to the MNF format.

C.4 Programming environment

MATLAB® is a programming platform optimized for solving engineering and scientific problems across multiple disciplines. It is one of the world's standard software applications in computational mathematics. Throughout this research the analytical simulations, with associated graphs, have been performed in MATLAB® R2014b using completely original code. The a priori hotspot identification process, as well as the performance metrics calculations have also been implemented in MATLAB® with data generated by the aforementioned FE solvers.

Appendix D

Appendix D Modal Strain Energy in FE simulation

The modal strain energy definitions derived here are applicable to multi degree of freedom systems represented by FE methods via modal reduction techniques.

D.1 Modal Strain Energy

Recalling the mass and stiffness orthogonal modal reduction basis for an FE model with N DOF and \hat{N} truncated modes, the expansion relationship between the physical and generalized coordinates is:

$$\{\mathbf{u}(t)\} = [\boldsymbol{\Phi}]\{\mathbf{q}(t)\}, \quad (D.1)$$

where the time dependency is explicitly introduced for added clarity.

We can assume a mass normalized normal base, so that the generalized mass and stiffness matrices become:

$$[\boldsymbol{\Phi}]^T[\mathbf{M}][\boldsymbol{\Phi}] = [\mathbf{I}] \quad \text{and} \quad [\boldsymbol{\Phi}]^T[\mathbf{K}][\boldsymbol{\Phi}] = [\bar{\Lambda}] = \begin{bmatrix} \omega_1^2 & & \\ & \ddots & \\ & & \omega_{\hat{N}}^2 \end{bmatrix} \quad (D.2)$$

The total strain energy $U(t)$ is:

$$\begin{aligned} U(t) &= \frac{1}{2}\{\mathbf{u}(t)\}^T[\mathbf{K}]\{\mathbf{u}(t)\} = \frac{1}{2}\{\mathbf{q}(t)\}^T[\boldsymbol{\Phi}]^T[\mathbf{K}][\boldsymbol{\Phi}]\{\mathbf{q}(t)\} \\ &= \frac{1}{2}\{\mathbf{q}(t)\}^T[\bar{\Lambda}]\{\mathbf{q}(t)\} = \frac{1}{2}\sum_n^{\hat{N}}\omega_n^2 q_n(t)^2 \end{aligned} \quad (D.3)$$

The diagonal terms of $\bar{\Lambda}$ are the \hat{N} eigenvalues of the system and define the modal strain energy U_n for each mode n according to

$$U_n = \frac{1}{2}\{\boldsymbol{\phi}_n\}^T[\mathbf{K}]\{\boldsymbol{\phi}_n\} = \frac{1}{2}\omega_n^2 \quad (D.4)$$

Eq. (D.3) can be further simplified in

$$U(t) = \sum_n U_n q_n(t)^2 \quad n=1, 2, \dots, \hat{N} \quad (D.5)$$

As expected in a \mathbf{K} -orthogonal basis the modal strain energy contributions are individually significant and independent from the excitation of the other modes.

$U_n q_n(t)^2$ represents the strain energy contribution of the n^{th} mode to the total deformation energy $U(t)$ and is the product of a function of time with the a priori quantity U_n , the strain energy of the n^{th} mode per unit modal participation q_n .

D.2 Element Modal Strain Energy

The definitions in (D.4) and (D.5) can now be transferred at element level.

Considering:

- r total number of FE elements for the selected reduced component,
- $U_i(t)$ strain energy of the i^{th} element,
- U_{ni} element modal strain energy for the i^{th} element and n^{th} mode.

The strain energy is the result of a volume integration, so the total energy for any given deformation at a given time is the sum of the strain energy in each single FE element volume.

$$U(t) = \sum_i^r U_i(t) \quad (D.6)$$

The terms $U_i(t)$ are provided by the element stiffness matrix and by the modal expansion equation (D.1) in a relation identical to Eq. (D.3) at element level:

$$U_i(t) = \frac{1}{2} \{\mathbf{u}(t)\}^T [\mathbf{K}_i] \{\mathbf{u}(t)\} = \frac{1}{2} \{\mathbf{q}(t)\}^T [\boldsymbol{\Phi}]^T [\mathbf{K}_i] [\boldsymbol{\Phi}] \{\mathbf{q}(t)\} \quad (D.7)$$

Similarly to equation (D.6), U_n in (D.4) can be thought as the sum of the elemental modal strain energy across all the elements in a given mode.

The element modal strain energies are obtained by considering the global stiffness matrix as assembled by the superposition of individual element stiffness matrices

$$[\mathbf{K}] = \sum_i^r [\mathbf{K}_i] \quad (D.8)$$

Equation (D.4) becomes

$$U_n = \frac{1}{2} \{\boldsymbol{\phi}_n\}^T \sum_i^r [\mathbf{K}_i] \{\boldsymbol{\phi}_n\} = \sum_i^r \frac{1}{2} \{\boldsymbol{\phi}_n\}^T [\mathbf{K}_i] \{\boldsymbol{\phi}_n\} = \sum_i^r U_{ni} , \quad (D.9)$$

where the element modal strain energy for i^{th} element, n^{th} mode is defined as

$$U_{ni} = \frac{1}{2} \{\boldsymbol{\phi}_n\}^T [\mathbf{K}_i] \{\boldsymbol{\phi}_n\} \quad (D.10)$$

Considering now again the total energy in equation (D.5) as the sum of modal strain energies, and substituting U_n with Eq. (D.9) gives

$$U(t) = \sum_n^N U_n q_n(t)^2 = \sum_n^N \sum_i^r U_{ni} q_n(t)^2 \quad (D.11)$$

Inverting the summation order in (D.11) and equating with the definition of total strain energy in Eq. (D.6) and

$$U(t) = \sum_i^r U_i(t) = \sum_i^r \sum_n^N U_{ni} q_n(t)^2 \quad (D.12)$$

Albeit both (D.6) and (D.12) express the identical total deformation energy as the sum of r element contributions, it is specifically observed that in general for the i^{th} element the following inequality applies:

$$U_i(t) \neq \sum_n^N U_{ni} q_n(t)^2 \quad (D.13)$$

This is explained observing that in (D.7) the system eigenvectors are not in general exact eigenvectors also for subpart of the models and for the individual element stiffness matrices. In mathematical terms this stems from the consideration that, at element level, the product $[\Phi]^T [\mathbf{K}_i] [\Phi]$ will not, in general, result in a diagonal matrix and there will be coupling terms between modes that are regulated by the $\{\mathbf{q}(t)\}$ generalized coordinates. The local coupling between modes re-distributes the energy across the model, but the total energy is preserved, as expressed by (D.12).

The results expressed by (D.12) and (D.13) are useful to the understanding of the opportunities and the limits of a priori, or even a posteriori hotspot searches based on modal variables, and more specifically modal strain energy density.

In a hotspot prediction algorithm based on modal bases, a high value of U_{ni} (intended in relative terms) is indicative of potential hotspot; this is definitely not a sufficient condition (possible false positive). Even the a posteriori knowledge of the associated q_n modal variable, will not uniquely determine the location of the highest energy concentration until the interaction with the other modes has been clarified.

Both a priori and a posteriori positions are however valid to the degree that, especially at critical loading times, one mode might prevail over the others and/or for the locations where the excited modes don't interact also at local level.

List of References

- [1] M. Petyt, *Introduction to finite element vibration analysis*. Cambridge: Cambridge University Press, 1990.
- [2] J. L. H. Julie A. Bannantine, Jess J. Comer, *Fundamentals of metal fatigue analysis*. Prentice Hall, 1990.
- [3] R. I. Stephens, A. Fatemi, R. R. Stephens, and H. O. Fuchs, *Metal fatigue in engineering*. John Wiley & Sons, 2000.
- [4] N.W.M. Bishop and F. Sherratt, *Finite Element Based Fatigue Calculations*. Glasgow, UK: NAFEMS, 2000.
- [5] M. J. Gander and G. Wanner, “From Euler, Ritz, and Galerkin to Modern Computing,” *SIAM Rev.*, vol. 54, no. 4, pp. 627–666, 2012.
- [6] D. T. Anderson and B. Mills, “Dynamic analysis of a car chassis frame using the finite element method,” *Int. J. Mech. Sci.*, vol. 14, no. 12, pp. 799–808, 1972.
- [7] J. Oden, “Historical comments on finite elements,” in *A history of scientific computing*, New York: ACM, 1990, pp. 152–166.
- [8] A. A. Shabana, *Dynamics of multibody systems*. Cambridge University Press, 2013.
- [9] N. V. Orlandea, “Multibody Systems History of ADAMS,” *J. Comput. Nonlinear Dynam.*, vol. 11, 2016.
- [10] W. Schiehlen, “Multibody system dynamics: Roots and perspectives.,” *Multibody Syst. Dyn.* 1, 2 149–188, 1997.
- [11] R. W. Landgraf and A. Conle, “Trends in assuring the mechanical durability of automotive structures,” *SAE Tech. Pap.*, 1984.
- [12] J. W. Fash and R. A. Lund, “Enhancing the design development cycle through computer integrated engineering for durability,” *SAE Tech. Pap.*, 1987.
- [13] A. A. Shabana, “Flexible multibody dynamics: review of past and recent developments,” *Multibody Syst. Dyn.*, pp. 189–222, 1997.
- [14] R. I. Stephens, B. Dopker, E. J. Haug, W. K. Baek, L. P. Johnson, and T. S. Liu, “Computational fatigue life prediction of welded and non-welded ground vehicle components,” *SAE Tech. Pap.*, 1987.
- [15] W. K. Baek and R. I. Stephens, “Fatigue life prediction and experimental verification for an automotive suspension component using dynamic simulation and finite element analysis,” in *ASTM Special Technical Publication*, 1992, no. 1122, pp. 354–368.
- [16] F. Conle and C. Mousseau, “Using vehicle dynamics simulations and finite-element

results to generate fatigue life contours for chassis components," *Int. J. Fatigue*, vol. 13, no. 3, pp. 195–205, May 1991.

[17] R. R. J. Craig and M. C. C. Bampton, "Coupling of substructures for dynamic analyses.," *AIAA J.*, vol. 6, pp. 1313–1319, 1968.

[18] J. Ryu, H.-S. Kim, and S. Wang, "A Method of Improving Dynamic Stress Computation for Fatigue Life Prediction of Vehicle Structure," *SAE Tech. Pap.*, 1997.

[19] K. Bladh, "Virtual full vehicle durability testing of a coach," KTH Industrial Engineering and Management - Machine Design - Sweden, 2012.

[20] F. Ambrogi, C. Braccesi, and F. Cianetti, "State of Stress evaluation of structural elements by modal synthesis," in *proc. Adams European Conference, Rome*, 2000.

[21] K. Arczewski and J. Frączek, "Friction models and stress recovery methods in vehicle dynamics modelling," *Multibody Syst. Dyn.*, vol. 14, no. 3, pp. 205–224, 2005.

[22] C. Braccesi and F. Cianetti, "A procedure for the virtual evaluation of the stress state of mechanical systems and components for the automotive industry: development and experimental validation," *Proc. Inst. Mech. Eng. Part D J. Automob. Eng.*, vol. 219, no. 5, pp. 633–643, Jan. 2005.

[23] J. Wannenburg, "A study of of fatigue loading on automotive and transport," PhD Thesis, University of Pretoria, 2007.

[24] M. Veltri, "FEM Techniques for High Stress Detection in Accelerated Fatigue Simulation," in *XII International Conference on Recent Advances in Structural Dynamics, Southampton, UK*, 2016.

[25] R. Gopalakrishnan and H. N. Agrawal, "Durability analysis of full automotive body structures," *SAE Tech. Pap.*, 1993.

[26] E. Y. Kuo and S. G. Kelkar, "Vehicle body structure durability analysis," *SAE Tech. Pap.*, 1995.

[27] L. Huang, H. Agrawal, and V. Borowski, "Durability Analysis of a Vehicle Body Structure Using Modal Transient Methods," in *SPIE, The international Society for Optical Engineering*, 1997, pp. 407–414.

[28] L. Huang, H. Agrawal, and P. Kurudiyara, "Dynamic durability analysis of automotive structures," *SAE Tech. Pap.*, 1998.

[29] S. Vellaichamy, "Transient dynamic fatigue analysis using inertia relief approach with modal resonance augmentation," *SAE Tech. Pap.*, 2002.

[30] S. Donders, M. Brughmans, L. Hermans, and N. Tzannetakis, "The effect of spot weld failure on dynamic vehicle performance," *Sound Vib.*, vol. 39, no. 4, pp. 16–25, 2005.

[31] R. Potukutchi, K. Pal, H. Agrawal, and P. Perumalswami, "Practical approach for fast

durability analysis & iterations," *SAE Tech. Pap.*, 2006.

[32] F. A. Conle and C. C. Chu, "Fatigue analysis and the local stress-strain approach in complex vehicular structures," *Int. J. Fatigue*, vol. 19, no. 93, pp. 317–323, 1997.

[33] MSC Software Corporation, *MSC.Nastran Superelement User's Guide*. Santa Ana, CA, USA, 2004.

[34] A. K. Zaouk, D. Marzougui, and C. D. Kan, "Development of a Detailed Vehicle Finite Element Model Part II: Material Characterization and Component Testing," *Int. J. Crashworthiness*, vol. 5, no. 1, pp. 37–50, 2000.

[35] H. Agrawal, R. Gopalakrishnan, and C. Rivard, "Durability assessment of large automotive body structures using fatigue life analysis procedure (FLAP)," *Int. J. Comput. Appl. Technol.*, vol. 7, no. 3–6, pp. 250–270, 1994.

[36] H. Agrawal, A. Conle, R. Gopalakrishnan, and C. Rivard, "Upfront durability CAE analysis for Automotive Sheet Metal Structures," *SAE Int.*, 1996.

[37] F. Sherratt, N. W. M. Bishop, and T. Dirlit, "Predicting fatigue life from frequency domain data," *J. Eng. Integr. Soc.*, vol. 18, no. September, pp. 12–16, 2005.

[38] S. Dietz, H. Netter, and D. Sachau, "Fatigue life predictions by coupling finite element and multibody systems calculations," in *proceedings ASME DETC*, 1997.

[39] S. Dietz, K. Knothe, and W. Kortüm, "Fatigue life simulations applied to railway bogies," in *The 4TH international Conference on railway bogies and running gear*, 1998, pp. 21–23.

[40] C. Braccesi, F. Cianetti, and L. Landi, "Random loads fatigue. the use of spectral methods within multibody simulation," in *Proceedings of the ASME International Design Engineering Technical Conferences and Computers and Information in Engineering Conference - DETC2005*, 2005, vol. 1 B, pp. 1735–1745.

[41] M. Haiba, D. C. Barton, P. C. Brooks, and M. C. Levesley, "Review of life assessment techniques applied to dynamically loaded automotive components," *Computers & Structures*, vol. 80, no. 5–6, pp. 481–494, 2002.

[42] J. Wannenburg, S. P. Heyns, and A. D. Raath, "Application of a fatigue equivalent static load methodology for the numerical durability assessment of heavy vehicle structures," *Int. J. Fatigue*, vol. 31, no. 10, pp. 1541–1549, 2009.

[43] B. Lin, "A new method of d'Alembert's principle finite element based fatigue calculation with input of loads and accelerations," *SAE Tech. Pap.*, vol. 2, 2013.

[44] T. T. Rantalainen, A. M. Mikkola, and T. J. Björk, "Sub-modeling approach for obtaining structural stress histories during dynamic analysis," *Mech. Sci.*, vol. 4, no. 1, pp. 21–31, Feb. 2013.

[45] C. Braccesi, F. Cianetti, and L. Tomassini, "An innovative modal approach for frequency domain stress recovery and fatigue damage evaluation," *Int. J. Fatigue*, vol. 91, pp. 382–396, 2016.

- [46] Z.-Q. Qu, *Model order reduction techniques*. London: Springer London, 2004.
- [47] T. Rantalainen, "Simulation of Structural Stresss," Lappeenranta University of Technology, 2012.
- [48] S. Dietz, H. Netter, and D. Sachau, "Fatigue Life Pediction of a Railway Bogie under Dynamic Loads through Simulation," *Veh. Syst. Dyn. Int. J.*, vol. 6, 1998.
- [49] R. R. J. Craig and A. J. Kurdila, *Fundamentals of Structural Dynamics*. Wiley, 2006.
- [50] M. Anvari and B. Beigi, "Automotive body fatigue analysis - Inertia relief or transient dynamics?," *SAE Tech. Pap.*, 1999.
- [51] R. L. Bisplinghoff, H. Ashley, and R. L. Halfman, "Aeroelasticity." Dover Publication Inc., Mineola, New York, 1996.
- [52] H. G. Schaeffer, *MSC. NASTRAN Primer for Linear Analysis: Harry G. Schaeffer*. MSC Software Corporation, USA, 2001.
- [53] Y. S. Thipse, "A Methodology to overcome potential pitfall in simulating the physics in a multidisciplinary analysis involving inertia relief for static analysis," *SAE Tech. Pap.*, vol. 5, 2013.
- [54] B. Besselink and U. Tabak, "A comparison of model reduction techniques from structural dynamics, numerical mathematics and systems and control," *J. Sound Vib.*, vol. 332, no. 19, pp. 4403–4422, Sep. 2013.
- [55] J. M. Dickens, J. M. Nakagawa, and M. J. Wittbrodt, "A critique of mode acceleration and modal truncation augmentation methods for modal response analysis," *Comput. Struct.*, vol. 62, no. 6, pp. 985–998, 1997.
- [56] M. Veltri, J. Zeischka, and N. S. Ferguson, "FEM-MBS techniques for stress concentration prediction and accelerated fatigue simulation," in *Int. Conf. on Engineering Simulation: Effective Use and Best Practices, NAFEMS, Cheltenham, UK*, 2008.
- [57] M. Veltri, "FEM-MBS techniques for high stress prediction and accelerated simulation," in *Int. Conf. on Accelerating the Future of CAE, NAFEMS, Oxford, UK*, 2014, pp. 285–288.
- [58] D. Klerk, D. Rixen, and S. Voormeeren, "General framework for dynamic substructuring: history, review and classification of techniques," *AIAA J.*, vol. 46, no. 5, pp. 1169–1181, May 2008.
- [59] W. C. Hurty, "Vibrations of structural Systems by Component Mode Synthesis", " *J. Eng. Mech. Soc. Civ. Eng.*, vol. 86, no. 4, pp. 51–59, 1960.
- [60] R. MacNeal, "A hybrid method of component mode synthesis," *Comput. Struct.*, vol. 1, pp. 581–601, 1971.
- [61] Y. Lu and Z. Ma, "New method of component modal synthesis with high accuracy computational efficiency synthesis flexibility and adaptability," in *Proceedings of*

the International Modal Analysis Conference & Exhibit, 1985, vol. 1, pp. 291–298.

[62] A. Majed, E. E. Henkel, and C. Wilson, “Improved method of mixed-boundary component-mode representation for structural dynamic analysis,” *J. Spacecraft and Rockets*, vol. 42, no. 5, pp. 825–831, 2005.

[63] British Standard, “Code of practice for fatigue design and assessment of steel structures,” *BSI*, no. BS7608. 1993.

[64] British-Adopted European Standard, “Eurocode 3. Design of steel structures. Fatigue.” *BSI*, 2005.

[65] W. Schütz, “A history of fatigue,” *Eng. Fract. Mech.*, vol. 54, no. 2, pp. 263–300, 1996.

[66] *MIL-HDBK-5J: Metallic Materials and Elements for Aerospace Vehicle Structures*. U.S Department of Defence, 2003.

[67] *ASTM E739: Standard Practice for Statistical Analysis of Linear or Linearized Stress-Life (S-N) and Strain-Life (ε-N) Fatigue Data*. 1998.

[68] MSC Software Corp., *MSC Fatigue Theory Guide*. Newport Beach California, USA, 2016.

[69] J. Schijve, “Fatigue damage in aircraft structures , not wanted , but tolerated?,” *Int. J. Fatigue*, vol. 31, no. 6, pp. 998–1011, 2009.

[70] H. Neuber, “Theory of stress concentration for shear-strained prismatic bodies with arbitrary nonlinear stressstrain law,” *J. Appl. Mech.*, vol. 28, no. 4, pp. 544–550, 1961.

[71] T. Seeger and P. Heuler, “Generalized application of Neuber’s rule,” *J. Test. Eval.* 8, 199–204, 1980.

[72] K. Molski and G. Glinka, “A method of elastic –plastic stress and strain calculation at a notch root,” *Mater. Sci. Engng* 50, 93–100, 1981.

[73] G. Glinka, “Energy density approach to calculation of inelastic strain-stress near notches and cracks,” *Eng. Fract. Mech.*, vol. 22, no. 3, pp. 485–508, 1985.

[74] T. Łagoda, “Energy models for fatigue life estimation under uniaxial random loading. Part I: The model elaboration,” *Int. J. Fatigue*, vol. 23, no. 6, pp. 467–480, Jul. 2001.

[75] T. Łagoda, E. Macha, and W. Będkowski, “A critical plane approach based on energy concepts: application to biaxial random tension-compression high-cycle fatigue regime,” *Int. J. Fatigue*, vol. 21, pp. 431–443, 1999.

[76] T. Łagoda, “Energy models for fatigue life estimation under uniaxial random loading. Part II: Verification of the model,” *Int. J. Fatigue*, vol. 23, pp. 481–489, 2001.

[77] F. Berto and P. Lazzarin, "The volume-based Strain Energy Density approach applied to static and fatigue strength assessments of notched and welded structures," *Procedia Eng.*, vol. 1, no. 1, pp. 155–158, Jul. 2009.

[78] P. Lazzarin, F. Berto, F. Gomez, and M. Zappalorto, "Some advantages derived from the use of the strain energy density over a control volume in fatigue strength assessments of welded joints," *Int. J. Fatigue*, vol. 30, no. 8, pp. 1345–1357, Aug. 2008.

[79] J. Tang, V. Ogarevic, and C.-S. Tsai, "An integrated CAE environment for simulation-based durability and reliability design," *Adv. Eng. Softw.*, vol. 32, no. 1, pp. 1–14, Jan. 2001.

[80] M. Matsuishi and T. Endo, "Fatigue of metals subjected to varying stress," *Japan Soc. Mech. Eng. Fukuoka, Japan*, vol. 68, no. 2, pp. 37–40, 1968.

[81] A. K. Khosrovaneh and N. E. Dowling, "Fatigue loading history reconstruction based on the rainflow technique," *Int. J. Fatigue*, vol. 12, no. 2, pp. 99–106, 1990.

[82] R. M. Wetzel (ed.), "Fatigue under Complex Loading: Analyses and Experiments," *Advances in Engineering, AE-6, SAE*, 1977.

[83] NCode, *DesignLife User Guide*. HBM UK Ltd, 2012.

[84] J. Zeischka, M. Veltri, P. Adolfsson, U. Bruder, and M. Coleman, "Automated Durability Design of Crankshafts Based on MSC.Adams/Engine," in *Int. Conf. on Component and System Analysis Using Numerical Simulation Techniques, NAFEMS Gothenburg, Sweden*, 2005.

[85] N. E. Dowling, "Mean stress effects in stress-life and strain-life fatigue," *SAE Tech. Pap.*, 2004.

[86] W. Weibull, "A statistical distribution function of wide applicability," *Journal of applied mechanics*, vol. 18, pp. 293–297, 1951.

[87] W. Yao, K. Xia, and Y. Gu, "On the fatigue notch factor, Kf," *Int. J. Fatigue*, vol. 17, no. 4, pp. 245–251, 1995.

[88] A. Rupp, K. Störzel, and V. Grubisic, "Computer aided dimensioning of spot-welded automotive structures," *SAE Tech. Pap.*, 1995.

[89] H.-F. Henrysson, "Fatigue life predictions of spot welds using coarse FE meshes," *Fatigue Fract. Eng. Mater. Struct.*, vol. 23, no. 9, pp. 737–746, 2000.

[90] M. Fermér and H. Svensson, "Industrial experiences of FE-based fatigue life predictions of welded automotive structures," *Fatigue Fract. Eng. Mater. Struct.*, vol. 24, no. 7, pp. 489–500, 2001.

[91] J. J. F. Bonnen, H. Agrawal, M. A. Amaya, R. M. Iyengar, H. Kang, A. K. Khosrovaneh, T. M. Link, H.-C. Shih, M. Walp, and B. Yan, "Fatigue of Advanced High Strength Steel spot-welds," *SAE Tech. Pap.*, 2006.

- [92] J. Schijve, "Statistical distribution functions and fatigue of structures," *Int. J. Fatigue*, vol. 27, no. 9, pp. 1031–1039, 2005.
- [93] F. Proschan and N. D. Singpurwalla, "A new approach to inference from accelerated life in tests," *IEEE Trans. Reliab.*, vol. 29, no. 2, pp. 98–102, 1980.
- [94] Y. Ling, C. Shantz, S. Mahadevan, and S. Sankararaman, "Stochastic prediction of fatigue loading using real-time monitoring data," *Int. J. Fatigue*, vol. 33, no. 7, pp. 868–879, 2011.
- [95] M. Gobbato, J. B. Kosmatka, and J. P. Conte, "A recursive Bayesian approach for fatigue damage prognosis: An experimental validation at the reliability component level," *Mech. Syst. Signal Process.*, vol. 45, no. 2, pp. 448–467, 2014.
- [96] M. Corbetta, C. Sbarufatti, A. Manes, and M. Giglio, "Real-time prognosis of random loaded structures via Bayesian filtering: A preliminary discussion," *Eng. Fract. Mech.*, vol. 145, pp. 143–160, 2015.
- [97] T. Fawcett, "An introduction to ROC analysis," *Pattern Recognition Letters*, vol. 27, no. 8, pp. 861–874, 2006.
- [98] H. O. Fuchs, D. V Nelson, M. A. Burke, and T. L. Toomay, "Shortcuts in cumulative damage analysis," *SAE Tech. Pap.*, 1973.
- [99] D. F. Socie and P. J. Artwohl, "Effect of Spectrum editing on fatigue crack initiation and propagation in a notched member," in *Effect of Load Spectrum Variables on Fatigue Crack Initiation and Propagation*, ASTM International, 1980.
- [100] A. Hurd, "Combining accelerated laboratory durability with squeak and rattle evaluation," in *SAE Preprints*, 1991, no. 244, pp. 107–118.
- [101] H. Caruso and A. Dasgupta, "A Fundamental Overview of Accelerated -Testing - Analytic Models," in *Annual Reliability and Maintainability Symposium*, 1998, pp. 389–393.
- [102] C. Farrar and T. Duffey, "A review of methods for developing accelerated testing criteria," *Proc. 17th IMAC Int. Modal Anal. Conf.*, 1999.
- [103] J. Yan, X. Zheng, and K. Zhao, "Experimental investigation on the small-load-omitting criterion," *Int. J. Fatigue*, vol. 23, pp. 403–415, 2001.
- [104] X.-L. Zheng, "Modelling fatigue crack initiation life," *Int. J. Fatigue*, vol. 15, no. 6, pp. 461–466, Nov. 1993.
- [105] N. a. Kadhim, S. Abdullah, and a. K. Ariffin, "Effect of the fatigue data editing technique associated with finite element analysis on the component fatigue design period," *Mater. Des.*, vol. 32, no. 2, pp. 1020–1030, Feb. 2011.
- [106] F. A. Conle, "Durability analysis under complex multiaxial loading," *SAE Tech. Pap.*, 1987.
- [107] L. Huang and H. Agrawal, "Method of identifying critical elements in fatigue

analysis with Von Mises stress bounding and filtering modal displacement history using dynamic windowing," U.S. Patent No. 6,212,486 B1, 3 Apr., 2001.

- [108] ECS, *FEMFAT 4.8 BASIC, User Manual*. Magna Powertrain, 2009.
- [109] "SAE Fatigue Design and Evaluation Committee, meeting minutes." [Online]. Available: <http://www.fatigue.org/>.
- [110] K. N. Shenoy, "Finite Element Analysis of ATV Frame and Generation of Stress Tensors for Load-Time Histories," Master of Science thesis, The University of Toledo, 2002.
- [111] N. A. Kulkarni, "An Investigation into the Impact of Driver Motion on the Vehicle Dynamics of All Terrain Vehicles," Master of Science thesis, The University of Toledo, 2002.
- [112] G. V. Markale, "Virtual Prototyping of an All Terrain Vehicle for Durability Loads Prediction," Master of Science thesis, The University of Toledo, 2002.
- [113] *Theory of Flexible Bodies, ADAMS Flex, V2013*. MSC Software Corporation, USA.
- [114] T. Breitfeld and F. Buschbeck, "Finite element simulation," U.S. Patent No. 7,440,879, 21 Oct., 2008.
- [115] S. Timoshenko, *Vibration Problems in Engineering*. New York: D. Van Nostrand Co. Inc, 1937.
- [116] L. Meirovitch, *Principles and techniques of vibrations*. Prentice Hall, New Jersey, 1997.
- [117] X. Pitoiset, A. Preumont, and A. Kernilis, "Tools for a Multiaxial Fatigue Analysis of Structures Submitted to Random Vibrations," in *Proc European Conference on Spacecraft Structures Materials and Mechanical Testing*, 1998.
- [118] nCode, *DesignLife V8, Theory Guide*. HBM UK Ltd, 2012.
- [119] C. Leser, T. E. Renner, and D. C. Salmon, "Accurate shock absorber load modeling in an all terrain vehicle using black box neural network techniques," *SAE Tech. Pap.*, 2002.
- [120] G. Wang, D. Socie, and R. Mousseau, "Flexible Body Dynamic Simulation of an ATV Frame and Suspension System," in *North American MDI User Conference*, 2001.

